

Stéphane Sebban
Julien Gautier
David Ros
Philippe Zeitoun *Editors*

X-Ray Lasers 2012

Proceedings of the 13th International
Conference on X-Ray Lasers, 11–15 June
2012, Paris, France

Springer Proceedings in Physics

Volume 147

For further volumes:
www.springer.com/series/361

Stéphane Sebban • Julien Gautier • David Ros •
Philippe Zeitoun

Editors

X-Ray Lasers 2012

Proceedings of the 13th International
Conference on X-Ray Lasers, 11–15 June
2012, Paris, France



Springer

Editors

Stéphane Sebhan
Laboratoire d'Optique Appliquée
ENSTA
Palaiseau, France

David Ros
LPGP
Université Paris-Sud
Orsay, France

Julien Gautier
Laboratoire d'Optique Appliquée
ENSTA
Palaiseau, France

Philippe Zeitoun
Laboratoire d'Optique Appliquée
ENSTA
Palaiseau, France

ISSN 0930-8989

Springer Proceedings in Physics
ISBN 978-3-319-00695-6
DOI 10.1007/978-3-319-00696-3
Springer Cham Heidelberg New York Dordrecht London

ISSN 1867-4941 (electronic)

ISBN 978-3-319-00696-3 (eBook)

Library of Congress Control Number: 2013948223

© Springer International Publishing Switzerland 2014

This work is subject to copyright. All rights are reserved by the Publisher, whether the whole or part of the material is concerned, specifically the rights of translation, reprinting, reuse of illustrations, recitation, broadcasting, reproduction on microfilms or in any other physical way, and transmission or information storage and retrieval, electronic adaptation, computer software, or by similar or dissimilar methodology now known or hereafter developed. Exempted from this legal reservation are brief excerpts in connection with reviews or scholarly analysis or material supplied specifically for the purpose of being entered and executed on a computer system, for exclusive use by the purchaser of the work. Duplication of this publication or parts thereof is permitted only under the provisions of the Copyright Law of the Publisher's location, in its current version, and permission for use must always be obtained from Springer. Permissions for use may be obtained through RightsLink at the Copyright Clearance Center. Violations are liable to prosecution under the respective Copyright Law.

The use of general descriptive names, registered names, trademarks, service marks, etc. in this publication does not imply, even in the absence of a specific statement, that such names are exempt from the relevant protective laws and regulations and therefore free for general use.

While the advice and information in this book are believed to be true and accurate at the date of publication, neither the authors nor the editors nor the publisher can accept any legal responsibility for any errors or omissions that may be made. The publisher makes no warranty, express or implied, with respect to the material contained herein.

Printed on acid-free paper

Springer is part of Springer Science+Business Media (www.springer.com)

Preface

These proceedings comprise invited and contributed papers presented at the 13th International Conference on X-Ray Lasers (ICXRL 2012) which was held 11–15 June 2012 in Paris, in the famous Quartier Latin, inside the historical Center of Cordeliers. This conference is part of a continuing series dedicated to recent developments and applications of x-ray lasers and other coherent x-ray sources with attention to supporting technologies and instrumentation.

New results in the generation of intense, coherent x-rays and progress towards practical devices and their applications are reported in these proceedings, including areas of research in plasma-based x-ray lasers, 4th generation accelerator-based sources and higher harmonic generation.

Recent achievements related to the increase of the repetition rate up to 100 Hz and shorter wavelength collisional plasma-based soft x-ray lasers down to about 7 nm are presented. Seeding the amplifying plasma with a femtosecond high-order harmonic of infrared laser was foreseen as the required breakthrough to break the picosecond frontier. Numerical simulations based on the Maxwell-Bloch model are presented in these proceedings, transposing the chirped pulse amplification technique to the x-ray domain in order to increase the time over which the femtosecond seed can be amplified.

These proceedings also include innovative applications of soft x-ray lasers based on techniques and diagnostics relevant to topical domains such as EUV lithography, inertial confinement fusion, or warm dense matter physics.

We would like to thank the International Advisory Board for helping to organize the scientific program and the Local Organizing Committee for operation of the meeting. Also we would like to thank the Conference Secretary and the supporting staff for running the conference smoothly and editing these conference proceedings.

Paris, France

Stéphane Sebban
Julien Gautier
David Ros
Philippe Zeitoun

Conference Organization

Conference Chair

Stéphane Sebban

Conference Co-Chairs

David Ros

Philippe Zeitoun

International Advisory Board

Attwood David (LBNL, USA)

Balmer J. (Univ. of Bern, Switzerland)

Bulanov S. (APRI, Japan)

Daido H. (JAEA, Japan)

Dunn J. (LLNL, USA)

Feldhauss J. (Desy, Germany)

Fill E. (MPQ, Germany)

Janulewicz K.A. (GIST, Korea)

Kato Y. (GPI, Japan)

Klisnick A. (ISMO, France)

Lewis C.L.S. (Queen's Univ., UK)

Nam C.H. (KAIST, Korea)

Nickles P.V. (MBI, Germany/GIST, Korea)

Pert G.J. (Univ. of York, UK)

Rocca J.J. (Colorado State Univ., USA)

Rus B. (PALS, Czech)

Sebban S. (LOA, France)

Suckewer S. (Princeton Univ., USA)

Tallents G.J. (Univ. of York, UK)

Vinogradov A. (LPI, Russia)

Xu Z.Z. (SIOM, China)

Zhang J. (STU, China)

Local Organizing Committee

Kevin Cassou (LPGP)
Brigitte Cros (LPGP)
Sylvie Jacquemot (LULI)
Sophie Kazamias (LPGP)
Annie Klisnick (ISMO)
Julien Gautier (LOA)
Olivier Guilbaud (LPGP)
Gilles Maynard (LPGP)
Moana Pittman (LUMAT)
Fabien Tissandier (LOA)

Sponsors

Institutions

Centre national de recherché Scientifique (CNRS)
Ecole Polytechnique
Ecole Nationale Supérieure des Techniques Avancées (ENSTA)
Triangle de la physique
Institut Lasers et Plasma
GDR APPLIX

Companies

Micro-Controle
Spectra-Physics
Plug in
BFI Optilas
Roper
Amplitude technologies
Optoprim
Imagine Optic
Andor technology
Source Lab
Quantel

Contents

1	Coherent Pulses from a Seeded Free-Electron Laser in the Extreme Ultraviolet	1
	E. Allaria, D. Castronovo, G. De Ninno, S. Di Mitri, W. Fawley, E. Ferrari, L. Froehlich, L. Giannessi, B. Mahieu, G. Penco, C. Spezzani, and M. Trovo	
2	Enhancement of Efficiency of XUV Generation in Atomic Gases Irradiated by Intense Laser Fields	7
	A.V. Andreev, S.Y. Stremoukhov, and O.A. Shoutova	
3	All-Optical Raman XFEL, Based on the Electron Emission in a Transverse High Intensity Optical Lattice	13
	I.A. Andriyash, E. d'Humières, V.T. Tikhonchuk, and P. Balcou	
4	Optical Transforms Related to Coherent Imaging of Inclined Objects	19
	I.A. Artyukov, A.S. Busarov, N.L. Popov, and A.V. Vinogradov	
5	Soft-X-Ray Lasing down to 6.85 nm in Ni-Like Samarium	29
	J.E. Balmer, F. Staub, and F. Jia	
6	Fourier Optics Study of Traveling-Wave Excitation at Short-Wavelength Plasma-Lasing	35
	Davide Bleiner and Thomas Feurer	
7	Coherent Short-Wavelength Plasma Radiation for Lab-scale Nano-inspection Tools	39
	Davide Bleiner	
8	Ion Temperature and Cross-relaxation Effects on OFI Soft-X-Ray Laser	45
	A. Boudaa, G. Maynard, and B. Cros	

9	Study of Particle Correlation Effects on Line Profiles of Ni-Like Collisional XUV Laser Amplifier	49
	A. Calisti, S. Ferri, C. Mossé, B. Talin, A. Klisnick, L. Meng, D. Benredjem, and O. Guilbaud	
10	The LUNEX5 Project in France	55
	M.E. Couplie, C. Benabderrahmane, P. Betinelli, F. Bouvet, A. Buteau, L. Cassinari, J. Daillant, J.C. Denard, P. Eymard, B. Gagey, C. Herbeaux, M. Labat, A. Lestrade, A. Loulergue, P. Marchand, J.L. Marlats, C. Miron, P. Morin, A. Nadji, F. Polack, J.B. Pruvost, F. Ribeiro, J.P. Ricaud, P. Roy, T. Tanikawa, R. Roux, S. Bielawski, C. Evain, C. Szwaj, G. Lambert, A. Lifschitz, V. Malka, R. Lehe, A. Rousse, K. Ta Phuoc, C. Thaury, G. Devanz, M. Luong, B. Carré, G. LeBec, L. Farvacque, A. Dubois, and J. Lüning	
11	High Harmonic Generation Driven by Two Quasi-collinear Pulses	63
	S. Daboussi, S. Kazamias, K. Cassou, O. Guilbaud, M. Pittman, O. Delmas, O. Neveu, B. Cros, G. Maynard, and D. Ros	
12	Real-Time Observation of Laser Heated Metals with High Brightness Monochromatic X-Ray Techniques at Present and Their Future Prospects	69
	H. Daido, T. Shobu, T. Yamada, S. Yamashita, K. Sugihara, A. Nishimura, and T. Muramatsu	
13	Generation and Application of Coherent Radiation in the Water Window	77
	L.V. Dao, C. Hall, H.L. Vu, K.B. Dinh, N. Gaffney, E. Balaur, P. Hannaford, and T.A. Smith	
14	Time-Dependent Simulation of Carbon Illuminated by a High Intensity X-Ray Laser	83
	Alberto G. de la Varga, Pedro Velarde, François de Gaufridy, Manuel Cotelo, David Portillo, and Philippe Zeitoun	
15	Regenerative Laser Cavity Tuning for Efficient Soft-X-Ray Laser Operation	89
	O. Delmas, K. Cassou, O. Guilbaud, S. Kazamias, S. Daboussi, M. Pittman, O. Neveu, J. Demailly, and D. Ros	
16	X-Ray Laser Developments at PHELIX	97
	B. Ecker, B. Aurand, D.C. Hochhaus, P. Neumayer, B. Zielbauer, K. Cassou, S. Daboussi, O. Guilbaud, S. Kazamias, T.T.T. Le, E. Oliva, L. Li, H. Zhao, Q. Jin, D. Ros, P. Zeitoun, and T. Kuehl	
17	Parabolic Equation and Exact Transparent Boundary Conditions in X-Ray Optics—Application to Waveguides and Whispering Gallery Optics	105
	R.M. Feshchenko and A.V. Popov	

18 Harmonic Generation and Soft-X-Ray Laser with LASERIX: Source Development, Applications and Advanced Diagnosis	109
Olivier Guilbaud, Sophie Kazamias, Kevin Cassou, Moana Pittman, Sameh Daboussi, Olivier Delmas, Julien Demailly, Olivier Neveu, Chris Pouhe, Boris Vodungbo, Philippe Zeitoun, Lucy Wilson, Greg Tallents, Antonin Dusseix, Gabriel Richet, Aurelie Gense, Bich-Lien Nghiem, Brigitte Cros, Gilles Maynard, and David Ros	
19 Observation of the Laser-Induced Surface Dynamics Using the Single-Shot Soft X-Ray Laser Probe	117
N. Hasegawa, Y. Ochi, T. Kawachi, M. Nishikino, M. Ishino, T. Imazono, T. Kaihori, T. Morita, A. Sasaki, K. Terakawa, Y. Minami, M. Baba, T. Tomita, M. Yamamoto, M. Yamagiwa, and T. Suemoto	
20 Nano-meter Size Modification of Metal Surfaces Induced by Soft X-Ray Laser Single Pulse	121
Masahiko Ishino, Anatoly Faenov, Momoko Tanaka, Tatiana Pikuz, Satoshi Tamotsu, Noboru Hasegawa, Masaharu Nishikino, Sergei Starikov, Vladimir Stegailov, Genry Norman, Vladimir Fortov, Igor Skobelev, Takeshi Kaihori, and Tetsuya Kawachi	
21 Speckle Statistics, Coherence and Polarization of a Collisional Soft X-Ray Laser	125
K.A. Janulewicz, C.M. Kim, P.V. Nickles, H. Stiel, M. Nishikino, N. Hasegawa, and T. Kawachi	
22 Upscaling of X-Ray Laser Repetition Rate Using an OPCPA Architecture	137
Fei Jia, Felix Staub, and Jürg Balmer	
23 Source Development of Novel Coherent X-Rays and Their Applications in JAEA	143
T. Kawachi, A. Sasaki, M. Nishikino, M. Ishino, N. Hasegawa, T. Imazono, Y. Ochi, M. Tanaka, A.Y. Faenov, T.A. Pikuz, A. Pirozhkov, T. Esirkepov, T. Nakamura, M. Kando, S.V. Bulanov, K. Kondo, K. Janulewicz, C.M. Kim, H. Stiel, G. Norman, T. Suemoto, T. Tomita, K. Namikawa, M. Yamagiwa, and Y. Kato	
24 Characterization of Zn X-Ray Laser at PALS Centre, Its Applications in Dense Plasma Probing and Astrophysics	151
M. Kozlova, J. Nejdl, M. Krus, J. Prokupek, J. Dostal, B. Rus, A. Klisnick, L. Meng, F. Tissandier, C. Stehlé, R. Lefevre, U. Chaulagain, N. Champion, P. Barroso, F. Reix, P. Jagourel, J. Larour, F. Delmotte, C. Constancias, F. Suzuki-Vidal, and O. Acef	
25 Development of High Reflective Multilayer Mirrors at “Water Window” Wavelengths in IPOE	161
Haochuan Li, Jingtao Zhu, and Zhanshan Wang	

26 Time Resolved Holography Scheme Using a Table Top Soft X-Ray Laser	165
E.B. Malm, N.C. Monserud, P.W. Wachulak, C. Brown, W. Chao, E. Anderson, H. Xu, C.P. Hains, G. Balakrishnan, C.S. Menoni, J.J. Rocca, and M.C. Marconi	
27 Plasma Homogenization for Overcoming Refractive Losses in X-Ray Lasers	171
Leili Masoudnia and Davide Bleiner	
28 Temporal Coherence and Spectral Linewidth of Neon-Like XUV Lasers Pumped in the Quasi-steady State Regime	175
L. Meng, A. Klisnick, M. Kozlova, K. Bohacek, M. Krus, J. Prokupek, L. Urbanski, M.C. Marconi, M. Berrill, J.J. Rocca, O. Guilbaud, F. Tissandier, S. Sebban, P. Zeitoun, A. Calisti, S. Ferri, C. Mossé, and B. Talin	
29 Spectral Broadening of Ni-Like XUV Laser Lines	181
L. Meng, A. Calisti, S. Ferri, C. Mossé, B. Talin, D. Benredjem, O. Guilbaud, and A. Klisnick	
30 Visualization of Rapid Dynamic Interactions by Flash Soft X-Ray Microscopy	185
C.S. Menoni, S. Carbajo, I.D. Howlett, W. Chao, E.H. Anderson, A.V. Vinogradov, I.A. Artioukov, K. Buchanan, M.C. Marconi, and J.J. Rocca	
31 Using the X-FEL to Understand X-Ray Thomson Scattering for Partially Ionized Plasmas	193
Joseph Nilsen, Walter R. Johnson, and K.T. Cheng	
32 Development of Soft X-Ray Microscopy Using Fresnel Zone Plate for Observation of Laser-Induce Surface Dynamics	199
M. Nishikino, M. Baba, T. Suemoto, N. Hasegawa, M. Ishino, T. Kaihori, T. Kawachi, and M. Yamagiwa	
33 0.27 GW Soft X-Ray Pulse Using a Plasma-Based Amplification Chain	203
E. Oliva, M. Fajardo, P. Velarde, D. Ros, S. Sebban, and P. Zeitoun	
34 Harmonic Generation in Argon by Femtosecond Ti:Sapphire Laser .	209
Rabia Qindeel, Ricardo Elgul Samad, Anderson Zanardi de Freitas, Paulo Sergio Fabris de Matos, Edilson Lucena Falcão, and Nilson Dias Vieira Junior	
35 Demonstration of a 100 Hz Repetition Rate Soft X-Ray Laser and Gain-Saturated Sub-10 nm Table-Top Lasers	215
J.J. Rocca, B.A. Reagan, Y. Wang, D. Alessi, K. Wernsing, B.M. Luther, M.A. Curtis, M. Berrill, D. Martz, S. Wang, L. Yin, F. Furch, M. Woolston, D. Patel, V.N. Shlyaptsev, and C.S. Menoni	

36 Optical Correction of X-Ray Laser Illumination for Short-Wavelength Microscopy	227
Mabel Ruiz-Lopez, Felix Staub, and Davide Bleiner	
37 Repetitive XUV Discharge-Pumped Laser at 46.9 nm	231
Jiri Schmidt, Karel Kolacek, Oleksandr Frolov, Vaclav Prukner, and Jaroslav Straus	
38 Line-Focus Generation for X-Ray Laser Pumping	235
F. Staub, D. Bleiner, F. Jia, and J.E. Balmer	
39 Critical Components for XUV Probing of Laser Driven Shocks	239
C. Stehlé, R. Lefèvre, U. Chaulagain, N. Champion, P. Barroso, F. Reix, P. Jagourel, J. Larour, E. Melchakov, R. Mercier, F. Delmotte, M. Kozlova, J. Nejdl, M. Krus, J. Dostal, J. Prokupek, C. Constancias, F. Suzuki-Vidal, and O. Acef	
40 High Density Optical-Field-Ionization Soft X-Ray Lasers	243
F. Tissandier, S. Sebban, M. Kozlova, J. Gautier, P. Zeitoun, A. Klisnick, and G. Maynard	
41 Spectral Linewidth Measurement of a Ne-Like Ar Capillary Discharge Soft X-Ray Laser	257
L. Urbanski, M.C. Marconi, L.M. Meng, M. Berrill, O. Guilbaud, A. Klisnick, and J.J. Rocca	
42 Defect Tolerant Talbot Nanopatterning	263
L. Urbanski, M.C. Marconi, A. Isoyan, A. Stein, C.S. Menoni, and J.J. Rocca	
43 Imaging in Nanoscale Using Laser-Plasma Sources of Extreme Ultraviolet (EUV)	269
P.W. Wachulak, A. Bartnik, A. Baranowska-Korczyk, D. Pánek, P. Brůža, J. Kostecki, Ł. Węgrzyński, R. Jarocki, M. Szczurek, K. Fronc, D. Elbaum, and H. Fiedorowicz	
44 Experiments to Diagnose Plasma with a Soft X-Ray Laser Double-Frequency Grating Interferometry	277
C. Wang, H.H. An, Z.H. Fang, J.R. Sun, W. Wang, W.D. Zheng, X.M. Qiao, and S.J. Wang	
45 Heavy-Ion Spectroscopy with X-Ray Lasers at GSI	283
B. Zielbauer, B. Ecker, P. Neumayer, K. Cassou, S. Daboussi, O. Guilbaud, S. Kazamias, D. Ros, T. Kuehl, U. Eisenbarth, S. Goette, D. Winters, V. Bagnoud, and T. Stoehlker	
Index	287

Contributors

O. Acef SYRTE, Observatoire de Paris, UPMC, CNRS, LNE, Paris, France

D. Alessi National Science Foundation ERC for Extreme Ultraviolet Science and Technology, Fort Collins, USA; Department of Electrical and Computer Engineering, Colorado State University, Fort Collins, CO, USA

E. Allaria Elettra-Sincrotrone Trieste, Basovizza, Trieste, Italy

H.H. An Shanghai Institute of Laser Plasma, Shanghai, China

E.H. Anderson NSF ERC for Extreme Ultraviolet Science and Technology, Department of Electrical & Computer Engineering, Colorado State University, Fort Collins, CO, USA; NSF ERC for Extreme Ultraviolet Science and Technology and Center for X-ray Optics, LBNL, Berkeley, CA, USA

A.V. Andreev Physics Department, M.V. Lomonosov Moscow State University, Moscow, Russia

I.A. Andriyash Univ. Bordeaux, CNRS, CEA, CELIA (Centre Lasers Intenses et Applications), Talence, France

I.A. Artyukov P.N. Lebedev Physical Institute, Moscow, Russia

B. Aurand Johannes-Gutenberg Universität Mainz, Mainz, Germany; ExtreMe Matter Institute EMMI, Darmstadt, Germany; GSI Helmholtzzentrum fuer Schwerionenforschung, Darmstadt, Germany

M. Baba Institute of Solid State Physics, The University of Tokyo, Kashiwa, Chiba, Japan

V. Bagnoud Helmholtz Institute Jena, Jena, Germany; GSI Helmholtz Center for Heavy-Ion Research, Darmstadt, Germany

G. Balakrishnan Department of Electrical Engineering, University of New Mexico and Center for High Technology Materials, Albuquerque, NM, USA

E. Balař Department of Physics, La Trobe University, Melbourne, Australia; Australian Research Council Centre of Excellence for Coherent X-Ray Science, Melbourne, Australia

P. Balcou Univ. Bordeaux, CNRS, CEA, CELIA (Centre Lasers Intenses et Applications), Talence, France

J.E. Balmer Institute of Applied Physics, University of Bern, Bern, Switzerland

A. Baranowska-Korczyc Institute of Physics, Polish Academy of Sciences, Warsaw, Poland

P. Barroso GEPI, Observatoire de Paris, Univ. Paris-Diderot, CNRS, Paris, France

A. Bartnik Institute of Optoelectronics, Military University of Technology, Warsaw, Poland

C. Benabderrahmane Synchrotron SOLEIL, Saint-Aubin, France

D. Benredjem LAC, CNRS-Université Paris-Sud, Orsay, France

M. Berrill NSF-ERC for EUV Science and Technology, Colorado State University, Fort Collins, USA; National Science Foundation ERC for Extreme Ultraviolet Science and Technology, Fort Collins, USA; Department of Electrical and Computer Engineering, Colorado State University, Fort Collins, CO, USA; Oak Ridge National Laboratory, Oak Ridge, TN, USA

P. Betinelli Synchrotron SOLEIL, Saint-Aubin, France

S. Bielawski PhLAM/CERLA, Lille, France

D. Bleiner Institute of Applied Physics, University of Bern, Bern, Switzerland

K. Bohacek Institute of Physics of ASCR, Prague, Czech Republic

A. Boudaa Laboratoire de Physique et Chimie Quantique, Université M. Mammeri de Tizi-Ouzou, Hasnaoua, Algérie; Laboratoire de Physique des Gaz et des Plasmas, Univ. Paris-Sud, Orsay, France

F. Bouvet Synchrotron SOLEIL, Saint-Aubin, France

C. Brown Department of Electrical Engineering, Colorado State University and Engineering Research Center for Extreme Ultraviolet Science and Technology, Fort Collins, CO, USA

P. Brůža Czech Technical University, Prague, Czech Republic

K. Buchanan Physics Department, Colorado State University, Fort Collins, CO, USA

S.V. Bulanov Quantum Beam Science Directorate, JAEA, Kizugawa, Kyoto, Japan

A.S. Busarov P.N. Lebedev Physical Institute, Moscow, Russia

A. Buteau Synchrotron SOLEIL, Saint-Aubin, France

A. Calisti PIIM, CNRS-Aix-Marseille Université, Marseille, France

S. Carbajo NSF ERC for Extreme Ultraviolet Science and Technology, Department of Electrical & Computer Engineering, Colorado State University, Fort Collins, CO, USA

B. Carré CEA/DSM/IRAMIS/SPAM, Saclay, France

L. Cassinari Synchrotron SOLEIL, Saint-Aubin, France

K. Cassou CLUPS/LASERIX, Université Paris Sud XI, Orsay Cedex, France; LPGP, Univ. Paris-Sud, UMR 8578, CNRS, Orsay Cedex, France

D. Castronovo Elettra-Sincrotrone Trieste, Basovizza, Trieste, Italy

N. Champion Lerma, Observatoire de Paris, UPMC, CNRS, Paris, France

W. Chao NSF ERC for Extreme Ultraviolet Science and Technology, Department of Electrical & Computer Engineering, Colorado State University, Fort Collins, CO, USA; NSF ERC for Extreme Ultraviolet Science and Technology and Center for X-ray Optics, LBNL, Berkeley, CA, USA

U. Chaulagain Lerma, Observatoire de Paris, UPMC, CNRS, Paris, France

K.T. Cheng Lawrence Livermore National Laboratory, Livermore, CA, USA

C. Constancias CEA-LETI, Grenoble, France

Manuel Cotelo Instituto de Fusión Nuclear, Universidad Politécnica de Madrid, Madrid, Spain

M.E. Couprise Synchrotron SOLEIL, Saint-Aubin, France

B. Cros LPGP, Univ. Paris-Sud, UMR 8578, CNRS, Orsay Cedex, France

M.A. Curtis National Science Foundation ERC for Extreme Ultraviolet Science and Technology, Fort Collins, USA; Department of Electrical and Computer Engineering, Colorado State University, Fort Collins, CO, USA

E. d'Humières Univ. Bordeaux, CNRS, CEA, CELIA (Centre Lasers Intenses et Applications), Talence, France

S. Daboussi CLUPS/LASERIX, Université Paris Sud XI, Orsay Cedex, France; LPGP, Univ. Paris-Sud, UMR 8578, CNRS, Orsay Cedex, France

H. Daido Applied Laser Technology Institute Tsuruga Head Office, Japan Atomic Energy Agency, Tsuruga, Fukui, Japan; Quantum Beam Directorate, Japan Atomic Energy Agency, Kizugawa, Kyoto, Japan

J. Daillant Synchrotron SOLEIL, Saint-Aubin, France

L.V. Dao Centre for Atom Optics and Ultrafast Spectroscopy, Swinburne University of Technology, Melbourne, Australia; Australian Research Council Centre of Excellence for Coherent X-Ray Science, Melbourne, Australia

Anderson Zanardi de Freitas Centro de Lasers e Aplicações, IPEN, CNEN/SP, Sao Paulo, Brazil

François de Gaufridy Instituto de Fusión Nuclear, Universidad Politécnica de Madrid, Madrid, Spain; Institute of Physics, Czech Academy of Sciences, Prague, Czech Republic

Paulo Sergio Fabris de Matos Centro de Lasers e Aplicações, IPEN, CNEN/SP, Sao Paulo, Brazil

G. De Ninno Elettra-Sincrotrone Trieste, Basovizza, Trieste, Italy; Dept. of Physics, University of Nova Gorica, Nova Gorica, Slovenia

O. Delmas CLUPS/LASERIX, Université Paris Sud XI, Orsay Cedex, France; Amplitude Technologies, Lisses, France; LPGP, Univ. Paris-Sud, UMR 8578, CNRS, Orsay Cedex, France

F. Delmotte LCF, Institut d'Optique, CNRS, PXI, Palaiseau, France

J. Demainly CLUPS/LASERIX, Université Paris Sud XI, Orsay Cedex, France; Laboratoire de Physique des Gaz et Plasma, CNRS-Université Paris Sud, Orsay, France

J.C. Denard Synchrotron SOLEIL, Saint-Aubin, France

G. Devanz CEA/DSM/IRFU/SACM, Saclay, France

Alberto G. de la Varga Instituto de Fusión Nuclear, Universidad Politécnica de Madrid, Madrid, Spain

S. Di Mitri Elettra-Sincrotrone Trieste, Basovizza, Trieste, Italy

K.B. Dinh Centre for Atom Optics and Ultrafast Spectroscopy, Swinburne University of Technology, Melbourne, Australia; Australian Research Council Centre of Excellence for Coherent X-Ray Science, Melbourne, Australia

J. Dostal IoP/PALS Center, Prague, Czech Republic

A. Dubois LCPMR, Paris-VI, France

Antonin Dusseix Laboratoire de Physique des Gaz et Plasma, CNRS-Université Paris Sud, Orsay, France

B. Ecker Helmholtz Institute Jena, Jena, Germany; Johannes-Gutenberg Universität Mainz, Mainz, Germany

U. Eisenbarth GSI Helmholtz Center for Heavy-Ion Research, Darmstadt, Germany

D. Elbaum Institute of Physics, Polish Academy of Sciences, Warsaw, Poland

T. Esirkepov Quantum Beam Science Directorate, JAEA, Kizugawa, Kyoto, Japan

C. Evain PhLAM/CERLA, Lille, France

P. Eymard Synchrotron SOLEIL, Saint-Aubin, France

A.Y. Faenov Quantum Beam Science Directorate, JAEA, Kizugawa, Kyoto, Japan; Joint Institute for High Temperatures, Russian Academy of Science, Moscow, Russia

M. Fajardo Centro de Física dos Plasmas, Instituto Superior Técnico, Lisbon, Portugal

Edilson Lucena Falcão Physics Department, UFPE, Recife, Brazil

Z.H. Fang Shanghai Institute of Laser Plasma, Shanghai, China

L. Farvacque ESRF, Grenoble, France

W. Fawley Elettra-Sincrotrone Trieste, Basovizza, Trieste, Italy

E. Ferrari Elettra-Sincrotrone Trieste, Basovizza, Trieste, Italy; Dept. of Physics, University of Nova Gorica, Nova Gorica, Slovenia

S. Ferri PIIM, CNRS-Aix-Marseille Université, Marseille, France

R.M. Feshchenko P.N. Lebedev Physical Institute of RAS, Moscow, Russia

Thomas Feurer Institute of Applied Physics, University of Bern, Bern, Switzerland

H. Fiedorowicz Institute of Optoelectronics, Military University of Technology, Warsaw, Poland

Vladimir Fortov Joint Institute for High Temperatures, Russian Academy of Sciences, Moscow, Russia

L. Froehlich Elettra-Sincrotrone Trieste, Basovizza, Trieste, Italy

Oleksandr Frolov Pulse Plasma Systems Department, Institute of Plasma Physics AS CR, v.v.i., Prague, Czech Republic

K. Fronec Institute of Physics, Polish Academy of Sciences, Warsaw, Poland

F. Furch National Science Foundation ERC for Extreme Ultraviolet Science and Technology, Fort Collins, USA; Department of Physics, Colorado State University, Fort Collins, CO, USA

N. Gaffney Centre for Atom Optics and Ultrafast Spectroscopy, Swinburne University of Technology, Melbourne, Australia; Australian Research Council Centre of Excellence for Coherent X-Ray Science, Melbourne, Australia

B. Gagey Synchrotron SOLEIL, Saint-Aubin, France

J. Gautier Laboratoire d'Optique Appliquée, ENSTA, Palaiseau, France

Aurelie Gense Laboratoire de Physique des Gaz et Plasma, CNRS-Université Paris Sud, Orsay, France

L. Giannessi Elettra-Sincrotrone Trieste, Basovizza, Trieste, Italy; ENEA, Frascati, Italy

S. Goette GSI Helmholtz Center for Heavy-Ion Research, Darmstadt, Germany

O. Guilbaud CLUPS/LASERIX, Université Paris Sud XI, Orsay Cedex, France; LPGP, Univ. Paris-Sud, UMR 8578, CNRS, Orsay Cedex, France

C.P. Hains Department of Electrical Engineering, University of New Mexico and Center for High Technology Materials, Albuquerque, NM, USA

C. Hall Centre for Atom Optics and Ultrafast Spectroscopy, Swinburne University of Technology, Melbourne, Australia; Australian Research Council Centre of Excellence for Coherent X-Ray Science, Melbourne, Australia

P. Hannaford Centre for Atom Optics and Ultrafast Spectroscopy, Swinburne University of Technology, Melbourne, Australia; Australian Research Council Centre of Excellence for Coherent X-Ray Science, Melbourne, Australia

N. Hasegawa Quantum Beam Science Directorate, Japan Atomic Energy Agency, Kizugawa, Kyoto, Japan

C. Herbeaux Synchrotron SOLEIL, Saint-Aubin, France

D.C. Hochhaus ExtreMe Matter Institute EMMI, Darmstadt, Germany; Goethe-Universität Frankfurt, Frankfurt, Germany

I.D. Howlett NSF ERC for Extreme Ultraviolet Science and Technology, Department of Electrical & Computer Engineering, Colorado State University, Fort Collins, CO, USA

T. Imazono Quantum Beam Science Directorate, Japan Atomic Energy Agency, Kizugawa, Kyoto, Japan

M. Ishino Quantum Beam Science Directorate, Japan Atomic Energy Agency, Kizugawa, Kyoto, Japan

A. Isoyan Synopsys Inc., Hillsboro, OR, USA

P. Jagourel GEPI, Observatoire de Paris, Univ. Paris-Diderot, CNRS, Paris, France

K.A. Janulewicz Advanced Photonics Research Institute, Gwangju Institute of Science and Technology, Gwangju, Rep. of Korea

R. Jarocki Institute of Optoelectronics, Military University of Technology, Warsaw, Poland

F. Jia Institute of Applied Physics, University of Bern, Bern, Switzerland

Q. Jin Institute of Modern Physics, Chinese Academy of Sciences, Lanzhou, People's Republic of China

Walter R. Johnson University of Notre Dame, Notre Dame, IN, USA

- T. Kaihori** Quantum Beam Science Directorate, Japan Atomic Energy Agency, Kizugawa, Kyoto, Japan
- M. Kando** Quantum Beam Science Directorate, JAEA, Kizugawa, Kyoto, Japan
- Y. Kato** Quantum Beam Science Directorate, JAEA, Kizugawa, Kyoto, Japan
- T. Kawachi** Quantum Beam Science Directorate, Japan Atomic Energy Agency, Kizugawa, Kyoto, Japan
- S. Kazamias** CLUPS/LASERIX, Université Paris Sud XI, Orsay Cedex, France; LPGP, Univ. Paris-Sud, UMR 8578, CNRS, Orsay Cedex, France
- C.M. Kim** Advanced Photonics Research Institute, Gwangju Institute of Science and Technology, Gwangju, Rep. of Korea
- A. Klisnick** ISMO, CNRS-Université Paris-Sud, Orsay, France
- Karel Kolacek** Pulse Plasma Systems Department, Institute of Plasma Physics AS CR, v.v.i., Prague, Czech Republic
- K. Kondo** Quantum Beam Science Directorate, JAEA, Kizugawa, Kyoto, Japan
- J. Kostecki** Institute of Optoelectronics, Military University of Technology, Warsaw, Poland
- M. Kozlova** Institute of Physics of ASCR, Prague, Czech Republic; IoP/PALS Center, Prague, Czech Republic
- M. Krus** Institute of Physics of ASCR, Prague, Czech Republic; IoP/PALS Center, Prague, Czech Republic
- T. Kuehl** Helmholtz Institute Jena, Jena, Germany; GSI Helmholtz Center for Heavy-Ion Research, Darmstadt, Germany; ExtreMe Matter Institute EMMI, Darmstadt, Germany; Johannes-Gutenberg Universität Mainz, Mainz, Germany; GSI Helmholtzzentrum fuer Schwerionenforschung, Darmstadt, Germany
- M. Labat** Synchrotron SOLEIL, Saint-Aubin, France
- G. Lambert** Laboratoire d'Optique Appliquée, Palaiseau, France
- J. Larour** LPP, Ecole Polytechnique, UPMC, CNRS, Palaiseau, France
- T.T.T. Le** Laboratoire d'Optique Appliquée, Palaiseau cedex, France
- G. LeBec** ESRF, Grenoble, France
- R. Lefevre** Lerma, Observatoire de Paris, UPMC, CNRS, Paris, France
- R. Lehe** Laboratoire d'Optique Appliquée, Palaiseau, France
- A. Lestrange** Synchrotron SOLEIL, Saint-Aubin, France
- Haochuan Li** Institute of Precision Optical Engineering (IPOE), Physics Department, Tongji University, Shanghai, China

- L. Li** Laboratoire d'Optique Appliquée, Palaiseau cedex, France
- A. Lifschitz** Laboratoire d'Optique Appliquée, Palaiseau, France
- A. Loulergue** Synchrotron SOLEIL, Saint-Aubin, France
- M. Luong** CEA/DSM/IRFU/SACM, Saclay, France
- B.M. Luther** National Science Foundation ERC for Extreme Ultraviolet Science and Technology, Fort Collins, USA; Department of Electrical and Computer Engineering, Colorado State University, Fort Collins, CO, USA
- J. Lüning** LCPMR, Paris-VI, France
- B. Mahieu** Elettra-Sincrotrone Trieste, Basovizza, Trieste, Italy; Dept. of Physics, University of Nova Gorica, Nova Gorica, Slovenia
- V. Malka** Laboratoire d'Optique Appliquée, Palaiseau, France
- E.B. Malm** Department of Electrical Engineering, Colorado State University and Engineering Research Center for Extreme Ultraviolet Science and Technology, Fort Collins, CO, USA
- P. Marchand** Synchrotron SOLEIL, Saint-Aubin, France
- M.C. Marconi** NSF Engineering Research Center for Extreme Ultraviolet Science & Technology and Department of Electrical and Computer Engineering, Colorado State University, Fort Collins, CO, USA
- J.L. Marlats** Synchrotron SOLEIL, Saint-Aubin, France
- D. Martz** National Science Foundation ERC for Extreme Ultraviolet Science and Technology, Fort Collins, USA; Department of Electrical and Computer Engineering, Colorado State University, Fort Collins, CO, USA
- Leili Masoudnia** Institute of Applied Physics, University of Bern, Bern, Switzerland
- G. Maynard** LPGP, Univ. Paris-Sud, UMR 8578, CNRS, Orsay Cedex, France
- E. Mel'tchakov** LCF, Institut d'Optique, CNRS, PXI, Palaiseau, France
- L.M. Meng** ISMO, CNRS-Université Paris-Sud, Orsay, France
- C.S. Menoni** NSF Engineering Research Center for Extreme Ultraviolet Science & Technology and Department of Electrical and Computer Engineering, Colorado State University, Fort Collins, CO, USA; National Science Foundation ERC for Extreme Ultraviolet Science and Technology, Fort Collins, USA
- R. Mercier** LCF, Institut d'Optique, CNRS, PXI, Palaiseau, France
- Y. Minami** Institute of Solid State Physics, The University of Tokyo, Kashiwa, Chiba, Japan
- C. Miron** Synchrotron SOLEIL, Saint-Aubin, France

N.C. Monserud Department of Electrical Engineering, Colorado State University and Engineering Research Center for Extreme Ultraviolet Science and Technology, Fort Collins, CO, USA

P. Morin Synchrotron SOLEIL, Saint-Aubin, France

T. Morita Quantum Beam Science Directorate, Japan Atomic Energy Agency, Kizugawa, Kyoto, Japan

C. Mossé PIIM, CNRS-Aix-Marseille Université, Marseille, France

T. Muramatsu Applied Laser Technology Institute Tsuruga Head Office, Japan Atomic Energy Agency, Tsuruga, Fukui, Japan

A. Nadji Synchrotron SOLEIL, Saint-Aubin, France

T. Nakamura Quantum Beam Science Directorate, JAEA, Kizugawa, Kyoto, Japan

K. Namikawa Research Institute for Science & Technology, Tokyo University of Science, Noda, Chiba, Japan

J. Nejdl IoP/PALS Center, Prague, Czech Republic

P. Neumayer ExtreMe Matter Institute EMMI, Darmstadt, Germany

O. Neveu LPGP, Univ. Paris-Sud, UMR 8578, CNRS, Orsay Cedex, France; LASERIX, CLUPS, Univ. Paris-Sud, CNRS, Orsay Cedex, France

Bich-Lien Nghiem Laboratoire de Physique des Gaz et Plasma, CNRS-Université Paris Sud, Orsay, France

P.V. Nickles WCU Dept. of Nanobio Materials and Electronics, Gwangju Institute of Science and Technology, Gwangju, Rep. of Korea

Joseph Nilsen Lawrence Livermore National Laboratory, Livermore, CA, USA

M. Nishikino Quantum Beam Science Directorate, Japan Atomic Energy Agency, Kizugawa, Kyoto, Japan

A. Nishimura Applied Laser Technology Institute Tsuruga Head Office, Japan Atomic Energy Agency, Tsuruga, Fukui, Japan; Quantum Beam Directorate, Japan Atomic Energy Agency, Kizugawa, Kyoto, Japan

G. Norman Joint Institute for High Temperatures, Russian Academy of Sciences, Moscow, Russia; Moscow Institute of Physics and Technology, Moscow, Russia

Y. Ochi Quantum Beam Science Directorate, Japan Atomic Energy Agency, Kizugawa, Kyoto, Japan

E. Oliva Laboratoire d'Optique Appliquée, ENSTA ParisTech, École Polytechnique ParisTech, CNRS, UMR 7639, Palaiseau, France; Laboratoire d'Optique Appliquée, Palaiseau cedex, France

D. Patel National Science Foundation ERC for Extreme Ultraviolet Science and Technology, Fort Collins, USA; Department of Electrical and Computer Engineering, Colorado State University, Fort Collins, CO, USA

D. Pánek Czech Technical University, Prague, Czech Republic

G. Penco Elettra-Sincrotrone Trieste, Basovizza, Trieste, Italy

T.A. Pikuz Quantum Beam Science Directorate, JAEA, Kizugawa, Kyoto, Japan

Tatiana Pikuz Quantum Beam Science Directorate, Japan Atomic Energy Agency, Kyoto, Japan; Joint Institute for High Temperatures, Russian Academy of Sciences, Moscow, Russia

A. Pirozhkov Quantum Beam Science Directorate, JAEA, Kizugawa, Kyoto, Japan

M. Pittman LASERIX, CLUPS, Univ. Paris-Sud, CNRS, Orsay Cedex, France

F. Polack Synchrotron SOLEIL, Saint-Aubin, France

A.V. Popov Pushkov Institute of Terrestrial Magnetism, Ionosphere and Radiowave Propagation, Troitsk, Russia

N.L. Popov P.N. Lebedev Physical Institute, Moscow, Russia

David Portillo Instituto de Fusión Nuclear, Universidad Politécnica de Madrid, Madrid, Spain

Chris Pouhe Laboratoire de Physique des Gaz et Plasma, CNRS-Université Paris Sud, Orsay, France

J. Prokupek Institute of Physics of ASCR, Prague, Czech Republic; IoP/PALS Center, Prague, Czech Republic

Vaclav Prukner Pulse Plasma Systems Department, Institute of Plasma Physics AS CR, v.v.i., Prague, Czech Republic

J.B. Pruvost Synchrotron SOLEIL, Saint-Aubin, France

X.M. Qiao Institute of Applied Physics and Computational Mathematics, Beijing, China

Rabia Qindeel Centro de Lasers e Aplicações, IPEN, CNEN/SP, São Paulo, Brazil

B.A. Reagan National Science Foundation ERC for Extreme Ultraviolet Science and Technology, Fort Collins, USA; Department of Electrical and Computer Engineering, Colorado State University, Fort Collins, CO, USA

F. Reix GEPI, Observatoire de Paris, Univ. Paris-Diderot, CNRS, Paris, France

F. Ribeiro Synchrotron SOLEIL, Saint-Aubin, France

J.P. Ricaud Synchrotron SOLEIL, Saint-Aubin, France

Gabriel Richet Laboratoire de Physique des Gaz et Plasma, CNRS-Université Paris Sud, Orsay, France

J.J. Rocca NSF Engineering Research Center for Extreme Ultraviolet Science & Technology and Department of Electrical and Computer Engineering, Colorado State University, Fort Collins, CO, USA; National Science Foundation ERC for Extreme Ultraviolet Science and Technology, Fort Collins, USA; Department of Physics, Colorado State University, Fort Collins, CO, USA

D. Ros CLUPS/LASERIX, Université Paris Sud XI, Orsay Cedex, France; LPGP, Univ. Paris-Sud, UMR 8578, CNRS, Orsay Cedex, France

A. Rousse Laboratoire d'Optique Appliquée, Palaiseau, France

R. Roux Laboratoire de l'Accélérateur Linéaire, Orsay, France

P. Roy Synchrotron SOLEIL, Saint-Aubin, France

Mabel Ruiz-Lopez Institute of Applied Physics, University of Bern, Bern, Switzerland

B. Rus IoP/PALS Center, Prague, Czech Republic

Ricardo Elgul Samad Centro de Lasers e Aplicações, IPEN, CNEN/SP, São Paulo, Brazil

A. Sasaki Quantum Beam Science Directorate, Japan Atomic Energy Agency, Kizugawa, Kyoto, Japan

Jiri Schmidt Pulse Plasma Systems Department, Institute of Plasma Physics AS CR, v.v.i., Prague, Czech Republic

S. Sebban Laboratoire d'Optique Appliquée, ENSTA ParisTech, École Polytechnique ParisTech, CNRS, UMR 7639, Palaiseau, France

V.N. Shlyaptsev National Science Foundation ERC for Extreme Ultraviolet Science and Technology, Fort Collins, USA; Department of Electrical and Computer Engineering, Colorado State University, Fort Collins, CO, USA

T. Shobu Applied Laser Technology Institute Tsuruga Head Office, Japan Atomic Energy Agency, Tsuruga, Fukui, Japan; Quantum Beam Directorate, Japan Atomic Energy Agency, Kizugawa, Kyoto, Japan

O.A. Shoutova Physics Department, M.V. Lomonosov Moscow State University, Moscow, Russia

Igor Skobelev Joint Institute for High Temperatures, Russian Academy of Sciences, Moscow, Russia

T.A. Smith School of Chemistry, University of Melbourne, Melbourne, Australia; Australian Research Council Centre of Excellence for Coherent X-Ray Science, Melbourne, Australia

C. Spezzani Elettra-Sincrotrone Trieste, Basovizza, Trieste, Italy

Sergei Starikov Joint Institute for High Temperatures, Russian Academy of Sciences, Moscow, Russia; Moscow Institute of Physics and Technology, Moscow, Russia

F. Staub Institute of Applied Physics, University of Bern, Bern, Switzerland

Vladimir Stegailov Joint Institute for High Temperatures, Russian Academy of Sciences, Moscow, Russia; Moscow Institute of Physics and Technology, Moscow, Russia

C. Stehlé Lerma, Observatoire de Paris, UPMC, CNRS, Paris, France

A. Stein Center for Functional Nanomaterials, Brookhaven National Laboratory, Upton, NY, USA

H. Stiel Max-Born Institute for Nonlinear Optics and Short Pulse Spectroscopy, Berlin, Germany

T. Stoehlker Helmholtz Institute Jena, Jena, Germany; GSI Helmholtz Center for Heavy-Ion Research, Darmstadt, Germany

Jaroslav Straus Pulse Plasma Systems Department, Institute of Plasma Physics AS CR, v.v.i., Prague, Czech Republic

S.Y. Stremoukhov Physics Department, M.V. Lomonosov Moscow State University, Moscow, Russia

T. Suemoto Institute of Solid State Physics (ISSP), University of Tokyo, Kashiwa, Chiba, Japan

K. Sugihara Applied Laser Technology Institute Tsuruga Head Office, Japan Atomic Energy Agency, Tsuruga, Fukui, Japan

J.R. Sun Shanghai Institute of Laser Plasma, Shanghai, China

F. Suzuki-Vidal Imperial College, London, UK

M. Szczerk Institute of Optoelectronics, Military University of Technology, Warsaw, Poland

C. Szwaj PhLAM/CERLA, Lille, France

K. Ta Phuoc Laboratoire d'Optique Appliquée, Palaiseau, France

B. Talin PIIM, CNRS-Aix-Marseille Université, Marseille, France

Greg Tallents University of York, York, UK

Satoshi Tamotsu Division of Natural Science, Faculty, Nara Women's University, Nara, Japan

M. Tanaka Quantum Beam Science Directorate, Japan Atomic Energy Agency, Kyoto, Japan

T. Tanikawa Synchrotron SOLEIL, Saint-Aubin, France

K. Terakawa Institute of Solid State Physics, The University of Tokyo, Kashiwa, Chiba, Japan

C. Thaury Laboratoire d'Optique Appliquée, Palaiseau, France

V.T. Tikhonchuk Univ. Bordeaux, CNRS, CEA, CELIA (Centre Lasers Intenses et Applications), Talence, France

F. Tissandier LOA, Ecole Polytechnique, CNRS, Paris, France; Laboratoire d'Optique Appliquée, ENSTA, Palaiseau, France

T. Tomita Department of Ecosystem Engineering, The University of Tokushima, Tokushima, Japan; Faculty of Engineering, University of Tokushima, Tokushima, Japan

M. Trovo Elettra-Sincrotrone Trieste, Basovizza, Trieste, Italy

L. Urbanski NSF Engineering Research Center for Extreme Ultraviolet Science & Technology and Department of Electrical and Computer Engineering, Colorado State University, Fort Collins, CO, USA

P. Velarde Instituto de Fusión Nuclear, Universidad Politécnica de Madrid, Madrid, Spain

Nilson Dias Vieira Junior Centro de Lasers e Aplicações, IPEN, CNEN/SP, São Paulo, Brazil

A.V. Vinogradov P.N. Lebedev Physical Institute, Moscow, Russia

Boris Vodungbo Laboratoire d'Optique Appliquée, ENSTA ParisTech – CNRS – École Polytechnique, Palaiseau, France

H.L. Vu Centre for Atom Optics and Ultrafast Spectroscopy, Swinburne University of Technology, Melbourne, Australia; Australian Research Council Centre of Excellence for Coherent X-Ray Science, Melbourne, Australia

P.W. Wachulak Institute of Optoelectronics, Military University of Technology, Warsaw, Poland

C. Wang Shanghai Institute of Laser Plasma, Shanghai, China

S. Wang National Science Foundation ERC for Extreme Ultraviolet Science and Technology, Fort Collins, USA; Department of Electrical and Computer Engineering, Colorado State University, Fort Collins, CO, USA

S.J. Wang Shanghai Institute of Laser Plasma, Shanghai, China

W. Wang Shanghai Institute of Laser Plasma, Shanghai, China

Y. Wang National Science Foundation ERC for Extreme Ultraviolet Science and Technology, Fort Collins, USA; Department of Electrical and Computer Engineering, Colorado State University, Fort Collins, CO, USA

Zhanshan Wang Institute of Precision Optical Engineering (IPOE), Physics Department, Tongji University, Shanghai, China

K. Wernsing National Science Foundation ERC for Extreme Ultraviolet Science and Technology, Fort Collins, USA; Department of Electrical and Computer Engineering, Colorado State University, Fort Collins, CO, USA

L. Węgrzyński Institute of Optoelectronics, Military University of Technology, Warsaw, Poland

Lucy Wilson University of York, York, UK

D. Winters GSI Helmholtz Center for Heavy-Ion Research, Darmstadt, Germany

M. Woolston National Science Foundation ERC for Extreme Ultraviolet Science and Technology, Fort Collins, USA; Department of Electrical and Computer Engineering, Colorado State University, Fort Collins, CO, USA

H. Xu Department of Electrical Engineering, University of New Mexico and Center for High Technology Materials, Albuquerque, NM, USA

T. Yamada Applied Laser Technology Institute Tsuruga Head Office, Japan Atomic Energy Agency, Tsuruga, Fukui, Japan

M. Yamagiwa Quantum Beam Science Directorate, Japan Atomic Energy Agency, Kizugawa, Kyoto, Japan

M. Yamamoto Department of Ecosystem Engineering, The University of Tokushima, Tokushima, Japan

S. Yamashita Applied Laser Technology Institute Tsuruga Head Office, Japan Atomic Energy Agency, Tsuruga, Fukui, Japan

L. Yin National Science Foundation ERC for Extreme Ultraviolet Science and Technology, Fort Collins, USA; Department of Electrical and Computer Engineering, Colorado State University, Fort Collins, CO, USA

P. Zeitoun Laboratoire d'Optique Appliquée, ENSTA ParisTech, École Polytechnique ParisTech, CNRS, UMR 7639, Palaiseau, France

H. Zhao Institute of Modern Physics, Chinese Academy of Sciences, Lanzhou, People's Republic of China

W.D. Zheng Institute of Applied Physics and Computational Mathematics, Beijing, China

Jingtao Zhu Institute of Precision Optical Engineering (IPOE), Physics Department, Tongji University, Shanghai, China

B. Zielbauer GSI Helmholtz Center for Heavy-Ion Research, Darmstadt, Germany; Helmholtz Institute Jena, Jena, Germany; GSI Helmholtzzentrum fuer Schwerionenforschung, Darmstadt, Germany

Chapter 1

Coherent Pulses from a Seeded Free-Electron Laser in the Extreme Ultraviolet

E. Allaria, D. Castronovo, G. De Ninno, S. Di Mitri, W. Fawley, E. Ferrari,
L. Froehlich, L. Giannessi, B. Mahieu, G. Penco, C. Spezzani, and M. Trovo

Abstract We report results of a free-electron laser operating with the high gain harmonic generation configuration in the wavelength range from 60 to 20 nm. With the recent experiments done at the FERMI free-electron laser facility in Trieste we demonstrated the capability of the used method to produce highly coherent pulses allowing to improve the performances of FELs in the EUV spectral range overcoming some of the limitations that are typical of systems based on the self amplified spontaneous emission (SASE). Taking advantage of the seeding scheme adopted for FERMI high photon energy stability and a very high longitudinal and transverse coherence have been measured. The operation of the FERMI FEL facility will allow improving the use of the FEL light for those experiments that require a small spectral bandwidth or a precise control of the photon energy.

1 Introduction

FERMI@Elettra is a fourth generation light source under commissioning that has been built at the Elettra laboratory in Trieste. When in operation FERMI@Elettra will allow the Elettra user community to perform new kinds of experiments that could exploit the characteristic of such a new light source like short pulses and high peak intensity.

Free electron lasers have been recognized since the first proposal [1] and demonstration [2, 3] as possible sources that could be efficiently used for the generation of laser like pulses in the x-ray spectral range. Although it has been necessary to

E. Allaria (✉) · D. Castronovo · G. De Ninno · S. Di Mitri · W. Fawley · E. Ferrari ·
L. Froehlich · L. Giannessi · B. Mahieu · G. Penco · C. Spezzani · M. Trovo
Elettra-Sincrotrone Trieste, S.S. 14—km 163.5 in Area Science Park, 34012 Basovizza, Trieste,
Italy
e-mail: enrico.allaria@elettra.trieste.it

G. De Ninno · E. Ferrari · B. Mahieu
Dept. of Physics, University of Nova Gorica, Nova Gorica, Slovenia

L. Giannessi
ENEA, Frascati, Italy

wait for the technology to be mature in order to support the requirements for x-rays FELs, the theory of high gain single pass FELs was developed [4, 5] showing how the self amplified spontaneous emission (SASE) FELs could be designed to operate in the x-ray spectral range. Since the first theoretical works, several projects have been done for demonstrating and use such a capability.

After first experiments in the infrared [6] and in the visible [7] the wavelength range has been rapidly extended from the VUV [8] up to the soft x-ray [9]. More recently the final goal to reach the hard x-ray spectral range has been achieved showing FEL operations at 1.5 and 1.2 Ångstrom [10, 11].

The recent progress on short wavelength FELs has been accompanied by the progress of other sources of laser-like pulses in the VUV and soft x-ray spectral range. Several methods have been proposed and studied for the generation of x-ray laser-like pulses that use the nonlinear response of materials to very high power laser pulses in the visible and near infrared [12–16].

In this work we will report about the recent results achieved at FERMI@Elettra with the first seeded FEL operated in the range between 65 and 20 nm.

2 The FERMI@Elettra Free Electron Laser

The FERMI FELs will produce photons in the ultraviolet and soft x-ray range, between 80 and 4 nm (Fig. 1).

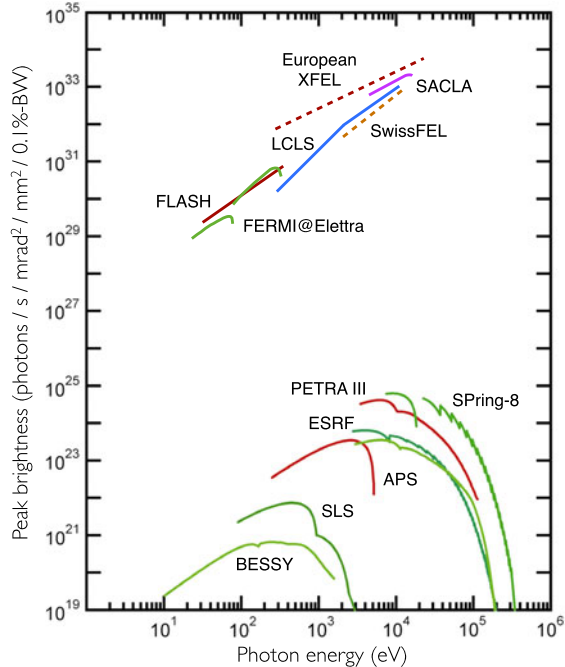
Three experimental programs define the scientific case and have driven the design of the facility. The three FERMI experimental beamlines, Diffraction and Projection Imaging (DiProI), Elastic and Inelastic Scattering (EIS), Low Density Matter (LDM), require for their experiments high peak brightness, fully coherent, narrow and stable bandwidth photon pulses. Wavelength tunability and variable polarization, circular and linear, are also required [17, 18].

In order to cover the large spectral range FERMI has been designed with two FEL lines. FEL-1, based on a High Gain Harmonic Generation (HGHG) [19] single stage, is seeded by an external UV laser at about 260 nm [20]. FEL-1 produces photons in the wavelength range between 80 and 20 nm (15 eV to 62 eV). To reach 4 nm wavelength (310 eV), starting from an external seed laser in the UV range, a double stage HGHG cascade has been adopted for FEL-2.

Both FELs use the high energy and brightness electron bunches produced by a linear accelerator (Fig. 2). The accelerator is based on a normal conducting LINAC working at 3 GHz RF frequency and 50 Hz repetition rate. The high brightness electron beam is generated by a photocathode RF gun. Two stages of magnetic compression are used to get extremely short electron bunches (less than 1 ps) with high peak current.

A fourth harmonic RF structure (12 GHz, X-band) provides the longitudinal phase space linearization needed to optimize the compression process. At high compression factors, i.e. high peak bunch currents, micro-bunching instabilities are predicted; to cure them, a laser heater [21] is installed at 100 MeV to increase in a controlled way the incoherent energy spread of the electron beam.

Fig. 1 Diagram showing the expected performance of FERMI in terms of peak brilliance as compared to other FEL and synchrotron radiation facilities (Image from: P. Schmüser, M. Dohls, J. Rossbach, and C. Behrens, Free-Electron Lasers in the Ultraviolet and X-Ray Regime: Physical Principles, Experimental Results, Technological Realization, 2nd edition to be printed in Springer-Verlag, Berlin (2013))



Each stage of the two FEL lines is made up by the modulator, where the electron beam is seeded by the external laser, a dispersive bunching section, and the radiator, where the interaction between the electron beam and the produced coherent radiation produces the exponential growth of the FEL radiation. In Fig. 3 we show the schematic layout of the first FEL, FEL-1, that is based on a single stage harmonic generation.

For both FEL-1 and FEL-2 the final radiator is made up by six APPLE-II undulators, with magnetic periods of 55 and 35 mm respectively. APPLE-II undulators provide full control of the polarization of the FEL radiation and the variable gap allows changing the wavelength of the emitted radiation.

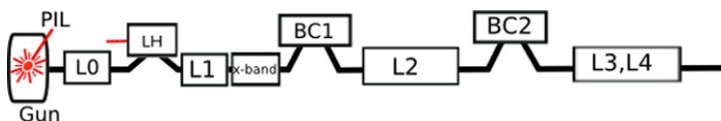


Fig. 2 Schematic layout of the FERMI linear accelerator. Electron bunches are produced in the *Gun* by 5 ps pulses from a Photo-Injector Laser (*PIL*). A first acceleration structure (*L0*) is used to accelerate the beam up to 100 MeV, where there is the laser heater (*LH*). Further acceleration is produced by *L1*, and an *x-band* cavity is used to linearize the phase space before the first bunch compressor (*BC1*). Further acceleration is produced by *L2* and *L3*, *L4* and if needed additional compression can be achieved using the second bunch compressor chicane (*BC2*)

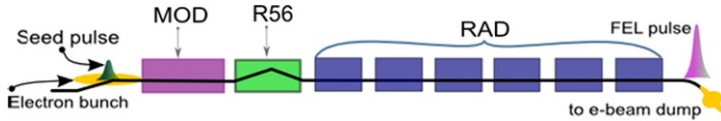


Fig. 3 Schematic layout of the FERMI first FEL, FEL-1. One modulator (*MOD*), a dispersive section (*R56*) and 6 APPLE-II undulators for the final radiator (*RAD*) define the first FEL of FERMI

Table 1 FEL parameters achieved so far with FERMI FEL-1

Parameter	Value achieved	Units
Wavelength range	65–20	nm
Photon energy range	19–62	eV
Bandwidth (rms)	22 (@32 nm)	meV
Relative bandwidth (rms)	5e-4 (@32 nm)	
Polarization	Hor/Circ	
Energy per pulse	20–50	μ J
Pulse length (FWHM)	\sim 100	fs (estimated)
FEL mode	TEM_{00}	

3 FEL Achieved Performance

During the first year of commissioning the FEL performance has been continuously improving. After few months from the first produced photons it has been possible to achieve the level of several tens of micro joules over the FEL-1 spectral range (Table 1). It has been also possible to demonstrate the high quality and coherence of FERMI FEL pulses [22]. This significantly improved what was generally available from other FEL sources working in a similar spectral range.

Taking advantage of the adopted scheme and of the variable gap undulators adopted for FERMI also the tunability of the FEL wavelength has been easily implemented and changes of wavelength over the whole spectral range have been done. Figure 4 reports a series of FEL spectra acquired during a shift where the FEL wavelength has been varied from about 20 nm up to 40 nm.

With the FEL parameters reported in Table 1, FERMI also started to provide photons to the three experimental stations [18] for the first pilot experiments [23].

4 Conclusions

The first FERMI FEL, FEL-1, has been operated since two years and recently reached fairly intense photon fluxes, producing tens of μ J, approaching the project design goals. With the already achieved photon flux the FEL-1 is showing the benefit of the seeding scheme adopted at FERMI demonstrating good single shot spectra

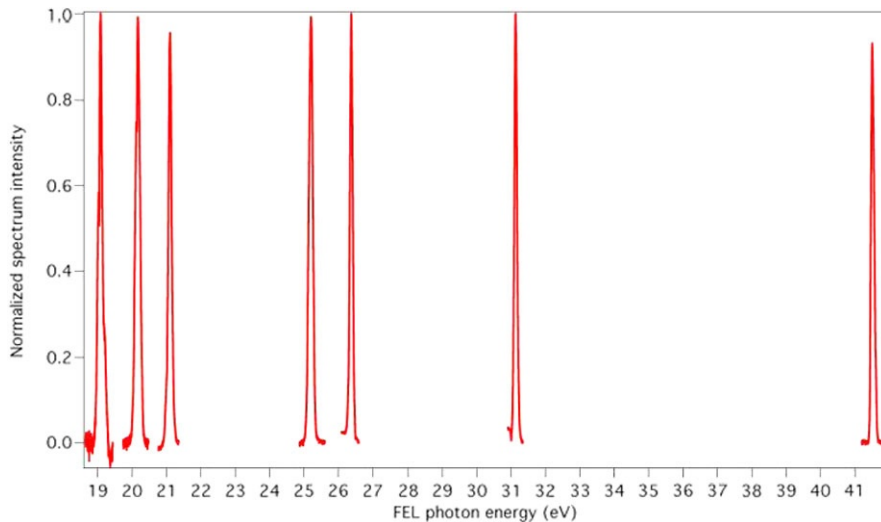


Fig. 4 Series of FEL spectra acquired during experiments that required the FEL tuning in the range 20–40 nm. Reported data are an average of 100 consecutive spectra showing that FERMI spectra are not only narrow bandwidth (tens of meV) but also very stable

with narrow bandwidth and excellent central wavelength stability. A very good degree of transverse coherence has been also observed. FEL tunability and variable polarization have been successfully set into operation.

References

1. Madey, J.M.J.: Stimulated emission of bremsstrahlung in a periodic magnetic field. *J. Appl. Phys.* **42**, 1906–1913 (1971)
2. Elias, L.R., Fairbank, W.M., Madey, J.M.J., Schwettman, H.A., Smith, T.I.: Observation of stimulated emission of radiation by relativistic electrons in a spatially transverse magnetic field. *Phys. Rev. Lett.* **36**, 717–720 (1976)
3. Deacon, D.A.G., et al.: First operation of a free electron laser. *Phys. Rev. Lett.* **38**, 892–894 (1977)
4. Colson, W.B.: Theory of a free electron laser. *Phys. Lett. A* **59**, 187–190 (1976)
5. Dattoli, G., Renieri, A., Torre, A.: Lectures on the Free Electron Laser Theory and Related Topics. World Scientific, Singapore (1993)
6. Hogan, M.J., et al.: Measurements of gain larger than 10^5 at 12 μm in a self amplified spontaneous emission free electron laser. *Phys. Rev. Lett.* **81**, 4867–4871 (1998)
7. Milton, S., et al.: Exponential gain and saturation of a self amplified spontaneous emission free electron laser. *Science* **292**, 2037–2041 (2001)
8. Ayvazyan, V., et al.: Generation of GW radiation pulses from VUV free-electron laser operating in the femtosecond regime. *Phys. Rev. Lett.* **88**, 104802 (2002)
9. Ackermann, W., et al.: Operation of a free-electron laser from the extreme ultraviolet to the water window. *Nat. Photonics* **1**, 336–342 (2007)
10. Emma, P., et al.: First lasing and operation of an angstrom-wavelength free-electron laser. *Nat. Photonics* **4**, 641–647 (2010)

11. Pile, D.: X-rays: first light from SACLA. *Nat. Photonics* **5**, 456–457 (2011)
12. McPherson, A., Gibson, G., Jara, H., Johann, U., Luk, T.S., McIntyre, I.A., Boyer, K., Rhodes, C.K.: Studies of multiphoton production of vacuum-ultraviolet radiation in the rare gases. *J. Opt. Soc. Am. B* **21**, 595 (1987)
13. Li, X.F., L'Huillier, A., Ferray, M., Lompré, L.A., Mainfray, G.: Multiple-harmonic generation in rare gases at high laser intensity. *Phys. Rev. A* **39**, 5751 (1989)
14. Daido, H.: Review of soft x-ray laser researches and developments. *Rep. Prog. Phys.* **65**, 1513 (2002)
15. Tallents, G.J.: The physics of soft x-ray lasers pumped by electron collisions in laser plasmas. *J. Phys. D* **36**, R259 (2003)
16. Zeitoun, Ph., et al.: A high-intensity highly coherent soft X-ray femtosecond laser seeded by a high harmonic beam. *Nature* **431**, 426–429 (2004)
17. Bocchetta, C.J., et al.: FERMI@Elettra FEL Conceptual Design Report (2007)
18. Allaria, E., Callegari, C., Cocco, D., Fawley, W.M., Kiskinova, M., Masciovecchio, C., Parmigiani, F.: The FERMI@Elettra free-electron-laser source for coherent x-ray physics: photon properties, beam transport system and applications. *New J. Phys.* **12**, 075002 (2010)
19. Yu, L.H.: Generation of intense UV radiation by subharmonically seeded single-pass free-electron lasers. *Phys. Rev. A* **44**, 5178 (1991)
20. Allaria, E., De Ninno, G.: Soft-X-ray coherent radiation using a single-cascade free-electron laser. *Phys. Rev. Lett.* **99**, 014801 (2007)
21. Huang, Z., Borland, M., Emma, P., Wu, J., Limborg, C., Stupakov, G., Welch, J.: Suppression of microbunching instability in the linac coherent light source. *Phys. Rev. Spec. Top. Accel. Beams* **7**, 074401 (2004)
22. Allaria, E., et al.: Highly coherent and stable pulses from the FERMI seeded free-electron laser in the extreme ultraviolet. *Nat. Photonics* **6**, 699–704 (2012)
23. Allaria, E., et al.: Tunability experiments at the FERMI@Elettra free-electron laser. *New J. Phys.* **14**, 113009 (2012)

Chapter 2

Enhancement of Efficiency of XUV Generation in Atomic Gases Irradiated by Intense Laser Fields

A.V. Andreev, S.Y. Stremoukhov, and O.A. Shoutova

Abstract We present the results of the theoretical study of the high-order harmonic generation (HHG) in atomic gases. It is shown that the photoemission spectra exhibit unusual behavior when the laser field strength approaches near-atomic values. In subatomic field strength the cut-off frequency increases linearly with laser pulse intensity. However, when the field strength approaches near-atomic region firstly cut-off frequency slows down and then saturates. To interpret such kind of photoemission spectrum behavior we have proposed the light-atom interaction theory based on the use of eigenfunctions of boundary value problem for “an atom in the external field” instead of the traditional basis of the “free atom” eigenfunctions.

1 Introduction

In spite of the twenty-year history, the effect of the HHG is still under a great interest of both experimentalists and theoreticians. From a practical point of view, the HHG is one of the effective mechanisms for producing a coherent emission in broad region of electromagnetic wave spectrum. The presence of plateau region in the harmonic amplitude distribution in extreme ultraviolet (XUV) region affords grounds for development of subfemtosecond pulse formation methods. As a result, the new frontiers are opened up in science by extending the nonlinear optics and time-resolved spectroscopy to the XUV region [1] and pushing ultrafast science to the attosecond domain, enabling XUV spectroscopy and imaging of molecular orbitals [2], surface dynamics [3], and electron motion. The HHG is the reliable route to produce attosecond light pulses [4, 5] and is therefore fundamental to attosecond science [6].

At present days, the efficiency of conversion to high-order harmonics is really too small to consider this emission as a real coherent XUV source for biology, plasma diagnostics, medicine, microscopy, photolithography, etc. Hence, the search

A.V. Andreev · S.Y. Stremoukhov (✉) · O.A. Shoutova

Physics Department, M.V. Lomonosov Moscow State University, Leninskie Gory, 1, build. 2,
119991, Moscow, Russia

e-mail: sustrem@gmail.com

for ways of increasing the cut-off frequency and the HHG efficiency in the XUV spectral range is still among the most topical problems of nonlinear optics.

The HHG effect was observed with the large number of periodic table elements having usually small and middle atomic numbers [7]. Up to now, there has been developed a number of different theoretical models to describe the dynamics of an atomic electron in a strong laser field. These models are based on different approximations, which are usually valid in the restricted area of laser pulse field strength. Here, we use the non-perturbative theory of light-atom interaction [8] which is equally applicable for both weak and strong laser fields.

2 Basic Statements of Theory

In the non-relativistic case, the theory of light-atom interaction is based on the time dependent Schrodinger equation TDSE:

$$i\hbar \frac{\partial \psi(\vec{r}, t)}{\partial t} = \left[\frac{1}{2m} \left(\vec{p} - \frac{e}{c} \vec{A}(t) \right)^2 + U(r) \right] \psi(\vec{r}, t), \quad (1)$$

where $U(\vec{r})$ is the potential energy of electron in the intra-atomic field, and $\vec{A}(t)$ is the vector potential of the external electromagnetic wave. The traditional approaches to the analysis of the TDSE are based on the expansion of the wave function in the series of “free atom” eigenfunctions.

The eigensolutions of the boundary value problem for Hamiltonian of the TDSE,

$$\left[\frac{1}{2m} \left(\vec{p} - \frac{e}{c} \vec{A}(t) \right)^2 + U(r) \right] \varphi_N(\vec{r}, t) = E_N \varphi_N(\vec{r}, t), \quad (2)$$

have been found in [8]. There are the following relationships between the eigenfunctions of the problem (2) and the “free atom” eigenfunctions $u_n(\vec{r})$:

$$\varphi_N(\vec{r}, t) = u_n(\vec{r}) \hat{V}^{-1}, \quad \hat{V} = \exp\left(-i \frac{q}{\hbar c} \vec{A}(t) \vec{r}\right). \quad (3)$$

The eigenvalues of the problem (2) coincide exactly with the “free atom” eigenvalues $E_N = E_n$.

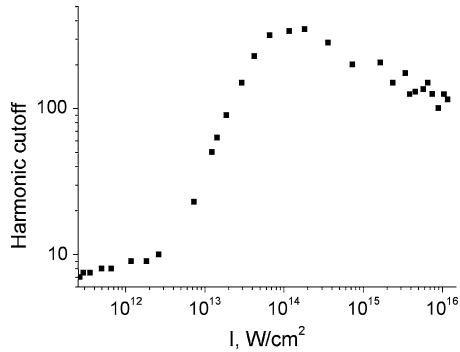
The bases of the eigenfunctions of a “free atom” boundary value problem and the basis of $\varphi_n(\vec{r}, t)$ are related one-to-one by the transformations [9, 10]. So, we can expand the wavefunction of the TDSE (1) into series of free atom eigenfunctions

$$\psi = \sum_{nlm} a_{nlm}(t) u_{nlm}(\vec{r})$$

and then use the relations of one-to-one transformations [9, 10] to calculate the matrix elements of operators. Executing some evident transformations we get the following set of differential equations for probability amplitudes of discrete and continuum spectrum states

$$i\hbar \frac{da_n}{dt} = \sum_{m,k} V_{nk}^{-1} E_k V_{km} a_m.$$

Fig. 1 Cut-off frequency as a function of the laser pulse intensity



It is well known, that the number of discrete states of any hydrogen-like atom is infinite and there is an innumerable number of continuum spectrum states. The developed approach provides the consistent mathematical procedure of a selection of atomic levels playing the main role in evolution of a state of the atom in an external laser field.

3 Numerical Research

In numerical simulations we assume that a single silver atom interacts with the pulse of Ti:Sapphire laser (the wavelength $\lambda = 800 \text{ nm}$). The pulse duration is assumed as $\tau = 27 \text{ fs}$. The amplitude of the laser field strength E_0 is varied in the wide range starting from a significantly subatomic to near-atomic values. As we have discussed in our previous work [9] if the laser field strength lies in the interval $I < 1.83 \cdot 10^{16} \text{ W}/\text{cm}^2$ then the approximately complete basis of states forms the following 284 levels of a silver atom: $5s$ (GS), $5p$, $5d$, $6p$ of the discrete spectrum and 280 states of continuum spectrum with orbital quantum numbers $l = 0-3$.

The spectrum of atomic response field in the far-field zone is proportional to the spectrum of the atomic current, which is given by

$$\vec{J}(t) = \frac{q}{m} \sum_{n,m,p,q} a_n^*(t) a_m(t) V_{np}^{-1}(t) \vec{p}_{pq} V_{qm}(t). \quad (4)$$

Our numerical calculations yield a series of harmonic emission spectra. In subatomic region the spectrum consists of the sequence of the odd harmonics of incident field carrier frequency. When the laser field strength approaches to near-atomic ones, the shape of the response spectrum is changed. There appear tendencies for growing of its width and formation of plateau. Further increase in the amplitude of the external field strength allows us to observe well-defined plateau with the definite cut-off frequency (CF). The results of computer calculations of the CF as a function of the laser pulse intensity is presented in Fig. 1. One can see that in the weak field range ($I < 2.9 \cdot 10^{13} \text{ W}/\text{cm}^2$) there is the quadratic growth of cut-off frequency with the field strength. However, at laser pulse intensity $I > 10^{14} \text{ W}/\text{cm}^2$ the CF

is saturated, i.e. it ceases to be intensity dependent. The reason of such behavior is quite obvious if we take into account that the probability of electron ionization approaches to unity in this region of pulse intensity. It means that the atomic electron is mostly localized in the continuum spectrum states and it does not collide with its parent ion. So, the results of computer modeling show that the most probable reason of the cutoff frequency saturation is the total ionization of the irradiated atom. The behavior of cut-off frequency dependence presented in Fig. 1 is in a good agreement with experimental observed results [7].

4 Propagation and Dispersion Effects

In order to illustrate qualitatively the difference between the frequency-angular spectra of a single atom response and an ensemble of atoms we shall use further the simplest dispersion model.

In the case when the atoms of an ensemble are identical, the spectrum of the atomic current (4) is

$$\vec{J}(\vec{k}, \omega) = \sum_{i=1}^N \vec{J}_i(\omega) \exp\left[i \frac{\omega}{c} (\vec{n}(\omega) - \vec{n}_0(\omega_0)) \vec{r}_i\right] = \vec{J}_0(\omega) f(\vec{k}, \vec{k}_0),$$

where $\vec{J}_0(\omega)$ is the spectrum of a single atom current and the form factor $f(\vec{k}, \vec{k}_0)$ is defined by

$$f(\vec{k}, \vec{k}_0) = \int \rho_\omega(\vec{r}) \exp\left[i \frac{\omega}{c} (\vec{n}(\omega) - \vec{n}_0(\omega_0)) \vec{r}\right] dV. \quad (5)$$

Here, $\rho_\omega(\vec{r})$ is an effective density of responding atoms, which is the product of density of atoms and the ω/ω_0 power of the amplitude spatial distribution of driving laser pulse in irradiated volume.

According to the Lorentz classical theory the refractive index for electromagnetic wave propagating in ionized gaseous medium is given by

$$n(\omega) \approx 1 - \frac{1}{2} \left[\sum_{\alpha} \frac{\omega_{p\alpha}^2}{\omega^2 - \omega_{0\alpha}^2 + i\omega\gamma_{\alpha}} + \frac{\omega_{pe}^2}{\omega^2 + i\omega\gamma_e} \right],$$

where

$$\omega_{p\alpha(e)} = \sqrt{\frac{4\pi e^2 N_{\alpha(e)}}{m V}}$$

is the plasma frequency corresponding to neutral atoms ($\alpha = I$), ions ($\alpha = II$), and free electrons (e); N_α is the number of neutral atoms and ions in the irradiated volume V , and N_e is the number of free electrons.

In the case of the Gaussian incident beam the effective density of responding atoms can be approximated as follows

$$\rho_\omega(\vec{r}) = \frac{N_0}{V} \left[\exp\left(-\frac{z^2}{L^2} - \frac{\rho^2}{d^2}\right) \right]^{\omega/\omega_0},$$

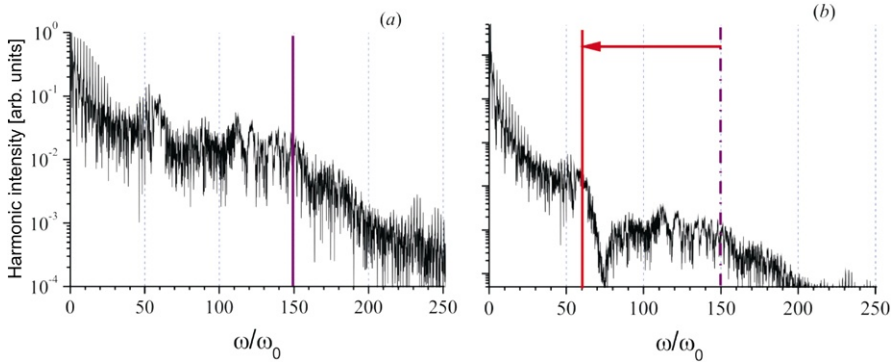
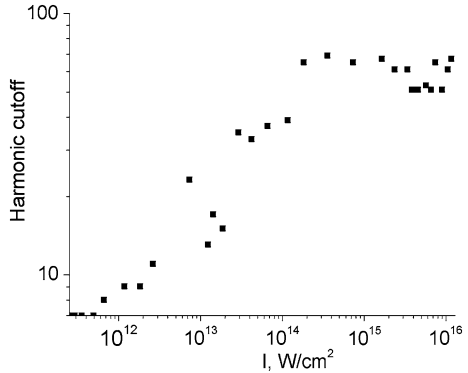


Fig. 2 The comparison of photoemission spectra generated in silver by a single atom **(a)** and an ensemble of atoms **(b)** at the laser pulse intensity $I = 2.37 \cdot 10^{15} \text{ W/cm}^2$

Fig. 3 The CF of an ensemble of atoms as a function of a laser pulse intensity



where d is the focal waist of a driving laser beam, and L depends both on the confocal parameter of driving laser beam and a spatial distribution of an atomic density in the laser plume produced by the pump laser pulse. We have assumed that the laser beam is propagated along the z axis.

By taking into account the typical experimental conditions we have calculated the function $|f(\vec{k}, \vec{k}_0)|^2$ defined by Eq. (5). Figure 2 shows in comparison the single atom response spectrum (Fig. 2a) and spatially distributed ensemble of atoms (Fig. 2b). One can see that the CF in atomic ensemble spectrum is significantly shifted in the long wave region in comparison with the CF in spectrum of single atom response. Figure 3 shows the integral dependency of the CF as function of laser pulse intensity which is calculated for spatially distributed ensemble of atoms. In these calculations we have taken into account that the ionization probability depends on the peak pulse intensity [9].

5 Conclusions

In this paper, the saturation of the CF of the photoemission spectra generated in a silver by a femtosecond laser pulses has been demonstrated theoretically. The theoretical analysis is based on the non-perturbative theory of nonlinear atomic response, which enables us to vary the laser field strength in wide region from a subatomic to an over-atomic values. The results of computer simulations have shown that the CF of single atom response is saturated. However, the dispersion effects in spatially distributed ensemble of atoms reduce CF significantly. Hence, the development of the dispersion-suppressed schemes of HHG can play the decisive role in the practical applications of this effect.

Acknowledgements This work was supported by the Russian Foundation for Basic Research, grant nos. 12-02-00969 and 12-02-31843.

References

1. Papadogiannis, N.A., et al.: Phys. Rev. Lett. **90**, 133902 (2003)
2. Itatani, J., et al.: Nature (London) **432**, 867 (2004)
3. Tobey, R.I., et al.: Opt. Lett. **32**, 286 (2007)
4. Paul, P.M., et al.: Science **292**, 1689 (2001)
5. Drescher, M., et al.: Science **291**, 1923 (2001)
6. Corkum, P.B., et al.: Nat. Phys. **3**, 381 (2007)
7. Ganeev, R.A.: Phys. Usp. **52**, 55 (2009) [UFN **179**, 65 (2009)]
8. Andreev, A.V.: Zh. Èksp. Teor. Fiz. **116**, 793 (1999) [JETP **89**, 421 (1999)]
9. Andreev, A.V., et al.: JETP Lett. **93**, 476 (2011)
10. Andreev, A.V., et al.: Eur. Phys. J. D **66** (2012)

Chapter 3

All-Optical Raman XFEL, Based on the Electron Emission in a Transverse High Intensity Optical Lattice

I.A. Andriyash, E. d’Humières, V.T. Tikhonchuk, and P. Balcou

Abstract We present a new scheme of X-ray free electron laser, based on the interaction between a moderately relativistic electron bunch, and a transverse high intensity optical lattice. Gain scaling laws in the small signal regime are derived analytically, and confirmed from Particle-In-Cell simulations. The nature of amplification and saturation are discussed. The resulting all-optical Raman X-ray laser opens perspectives for ultra-compact X-ray coherent light sources.

1 Introduction

Numerous applications of UV/X-ray radiation in science and industry demand compact sources of high-quality coherent light in very short wavelength ranges. A well known solution is represented by X-ray free electron lasers (XFEL), where electrons with relativistic energies scatter X-ray light in a magnetic undulator. Most conventional XFELs are based on the mechanism of stimulated inverse Compton scattering (SICS), and require long amplification lengths and highly mono-energetic, low divergent electron beams. Such restrictions result in large sizes and costs of such devices.

A more compact solution is possible using a laser wave as an “optical wiggler”, and reaching a regime of parametric instability called stimulated Raman scattering (SRS). Resonant coupling of electron collective oscillations with the scattered and pump waves provides much higher gain than SICS and this scheme may be applied to the relativistic electron beams obtained via laser wake-field accelerators (LWFA). The challenge here is in the severe limitations on the quality of electron beam [1], which cannot be met in presently existing compact laser accelerating systems [2].

I.A. Andriyash (✉) · E. d’Humières · V.T. Tikhonchuk · P. Balcou
Univ. Bordeaux, CNRS, CEA, CELIA (Centre Lasers Intenses et Applications), 33400 Talence,
France
e-mail: igor.andriyash@gmail.com

Present address:
I.A. Andriyash
CELIA, 351, Cours de la Libération, 33405 Talence, France

A new promising scheme, recently proposed in [3], considers overlapping two transverse co-polarized laser pulses of equal frequency, thus obtaining a standing electromagnetic wave, called a *high intensity optical lattice*, with a wave-vector perpendicular to the beam axis [4]. The optical lattice provides a transverse confinement for electrons via the ponderomotive force and at the same time acts as a pump for the scattered radiation. Confinement of electrons prevents beams divergence along lattice wave-vector, and creates a new, controllable collective electron mode defined by the laser field. We investigate amplification in numerical simulations and describe it analytically using a hydrodynamic model of electron plasma interacting with laser and scattered fields.

2 Dynamics of Relativistic Electrons in a High Intensity Optical Lattice

We consider the geometry, where electrons are injected along z -axis into the optical lattice formed by two laser pulses, counter-propagating along x -axis. Laser radiation is considered of sub-relativistic intensity, $I \lesssim 10^{18} \text{ W/cm}^2$, so the dimensionless amplitude, $a_0 = 0.85 \cdot 10^{-9} \cdot \lambda_0 \sqrt{I}$ is small, where intensity I is in W/cm^2 and λ_0 is the laser wavelength in microns.

The dynamics of relativistic electrons in electromagnetic field is conveniently described in the reference system moving with an average electron velocity $v_b = c\beta_b \lesssim 1$. In this frame an observer “sees” laser beams as oblique to the beam axis with an angle, defined as $k_{0\perp}/k_{0\parallel} = 1/\gamma_b\beta_b \ll 1$, where $\gamma_b = (1 - \beta_b^2)^{-1/2}$ is the beam Lorentz factor. Electron motion in this frame is non-relativistic, and the wavelength of the scattered electromagnetic wave is close to the one of the pump.

Injection of electrons into the lattice may be described as a relatively slow switch-on of the external electromagnetic field given by sum of the laser pulses

$$a_L = a_1 + a_2 = 2a(t) \sin(k_{0\perp}x) \cos(\omega_0 t + k_{0\parallel}z), \quad (1)$$

where the field amplitude grows during the time t_{inj} up to a_0 . Electron with transverse velocity, $v_\perp \leq \sqrt{2}a_0c$, may be trapped in the ponderomotive potential of the lattice and will oscillate along the closed phase trajectory $[x(t), p_x(t)]$. Particles with lower initial velocities, are trapped before the end of injection and the further growth of potential adiabatically compresses their phase trajectories thus increasing the velocity amplitude. If the time of injection is much bigger than the typical period of particle oscillation, the beam may be significantly compressed [4]. Electron oscillations in optical lattice potential $U_p(x) = m_e a_0^2 c^2 \sin^2 k_{0\perp} x$, follow elliptic phase trajectories. Approximating electron trajectories with harmonic law $x_e = x_m \cos(\Omega t)$, we may estimate the frequency as,

$$\Omega \simeq \Omega_0 (k_{0\perp} x_m)^{-1} \sin k_{0\perp} x_m, \quad (2)$$

where x_m is the oscillation amplitude and $\Omega_0 = \sqrt{2}a_0 k_{0\perp} c$ is a frequency of small-amplitude oscillations.

3 Collective Properties of Electrons, Trapped in a Lattice Potential

We study the collective electron dynamics in a fluid approach, i.e. electron motion follows the hydrodynamic equations, interacting with electromagnetic field via the ponderomotive force. In this simplified model, we neglect electrons electrostatic potential and longitudinal temperature, and consider the transverse temperature not to exceed the trapping limit. Interaction is described with the following set of equations:

$$\partial_t n_e + \nabla \cdot (n_e \mathbf{u}) = 0, \quad (3a)$$

$$\partial_t u_x + \nabla_x P_{xx}/m_e n_e + \nabla_x U_p = 0, \quad (3b)$$

$$\partial_t u_z + \nabla_z U_p = 0, \quad (3c)$$

$$((\partial_t - i\omega_0)^2 - c^2 \nabla^2) \bar{a} = -(4\pi e^2/m_e) n_e \bar{a}, \quad (3d)$$

where \mathbf{u} is an electron fluid velocity. Enveloped vector potential \bar{a} is defined as $a = \Re[\bar{a} \exp(-i\omega_0 t + ik_0 z)]$ and it varies slowly in time creating the ponderomotive potential $U_p = m_e(c/2)^2 |\bar{a}|^2$. Trapped beam follows adiabatic equation of state along the x -direction, so electron pressure reads $P_{xx} = m_e v_\perp^2 n^3 / 3n_0^2$, where $v_\perp = c\delta\beta_\perp$ is defined by the transverse velocity spread. Considering equilibrium between lattice potential and electron pressure, we may find the unperturbed transverse distribution of electron density

$$n_e = n_0 \sqrt{1 - \xi^2},$$

where $\xi = x/L$ is a coordinate normalized to the beam width $L = v_\perp / (\sqrt{2} a_0 k_{0\perp} c)$, and $n_0 = n_e(0)$ is a maximum of the electron density.

In the linear approach, we consider the collective electron modes as a first-order perturbation of the beam position Δ_x , defined as $\xi = (x + \Delta_x)/L$. Without a signal wave, there is no longitudinal force $\partial_z U_p$ in Eq. (3b) and from Eqs. (3a)–(3d) it follows:

$$\partial_t^2 \Delta_x = -\Omega^2 \Delta_x,$$

which describes the collective beam mode with a frequency $\omega_b = \Omega$.

The amplified small-amplitude signal wave a_s interacts with electrons via first-order perturbation of ponderomotive potential $U_p^{(1)} = m_e(c/2)^2 \bar{a}_s \bar{a}_L^* + \text{c.c.}$, where c.c. stands for the complex conjugation. Assuming the plane signal wave we neglect diffraction terms in Eqs. (3a)–(3d) and linearize the system in Fourier domain to obtain the dispersion equation:

$$(\omega^2 - \Omega^2)((\omega - \omega_0)^2 - (k_z - k_{0\parallel})^2 c^2 - \tilde{\omega}_p^2) = G\alpha\omega_0^4, \quad (4)$$

where $\alpha = (\omega_p a_0 k_z c k_{0\perp} L / \omega_0^2)^2$ is a coupling coefficient between electromagnetic and electron beam modes, and coefficient G is due to the coupling inhomogeneity. In case of a plane signal wave, the coupling is $\propto \xi^2 \sqrt{1 - \xi^2}$, and we may estimate $G \simeq 0.2$.

Amplification of the Stokes mode is described by the complex frequency in Eq. (4) with a real part $\omega \simeq \Omega$ and imaginary part Γ corresponding to an exponential growth rate. Typically, $\alpha \ll (\Omega/\omega_0)^3$, and the coupling of electromagnetic and electron modes is weak, and imaginary part of solution approximately reads:

$$\Gamma/\omega_0 = 0.5\sqrt{G\alpha\omega_0/\Omega}. \quad (5)$$

Such amplification may be saturated by the longitudinal trapping of electrons in the potential $|\bar{a}_s \bar{a}_L^*|$, resulting a full particle bunching $n_e \sim n_0 \exp(-i\Omega t) + \text{c.c.}$. From Eq. (3d), the maximal signal amplitude can be deduced as:

$$\langle a_s \rangle / a_0 \simeq (k_{0\perp} L) \omega_p^2 / (\Omega \omega_0). \quad (6)$$

4 Numerical Simulations of SRS

Numerical investigation of SRS in the electron beam frame and verification of Eqs. (5), (6) was done with help of the reduced electromagnetic particle-in-cell 2D code EWOK. The code algorithm is based on a general particle-in-cell approach; it calculates the enveloped vector potential \hat{a} from electromagnetic equation, reduced by neglecting second order terms $\partial_t^2 \hat{a}$ and $\partial_z^2 \hat{a}$, and Fourier transforming over x -coordinate $\partial_x^2 \hat{a} \rightarrow -k_x^2 \hat{a}_{k_x}$. The code is able to account for electrostatic field of electrons by solving the Poisson equation and it was verified that for the electron densities and energies, typical for LWFA beams, and short propagation distances, for which the space-charge effects on SRS development may be neglected.

For the numerical study we consider 4 kA current of electrons with average energies of 5 MeV; a normalized emittance of 1 mm·mrad; and a transverse size of the beam assumed around few micro-meters. The optical lattice is created by two laser beams at a wavelength of 1 μm , intensity $1.6 \cdot 10^{16} \text{ W/cm}^2$ and linear amplitude ramp of 20 μm . A plane seed wave with amplitude $a_s = 10^{-6}$ is injected into the simulation domain at the left boundary and it circulates in the system due to the periodic boundary conditions. The scattered field, measured at the right boundary, is presented in Fig. 1a; it exhibits an exponential growth with a rate $\Gamma/\omega_0 = 1.8 \cdot 10^{-3}$. Amplification saturates after 600 μm at a signal amplitude $a_s = 1.4 \cdot 10^{-4}$, when modulation of electron density results in a full bunching (see Fig. 1b).

The spectral-spatial characteristics of electron-scattered light interaction may be studied by measuring electron density and scattered wave along the x -axis of simulation domain and projecting temporal oscillations to the Fourier domain. Electron collective modes are mainly localized at the frequency $\Omega = \sqrt{2} a_0 k_{0\perp} c = 0.016 \omega_0$ and their transverse profile is in a good qualitative agreement with the one predicted in analytic study $\propto \xi^2 \sqrt{1 - \xi^2}$ (see Fig. 1c). The second harmonic of electron oscillations 2Ω can be also observed on the beam axis, but does not contribute to the amplification. In Fig. 1d, one may see the amplified scattered light at Stokes frequency $\omega_s = \omega_0 - \Omega$, with a quasi-plane profile, slightly modulated due to the electron density distribution.

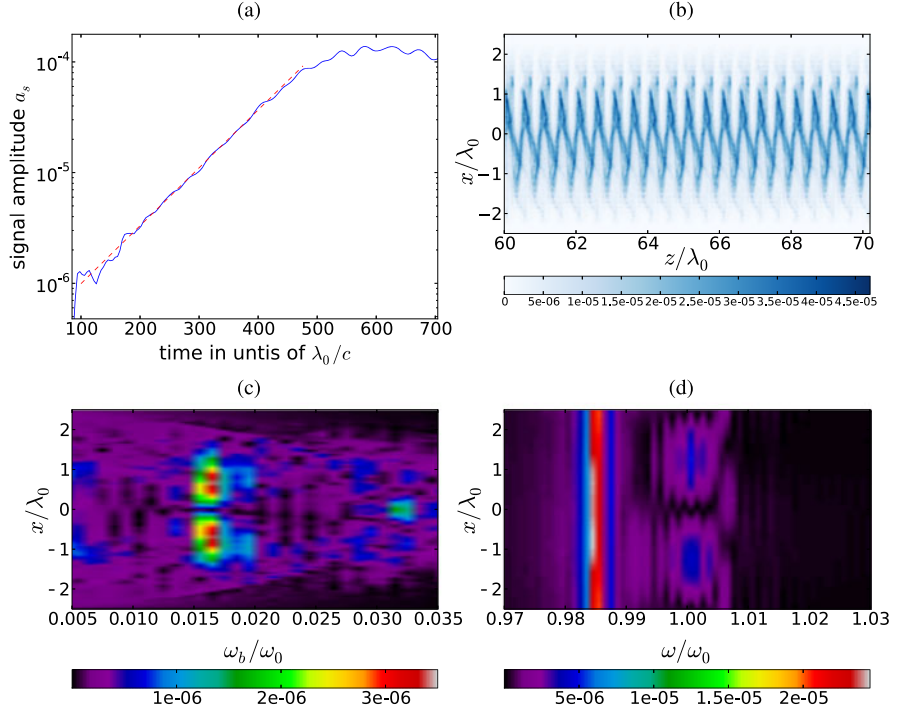


Fig. 1 Evolution of the signal dimensionless amplitude at the right boundary at the beam axis (a), fitted exponential growth with rate $\Gamma/\omega_0 = 1.9 \cdot 10^{-3}$ (dashed line); electron density distribution at saturation $600\lambda_0/c$ (b); spectral-spatial distribution of electron beam (c) and electromagnetic (d) modes

Growth rate and saturation level, provided by Eqs. (5), (6), read $\Gamma/\omega_0 = 1.7 \cdot 10^{-3}$ and $a_s = 1.4 \cdot 10^{-4}$ and are in perfect agreement with the values observed in the simulations. These estimates may be used for more realistic parameters—laser-accelerated electron beam of 20 pC, with average electron energy 40 MeV interacts with an optical lattice, created by laser light with intensity of $2.5 \cdot 10^{17} \text{ W/cm}^2$. For a case of cold electrons amplification proceeds on a millimeter length and results into the generation of a beam of 17 keV photons, with a total energy of the order of 1 μJ .

To conclude, we have demonstrated theoretically a new Raman process of amplification of coherent X-rays in the interaction between a relativistic electron bunch and a high intensity optical lattice. Presented estimates indicate the possibility for experimental demonstration of the process in a compact setup. The Raman XFEL should further studied as a way to create a ultra-compact coherent X-ray sources, up to the hard X-ray range.

References

1. Sprangle, P., Hafizi, B., Peñano, J.R.: Phys. Rev. Spec. Top. Accel. Beams **12**, 050702 (2009)
2. Lundh, O., et al.: Nat. Phys. **7**, 219 (2011)
3. Balcou, P.: Eur. Phys. J. D **59**, 525 (2010)
4. Andriyash, I.A., Balcou, P., Tikhonchuk, V.T.: Eur. Phys. J. D **65**, 533 (2011)

Chapter 4

Optical Transforms Related to Coherent Imaging of Inclined Objects

I.A. Artyukov, A.S. Busarov, N.L. Popov, and A.V. Vinogradov

Abstract The theory of coherent reflection imaging of inclined objects at grazing angles of illumination is developed on the basis of the parabolic wave equation. A new optical transformation connecting image and object field distributions is presented. The codes for simulation the properties of practical optical systems are created. Simulation results for parameters close to an X-ray laser experiment are given.

1 Introduction

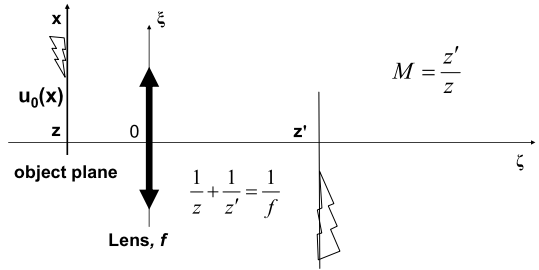
The development of laboratory X-ray lasers [1, 2] and accelerator based 3rd and 4th generation light sources [3, 4] makes coherent X-ray beams available to many researches and various applications. As for imaging and microscopy the coherence of novel X-ray sources offers several advantages and opportunities: phase retrieval technique and lensless imaging with wavelength resolution; quantitative, diffraction and interferometric microscopy; reduction of radiation loading on the investigated objects and environment and possibility to capture a diffraction pattern or an image with subpicosecond exposure prior to its degradation etc. The theoretical basis for coherent X-ray imaging, including Fresnel propagation theory and phase retrieval is well developed and routinely used for transparent objects [5, 6]. However many objects are opaque and cannot be studied in the transmission mode. Therefore there is a quest for coherent imaging methods in a reflection mode which should be suitable for grazing incidence illumination of objects as far as we speak about soft and hard X-rays [7–9]. In these papers the efforts have been made to modify the Kirchhoff diffraction integral for application to lensless imaging of obliquely illuminated reflective objects. Another approach based on the parabolic wave equation (PWE)

$$2ik \frac{\partial u}{\partial z} + \frac{\partial^2 u}{\partial x^2} = 0 \quad (1)$$

for slowly varying wave field $u(x, z) = e^{-ikz} E(x, z)$ is given in [10–13]. In the present paper we extend this approach to imaging of inclined objects with an ideal

I.A. Artyukov (✉) · A.S. Busarov · N.L. Popov · A.V. Vinogradov
P.N. Lebedev Physical Institute, 53 Leninsky Prospekt, 119991 Moscow, Russia
e-mail: iart@sci.lebedev.ru

Fig. 1 Coordinate system for paraxial optics Fresnel transform (2)



lens. As a result new optical transformations are obtained. They extend the general relations of Fresnel propagation theory [5, 14] to the case of objects tilted to the axis of an optical system.

2 Imaging Transform in Fresnel Optics

The Fresnel propagation theory gives the following formula for the optical field in the space (ξ, ζ) behind the lens [14] (see Fig. 1) in terms of the field distribution $u_0(x)$ of the object located at distance z from the lens:

$$u(\xi, \zeta) = C(\xi, \zeta) \int_{-\infty}^{\infty} dx \cdot u_0(x) \cdot \exp\left\{ik\left[\frac{x^2}{z} - \frac{(\frac{\xi}{z} + \frac{x}{z})^2}{\frac{1}{\zeta} - \frac{1}{z'}}\right]\right\}, \quad (2)$$

where z' being optically conjugated with z , so as $\frac{1}{z} + \frac{1}{z'} = \frac{1}{f}$, f is the focal length of an ideal lens represented as usual by a phase factor $T(x) = \exp\{-\frac{ikx^2}{2f}\}$ and

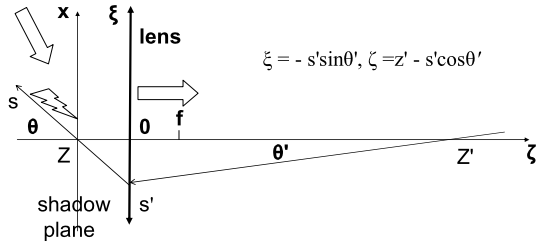
$$C(\xi, \zeta) = \sqrt{\frac{k}{2\pi iz\zeta}} \frac{\exp\{\frac{ik\xi^2}{2\zeta}\}}{\sqrt{\frac{1}{\zeta} - \frac{1}{z'}}}. \quad (3)$$

Formulas (2), (3) can be obtained by successive application of Fresnel propagation integral to the object field and then to the field distribution on the surface of the lens. Important that the field $u_0(x)$ in (2) is taken in the plane normal to the beam k vector which coincides with the optical axis throughout this paper. For $\zeta \rightarrow z'$ formula (2) converges to

$$u(\xi) = \frac{\exp\{\frac{ik\xi^2}{2z'}(\frac{1}{M} + 1)\}}{i\sqrt{M}} u_0\left(-\frac{\xi}{M}\right), \quad M = \frac{z'}{z}, \quad (4)$$

i.e. represents (as it should be) the magnified and inversed image of the object $u_0(s)$ [14].

Fig. 2 Coordinate system for paraxial wave propagation and imaging in the case of inclined object (Sects. 2–4)



3 Free Space Propagation from a Tilted Object

Suppose now that an object is inclined to the optical axis at an angle θ (see Fig. 2). Then as was shown in [12, 13] the field in the vertical (“shadow”) plane located at the right edge of the object is given by

$$u_0(x) = \sqrt{\frac{k}{2\pi i \cos \theta}} x \int_0^\infty \frac{u_0(s)}{s^{\frac{3}{2}}} ds \cdot \exp\left\{\frac{ik(x - s \cdot \sin \theta)^2}{2s \cdot \cos \theta}\right\}, \quad x > 0; \quad (5)$$

$$u_0(x) = 0, \quad x < 0,$$

s here is the coordinate in the tilted object plane. Formula (5) is the exact solution to PWE (1) for $x > 0$ corresponding to object field $u_0(s)$ and a reasonable approximation to the diffracted field of a restricted ($u_0(s) = 0$ for $s < 0$) object for $x < 0$.¹ The result (5) extends the Fresnel propagation integral to a tilted object, giving the shadow field distribution corresponding to the tilted object $u_0(s)$.

4 The Wave Field of a Tilted Object Behind the Lens

To find the wave field of a tilted object transmitted through the lens one has to install (5) into (2), integrate over x in the shadow plane and obtain:

$$u(\xi, \zeta) = \frac{1}{2\pi} \sqrt{\frac{l(\zeta)}{z\zeta \cos \theta}} \exp\left\{\frac{ik\xi^2}{2\zeta} \left[1 - \frac{l(\zeta)}{\zeta}\right]\right\} \times \int_0^\infty \frac{ds \cdot u_0(s)}{s^{\frac{3}{2}}(A + i\gamma)} \exp\left\{\frac{ik}{2} \frac{s \cdot \sin^2 \theta}{\cos \theta}\right\} F(\eta) \exp(\eta^2). \quad (6)$$

$$\frac{1}{l(\zeta)} = \frac{1}{\zeta} - \frac{1}{z'}, \quad A(s) = \frac{1}{z} - \frac{l(\zeta)}{z^2} + \frac{1}{s \cdot \cos \theta} = \frac{z \cdot z' - \zeta(z + z')}{z^2(z' - \zeta)} + \frac{1}{s \cdot \cos \theta},$$

$$\eta(s) = i \sqrt{\frac{ik}{2A(s)}} B, \quad B = \frac{\xi \cdot l(\zeta)}{z\zeta} + \operatorname{tg} \theta, \quad (7)$$

$$F(\eta) = \exp(-\eta^2) - \eta \sqrt{\pi} [1 - \Phi(\eta)], \quad \Phi(\eta) = \frac{2}{\sqrt{\pi}} \int_0^\eta \exp(-t^2) \cdot dt,$$

¹The details concerning application of PWE in X-ray optics and other fields can be found in [5, 15, 16].

a small positive value $\gamma \rightarrow 0$ is introduced to provide the convergence of the integral over the shadow plane. Expression (6) can be used to find the radiation field entering a detector arbitrarily oriented in space (ξ, ζ) . Further in this paper basing on (6) the relation between optical fields $u_0(s)$ and $u(s')$ in the object and detector planes will be found.

5 The Image Field Distribution

The evident question is: what is the optimal location of the detector plane providing a perfect image of a tilted object $u_0(s)$? The intuitive answer is: the best similarity between image and object is expected when the detector plane is optically conjugated with the object plane. This plane is exhibited in Fig. 1 by a ray traveling along the tilted object and refracted in the lens. The following relation is valid if object and detector planes are optically conjugated:

$$\begin{aligned} \xi &= (\zeta - z') \operatorname{tg} \theta', \quad \text{where } \operatorname{tg} \theta' = \frac{z}{z'} \operatorname{tg} \theta, \text{ and} \\ \xi &= -s' \cdot \sin \theta', \quad \zeta = z' - s' \cdot \cos \theta'. \end{aligned} \quad (8)$$

Taking into account (8) and (7) we observe that in the detector plane:

$$B = 0, \quad \eta = 0 \quad \text{and} \quad A(s) = \frac{1}{\cos \theta} \left(\frac{1}{s} - \frac{1}{s^*(s')} \right), \quad (9)$$

where

$$s^*(s') = \frac{zs' \cdot \sin \theta'}{z' \cdot \sin \theta - s' \cdot \sin(\theta + \theta')} \quad (10)$$

is the counter image of s' .

With (8)–(10) formula (6) for the field of the image is considerably simplified and results in

$$\begin{aligned} u(s') &= -\frac{s^*}{2\pi} \sqrt{\frac{M \cos \theta}{s' \cos \theta'}} \cdot \exp \left\{ -\frac{iks' \sin^2 \theta'}{2 \cos \theta'} \right\} \\ &\times \int_0^\infty \frac{ds}{\sqrt{s}} \frac{u_0(s)}{s - s^* - i\gamma} \exp \left\{ \frac{iks \cdot \sin^2 \theta}{2 \cos \theta} \right\}. \end{aligned} \quad (11)$$

The values θ' and s^* here are determined by the geometrical parameters of the system according to (8) and (10).

Formula (11) gives the optical field $u(s')$ at the detector plane in terms of the field distribution $u_0(s)$ at the object. It is the direct extension of Fresnel paraxial formula (4) to the case of a tilted object. The qualitative difference between (4) and (11) is that for tilted object in general case the proportionality (similarity) between the image ($|u(s')|^2$) and object ($|u_0(s)|^2$) does not exist. Of course for $\theta \rightarrow \pi/2$ formula

(11) transforms into (4). To be convinced, note that for $\theta \rightarrow \pi/2$ the exponential factor in the integrand in (11) is large and the following relation holds:

$$\lim_{t \rightarrow \infty} \frac{e^{itx}}{x - i\gamma} = 2i\pi\delta(x). \quad (12)$$

Then formula (11) is reduced to

$$u(s') = \frac{1}{i} \sqrt{\frac{Ms^* \cos \theta}{s' \cos \theta'}} \cdot \exp \left\{ \frac{iks'^2 \operatorname{tg} \theta \sin(\theta + \theta')}{2M[z' \sin \theta - s' \sin(\theta + \theta')]} \right\} u_0(s^*). \quad (13)$$

The common features of (4) and (13) are: (a) the object intensity distribution $|u_0(s)|^2$ is reproduced with some scaling in the detector plane and (b) the phase factor depends only on the optical scheme geometry and does not depend on the structure of the object $u_0(s)$. These features do not appear for general formula (11). The dimensionless parameter responsible for transition from (11) to (13) is $\Phi = \frac{2\lambda \cos \theta}{a \sin^2 \theta}$ (a is the object feature size), introduced earlier in [11]. So for $\Phi \ll 1$, that means normally illuminated object, $\theta \approx \pi/2$, and wavelength $\lambda = 2\pi/k$ small as compared to the feature size a , we arrive from general wave optics expression (11) to formula (13) representing the wave field which is characteristic for paraxial geometrical optics. It is easy to check that for $\theta \approx \pi/2$ formula (13) transforms exactly into (4). In the opposite case $\Phi \gg 1$, small feature size a and low tilt angle $\theta \rightarrow 0$, the image field (11) takes the form

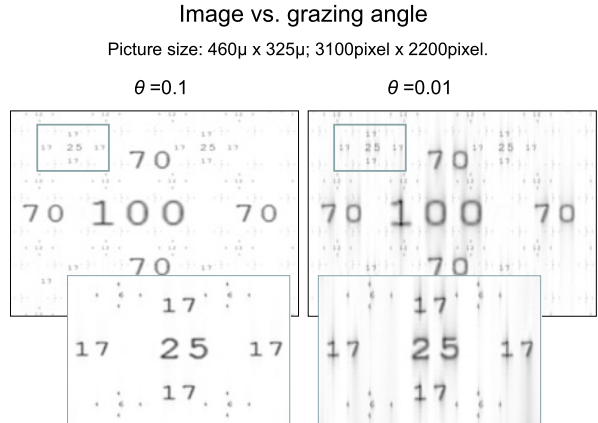
$$u(s') = -\frac{s^*}{2\pi} \sqrt{\frac{M \cos \theta}{s' \cos \theta'}} \cdot \exp \left\{ -\frac{iks' \sin^2 \theta'}{2 \cos \theta'} \right\} \times \left[i\pi \frac{u_0(s^*)}{\sqrt{s^*}} + \int_0^\infty \frac{u_0(s) ds}{\sqrt{s}} P \frac{1}{s - s^*} \right], \quad (14)$$

consisting of two parts. The first, local additive, reproduces the shape of the object field $u_0(s)$ and the second, integral additive, introduces the blurring of the ideal image. So it clearly demonstrates that tilting of an object not only distorts (formula (13)) but also blurs the image.

6 Simulation Results

To illustrate the obtained results the calculations have been made for an idealized optical scheme containing a zone plate with the focal length $f = 0.1$ cm and other parameters close to those achieved for laboratory X-ray lasers: wavelength $\lambda = 10$ nm, $z = z' = 0.2$ cm (one to one imaging). Numerical aperture was taken as large as $NA = 0.5$ in order to separate and investigate the influence of the object tilting on the image quality. The calculated images of a table of figures in the planes optically conjugated to the tilted object are shown in Fig. 3 for grazing angles $\theta = 0.1$ and $\theta = 0.01$. The sizes of the original table are $460 \mu \times 325 \mu$. The size of a number is proportional to its value. The large insets are zoomed versions of the corresponding boxes in the left upper corners of the pictures. It can be observed that for $\theta = 0.1$

Fig. 3 Coordinate calculated images of a table inclined at grazing angles 0.1 and 0.01 rad. The wavelength $\lambda = 10 \text{ nm}$, the parameters of the optical system are: $f = 0.1 \text{ cm}$, $NA = 0.5$, $z = z' = 0.2 \text{ cm}$ (see Fig. 2 and Sect. 5) in the case of inclined objects (Sects. 2–4)



the image of a tilted table in optically conjugated plane is rather perfect, whereas for $\theta = 0.01$ some blurring appears. Similar effect was observed in calculated images of the text pages. The results of such calculations can be used for simulation and evaluation of spatial resolution and field of view of practical optical systems.

7 Discussion

Consider the conditions for the applicability of our approach. The use of PWE implies the following approximation to the plane wave solution of the wave equation [15, 16]:

$$E(x, z) = e^{iqx + i\sqrt{k^2 - q^2}z} \approx e^{ikz}u(x, z), \quad u(x, z) = \exp\left\{iqx - i\frac{q^2}{2k}z\right\}, \quad q \ll k. \quad (15)$$

This wave corresponds to the space harmonic $u_0(s) = e^{ivs}$ in the tilted object plane where $v = 2\pi/a$ can be found by taking $x = s \sin \theta$ and $z = -s \cos \theta$ in (15):

$$v = q \sin \theta + \frac{q^2}{2k} \cos \theta, \quad \text{or} \quad q = \frac{v}{\sin \theta} \Psi(\Phi), \quad (16)$$

where

$$\Psi(\Phi) = \frac{2}{\Phi}(\sqrt{1 + \Phi} - 1) = \begin{cases} 1, & \Phi \ll 1 \\ \frac{2}{\sqrt{\Phi}}, & \Phi \gg 1 \end{cases} \quad (17)$$

and $\Phi = \frac{2v \cos \theta}{k \sin^2 \theta}$ is the same parameter mentioned in the end of the previous section and introduced in [11]. Formulas (15)–(17) can be used to find the divergence of the beam diffracted by a tilted object:

$$\Delta\theta = \frac{q}{k} = (\sqrt{1 + \Phi} - 1) \operatorname{tg} \theta = \begin{cases} \frac{\lambda}{a \sin \theta}, & \Phi \ll 1, \\ \sqrt{\Phi} \operatorname{tg} \theta, & \Phi \gg 1, \end{cases} \quad (18)$$

where $\lambda = 2\pi/k$ is the wavelength and $a = 2\pi/\nu$ —the feature size in the object plane. For $\theta = \pi/2$ formula (18) gives the result of the Fresnel propagation theory: $\Delta\theta = \lambda/a$. For $\Phi \ll 1$ it gives the intuitively evident estimate for the case of a tilted object: $\Delta\theta = \lambda a \sin\theta$. And for $\Phi \gg 1$ it leads to a new result valid for objects tilted at very low angles.

The evident condition for using PWE is low beam divergence: $\Delta\theta = q/k \ll 1$ (see (15)). To investigate it in more details introduce a small value $\alpha \ll 1$ to write the applicability condition as:

$$\frac{q}{k} < \alpha. \quad (19)$$

Taking q from (16) one obtains from here the following requirement for the validity of PWE approach:

$$\frac{a}{\lambda} > \frac{2}{\alpha^2 \cos\theta + 2\alpha \sin\theta}. \quad (20)$$

Combining (20) with the condition $\Phi \gg 1$ gives the range of grazing angles and feature sizes where the diffraction patterns of a tilted object are expected to considerably differ from those obtained at coherent normal incidence illumination:

$$\frac{2\cos\theta}{\sin^2\theta} > \frac{a}{\lambda} > \frac{2}{\alpha^2 \cos\theta + 2\alpha \sin\theta}. \quad (21)$$

Inequality (20) as well as right-hand side of (21) are important as they express the applicability condition of PWE for an arbitrary observation angle θ which we consider to be specular relative to the angle of object illumination. As it is seen from (21) it changes from $a > \lambda/\alpha$ for $\theta = \pi/2$ —Fresnel propagation theory, to $a > 2\lambda/\alpha^2$ —the imaging at very low angles $\theta \rightarrow 0$. Finally apply (15)–(17) to investigate the spatial resolution for paraxial (in the frames of validity of PWE) imaging of inclined objects. For this purpose $\Delta\theta = q/k$ in (18) can be considered as the numerical aperture NA of an optical system used for imaging. Then one obtains the spatial resolution δ in the form:

$$\delta \approx \frac{2\lambda}{(NA)^2 \cos\theta + 2NA \sin\theta}, \quad (22)$$

which for $\theta = \pi/2$ reduces to the well-known criteria $\delta \approx \lambda/NA$. It is worth noting that estimations of this section are valid to the order of magnitude especially taking into account that unlike the Fresnel theory according to (15), (16) the diffraction diagram for a tilted object is asymmetrical and shifted away from the object surface even for a symmetrical feature. Also formula (22) implies that the apertures of the diffracted beam (corresponding to the feature size a) and that of the optical system are matched and therefore all the necessary information is collected at the detector. However the similarity between an object and image does not necessarily occur. Even in the ideal case their field distributions are related by the general transform (11), which provides reproduction of the object only for $\Phi \ll 1$.

8 Conclusions

The developed theory and obtained simulation results reveal the following features of coherent reflection imaging at grazing angles:

1. The coherent image of an inclined object appears in an optically conjugated surface.
2. The image quality depends on the value of $\Phi = 2\lambda \cos \theta / (a \sin^2 \theta)$, a —is feature size, θ —grazing angle.
3. Calculations showed that image-to-object similarity keeps up to very small grazing angles.
4. The method can be extended to practical optical schemes. Gratings or crystals have to be added for tilting of the wavefront.

Acknowledgements The authors are grateful to A.V. Kraiskii, S.I. Mikhailov and I.G. Zubarev for fruitful discussions. The work was supported in part by RFBR Project # 10-02-00991-a.

References

1. Suckewer, S., Jaeglé, P.: X-Ray laser: past, present, and future. *Laser Phys. Lett.* **6**(6), 411–436 (2009)
2. Berrill, M., Alessi, S., Wang, Y., Domingue, S., Martz, D., Luther, B., Liu, Y., Rocca, J.: Improved beam characteristics of solid-target soft x-ray laser amplifiers by injection-seeding with high harmonics. *Opt. Lett.* **35**, 2317 (2010)
3. Schmuser, P., Dohlus, M., Rossbach, J.: Ultraviolet and Soft X-Ray Free-Electron Lasers. Springer Tracts in Modern Physics, vol. 229. Springer, Berlin (2008)
4. Kim, K.J., Shvyd'ko, Yu.V., Lindberg, R.R.: An X-ray free-electron laser oscillator for record high spectral purity, brightness, and stability. *Synchrotron Radiat. News* **25**(1), 25–31 (2012)
5. Paganin, D.M.: Coherent X-ray Optic. Clarendon Press, Oxford (2005)
6. Nugent, K.: Coherent methods in the X-ray sciences. *Adv. Phys.* **59**(1), 1–99 (2010)
7. Fenter, F., Park, C., Kohli, V., Zhang, Z.: Image contrast in X-ray reflection interface microscopy: comparison of data with model calculations and simulations. *J. Synchrotron Radiat.* **15**, 558–571 (2008)
8. Marathe, S., Kim, S.S., Kim, S.N., Kim, C., Kang, H.C., Nickles, P.V., Noh, D.Y.: Coherent diffraction surface imaging in reflection geometry. *Opt. Express* **18**, 7253–7262 (2010)
9. Roy, S., Parks, D., Seu, K.A., Su, R., Turner, J.J., Chao, W., Anderson, E.H., Cabrini, S., Kevan, S.D.: Lensless X-ray imaging in reflection geometry. *Nat. Photonics* **5**, 243–245 (2011)
10. Artyukov, I.A., Popov, A.V., Vinogradov, A.V.: Wave field transformation at coherent imaging of a flat reflection mask. In: Proc. SPIE, art. id 745114 (2009)
11. Artyukov, I.A., Mitrofanov, A.N., Popov, A.V., Vinogradov, A.V.: Theory and computation towards coherent reflection imaging of tilted objects. In: X-ray Lasers 2010: Proceedings of the 12th International Conference on X-ray Lasers, pp. 329–340. Springer, Berlin (2010)
12. Artyukov, I.A., Mikhailov, S.I., Popov, N.L., Vinogradov, A.V.: Theoretical study of coherent reflection imaging at grazing angles. In: Proc. SPIE, vol. 8140 (2011)
13. Artyukov, I.A., Vinogradov, A.V., Popov, N.L., Seleznev, V.N.: Simulation of grazing-incidence coherent imaging. *Quantum Electron.* **42**(2), 140–142 (2012)
14. Papoulis, A.: Systems and Transforms with Applications in Optics. McGraw-Hill, New York (1968)

15. Vinogradov, A.V., Popov, A.V., Kopylov, Yu.V., Kurokhtin, A.N.: Numerical Simulation of X-Ray Diffractive Optics. A&B Publishing House, Moscow (1999)
16. Mireille, L.: Parabolic Equation Methods for Electromagnetic Wave Propagation. Institution of Electrical Engineers, Michel Faraday House, London (2000)

Chapter 5

Soft-X-Ray Lasing down to 6.85 nm in Ni-Like Samarium

J.E. Balmer, F. Staub, and F. Jia

Abstract We report on recent progress achieved in X-ray laser research at the Institute of Applied Physics of the University of Bern. Using the 10-TW Nd:glass CPA (chirped-pulse amplification) laser system and the grazing-incidence pumping (GRIP) scheme, intense soft-X-ray lasing has been obtained on the $4d \rightarrow 4p$, $J = 0-1$ line of samarium (Sm, $Z = 62$) at 7.36 nm, with weak lasing observed at 6.85 nm. This was achieved with main pulse energies of 10–12 J and a pulse duration of 1.5 ps. Crucial to these results was the introduction of a second, relatively intense (22.7 %) prepulse ~ 30 ps before the main pulse, in addition to the 13.4 % prepulse incident on target several nanoseconds before the main pulse.

1 Introduction

The recent introduction of the grazing-incidence pumping (GRIP) scheme has greatly improved the efficiency of soft-X-ray lasers operating in the 10–20 nm region. Given the dramatic reduction in pump energy required—substantially less than 1 J, for example, in the case of the 18.9-nm laser of Ni-like molybdenum—the repetition rates of these lasers have increased from single shot to the 10-Hz regime [1–3]. With pump energies required for saturated lasing as low as 2–3 J, the 11.9- and 11.4-nm lasers in Ni-like Sn and Sb demonstrated in single-shot experiments are potential candidates for operation at few-Hz repetition rates [4, 5], as is the 10.9-nm laser in Ni-like Te pumped with a total energy on target of less than 4 J at 1-Hz repetition rate [6]. When attempting to move towards shorter wavelengths, one is confronted with the strong wavelength scaling of pump energy and optimum density for gain. Taking the $4d \rightarrow 4p$ lasing lines as given, shorter wavelength goes with higher atomic number, Z . As the atomic number gets larger, both the optimum density and electron temperature increase. The strong wavelength scaling of the electron temperature leads to a rapid increase in pump energy required. Simulations [7] predict that saturated sub-10-nm lasing should be feasible with 5–10 J

J.E. Balmer (✉) · F. Staub · F. Jia
Institute of Applied Physics, Sidlerstrasse 5, 3012 Bern, Switzerland
e-mail: balmer@iap.unibe.ch

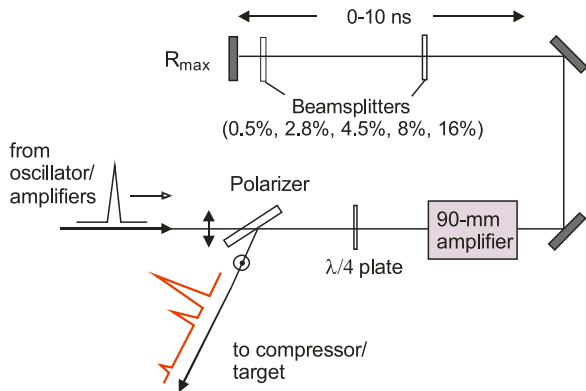
of pump energy, and ~ 50 J would be required in the GRIP scheme to generate an X-ray laser in the water window (2.5–4.4 nm). The optimum density has been predicted to increase from $\sim 2 \times 10^{20} \text{ cm}^{-3}$ for Ni-like silver ($Z = 47$, $\lambda = 13.9 \text{ nm}$) to $\sim 10^{21} \text{ cm}^{-3}$ for Ni-like samarium ($Z = 62$, $\lambda = 7.36 \text{ nm}$) [8]. The latter equals the critical density for Nd:glass lasers, with the consequence that the optimum density for gain becomes higher than the critical density for Nd:glass (and Ti:Sapphire) driver lasers when moving towards still shorter wavelengths. The maximum is however relatively broad, so that reasonable gain is expected at densities within a factor of $\sim 2 \times$ of the optimum. With regard to the GRIP scheme, the optimum angle, given by $n_e = n_c \sin^2 \theta$, where n_c is the critical density for the pump wavelength, approaches 90° , i.e., normal incidence, as the optimum density approaches n_c . Obviously, in this case, the main advantages of grazing-incidence pumping such as enhanced absorption due to increased path length in the plasma are lost and one is left with the standard transient-collisional-excitation (TCE) scheme.

In this work, we report on X-ray lasing close to saturation on the $4d \rightarrow 4p$, $J = 0-1$ line of Sm at a wavelength of 7.36 nm, using the GRIP scheme at an angle of 50° . This was achieved with a main pumping pulse energy of 11 J in a 1.5-ps pulse, applying a triple-pulse scheme in which a first (few-percent) prepulse, preceding the main pulse by several nanoseconds, is followed by a second, relatively intense (22.7 %) prepulse 26 ps before the main pulse. As in most of our previous work, the prepulses are collinear with the main pulse, compressed to 1.5 ps, and irradiate the target at the GRIP angle.

2 Experimental Setup

The experiments were conducted using the existing 1054-nm Nd:glass CPA laser system (BeAGLE facility) that is capable of providing a maximum output energy of ~ 20 J in a 1.5-ps duration pulse at a rate of 1 shot every 25 minutes. The maximum energy of the system is limited by the damage threshold of the $190 \times 350 \text{ mm}^2$ size, 1740-lines/mm compressor gratings, given as 250 mJ/cm^2 by the manufacturer. Prepulses are generated as in our previous experiments by introducing beamsplitters with reflectivities of 0.5, 2.8, 4.5, 8, or 16 % into the double-passed beam path of the final amplifier (see Fig. 1). This scheme has the advantage that the prepulses are propagating along the same path as the main pulse, thus minimizing the variations in pulse overlap at the line focus. The drawback is that this scheme generates a series of post-pulses that, although not influencing the X-ray laser output itself, represent some loss in overall efficiency. If we denote by E_0 the pulse energy entering the prepulse generator equipped with two beamsplitters having reflectivities R_1 and R_2 , respectively, the relevant pulse sequence at the line focus consists of three pulses having energies of $E_1 = R_1 E_0$, $E_2 = R_2 (T_1)^2 E_0$, and $E_M = (T_1 T_2)^2 E_0$, where E_M denotes the energy of the main pulse and $T_i = 1 - R_i$. As an example, the two beamsplitters having reflectivities of 8 % and 16 % used in the experiments described below, generate prepulses of 13.4 % and 22.7 % of the main pulse energy, respectively.

Fig. 1 Schematic of the prepulse scheme used in the present experiments



The beam containing the main pulse as well as the prepulses is expanded to 130 mm in the last spatial filter telescope, compressed to 1.5 ps, and focused by a combination of an $f = 80$ cm doublet and an $f = 30.4$ cm (12'') spherical mirror to produce a 12-mm long and 50- μm wide line focus (FWHM, measured at low power) at a GRIP angle of 50° (see Fig. 2). This configuration results in a traveling-wave velocity of $v_{\text{exc}} = 1.41c$ along the target, and thus a temporal mismatch of $\Delta t \approx 12$ ps between the pump pulse and the X-ray laser pulse at the output end of the target. A slight tilt (0.09°) and shift (11 mm) of the second compressor grating is used to reduce the traveling-wave velocity to $v_{\text{exc}} = c$ [9].

The main diagnostics of the soft X-ray emission from the plasma is an on-axis, time-integrating XUV spectrometer that consists of a 1200-lines/mm, aberration-corrected Hitachi grating (radius of curvature: 5649 mm), working at a grazing-incidence angle of 3°. The grating disperses the incident radiation onto a 40-mm diameter P20 phosphor screen, which is imaged to a cooled CCD camera having a pixel size of $23 \times 23 \mu\text{m}^2$. The wavelength coverage of the spectrometer is

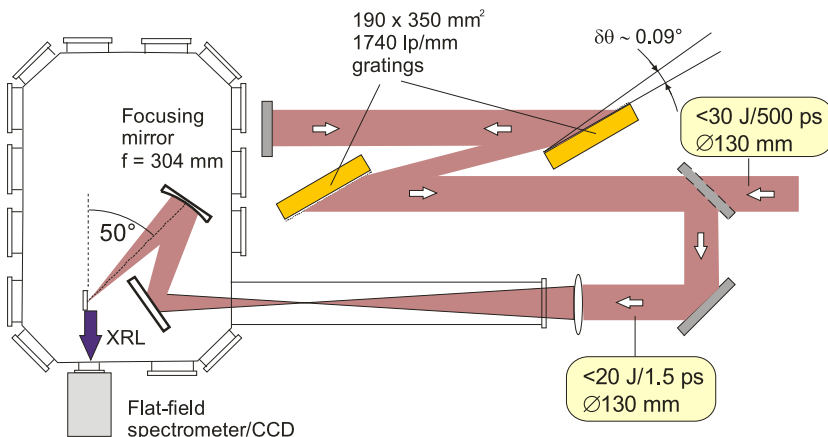


Fig. 2 Schematic of the focusing scheme used in the present experiments

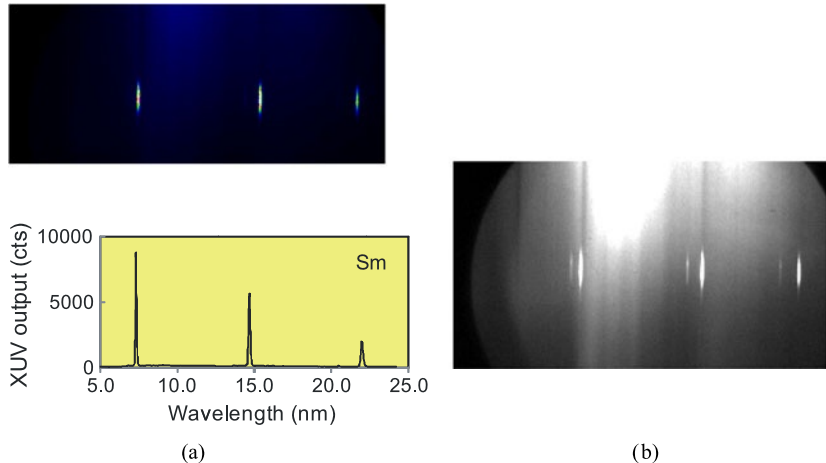


Fig. 3 (a) On-axis spectrum showing the 7.36-nm, $4d \rightarrow 4p$, $J = 0-1$ lasing line of Ni-like Sm in first, second, and third order for a pump energy of 12.6 J in a 1.5-ps pulse, (b) overexposed spectrum showing the short-wavelength $4d(3/2, 3/2) \rightarrow 4p(3/2, 1/2)$, $J = 0-1$ lasing line at 6.85 nm

$\sim 5-25$ nm with a spectral resolution of ~ 0.2 nm. The relatively poor resolution is a consequence of the slitless operation of the spectrometer, which results in a measured linewidth being dominated by source broadening.

3 Results and Discussion

The experiments on Ni-like samarium lasing were guided by our previous results demonstrating saturated lasing in Ni-like Sn and Ba at wavelengths of 11.9 and 9.2 nm, respectively [4, 10]. In the case of the Sn laser, after implementation of the traveling-wave scheme, it was found that a triple-pulse pumping scheme, with a second prepulse less than 100 ps before the ~ 2.5 -J main pulse, led to a dramatic increase of the X-ray laser output. Intense lasing was obtained with a weak (0.5 %) first prepulse at 2.8 ns and a second, 16 % prepulse at ~ 50 ps before the main pulse. This was subsequently confirmed by the Ba results, where saturated lasing with 9 J of main pulse energy was observed when the first prepulse was increased to 2.8 %, while the second prepulse (16 %) was set at 43 ps before the main pulse.

For the Sm experiments, targets were prepared in the form of ~ 1 - μ m thick layers coated onto glass slides and stored either in vacuum or in an argon-filled container. Figure 3 shows the on-axis spectrum of a shot taken with a main pulse energy of 12.6 J in a 1.5-ps pulse, a 13.4 % first prepulse at 3 ns and a 22.7 % second prepulse at 26 ps before the main pulse. This corresponds to irradiances of 2×10^{14} , 3×10^{14} , and 1.4×10^{15} W/cm $^{-2}$, respectively, for the three pulses. Clearly, the 7.36-nm lasing line is seen to dominate the spectrum in first, second, and third order. According to the previous calibration of our diagnostics, the output energy of this

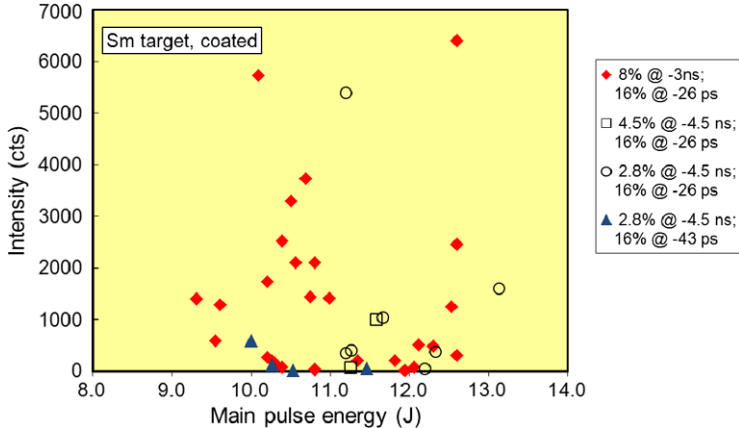


Fig. 4 7.36-nm line intensity of Ni-like Sm vs. main pulse pumping energy, showing large output variation

shot is 3–4 μ J. Comparison with the Ni-like Sn and Ba data, taking into account the scaling of the saturation irradiance as a function of atomic number [11] implies that this is very close to or even exceeding saturation.

Starting from the prepulse configuration of the 9.2-nm Ba laser discussed above, a series of shots was taken to optimize the 7.36-nm Sm laser output for a range of the amplitudes and delays of the two prepulses. Due to the low repetition rate of the driver laser system, only a limited scan in this multi-dimensional parameter space (delay and amplitude of the two prepulses, energy of the main pulse) was practically possible. Figure 4 shows the measured 7.36-nm laser intensity as a function of the main pulse energy for various time delays of the main pulse relative to the peaks of the first and second prepulse. It is seen that lasing is achieved for main pulse energies as low as \sim 9 J, but that very large output variations occur even under nominally identical pumping conditions.

Output variations may be caused, for example, by spurious prepulses generated in the amplifier chain, well-known in the case of regenerative amplifiers such as the one used in our system. Indeed, the prepulse monitor, a fast photodiode (risetime 0.7 ns) coupled to a 1-GHz oscilloscope, reveals a prepulse of 5×10^{-6} of the main pulse energy at \sim 6 ns before the arrival of the main pulse. However, since this pulse is at a very low level and observed on all the shots, it may be excluded as the main cause for the output variations. More likely, on the other hand, are main pulse irradiance variations in the line focus caused by excessive values of the B-integral [12] of the beam exiting the compressor. The B-integral is a measure of the nonlinear phase shift accumulated during propagation, defined as

$$B = \frac{2\pi}{\lambda} \int \gamma I(z) dz$$

where λ denotes the wavelength, γ the nonlinear index of refraction in SI units and I the irradiance. As has been shown in [13], the quality of the (line) focus becomes

severely degraded for values of the B-integral above ~ 4 . In our case, after the compressor, the 10-TW/130-mm diameter beam propagates through ~ 5 m in ambient air and enters the vacuum chamber through a 28-mm thick BK7 glass focusing doublet and a 25-mm thick BK7 glass window. Using published data of γ for BK7 glass and air [12], this results in a value of the B-integral of ~ 10 [14]. Installation of the compressor in a vacuum vessel would reduce this to $B < 1$, however, this has not been possible so far because of space limitations in our laboratory. Since the main contribution to the B-integral originates from propagation in glass, work is currently under way to modify the focusing scheme in order to replace the focusing doublet by reflective optics [14]. With the additional replacement of the vacuum window by a somewhat thinner one, values of $B < 3$ will be achieved.

Acknowledgements The authors would like to thank B. Locher for expert technical assistance and target preparation. This work was supported in part by the Swiss National Science Foundation. F. Staub was supported by the Swiss National Science Foundation under D. Bleiner's Förderungsprofessur (grant PP00P2-133564/1).

References

1. Keenan, R., et al.: High-repetition-rate grazing-incidence pumped X-ray laser operating at 18.9 nm. *Phys. Rev. Lett.* **94**, 103901 (2005)
2. Larotonda, M.A., et al.: Characteristics of a saturated 18.9-nm tabletop laser operating at 5-Hz repetition rate. *IEEE J. Sel. Top. Quantum Electron.* **10**, 1363 (2004)
3. Rocca, J.J., et al.: Saturated 13.2-nm high-repetition-rate laser in nickel-like cadmium. *Opt. Lett.* **30**, 2581 (2005)
4. Grünig, M., et al.: Saturated x-ray lasing in Ni-like Sn at 11.9 nm using the GRIP scheme. *Opt. Commun.* **282**, 267 (2009)
5. Imesch, C., et al.: Gain-saturated Ni-like antimony laser at 11.4 nm in grazing-incidence pumping geometry. *Opt. Commun.* **283**, 66 (2010)
6. Alessi, D., et al.: Gain-saturated 10.9-nm tabletop laser operating at 1 Hz repetition rate. *Opt. Lett.* **35**, 414 (2010)
7. Shlyaptsev, V.N., et al.: Numerical study of transient and capillary x-ray lasers and their applications. In: Proc. 9th Int. Conf. X-Ray Lasers. IOP Conf. Ser., vol. 186, p. 325 (2005)
8. Pert, G.J.: Optimizing the performance of nickel-like collisionally pumped x-ray lasers. *Phys. Rev. A* **73**, 033809 (2006)
9. Chanteloup, J.-C., et al.: Pulse-front control of 15-TW pulses with a tilted compressor and application to the subpicosecond traveling-wave pumping of a soft-x-ray laser. *J. Opt. Soc. Am. B* **17**, 151 (2000)
10. Staub, F., et al.: Soft-x-ray lasing in nickel-like barium at 9.2 nm using the grazing-incidence scheme. *Opt. Commun.* **285**, 2118 (2012)
11. Sasaki, A., et al.: The gain distribution of the transient collisional excited X-ray lasers. *J. Quant. Spectrosc. Radiat. Transf.* **71**, 665 (2001)
12. Brown, D.C.: High-Peak-Power Nd: Glass Laser Systems. Springer, Berlin (1981)
13. Seznec, S., et al.: Towards the 10^{19} – 10^{20} W/cm $^{-2}$ regime with amplified chirped pulses: basic limitations and solutions. *Opt. Commun.* **87**, 331 (1992)
14. Staub, F., et al.: Line-focus generation for X-ray laser pumping. In: Sebban, S., et al. (eds.) X-Ray Lasers 2012. Springer Proceedings in Physics, vol. 147. Springer, Cham (2013). Chapter 38 in this book

Chapter 6

Fourier Optics Study of Traveling-Wave Excitation at Short-Wavelength Plasma-Lasing

Davide Bleiner and Thomas Feurer

Abstract Traveling-wave excitation close to the speed of light implies small-angle target-irradiation. Yet, short-wavelength lasing needs large irradiation angles. Pulse-front back-tilt is considered to overcome such trade-off. Pulse-front tilt by means of compressor misalignment was found effective only if coupled with a strong front-end imaging/focusing component.

1 Introduction

Laser-induced plasma-columns serve as gain media for short-wavelength coherent emission. In traveling-wave excitation (TWE) one matches the propagation of the amplified spontaneous emission (ASE) along the plasma column to the speed of light c . For a given irradiation angle γ the nominal TWE speed is obtained as $v_{\text{TWE}} = c / \cos \gamma$. However, for *short-wavelength* amplification the pump pulse must be deposited deeper into the plasma, where higher electron density is found. For this purpose target irradiation must be at large angle, as the optical penetration scales as $n_c \sin^2 \gamma$, where n_c is the critical density. The latter requirement of *large* angles poses a trade-off with TWE close to $1c$ that requires *small* angle irradiation.

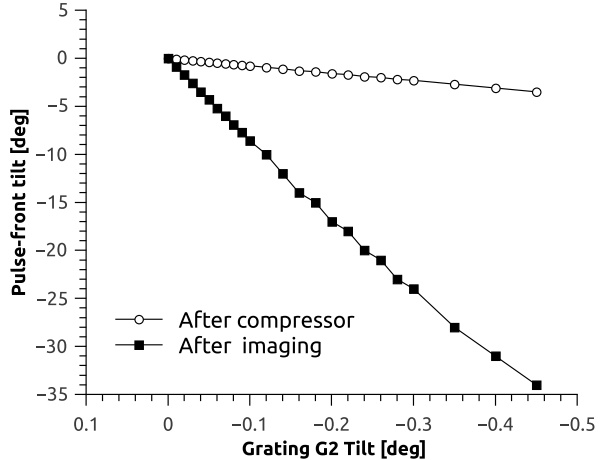
In chirped-pulse amplification (CPA) a stretched-pulse is amplified and then recompressed in a grating pair (compressor) [1–4]. The two compressor gratings must be perfectly parallel to achieve optimum recompression over the entire beam diameter. In this work the grating pair is intentionally misaligned, in order to tune a controlled amount of pulse-front *back-tilt*. Thus, for large irradiation angles one could in principle still have the TWE speed close to c as the *pulse-front* gives the effective TWE speed. Aim of this work was to investigate quantitatively such technique. A one-dimensional Fourier optics code was written for computing the parametric dependence between the compressor misalignment and the pulse characteristics. Experimental data on the pulse structure and TWE speed were available and used for comparison.

D. Bleiner (✉) · T. Feurer

Institute of Applied Physics, University of Bern, Sidlerstrasse 5, Bern, 3012, Switzerland

e-mail: bleiner@iap.unibe.ch

Fig. 1 Pulse-front back-tilt right after the compressor and at the target (“after imaging”) as a function of G2 tilt. The magnification is essential to achieve TWE compensation



2 Fourier Optics Model

Fourier optics considers [5], within the paraxial approximation, a set of superposed plane waves in order to obtain the natural modes of the propagation medium itself, i.e. the E field characteristics over space and time. The free-space propagation (FSP) transfer function is expressed as follows, with propagation in the z -axis and radial isotropy over the transverse dimension r :

$$E_{FSP}(k_r, \Omega) = E_o(k_r, \Omega) \exp\left[-ikz - \frac{iz}{2k} k_r^2\right] \quad (1)$$

The grating-dispersion (GD) transfer function is expressed as follows:

$$E_{GD}(k_r, \Omega) = \frac{1}{b} E_o\left(\frac{k_r + \gamma\Omega}{b}, \Omega\right) \quad (2)$$

where the constant $b = \cos\alpha/\cos\beta_o$ is the beam size change upon diffraction, with the angle of incidence α and the diffraction angle β_o at the center frequency ω_o . The coupling between wavevector and frequency is determined by $\gamma = 2\pi M/(\omega_o G \cos\beta_o)$, with the diffraction order M and the grating period G . The relative frequency $\Omega = \omega - \omega_o$ is used throughout. Repeated application of Eqs. (1) and (2) computes the E_{out} at setup’s exit. The second order phase term (chirp) of a grating compressor is obtained by the following expression:

$$\phi_2 = -\frac{i\Delta}{k} \gamma_1^2 \Omega^2 = \frac{\lambda_o}{2\pi c^2} \left(\frac{\lambda_o}{G}\right)^2 \frac{L}{\cos^3 \beta_o} \Omega^2 \quad (3)$$

with the orthogonal grating separation L . Tilting the second grating by ε causes all subsequent angles of incidence to change accordingly. Finally, the target is some distance away from the last grating and the transfer function of an imaging/focusing component with the focal length f is as follows:

$$E_{img}(r, \Omega) = E_o(x, \Omega) \exp\left[\frac{ik}{2f} r^2\right] \quad (4)$$

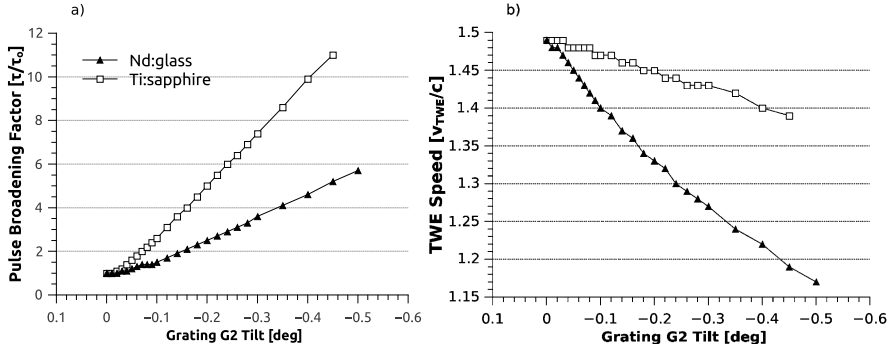


Fig. 2 Comparison of pro and contra of the discussed technique: **a**) pulse broadening at the beam boundary with respect to the best compression as a function of G2 tilt; **b**) Traveling-wave excitation (TWE) speed in units of speed of light as a function of G2 tilt

The computations were performed for the Nd:glass laser wavelength of 1054 ± 2 nm. For comparison results have been generated for a Ti:sapphire laser. The Gaussian beam radius was 66 mm and focused using a $f = 609.6$ mm mirror under an angle of 48° . The compressor had gratings with $G = 1740$ lp/mm, and the slant distance Δ was optimized by the code for a pulse stretch per bandwidth of 296 ps/nm. The roof mirror has a half-distance $d = 1360$ mm. The angle of incidence of the stretched pulse on the first grating was 60.8° .

3 Traveling-Wave Compensation with Misaligned Compressor

Figure 1 indicates that pulse back-tilt due to compressor misalignment is much smaller than the few tens of degrees required for TWE compensation, and mostly is enhanced by the imaging stage proportionally to the magnification. In fact, for given beam width a shorter line focus means a steeper back-tilt of the pulse-front. The misalignment of the compressor causes concomitant degradation of the pulse compression. Figure 2.a shows that the grating tilt can degrade the pulse temporal width. Clearly, short wavelength and small bandwidth mitigate the effect.

Finally, the combined effect on the TWE speed is shown, as a function of compressor misalignment, on Fig. 2.b. The nominal TWE speed at 48° is $1.5c$ but for half-degree grating tilt, and considering a 5-fold demagnification, a reduction of TWE speed down to $1.1c$ is computed for the 1054 nm wavelength. Experimental validation of the TWE speed was done using a streak camera connected to the target by means of optical fibers to the two extremes of the line focus. The data confirmed a TWE of $1.1c$. Experimental measurements of the pump pulse duration, using an autocorrelator showed a pulse duration of 2.7 ± 0.8 ps, whereas the theoretical Fourier-limited pulse duration is computed as 0.82 ps. This indicates a broadening of a factor of 3 by means of misalignment.

4 Conclusions

Pulse-front tilt to compensate TWE at large target-irradiation angle was shown to be effective only if coupled with a >5-fold front-end imaging/focusing component. Pulse broadening at the beam boundary can be however large, depending on wavelength and bandwidth. The Nd:glass laser showed best suitability.

Acknowledgements The present work was supported by the Swiss National Science Foundation under the grant number PP00P2-133564/1. Contributions from F. Staub, J.E. Balmer, Ch. Imesch are acknowledged.

References

1. Fiorini, C., Sauteret, C., Rouyer, C., Blanchot, N., Seznec, S., Migus, A.: IEEE J. Quantum Electron. **30**, 1662 (1994)
2. Pretzler, G., Kasper, A., Witte, K.J.: Appl. Phys. B **70**, 1 (2000)
3. Chanteloup, J.C., Salmon, E., Sauteret, C., Migus, A., Zeitoun, Ph., Klisnick, A., Carillon, A., Hubert, S., Ros, D., Nickles, P., Kalachnikov, M.: J. Opt. Soc. Am. B **17**, 151 (2000)
4. Akturk, S., Gu, X., Zeek, E., Trebino, R.: Opt. Express **12**, 4399 (2004)
5. Diels, J.C., Rudolph, W.: Ultrashort Laser Pulse Phenomena. Elsevier, Amsterdam (2006)

Chapter 7

Coherent Short-Wavelength Plasma Radiation for Lab-scale Nano-inspection Tools

Davide Bleiner

Abstract Coherent short-wavelength plasma radiation demonstrated a number of advantages for nano-inspection. Contending technologies are here discussed and strategies for X-ray laser optimizations are highlighted, thus bridging the gap between proof-of-principle or enabling tools.

1 Introduction

The continuing progress towards even smaller devices put forward a challenge to the nano-fabrication and nano-inspection “tools” that have to be made available before the next generation of nano-devices comes into realization. This is the premise for short-wavelength light sources given their potential for high-resolution. A number of applications are thus depending on such *enabling tools*. For instance, *magnetization dynamics* bears enormous technological significance for a number of new devices. We need however more resolution to understand basic interactions, such as spin-torque phenomena or the laser-assisted spin-manipulation. We need also nano-fabrication tools to develop new magnetic materials of improved purity. Also, *coherent diffraction* by nano-structures, such as protein nano-crystals and 2D crystals, bears the interest of resolving new structures and provide insights on molecular functions. Such “*lensless imaging*” has the interest of overcoming limitations brought by X-ray optics. As an additional example, *spectroscopy of correlated electron materials* shows its relevance to investigate metal-insulator transitions, high-temperature superconductivity, giant magneto-resistance, etc, if tools with the required meV resolution are accessible. Increasing evidence of the importance of nanoscale heterogeneities points at nano-scale spatial resolution. A similar consideration applies to time-resolution.

To address such needs, several countries invested hundreds of millions for the construction of X-ray Free-electron Lasers (xFEL). The FLASH (Germany) for instance, offering radiation in the extreme UV and soft X-ray domains, began operation in 2005. The LCLS system (USA) pushed the limit into the hard X-ray in

D. Bleiner (✉)

Institute of Applied Physics, University of Bern, Sidlerstrasse 5, Bern, 3012, Switzerland
e-mail: bleiner@iap.unibe.ch

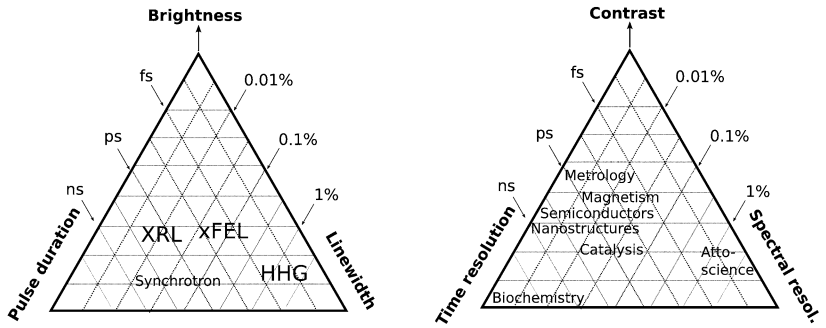


Fig. 1 Capabilities of the main short-wavelength sources and specification for several scientific cases

2009. The SACLA system in Japan, also in the hard X-ray, initiated in 2011. Other xFEL projects are making their way in Switzerland, Italy, Germany, and South Korea. Figure 1 compares a number of short-wavelength sources with the requirements for some nano-science cases. Plasma-based X-ray lasers (XRL) stretch over quite a few of the mentioned applications. This background offers a promising perspective for *laboratory-scale* nano-inspection tools.

2 XRL Bridging the Gap Between Proof-of-Principle and Enabling Tools

Proof-of-principle research tools are: (i) science-oriented, (ii) system-upgradable, (iii) of strategic interest. On the other hand, *enabling* tools are: (i) practice-oriented, (ii) platform-accessible, in terms of footprint and cost, and (iii) of productivity-interest. For instance, actinic metrology tools for EUV lithography belong to the latter case, whereas the xFEL to the former. The XRL has some intrinsic advantages, such as the low cost and footprint, or the spectral purity, to make it useful for *lab-scale* proof-of-principle studies as well as for *actinic* nano-inspection. Figure 2 summarizes the development for lab-scale XRL systems, showing how development matched with computational predictions. Table 1 quantifies productivity and cost, based on bibliometric data for the xFEL and the XRL communities. The publication output for the XRL was as low as 37 % of the xFEL community output. The latter advanced at a pace of a paper every 7.9 days, versus the 21.5 days to see a new XRL paper. Citations are 23 % for XRL versus xFEL. Nevertheless, the cost associated with xFEL instrumentation is remarkably higher, namely 300 times higher than that of a single XRL. Hence, one XRL paper costed approx. 100 kUSD versus the 2,300 kUSD for a xFEL one.

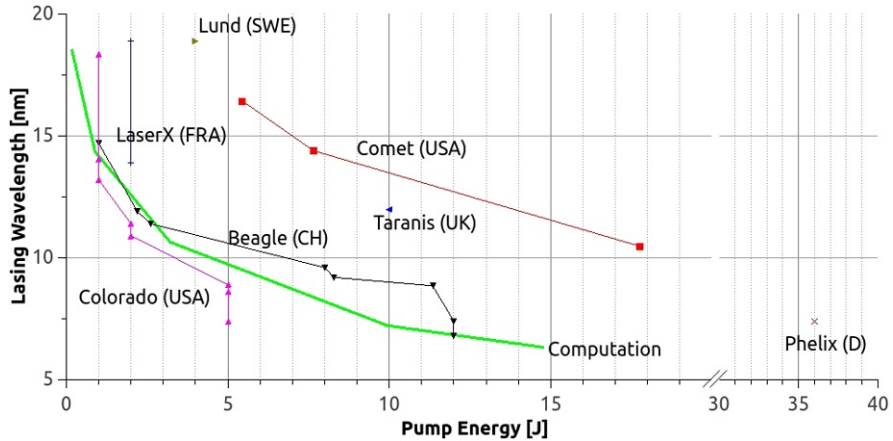


Fig. 2 Major laboratory-scale X-ray lasers systems based on coherent plasma emission. The computational prediction agrees with experimental achievements: a 10-fold pump increase for a 2-fold wavelength reduction

Table 1 Bibliometric analysis for xFEL and XRL communities in the last 5 year, realized on May 9th, 2012, using the *Web of Knowledge* interface accessing all data bases

	Communities		
	xFEL	XRL	xFEL/XRL
Publications	230	85	2.7x
Publication rate [p.a.]	46	17	2.7x
Days to paper	7.9	21.5	0.4x
Citations	1957	443	4.4x
Citation/Publications	8.5	5.2	1.6x
Construction Cost [M USD]	539	15	35.9x
Cost of paper [M USD]	2.3	0.1	23x
Cost of citation [k USD]	275	14	19.6x

3 Perspectives for XRL Development

Figure 3 compares the main short-wavelength sources in average output power and optical étendue and shows that one can identify specific domains of implementations. Besides, the potential for the XRL to fill the existing gap with contending technologies is shown. The XRL could reduce the gap with accelerator-based facilities on three steps: (i) reduction of the optical étendue, (ii) increase of the repetition rate, (iii) increase of conversion efficiency. The reduction of the étendue implies optimization of the source size as well as the beam divergence. Several groups have shown improvements of the collimation by means of seeding or line-focusing [3]. Ruiz et al. [4] have shown illumination improvements by either relay-imaging or telecentric correction. The increase of repetition rate from single shot operation to

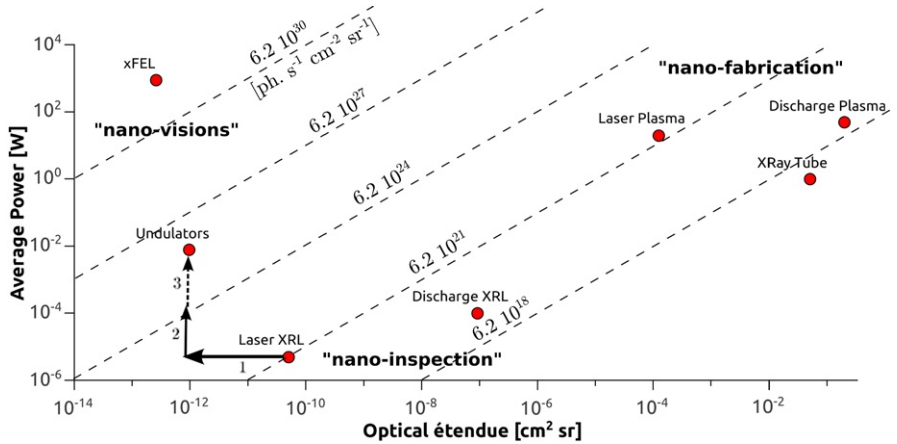
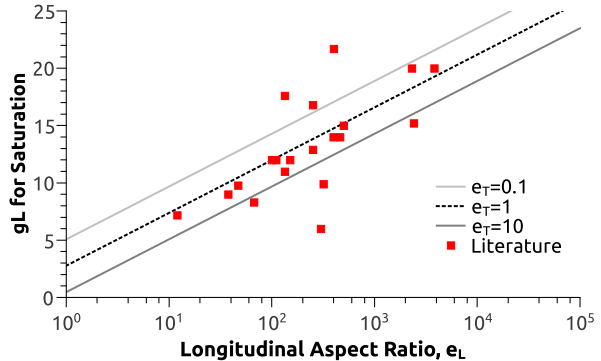


Fig. 3 Average source power versus optical étendue for a number of short-wavelength sources, and brightness in photons at 100 eV (dashed lines). The potential for the XRL to fill the existing gap with accelerator sources is indicated as: (1) reduction of source size and X-ray collimation, (2) increase of repetition rate, (3) optimization of plasma geometry and waveguiding

Fig. 4 Gain-length product at saturation as a function of longitudinal plasma aspect ratio (e_L), as predicted with own scaling law (see text). Literature data are plotted for benchmarking



10 Hz [5] or even 100 Hz [1, 6] is subject of ongoing research. Finally, the enhancement of the conversion efficiency by means of seeding and optimization of active volume geometry is to be mentioned [2].

The gain-length product for saturation is a function of active-volume geometry, i.e. longitudinal (e_L) and transverse (e_T) aspect ratio, and we proposed the following scaling-law: $G_{sat} = 2.7 + 2 \ln[e_L / \sqrt{e_T}]$ [7]. This expression shows that for an ordinary line focus with a plasma column of $e_L = 300$ and $e_T \approx 1$, then $G_{sat} \approx 14$, in agreement with experimental observations (Fig. 4). In terms of conversion efficiency, the problem is addressed considering both the efficient deposition of the pump pulse and the efficient extraction of the short-wavelength signal. Masoudnia et al. [8] showed that the pump delivery angle can alter the active volume geometry and thus the saturation gain-length product. The propagation of the short-wavelength signal can be described with a complex wave-vector, $k = \beta + i\alpha$,

obtained plugging the expression for the plasma dielectric constant into the dispersion for a transverse wave. Fill [9] has shown that $\alpha = \frac{-g}{2}$ and $\beta = \frac{2\pi}{\lambda} \sqrt{\epsilon}$, where g is the gain, λ is the wavelength, and ϵ is the optical permittivity. Thus k is steered by an electron density gradient term β and a gain-guiding term α . Fill has also given an expression to determine the relative importance of α versus β , namely α is dominating for $\frac{\lambda n_e}{g} < 8.75 \cdot 10^{11}$. For $\lambda = 12$ nm and $n_e \approx 10^{20}$ one obtains that gain-guiding is dominating only when the gain is above 137 cm^{-1} . Both forms of refraction however point at the identical solution: *plasma homogenization*. The use of pre-pulses indeed helped to relax plasma gradients prior to the delivery of the main pulse. The use of hollow cylinder targets is being investigated in our group to confine the plasma. Weber et al. [10] has reported the performance for transverse irradiation of micro-cavities, through a side opening. Masoudnia et al. [8] have shown computational predictions for the case of longitudinal irradiation at GRIP condition. Plasma reflection of incoming beam would not cause pump loss, since trapped in the cavity. The solution is interesting also for high repetition rate XRL, because the hollow target can be rotated such that ablation and re-deposition can lead to target self-healing.

4 Conclusions

Scientific cases proposed for the xFELs are partly suitable for the XRL. In comparison to the former, the latter has shown a productivity of 37 %, but for a modest cost of a few percent of the xFEL. Besides such investment factors, the unmatched linewidth of $<10^{-4}$, the pulse duration of a few ps, and the high single-shot brightness are interesting technical factors. At the moment, XRL are limited by the optical étendue and the repetition rate. Strategies for reducing the gap have been discussed. In terms of average power, the capillary discharge XRL shows a degree of maturity for nano-science applications [11]. The limitation of not being scalable to shorter wavelengths is irrelevant in imaging and spectroscopy, since the most of applications require sources with photon energy of 10–25 eV (or 120–50 nm in wavelength).

Acknowledgements The present work was supported by the Swiss National Science Foundation under the grant number PP00P2-133564/1. Contributions from F. Staub, J.E. Balmer, L. Masoudnia, M. Ruiz-Lopez, Th. Feurer are acknowledged.

References

1. Curtis, A.H., Reagan, B.A., Wernsing, K.A., Furch, F.J., Luther, B.M., Rocca, J.J.: Opt. Lett. **36**, 2164 (2011)
2. Oliva, E., Zeitoun, Ph., Sebban, S., Fajardo, M., Velarde, P., Cassou, K., Ros, D.: Opt. Lett. **34**, 2640 (2009)
3. Bleiner, D., Balmer, J.E., Staub, F.: Appl. Opt. **50**, 6689 (2011)

4. Ruiz-Lopez, M., Staub, F., Bleiner, D.: Optical correction of X-ray laser illumination for short-wavelength microscopy. In: Sebban, S., et al. (eds.) X-Ray Lasers 2012. Springer Proceedings in Physics, vol. 147. Springer, Cham (2013). Chapter 36 in this book
5. Guilbaud, O., et al.: Opt. Lett. **35**, 1326 (2010)
6. Tuemmler, J., Jung, R., Stiel, H., Nickles, P.V., Sandner, W.: Opt. Lett. **34**, 1378 (2009)
7. Bleiner, D.: Saturation gain-length product during short-wavelength plasma lasing. Appl. Phys. Lett. **101**, 081105 (2012)
8. Masoudnia, L., Bleiner, D.: Hohlraum target for overcoming refractive losses in plasma x-ray lasers. Laser Phys. (IOP) **23**, 056003 (2013)
9. Fill, E.E.: Opt. Commun. **67**, 441 (1998)
10. Weber, R., Cunningham, P.F., Balmer, J.E.: Appl. Phys. Lett. **53**, 2596 (1988)
11. Rocca, J.J.: Rev. Sci. Instrum. **70**, 3799 (1999)

Chapter 8

Ion Temperature and Cross-relaxation Effects on OFI Soft-X-Ray Laser

A. Boudaa, G. Maynard, and B. Cros

Abstract We present a theoretical investigation on the influence of ion temperature with cross-relaxation (CR) effects upon a collisionally pumped, optical-field-ionized (OFI) soft-X-ray laser (SXRL). Our results indicate that ion heating can induce a significant modification of the SXRL energy. However, whereas the CR rate is large in an OFI plasma, its contribution on the SXRL energy is found to be small.

1 Introduction

Soft-X-Ray lasers (SXRL) amplified in a plasma generated through OFI (Optical Field Ionization) have interesting properties in terms of application. In particular saturated amplification of spontaneous emission (ASE) with high gain has been experimentally demonstrated by focussing a high intensity infra-red (IR) beam in a xenon [1] or a krypton [2] gas target, at wavelength of respectively 41.8 nm and 32.8 nm. Moreover it has been shown that guiding [3] and seeding techniques [4] can lead to SXRL pulses having μJ energies together with high spatial and spectral coherence. The maximum of the SXRL energy has been obtained at relatively low pressure, around 20 mbar without guiding [1, 2] and 5 mbar with guiding [3]. At these pressures collisional broadening is small leading to a narrow line profile and to a high gain. Therefore the Doppler broadening can be dominating already at an ion temperature of few eV. It has been shown in [5] that such temperatures are reached in xenon or krypton plasmas generated by OFI, through the relaxation of strong collective interaction. In Sect. 2 we present an evaluation of the temperature effect on the ASE energy for a krypton target using typical values for the

A. Boudaa

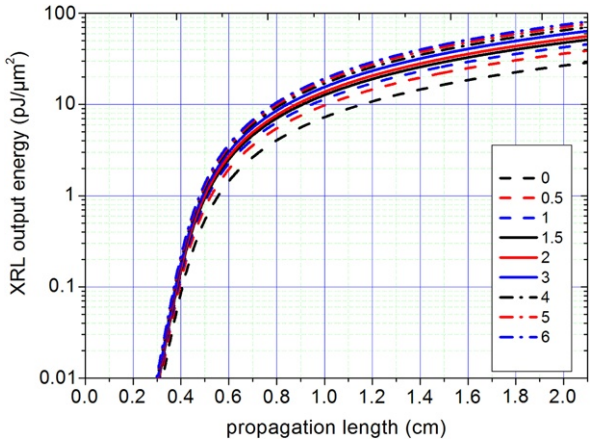
Laboratoire de Physique et Chimie Quantique, Université M. Mammeri de Tizi-Ouzou, Hasnaoua 15000, Algérie

A. Boudaa · G. Maynard (✉) · B. Cros

Laboratoire de Physique des Gaz et des Plasmas, Univ. Paris-Sud, 91405 Orsay, France

e-mail: gilles.maynard@u-psud.fr

Fig. 1 ASE energy versus plasma length for the 32.8 nm line of Kr^{8+} at 5 mbar. Each curve corresponds to a specific value of the ratio T_i/T_{eq} , indicated in the legend



experimental parameters. The calculations have been done by taking into account an inhomogeneous broadening in the gain.

In [5], it was shown that in the OFI plasma, the ions are strongly correlated. It means that the rate of elastic ion-ion collisions is quite high. These elastic collisions induce cross-relaxation (CR) effects that redistribute the excited ions over the Maxwellian velocity distribution. This relaxation has to be introduced in the Maxwell-Bloch equations. In our calculation, it has been done using the “strong-collision” model which assumes that the redistribution is uniform in velocity. In Sect. 3, we analyse how the CR can affect the results of Sect. 2.

2 Temperature Effect on ASE Without Cross-relaxation

To analyse the temperature effect on the ASE energy, we have introduced the inhomogeneous broadening in the COFIXE numerical code described in [3]. Here we present the results of a simplified calculation in 1D geometry, for a Kr gas with a pressure of 5 mbar irradiated by an IR beam with a maximum intensity of $9 \times 10^{16} \text{ W cm}^{-2}$ and 35 fs of duration. At such intensity, the Kr atoms get an ionization state of 8+, collisional excitation in the plasma then leads to ASE of the 32.8 nm line of the $3d^94d^1S_0$ - $3d^94p^1P_1$ transition. From [5] we deduce that the temperature T_i of the Kr^{8+} ions reaches an equilibrium value T_{eq} of 3.3 eV. In Fig. 1, are reported our results for the SXRL energy versus the plasma length, at several values of the ratio T_i/T_{eq} .

We can observe on Fig. 1 a significant influence of T_i on the ASE energy as soon as T_i becomes close to T_{eq} . It indicates that the ion temperature should indeed be included when considering SXRL in an OFI plasma.

Fig. 2a Same as Fig. 1, taking into account the CR effect and with $T_i/T_{eq} = 1$. Each curve corresponds to a specific value of the ratio T_1/T_a , given in the legend

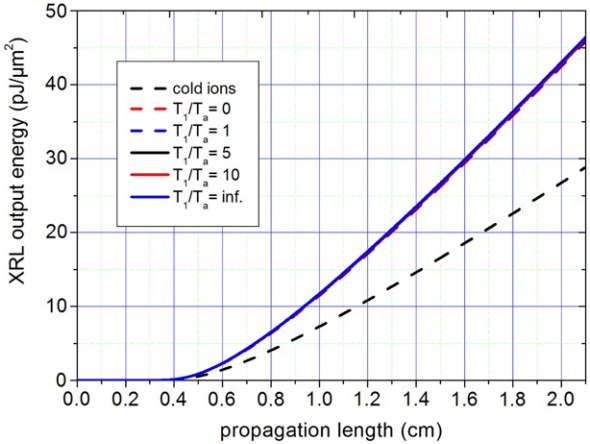
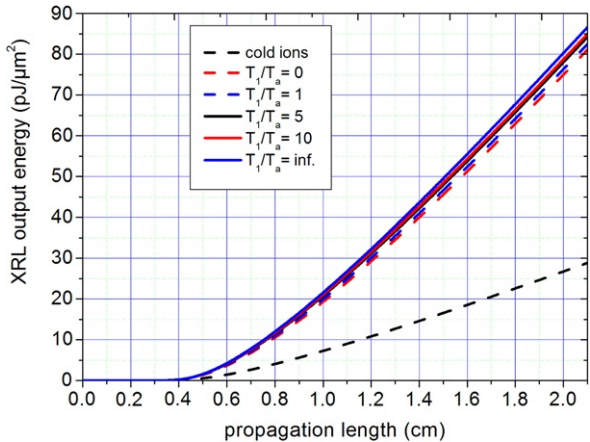


Fig. 2b Same as Fig. 2a, with $T_i/T_{eq} = 6$



3 Cross-relaxation Effects

CR of the ion population has been introduced in the COFIXE code through a relaxation term toward the Maxwellian distribution. The importance of the CR depends on the characteristic relaxation time noted T_a , which has to be compared to the characteristic gain recovery time noted T_1 . For $T_1/T_a \ll 1$, CR is negligible, we recover the standard inhomogeneous broadening. In the opposite limit $T_1/T_a \gg 1$, the CR is dominating, the velocity distribution of the amplifying ions remains Maxwellian. In that case the frequency profile of the gain is unchanged, as in the homogeneous case, with the difference that the profile is Maxwellian instead of being Lorentzian. A precise determination of T_1/T_a is a rather complex task (see [6]), but its value should be large, considering the strong coupling of the ions in an OFI plasma. As a first step, we have analysed the influence of the CR on the output ASE energy for several values of T_1/T_a between 0 and infinity. The results are reported on Fig. 2a for $T_i = T_{eq}$ and on Fig. 2b at a higher ion temperature $T_i = 6T_{eq}$.

We can observe on Fig. 2a, that, for $T_i/T_{eq} = 1$, the CR has a negligible effect on the ASE energy. In fact it is only at a much higher value of T_i , that the CR yields a significant modification of the ASE energy. As seen on Fig. 2b, even at $T_i/T_{eq} = 6$, the difference in energy considering either $T_1/T_a = 0$ or $T_1/T_a = \infty$ remains small.

4 Conclusion

The influence of strong ion-ion correlation (IIC) on ASE output energy in an OFI plasma have been investigated. Our results show that the main influence of IIC is to increase the Doppler broadening through the increase of the ion temperature up to few eV. The modification of the gain frequency profile through cross relaxation is a second order effect, which yields a significant contribution only for much higher temperatures. However cross relaxation can have a clearer signature when considering the amplification of a seeded signal. Moreover, as shown in [6], strong IIC should also be considered for the evaluation of collisional broadening. Therefore more investigations are needed in order to determine the full influence of strong IIC on SXRL amplification in a dense plasma.

References

1. Sebban, S., Haroutunian, R., et al.: Saturated amplification of a collisionally pumped optical-field-ionization soft X-ray laser at 41.8 nm. *Phys. Rev. Lett.* **86**, 3004–3007 (2001)
2. Sebban, S., Mocek, T., et al.: Demonstration of a Ni-like Kr optical-field-ionization collisional soft X-ray laser at 32.8 nm. *Phys. Rev. Lett.* **89**, 253901 (2002)
3. Cros, B., Mocek, T., et al.: Characterization of the collisionally pumped optical-field-ionized soft-x-ray laser at 41.8 nm driven in capillary tubes. *Phys. Rev. A* **73**, 033801 (2006)
4. Goddet, J.P., Sebban, S., et al.: Aberration-free laser beam in the soft x-ray range. *Opt. Lett.* **34**, 2438–2440 (2009)
5. Maynard, G., Lambert, F., et al.: Determination of the ion temperature in a plasma created by optical field ionization. *Contrib. Plasma Phys.* **47**, 352–359 (2007)
6. Calisti, A., et al.: Line profiles of Ni-like collisional XUV laser amplifiers: particle correlation effects. *High Energy Density Phys.* **9**, 516–522 (2013)

Chapter 9

Study of Particle Correlation Effects on Line Profiles of Ni-Like Collisional XUV Laser Amplifier

A. Calisti, S. Ferri, C. Mossé, B. Talin, A. Klisnick, L. Meng, D. Benredjem, and O. Guilbaud

Abstract We discuss the effects of particle correlations on the spectral broadening due to the radiator motion (Doppler broadening) for a Ni-like XUV laser line pumped in two different regimes (transient and quasi-steady state regimes) of collisional excitation. In a medium with gain, radiative transport effects modify the observed profile and these modifications depend on the homogeneous or inhomogeneous nature of the intrinsic profile (before amplification). The intrinsic line profile is usually described by a Voigt profile, which is the convolution of a Lorentzian profile due to the different homogeneous broadenings (electron collision-induced transitions and spontaneous emission) and an inhomogeneous Gaussian profile due to Doppler shifts (due to the radiator motion in the free-particle limit). In this paper, it is shown that accounting for the correlations between particles modifies noticeably the radiator-motion broadened profiles, whatever the densities and temperatures values.

1 Introduction

A better characterization of the spectral properties of existing plasma-based XUV lasers is necessary in order to improve the understanding of some characteristics of these lasers. In particular, the spectral width of the lasing line is an important parameter since it controls the temporal coherence of the source, as well as the shortest duration (Fourier-transform limit) that can be reached for a fully coherent pulse.

A. Calisti (✉) · S. Ferri · C. Mossé · B. Talin
PIIM, CNRS-Aix-Marseille Université, Marseille, France
e-mail: annette.calisti@univ-provence.fr

A. Klisnick · L. Meng
ISMO, CNRS-Université Paris-Sud, Orsay, France

D. Benredjem
LAC, CNRS-Université Paris-Sud, Orsay, France

O. Guilbaud
LPGP, CNRS-Université Paris-Sud, Orsay, France

Moreover, the relative contribution of homogeneous versus inhomogeneous broadening controls the existence of re-broadening of the laser linewidth when amplified in the saturation regime. XUV lasers pumped by collisional excitation of Ni-like ions are generated in plasmas with electronic densities and ionic and electronic temperatures very dependent on the parameters of the laser pulse used to induce plasma heating and collisional pumping ($N_e \sim 5 \times 10^{19}$ to $8 \times 10^{20} \text{ cm}^{-3}$, $T_e \sim 500$ to 1500 eV and $T_i \sim 20$ to 500 eV). For such conditions, plasmas are strongly coupled (plasma coupling parameter, $\Gamma \gg 1$) and the ionic interactions have to be taken into account.

In laser-produced plasmas, the main causes of spectral line broadenings are the spontaneous emission, the electronic collisions, the ionic Stark effect and the Doppler frequency shift. It is usual to consider that the spontaneous emission and electronic collisions contribute to the homogeneous broadening and ionic Stark effect and Doppler broadening contribute to inhomogeneous broadening as they are due to local inhomogeneities. Due to the variety of plasma conditions, the relative contributions of the different broadenings are very distinct.

In this article, the PPP line shape code [1] has been used to perform a detailed analysis of the various broadening mechanisms of the spectral profiles of the $4d - 4p$ ($J = 0-1$) Ni-like Ag lasing line at $\lambda = 13.9 \text{ nm}$ for conditions relevant for both transient and quasi-steady state (QSS) regimes of collisional excitation. A study on the accuracy of the free-particle Doppler approximation, versus densities and temperatures has been done by using classical molecular dynamics (MD) simulations.

2 Spectral Line Shape Modeling

Including the contribution of ionic emitter motion, the line shape function is given by:

$$I(\omega) = \Re e \frac{1}{\pi} \int_0^\infty e^{i\omega t} \langle e^{i\vec{k} \cdot \vec{r}(t)} \vec{d}(t) \cdot \vec{d}(0) \rangle dt \quad (1)$$

with \vec{d} the radiator dipole operator and $k = 2\pi/\lambda$.

Ignoring correlations between the ion translation $\vec{r}(t)$ and the dipole moment $\vec{d}(t)$:

$$I(\omega) = \Re e \frac{1}{\pi} \int_0^\infty e^{i\omega t} S_s(k, t) C(t) dt. \quad (2)$$

$S_s(k, t) = \langle e^{i\vec{k} \cdot \vec{r}(t)} \rangle$ is the self-structure factor and $C(t) = \langle \vec{d}(t) \cdot \vec{d}(0) \rangle$ the dipole autocorrelation function. In this work, the PPP line shape code [1] is used to calculate $C(t)$. The PPP code is a multi-electron radiator line broadening code developed to calculate theoretical spectral line profiles for a general emitter in a plasma, using data for atomic energy levels and radial matrix elements generated by atomic structure programs [2]. The line profile calculations are done in the framework of

the standard theory (quasi-static ion and electron impact approximations) or if necessary including the effects of ionic perturber dynamics by using the Frequency Fluctuation Model [3, 4]. The self-structure factor is well known in the free-particle limit (Doppler effect) resulting from the hypothesis that each radiating ion moves at constant velocity $\vec{r}(t) = \vec{v}t$ with a Maxwellian distribution of velocities, and is given by:

$$S_s(k, t) = e^{-k^2 t^2 / 2\beta m} \quad (3)$$

with $\beta = 1/k_B T$ and m the ion mass. Classical molecular dynamics simulation technique (MD) is a straightforward way to compute $S_s(k, t)$ taking into account interactions between ions. The plasma model consists of classical point ions interacting together through a coulombic potential screened by electrons and localized in a cubic box of side L with periodic boundary conditions. Newton's equations of particle motion are integrated by using a velocity-Verlet algorithm using a time-step consistent with energy conservation. Integrating the Newton's equation gives access to the positions and velocities, $\{\vec{r}^N(t), \vec{v}^N(t)\}$, of the N ions as a function of time and thus to the associated static and dynamic statistical properties such as structure factors, velocity correlation functions, diffusion coefficients, ion-ion collision rates, etc.

3 Results and Discussion

Spectral line shape calculations have been performed for Ni-like Ag laser $4d - 4p$ ($J = 0-1$) line at 13.9 nm for density and temperature ranges chosen to be consistent with population inversion induced by collisional excitation. Two series of results corresponding respectively to transient ($T_i = 20$ eV, $T_e = 200$ eV) and QSS ($T_i = T_e = 200$ eV) pumping regimes, are presented for different electronic densities. Figures 1 and 2 show the full widths at half maximum (FWHM) corresponding to the different mechanisms of broadening taken separately and together as a function of the electronic density for the transient and QSS pumping regimes respectively. It has been checked that the Stark effect associated with ion microfield has a negligible contribution to the line profile. Electronic collisions and spontaneous emission give rise to the lifetime broadening (blue chain plus crosses) which is homogeneous and increases linearly with N_e at a given T_e . The motion of an emitting ion yields a Doppler shift of the X-ray laser line. If we assume that each radiating ion moves at constant velocity $\vec{r}(t) = \vec{v}t$ with a Maxwellian distribution of velocities, the line profile is inhomogeneous and shows a Gaussian shape with a width (dashed black line) given by a simple analytical formula depending only on T_i . Accounting for both of the previous effects, the resulting spectral profile will be the convolution of the homogeneous and inhomogeneous profile, leading to the so-called Voigt profile with a width which is a complex combination of both homogeneous and inhomogeneous linewidths (dotted red line plus crosses). Similar results for the spectral profile of the $4d - 4p$ ($J = 0-1$) lasing line in Ni-like Mo have been obtained and are discussed in the framework of amplification in [5].

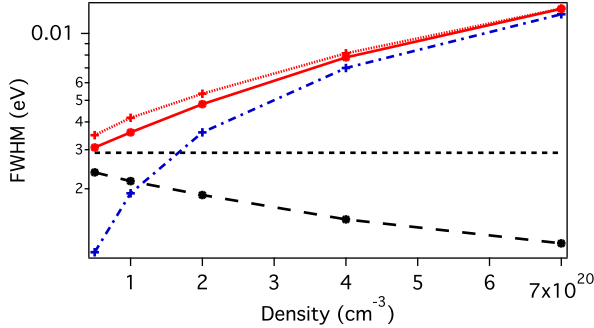
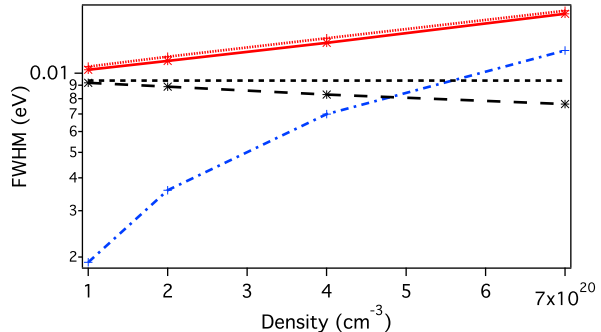


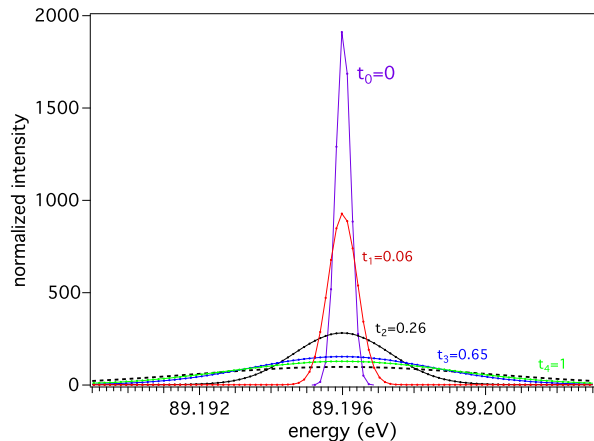
Fig. 1 Full width at half maximum versus density of the $4d - 4p$ laser line in the transient XUV case. Broadening due to: radiator motion in the free particle limit, i.e. Doppler broadening (dashed black line), accounting for particle interactions (broken black line plus stars), lifetime broadening (blue chain plus crosses) and total broadening (radiator motion + finite lifetime effects) in the free particle limit (dotted red line plus crosses) and accounting for interactions (full red line plus stars)

Fig. 2 Same as Fig. 1 in the QSS case



In order to account for velocity changing effects, the broadening due to the translational motion of the emitter (broken black line plus stars) has been obtained by using the self-structure factors computed by MD simulations. It can be seen that taking into account interactions between ion emitter and other ions of the plasma gives rise to a narrowing of the profile whatever the considered densities and this narrowing increases with the density. The line profile is no longer Gaussian, so the overall profile is no longer a Voigt profile. Moreover if during their effective lifetimes, the radiating and absorbing ions sample many velocities, not just one as it is supposed in the Doppler free particle limit, the effect of this velocity redistribution will be to homogenize the Doppler component of the intrinsic line profile. Figure 3 shows the evolution in time of the frequency distribution function of a population of radiating emitters chosen to have an initial velocity such as $\vec{k} \cdot \vec{v}(0) = 0$. Four different timescales of evolution have been considered, the largest one corresponding to the radiative lifetime (inverse of the lifetime broadening). It can be seen that the velocity redistribution is nearly complete during the radiative lifetime. Similar results have been obtained in the transient pumping regime case.

Fig. 3 Frequency distribution functions for conditions of the QSS pumping regime at $N_e = 10^{20} \text{ cm}^{-3}$. Times are in units of radiative lifetimes. The *black broken line* corresponds to the Doppler free particle limit



4 Conclusion

This paper concerns a study of the effects of particle correlations on the line broadening due to the radiator motion in the particular case of XUV laser lines. Two different pumping regimes have been considered, transient pumping regime for which ionic temperature is relatively low, so the plasma coupling parameter is large, and quasi steady state regime for which the ionic temperature is higher and the plasma coupling parameter of the order of 1. It has been shown that the effect of correlations cannot be neglected in evaluating Doppler effect for the two cases of interest. For all the considered densities and temperatures, by taking into account correlations between particles, the radiator-motion broadened profiles are modified in being homogenized by velocity redistribution in all the cases and narrowed essentially in the transient regime.

References

1. Calisti, A., et al.: Phys. Rev. A **42**, 5433 (1990)
2. Grant, I.P., et al.: Comput. Phys. Commun. **21**, 207 (1980)
3. Talin, B., et al.: Phys. Rev. A **51**, 1918 (1995)
4. Calisti, A., et al.: Phys. Rev. E **81**, 016406 (2010)
5. Meng, L., et al.: In: X-Ray Lasers 2012. Springer Proceedings in Physics, vol. 147. Springer, Cham (2013). Chapter 28 in this book

Chapter 10

The LUNEX5 Project in France

M.E. Couprie, C. Benabderrahmane, P. Betinelli, F. Bouvet, A. Buteau, L. Cassinari, J. Daillant, J.C. Denard, P. Eymard, B. Gagey, C. Herbeaux, M. Labat, A. Lestrade, A. Loulergue, P. Marchand, J.L. Marlats, C. Miron, P. Morin, A. Nadji, F. Polack, J.B. Pruvost, F. Ribeiro, J.P. Ricaud, P. Roy, T. Tanikawa, R. Roux, S. Bielawski, C. Evain, C. Szwaj, G. Lambert, A. Lifschitz, V. Malka, R. Lehe, A. Rousse, K. Ta Phuoc, C. Thaury, G. Devanz, M. Luong, B. Carré, G. LeBec, L. Farvacque, A. Dubois, and J. Lüning

Abstract LUNEX5 (free electron Laser Using a New accelerator for the Exploitation of X-ray radiation of 5th generation) aims at investigating the production of short, intense, and coherent pulses in the soft x-ray region. The single Free Electron Laser (FEL) line fed by either a superconducting Linear Accelerator of 400 MeV or a 0.4–1 GeV Laser Wake Field Accelerator (LWFA) enables seeding (High order Harmonic in Gas and Echo Enabled Harmonic Generation) for the advanced fourth generation source with the conventional accelerator, and single spike operation

M.E. Couprie (✉) · C. Benabderrahmane · P. Betinelli · F. Bouvet · A. Buteau · L. Cassinari · J. Daillant · J.C. Denard · P. Eymard · B. Gagey · C. Herbeaux · M. Labat · A. Lestrade · A. Loulergue · P. Marchand · J.L. Marlats · C. Miron · P. Morin · A. Nadji · F. Polack · J.B. Pruvost · F. Ribeiro · J.P. Ricaud · P. Roy · T. Tanikawa
Synchrotron SOLEIL, Saint-Aubin, France
e-mail: couprie@synchrotron-soleil.fr

R. Roux
Laboratoire de l'Accélérateur Linéaire, Orsay, France

S. Bielawski · C. Evain · C. Szwaj
PhLAM/CERLA, Lille, France

G. Lambert · A. Lifschitz · V. Malka · R. Lehe · A. Rousse · K. Ta Phuoc · C. Thaury
Laboratoire d'Optique Appliquée, Palaiseau, France

G. Devanz · M. Luong
CEA/DSM/IRFU/SACM, Saclay, France

B. Carré
CEA/DSM/IRAMIS/SPAM, Saclay, France

G. LeBec · L. Farvacque
ESRF, Grenoble, France

A. Dubois · J. Lüning
LCPMR, Paris-VI, France

for the fifth generation source with the LWFA. Two pilot user experiments for time-resolved studies of isolated species and solid state matter will take benefit of LUNEX5 FEL.

1 Introduction

Accelerator based X-ray light sources rely on the emission of synchrotron radiation by relativistic electrons (of normalized energy γ) in bending magnets and in periodic permanent magnetic structures, such as undulators. The so-called first generation took advantage of the parasitic synchrotron radiation emitted in the storage rings initially built for high energy physics. The second generation was developed on dedicated storage ring accelerators. The third generation arose with reduced emittances (product of the beam size by the divergence) and high number of installed undulators leading to a brightness increase and a partial transverse coherence. Indeed, a planar undulator creating a sinusoidal vertical field (amplitude B_0 , period λ_0), emits on axis at the resonant wavelength λ and its odd harmonics on axis, as a result from the interferences with the electron bunches through the successive periods: $\lambda = \lambda_0(1 + K^2/2)/2\gamma^2$ with $K = 0.94\lambda_0(\text{cm})B_0(\text{T})$. Fourth Generation Light Sources (4G) enable longitudinal coherence by setting in phase the emitting electrons thanks to the FEL process. A light wave of wavelength λ (spontaneous emission progressing along the undulator or stored in an optical cavity, or external seed) interacts with the electron bunch in the undulator, inducing an energy modulation of the electrons; which is gradually transformed into density modulation at the wavelength λ and leads to a coherent radiation emission. The first FEL experience was carried out in 1977 [1] on MARK-III at Stanford, USA using an oscillator configuration in the infra-red. Nowadays, two FEL on linear accelerator, LCLS [2] (Stanford, USA) and SACL [3] (Harima, Japan), are operating in the 1 Å region with 100–10 fs pulse and GW peak power. In the Self Amplified Spontaneous Emission configuration the spontaneous emission progress along the undulator and is amplified towards saturation [4]. The uncorrelated trains of radiation, which result from the interaction of electrons progressing jointly with the previously emitted spontaneous radiation, lead to spiky longitudinal and temporal distributions, apart from single spike operation for low charge regime [5]. Seeding either with amplified spontaneous emission from first stage undulators sent through a monochromator (so-called self seeding [6]) or with an external laser or a short wavelength coherent light source, such as High order Harmonics generated in gas, allows the saturation length to be shortened, the jitter to be reduced, and the longitudinal coherence to be improved [7–9]. The Echo Enabled Harmonic Generation (EEHG) scheme with a double electron–laser interaction can push the spectral range towards shorter wavelengths when operating on a high order harmonic of the seed wavelength [10–12]. The so-called Fifth Generation (5G) replacing the conventional linac by a Laser Wakefield Accelerator (LWFA), which provides GV/m of acceleration with very short bunches [13–15] is under progress with first observation of the spontaneous undulator radiation [16, 17] and FEL projects [18, 19].

2 LUNEX5 Constituting Elements

LUNEX5 (see Fig. 1) consists in a 400 MeV conventional superconducting accelerator and a 0.4–1 GeV LWFA accelerator, both feeding a common FEL line. It aims at investigating the production of short, intense, and coherent pulses in the soft x-ray region on advanced 4GLS using a Conventional Linear Accelerator (CLA) with the latest seeding schemes and ultra-short pulses of a few fs as well as on 5GLS first for qualifying LWFA with a FEL application, and for providing shorter FEL pulses.

The CLA includes a superconducting L band linac with a Desy-Zeuthen type photo-gun, a 1.3 GHz cryomodule for accelerating up to 200 MeV, a third harmonic cavity, a laser heater, a magnetic chicane, a diagnostic section, a second 1.3 GHz for accelerating module up to 400 MeV and the space for a possible additional third cryomodule. The cryomodules will be designed for future CW operation, the first nominal case of operation being at 50 Hz. 1.3 GHz 20 kW CW solid state amplifiers will be developed at SOLEIL. Lasers from CILEX (Centre Interdisciplinaire de Lumière Extrême) with APOLLON 10 PW laser and its “proximity centers” such as the 60 TW laser of LOA will be used for the LWFA before the dedicated one will be available. Transport to FEL line is achieved with variable permanent magnet quadrupoles. The FEL line comprises transport magnetic elements, dump dipole and in-vacuum undulators with periods of 30 (modulators) or 15 mm (radiators), with a cryogenic option [15]. At 3 mm gap, a peak field of 1.5 T (1.7 T) will be produced at room temperature with NdFeB magnet (at 77 K with PrFeB magnets) for a 15 mm period. The seeding laser system with a regenerative amplifier will be used for producing the High order Harmonics in Gas (HHG), generated in a gas cell for the Echo scheme (after tripling) and for the pump probe experiments of the pilot users. The FEL light will hit a first toroidal mirror (to be interchanged with a second one for the echo source point) for focusing on the exit slit; it will then pass through a double rotation monochromator operating in the Petersen mode to select and stabilize the photon energy and through two focusing mirror systems to be dispatched on the two experimental set-ups. Diagnostics will consist in standard bunch charge monitors, Optical Transition Radiation and fluorescent screens for beam transverse dimensions, standard stripline Beam Position Monitors (BPM) for the linac and cavity BPMs [16] for the undulator sections, a beam arrival time monitor, bunch length monitors and a RF deflecting cavity.

3 LUNEX5 Performances

Figure 2 shows the expected performances of LUNEX5. The spectrum covers the 4–40 nm range with the first, third and fifth harmonics, a fundamental peak power between 10 and 100 MW, corresponding to more than 10^{11} photons/pulse and 10^{27} peak brightness and harmonic peak power from 1 MW down to a few hundreds W. Each wavelength can be obtained with different configurations (amplifier, cascade with a High Order Harmonic seed, echo with 266 nm lasers, . . .). The FEL saturates

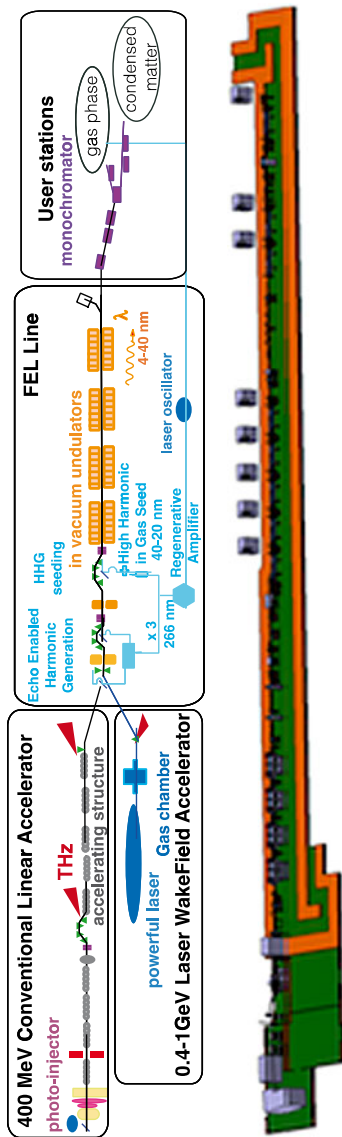


Fig. 1 LUNEX5 scheme and CATIA sketch. From the left: electron gun, superconducting accelerating sections (yellow) with the compression chicane in between, LWFA chamber, two echo chicanes and modulator-, radiator-undulators, monochromator, pilot user experimental stations, shielding walls in orange

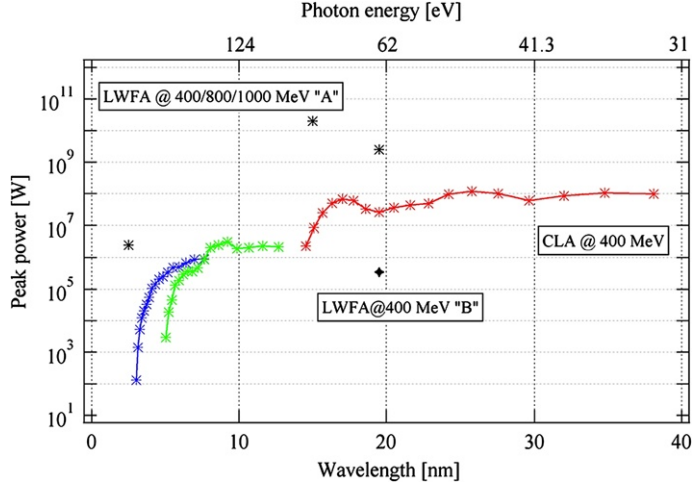


Fig. 2 FEL peak power versus wavelength. Calculations with an 400 MeV electron beam, with a 1.5π mm mrad emittance, a peak current of 400 A, a slice energy spread of 0.02 % (CLA) and A: 0.1, B: 0.5 % (LWFA), a bunch duration of 1 ps (CLA) and A: 2, B: 20 fs-RMS (LWFA)

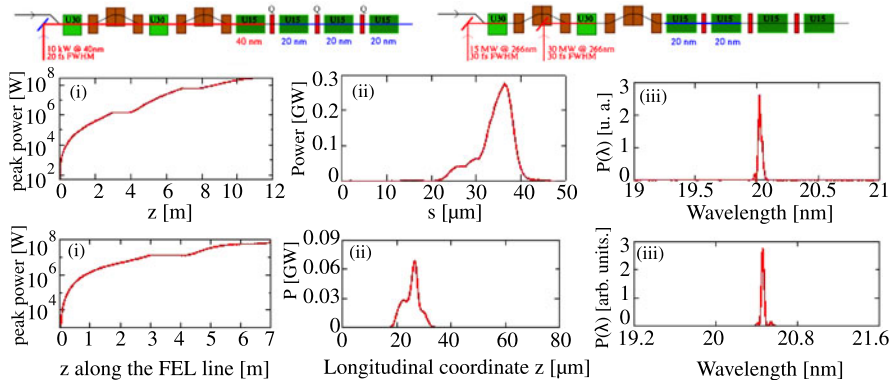


Fig. 3 GENESIS 4G+ FEL simulations at 20 nm. *Top:* cascade and echo schemes. Electron beam energy: 400 MeV, 0.01 % energy spread, 1.5π mm mrad emittance, 400 A peak current, 1 ps pulse duration. Seed: (*middle:* cascade): 20 fs FWHM with 10 kW peak power at 40 nm (*bottom:* echo) 30 fs FWHM, 15 MW and 30 MW at 266 nm. Exponential growth (*left*), FEL temporal (*center*) and spectral profile (*right*)

earlier in the echo case than in the cascade one (7 wrt 11 m), with slightly lower power (65 MW wrt 0.27 GW), longer pulses (24 wrt 17 fs) at the Fourier limit as shown in Fig. 3. Advanced 4GLS FEL can be tuned by a combined variation of the seed wavelength and the undulator gaps. 5G FEL performances critically depend on the electron beam quality and on the optimization of the transport line (see Fig. 4).

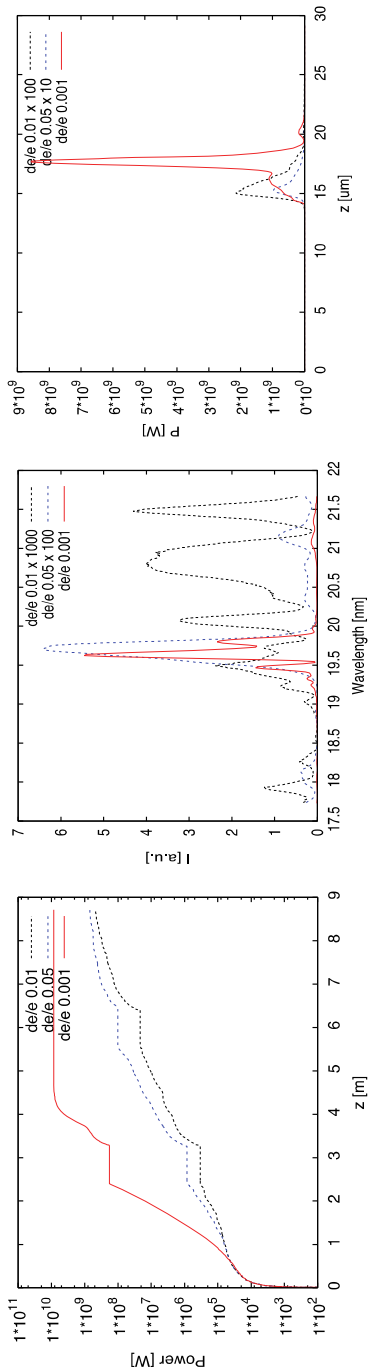


Fig. 4 SASE GENESIS 5G FEL simulations at 17 nm. Electron beam energy: 400 MeV, 0.1/0.5/1 % energy spread, 1π mm mrad emittance, 10 kA peak current, 2 fs RMS pulse duration. Undulator period: 12 mm; K = 1.408. Exponential growth (*left*), FEL temporal profile (*center*), spectral line (*right*)

4 LUNEX5 Experimental Stations

Pilot user experiments on isolated species and condensed matter will validate the LUNEX5 demonstrator radiation from a user point of view. So far, no user experiments have been carried out neither with HHG seeded FEL nor with Echo Enabled Harmonics. LUNEX5 has two end stations for time resolved pump-probe studies of isolated species (TR-AMO) and for condensed matter imaging exploiting the coherence. The TR-AMO end station will consist in a high resolution velocity map imaging (VMI) spectrometer allowing for spectroscopy of cold atoms/molecules, clusters or nanoparticles, issued from a multi-purpose source, combined with the full momenta characterization of both electrons and ions using a COLTRIMS type of spectrometer based on time-of-flight and particle 2D position detection (covariance mapping will be used for data analysis). Lensless imaging technique also relies on very stable setup and accurate algorithms to extract real space images. In first experiments magnetization dynamics will be triggered through intense fs laser irradiation and then probed by resonant x-ray magnetic scattering.

5 Conclusion

LUNEX5 is aiming for ultra short FEL pulses quest, production and use on a coupled CLA-LWFA based test facility for complementary use and test of new ideas, such as the recently proposed scheme [20] with three electron photon interactions which could enable to reach the 1 nm region. It will pave the way towards the next generation of light source (4GLS+, 5GLS).

References

1. Deacon, D.A.G., et al.: First operation of a free electron laser. *Phys. Rev. Lett.* **38**, 892–894 (1977)
2. Emma, P., et al.: First lasing and operation of an Å wavelength free-electron laser. *Nat. Photonics* **4**, 641 (2010)
3. Tanaka, H., Yabashi, M., et al.: A compact X-ray free-electron laser emitting in the sub-ångström region. *Nat. Photonics* **6**, 540–544 (2012)
4. Bonifacio, R., Pellegrini, C., Narducci, L.M.: Collective instabilities and high gain regime in a free electron laser. *Opt. Commun.* **50**, 373–378 (1984)
5. Din, Y., et al.: Measurements of ultralow emittance and ultrashort electron beams in the linac coherent light source. *Phys. Rev. Lett.* **102**, 254801 (2009)
6. Emma, P.: Hard X-ray self seeding at LCLS. In: Proceed. IPAC 12, New Orleans, USA, May 2012 (2012)
7. Yu, L.H., et al.: High-gain harmonic-generation free-electron laser. *Science* **289**, 932 (2000)
8. Lambert, G., et al.: Injection of harmonics generated in gas in a free electron laser providing intense and coherent extreme-UV light. *Nat. Phys.* **4**, 296–300 (2008)
9. Togashi, T., et al.: Extreme ultraviolet free electron laser seeded with high-order harmonic of Ti:sapphire laser. *Opt. Express* **1**, 317–324 (2011)

10. Stupakov, G.: Using the beam-echo effect for generation of short-wavelength radiation. *Phys. Rev. Lett.* **102**, 074801 (2009)
11. Xiang, D., et al.: Demonstration of the echo-enable harmonic generation technique for short-wavelength seeded free electron lasers. *Phys. Rev. Lett.* **105**, 114801 (2010)
12. Zhao, Z.T., et al.: Progress in SDUV-FEL and development of X-ray FELs in Shanghai. In: Proceeding 32nd Internat. FEL Conference, Malmö, Sweden, August 25–27, 2010, pp. 15–19 (2010)
13. Lundh, O., et al.: Few femtosecond, few kiloampere electron bunch produced by a laser-plasma accelerator. *Nat. Phys.* **7**, 219–222 (2011)
14. Nakajima, K.: Towards a table-top free-electron laser. *Nat. Phys.* **4**, 92 (2008)
15. Leemans, W., Esarey, E.: Laser-driven plasma-wave electron accelerators. *Phys. Today* **62**(3), 44 (2009)
16. Schlenvoigt, H.-P., et al.: A compact synchrotron radiation source driven by a laser-plasma wakefield accelerator. *Nat. Phys.* **4**, 130–133 (2008)
17. Fuchs, M., et al.: Laser-driven soft-X-ray undulator source. *Nat. Phys.* **5**, 826 (2009)
18. Fawley, W.M., et al.: A design for an XUV FEL driven by the laser-plasma accelerator at the LBNL LOASIS facility. In: Proceed. FEL06, Berlin, Germany, pp. 455–458 (2006)
19. Anania, M.P., et al.: The ALPHA-X beam line: towards a compact FEL. In: Proceedings IPAC10, Kyoto, Japan, p. 2263 (2010). <http://www.mpg.mpg.de/APS/gruener.php>
20. Xiang, D., Stupakov, G.: Triple modulator–chicane scheme for seeding sub-nanometer x-ray free-electron lasers. *New J. Phys.* **13**, 093028 (2011)

Chapter 11

High Harmonic Generation Driven by Two Quasi-collinear Pulses

S. Daboussi, S. Kazamias, K. Cassou, O. Guilbaud, M. Pittman, O. Delmas, O. Neveu, B. Cros, G. Maynard, and D. Ros

Abstract We have investigated the high harmonic generation driven by two quasi-collinear IR pulses separated by picosecond delay. Experiments were performed at the LASERIX facility using 50 fs pulses at 800 nm with energy up to 25 mJ. We have studied the generation of two high harmonic pulses from the same medium. In particular, we show how the ratio in energy of each pulse can be used to balance the perturbation induced by the first pulse in the generating gas.

1 Introduction

High order harmonic generation (HHG) from the interaction of an intense infrared (IR) laser and a gas target provides a coherent table-top radiation source in the extreme ultraviolet (XUV) range. Such a source can have a large scientific impact, particularly concerning applications. One of the most significant among them is the seeding of various types of soft x-ray laser (SXRL) amplifiers with high harmonic pulses from plasma-based x-rays [1, 2] to free electron lasers [3]. Traditionally, these amplifiers work in the amplification of spontaneous emission regime (ASE) which presents some limitations in terms of beam optical properties [4, 5]. A straightforward idea explored in several laboratories around the world is to use harmonic radiation to seed the SXRL thus combining the high output energy of SXRL sources with the spatial and temporal coherence of the harmonic source [6, 7]. In this work we concentrated on the possibility to generate from the same generating medium a double temporal structure with variable delay in the picosecond range in order to study more deeply the plasma-based SXRL seeding temporal aspects like polarization [8] and temporal gain construction [9]. For this type of experiment, the relevant temporal range of interest goes from few fs up to 10 ps.

S. Daboussi (✉) · S. Kazamias · K. Cassou · O. Guilbaud · O. Delmas · O. Neveu · B. Cros · G. Maynard · D. Ros
LPGP, Univ. Paris-Sud, UMR 8578, CNRS, bat 210, campus d'Orsay, 91405 Orsay Cedex, France
e-mail: sameh.daboussi@u-psud.fr

S. Daboussi · S. Kazamias · K. Cassou · O. Guilbaud · M. Pittman · O. Delmas · O. Neveu · D. Ros
LASERIX, CLUPS, Univ. Paris-Sud, CNRS, campus d'Orsay, 91405 Orsay Cedex, France

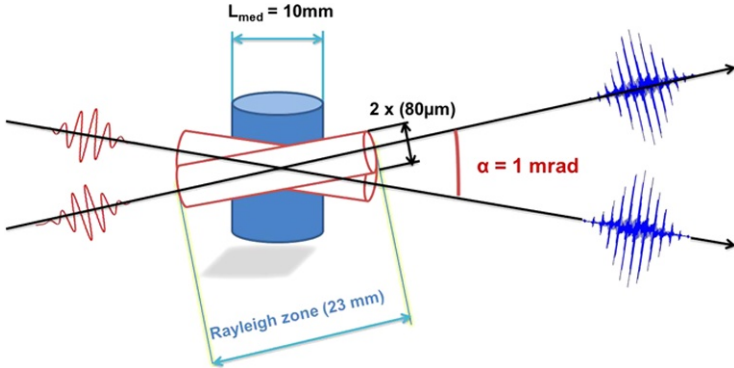


Fig. 1 Quasi-collinear process

2 Description of the Experiment

The pumping of two HHG beams by two close following infrared short pulses in the picosecond range is a non-trivial issue due to the ionization problem which is deleter for phase-matching [10]. A key issue for the present work is to investigate the possibility to generate two XUV pulses from the same medium and to study its temporal response. For this purpose it is required to characterize each pulse independently, in terms of total energy and also spectrum and beam characteristics. Extreme UV streak cameras could reach such temporal resolution but the complex working conditions they offer, together with their small dynamic range make them hard to use. We made the choice to use a slightly quasi-collinear double pulse excitation configuration. For this, two infrared beams generated in a Mach-Zehnder type interferometer with variable delay are focused, in the gas cell, with a small angle (1 mrad), so that they behave in the gas cell such as if they were collinear (see Fig. 1). The experimental investigation was carried out at LASERIX, a high-power laser facility fully dedicated to the development and applications of SXRL beams in the range of 7 to 30 nm [11]. The IR source used in our experiment is based on a low energy sampling from the amplified Ti:Sapphire laser system that provides 50 fs duration pulses centered at a wavelength of 800 nm. Due to pulse air compression, the maximum energy dedicated to HHG is limited to 25 mJ at a repetition rate of 10 Hz.

The schematic of our setup for quasi-collinear HHG is shown on Fig. 2. The incoming laser pulse is set into a Mach-Zehnder type system with an adjustable length arm in order to introduce a controllable delay (-100 ps, $+100$ ps) between the reflected and the transmitted pulses. The temporal resolution of the system was 6 fs due to motorized translation stage accuracy. A polarizer associated with a zero order half wave plate was installed in the path of the reflected beam in order to adjust its energy. Variable apertures were placed on both the reflected and the transmitted beams to adjust intensities and focusing geometries [12]. The two parallel beams are recombined with a 50/50 beam splitter with a small lateral separation and then

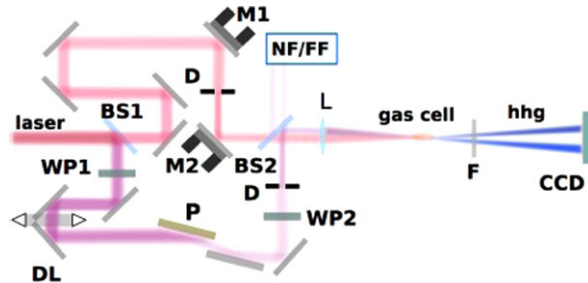


Fig. 2 Experimental setup for quasi-collinear HHG: *BS*, beamsplitter 50/50; *WP*, half wave plates; *P*, Brewster Polarizer; *NF*, real time near field control; *FF*, real time far field control. The polarization of the reflected pulse is controlled using the wave plate *WP2*. Reflected energy sent on the cell is adjusted with *WP1* + *P*

focused into the gas cell with 1100 mm lens with a small angle (1 mrad). The footprints of the two corresponding XUV beams were recorded 3 m further from the source on a backlit XUV CCD camera. The scattered laser light and high harmonic orders higher than 47 were blocked by an aluminum filter (0.2 μm width). After energy optimization in argon for HHG signal separately for each pulse, only a small portion of the available energy (10 mJ) was used in our configuration. The estimated energy per harmonic beam is 70 pJ using the CCD and filter calibration and referring to previous XUV NIST calibrated photodiode data obtained in similar conditions. In those conditions a precise laser alignment is crucial to achieve precise superposition of the beams in the focal region. A real time control of near and far fields showed that the two focal spots were superposed throughout the cell when varying the delay.

3 Temporal Response of the Generating Medium

3.1 Experimental Investigation

After optimization of each of the two individual HHG beams (Fig. 3(a, b)), the influence of the delay was analyzed for equivalent generation conditions on both arms (15 mbar of argon, IR intensity near $1.5 \times 10^{14} \text{ W/cm}^2$). Figure 4 shows the delay scan from 500 fs up to 100 ps of the normalized integrated signal for each beam as recorded with the CCD camera. Each of the two curves, reported in Fig. 4 yields the ratio between the measurement of the total integrated XUV signal generated by the first (resp. the second) IR beam in the double (Fig. 3(c)) and single pulse configurations (Fig. 3(a, b)). Each measurement was averaged over five laser shots and the experiment was repeated over several days. The represented error bars are attributed to HHG signal fluctuations due to shot to shot variations of laser pointing and mechanical instabilities of the delay line. As expected, the first pulse has a ratio which

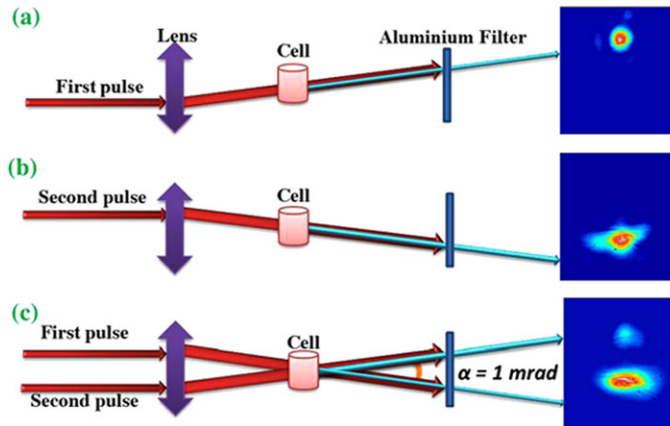


Fig. 3 (a,b) HHG generation with the first and the second beam respectively when the other driving beam is blocked. (c) HHG generation with the two IR pulses from the same

is closed to one, showing that it is not affected by the presence of the second one. The ratio slightly higher than one is not significant since it represents the ratio over two integrated signals measured with an interval of few tens of minutes. On the other hand, we can observe in Fig. 4 that the second pulse has a ratio value close to 0.5 for any kind of delay in the range studied. This indicates that HHG phase-matching for the second pulse is strongly perturbed by the ionization of the gas target generated by the first one. The phase matching condition has been optimized for one beam, that is in our case for the first HHG pulse. Therefore, due to ionization, the phase matching condition is no more satisfied for the second HHG pulse leading to a strong reduction of its energy. Moreover, as this reduction remains constant, one can deduce that the ionization rate does not seem to depend on the delay, even for a time as long as 100 ps.

3.2 Theoretical Estimations for Plasma Recombination Characteristic Time

In order to confirm this experimental observation, theoretical estimations were made for the evolution of the argon plasma at a pressure of 25 mbar with an optical field ionization rate around 5 % which represents the gas medium state after interaction with the first pulse. The ions and atoms are supposed to be at room temperature and the electron average temperature inferred from OFI calculations is close to 0.5 eV. In that case, neither hydrodynamic expansion nor ionization and excitation due to collisions have time to play a significant role. Therefore we have only to consider recombination processes. The direct recombination to the fundamental state having a time characteristic close to the millisecond, in fact only the recombination to highly excited states can have a significant rate. These states having a long life time, the

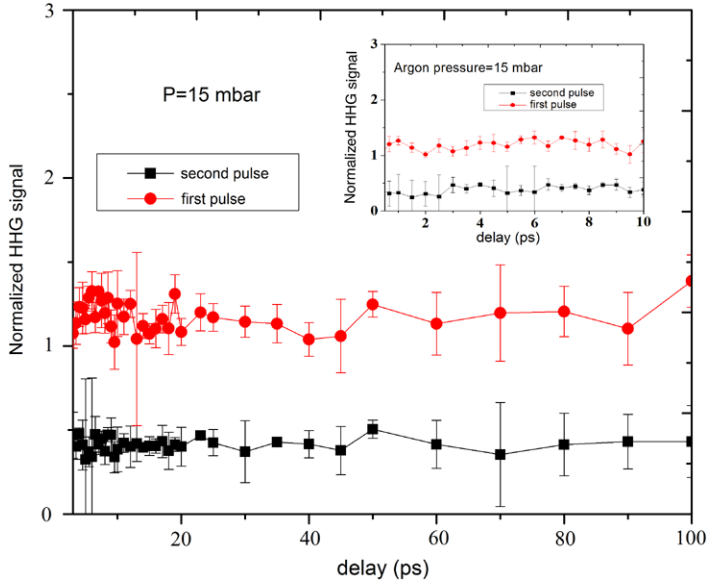


Fig. 4 Measured HHG signal generated by the first pulse (circle) and by the second pulse (square) as a function of the delay in 15 mbar of argon normalized with the respective single HHG beam. These measures correspond to encircled energy recorded on the CCD

radiative decay has a negligible contribution during 100 ps. However for HHG generation, the highly excited states act as ionized states because they are ionized by the IR beam at very low intensity well before the maximum of the harmonic generation. From our theoretical estimations [13–15] we have deduced that, in the considered condition, the plasma recombination time is of the order of 2 nanoseconds. This confirms the experimental observations that the plasma ionization remains constant within a delay range of few hundreds of picoseconds.

4 Conclusion

In conclusion, a full temporal study in the picosecond range of two XUV pulses generated from the same medium was done thanks to the quasi-collinear scheme. This double pulse can be used in the XUV-XUV pump-probe experiment or the SXRL seeding experiment. One advantage of our system is that, depending on the applications, it can be used even in quasi or fully collinear configuration. We theoretically demonstrated in this work that the recombination time of the plasma generated after interaction between the IR laser and the gas is longer than 2 ns, this was experimentally verified up to 100 ps. This result shows that IR driving laser with a repetition rate larger than 0.5 GHz are not recommended for efficient high harmonic generation in gas cell.

References

1. Zeitoun, P., et al.: Nature (London) **431**, 426 (2004)
2. Wanget, Y., et al.: Nat. Photonics **2**, 94 (2008)
3. Lambert, G., et al.: Nat. Phys. **4**, 296 (2008)
4. Guilbaud, O., et al.: Eur. Phys. J. D **40**, 125 (2006)
5. Guilbaud, O., et al.: Europhys. Lett. **74**, 823 (2006)
6. Goddet, J.P., et al.: Opt. Lett. **34**, 2438 (2009)
7. Berrill, M., et al.: Opt. Lett. **35**, 2317 (2010)
8. Oliva, E., et al.: Phys. Rev. A **84**, 13811 (2011)
9. Mocek, T., et al.: Phys. Rev. Lett. **95**, 173902 (2005)
10. Kazamias, S., et al.: Phys. Rev. Lett. **90**, 193901 (2003)
11. Zielbauer, B., et al.: Appl. Phys. B **100**, 731–736 (2010)
12. Kazamias, S., et al.: Eur. Phys. J. D **21**, 353 (2002)
13. Cros, B., et al.: Phys. Rev. A **73**, 033801 (2006)
14. Vlcek, V.: J. Phys. D **22**, 623 (1989)
15. Kapper, M.G., et al.: J. Appl. Phys. **109**, 113308 (2011)

Chapter 12

Real-Time Observation of Laser Heated Metals with High Brightness Monochromatic X-Ray Techniques at Present and Their Future Prospects

**H. Daido, T. Shobu, T. Yamada, S. Yamashita, K. Sugihara, A. Nishimura,
and T. Muramatsu**

Abstract We present the x-ray techniques for characterizing laser heated metals for welding and cutting techniques. At present, with an undulator (70 keV) as well as bending magnet (30 keV) sources at SPring-8 as a probe source, CW 300 W Ytterbium fiber laser irradiates an Aluminum slab as a sample. Simultaneously the x-ray beam probes the sample for real time observation of a molten pool. We observe the convection indicated by the motion of tungsten based particles as a tracer in the molten pool. During the cooling phase, the molten metal is solidified with residual stresses which are affected by the heating and convection processes. In this experiment the time and space resolution are \sim milli-second and several tens of μm , respectively. On the other hand, microscopic short transient phenomena also play a significant role for the quality of a solidified material. For this purpose, we need high energy short pulse x-ray sources. We try to discuss on the capability and limitation of present x-ray sources and the prospect of an ultra high brightness x-ray source as a complementary source for full characterization of the laser heated and cooling processes of metals.

1 Introduction

Precise characterization of laser heated metal is useful and important for high quality welding and thick metal cutting relevant to maintenance of nuclear plants and decommissioning. In this paper, we present x-ray techniques for real time observation of melting and solidification processes and their interpretation with use of a computer simulation technique.

H. Daido (✉) · T. Shobu · T. Yamada · S. Yamashita · K. Sugihara · A. Nishimura · T. Muramatsu
Applied Laser Technology Institute Tsuruga Head Office, Japan Atomic Energy Agency, Tsuruga,
Fukui 914-8585, Japan
e-mail: daido.hiroyuki@jaea.go.jp

H. Daido · T. Shobu · A. Nishimura
Quantum Beam Directorate, Japan Atomic Energy Agency, Kizugawa, Kyoto 619-0215, Japan

Fig. 1 Wide ranges of laser parameters are used for nuclear engineering such as laser peening, welding and cutting. In the pulsed irradiation regime, ultra-high intensity laser applications (beyond upper limit of the laser irradiance) and laser plasma based x-ray lasers are placed

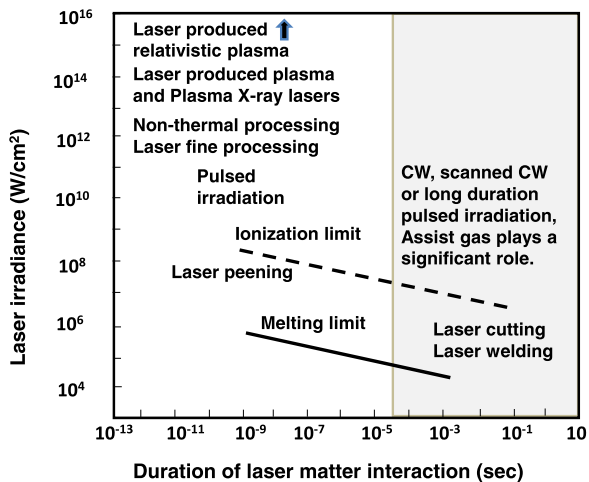


Figure 1 shows wide range of laser matter interaction studies [1] which contribute to the science and industries. Above the intensity of 10^{18} W/cm^2 which is beyond the figure, one can see the area of the ultra-high intensity laser matter interaction where the relativistic or nonlinear effects play a significant role [2]. We also find the intensity regime of plasma based soft x-ray lasers [3, 4]. In the pulsed irradiation regime, for the nuclear engineering, the laser peening [5, 6] is one of the most attractive techniques to make artificial stress distribution which strengthens the plant components. The non-thermal processing is useful for removal of materials without excessive melting [7, 8]. The ultra-short laser pulse makes nanometer structures on the surface of many materials [9]. The dashed and solid lines respectively represent ionization and melting limits. On the other hand, CW (continuous Wave), scanned CW or long duration pulsed irradiation is also quite useful for the nuclear plant engineering, such as laser welding and cutting. In this region an assist gas plays a significant role for melting and solidification.

The laser cutting of thick metallic materials are necessary for dismantling nuclear power plant and other nuclear facilities because a present fiber laser is powerful enough while it can enter into the narrow gap. The laser can melt and cut the thick metal without reactive force. Successful cutting is realized if the laser hits a fresh metal surface continuously with a help of assist gas flow which blow off the molten and vaporized metals. High quality welding is also necessary for the nuclear engineering. The detailed characterization of the laser welding phenomena is useful for it.

2 Experimental Setup

Dynamics of a molten pool surface taken by a high speed camera contribute to characterize a molten pool. However, visible light can provide only the surface of the

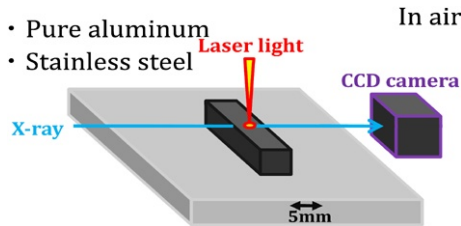


Fig. 2 Experimental setup of the real time observation of a CW 300 W laser heated Aluminum or stainless steel molten pool probed by an intense 30 keV or 70 keV x-ray beam, respectively with a band width of $<10^{-4}$ (the band width/the central energy). The laser illuminates for 5~10 seconds. The sample width is $\sim 1\sim 5$ mm

molten pool. If we need to see the interior of the molten pool, we need an intense high energy x-ray beam for imaging. In addition to this, if we would like to see a clear boundary between the solid and liquid phases we need an intense monochromatic x-ray source. For example, mass density difference between the solid and liquid iron is typically $\sim 10\%$ and we need \sim milli-second temporal resolution with long time continuous operation as well as a several tens of μm spatial resolution. An intense monochromatic x-ray beam delivered from SPring-8 whose significant feature is its ultra high brightness is suitable for this purpose. For real time observation of a laser heated Aluminum and iron based materials with $>$ a few mm thickness to see hydrodynamic phenomena, we need an intense 30 keV and 70 keV monochromatic x-ray beam, respectively. Figure 2 shows an example of the experimental setup.

3 Scenario of the Physical Processes and Experimental Result

Figure 3 show the expected physical processes of laser heated metals. A laser light is absorbed. This process includes fast and complicated processes such as free electron contribution to the absorption. Successive laser heating causes a phase change to make a molten pool. In this case, we call the heat conduction type melting. If the laser intensity increases, the regime moves into the key hole type [10]. In the pool, the convection is driven by the buoyancy for Aluminum or by the surface tension for stainless steel [11]. When the laser heating stops, the molten pool is cooled down and solidified. Then we find the residual stress distribution which is expected to be influenced by the processes happened previously.

The series of experiments have been performed with use of the setup shown in Fig. 2 [12]. Figure 4 shows an x-ray snap shot of the laser heated molten pool. The bending magnet based source coupled with a pair of crystal spectrometers delivers 30 keV x-ray with an intensity of 10^8 photons/second/mm 2 and the band width of 10^{-4} . The temporal resolution is ~ 10 msec which depends upon a frame rate of a camera. The dynamic behavior of laser heated molten pool is visible.

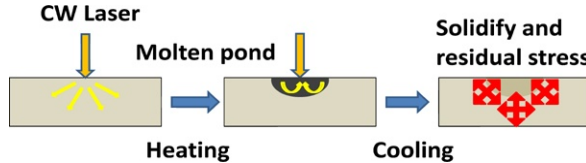


Fig. 3 The scenario of the laser heated Aluminum molten pool. From the *left* to the *right*, the laser heated pool whose solid liquid interface expands in radial direction with convection inside the pool. The laser stops. The molten pool begins to be solidified. The area of the pool decreases rapidly by cooling. The solidification is completed and the residual stress appears around the laser heated region

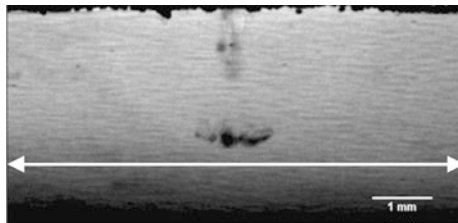


Fig. 4 An intense 30 keV x-ray beam makes it possible to make a real time movie of laser heated molten pool. The laser illuminates an Aluminum sample from the top and its power is 300 W. The thickness of the sample is 1 mm and the laser spot diameter is 1 mm. The solid liquid interface is clearly visible mainly owing to the monochromaticity of the beam. The *white horizontal line* represents 7.4 mm

4 Comparison Between the Experimental and the Computational Results

We have developed relevant multi-dimensional hydrodynamic simulation code SPLICE [13] based on the incompressible fluid model including solid, liquid and gaseous states. As we have described each processes briefly in Fig. 3. The details of the solidification processes should be given by other aspect of the physical models [14]. We have observed almost whole processes as an x-ray movie including heating, melting and a formation of molten pool, convection in a pool, solidification with residual stress formation.

Firstly, the dynamical behavior of the laser heated and solidified iron surface is described for the comparison between the experimental and computational results. The upper panel of Fig. 5 shows the precise observation of the surfaces using a high speed video camera in the visible spectral range having a frame rate of 12500 frames/second. The corresponding result obtained by the 3-dimensional hydrodynamic code is shown in the lower panel of Fig. 5. In this material, the temperature gradient causes unbalanced surface tension and the flow is driven by this force. If we switch off the surface tension artificially in the code, just a flat surface profile is visible. The computed result shows similar surface profile as observed by the high speed camera.

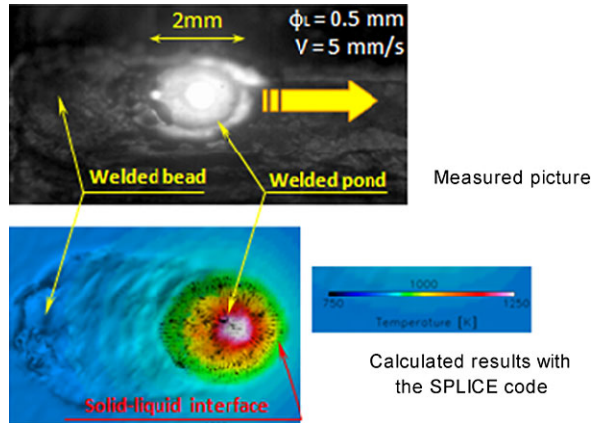


Fig. 5 The *upper panel* represents the snap shot of the 300 W, CW laser illuminated iron surface recoded by a high speed video camera in the visible spectral range. The laser illuminates from a reader to the paper. The scanning speed and its direction are 5 mm/second and the direction of the arrow, respectively. The spot size is 0.5 mm. The *lower panel* represents the result of the computer simulation. The welded beads are visible in both the panels

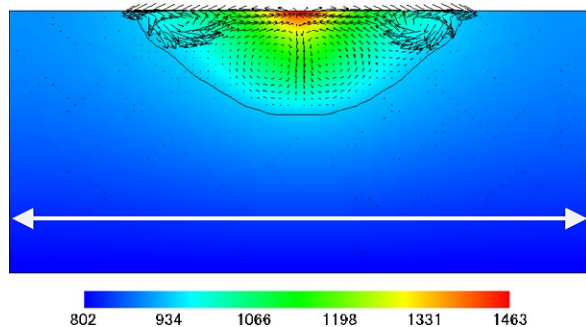
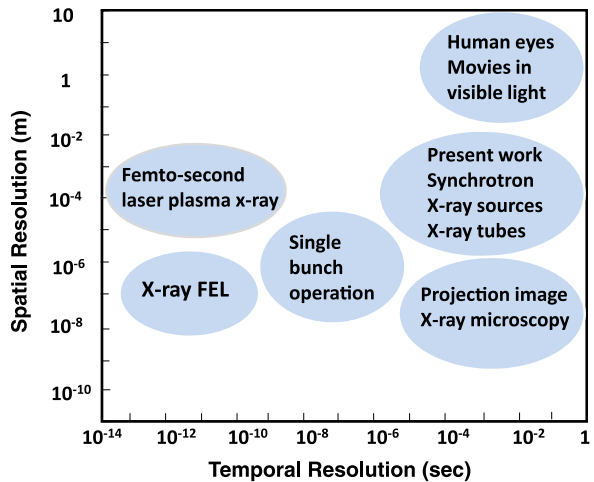


Fig. 6 The result of the SPLICE code which simulates the experiment shown in Fig. 4. The laser illuminates from the top to the central part of Aluminum sample where the high temperature region can be seen. The molten pool with clear liquid to solid interface is visible. The white horizontal line represents 10 mm. The scale of this figure is the same as that of Fig. 4. The size of the molten pool reasonably coincides with the experimental results. The arrows in the molten pool represent the directions of the convection which also coincide with the experimental results

Secondly, cross-sectional view of the molten pool is depicted. The size of the molten pool in the experiment is compared with the simulation result as shown in Fig. 6. The directions of the convection coincide with each other. The convective flow in the molten pool is clearly visible in this x-ray movie such as ~ 20 mm/second. The simulation result shows that the speed of the tracers is ~ 40 mm/second which is faster than the experimental one. After the complete solidification, the residual stress has been measured in the experiment. In this technique, if the stress is created at specific place inside the sample, lattice structure changes

Fig. 7 Spatial resolution vs. temporal resolution for various x-ray sources. Another important aspects of imaging include a field of view and duration of successive imaging (x-ray movie)



and the diffraction angle is broadened. The spectral broadening is interpreted into the residual stress. Subsequent scan inside the sample makes it possible to create a 3-dimensional stress distribution [15].

5 Outlook of the Ultra-intense X-Ray Techniques

Figure 7 represents the map of x-ray techniques in respect to the temporal and spatial resolutions including imaging [16] and diffraction.

High speed x-ray camera coupled with an undulator provides wide field of view (a few cm) with several tens of μm resolution and long time continuous operation of more than a few tens of seconds with milli-second temporal resolution which depends upon the frame rate of the x-ray camera. The whole process including laser irradiation and cooling can be identified quite successfully as described previously. However, if one would like to see precisely the specific parts, for example as shown in Fig. 4, the melting front is not resolved sufficiently. We need higher temporal and spatial resolutions such as < a few $\mu\text{-second}$ and < a few μm . During the solidification phase, we also need much higher resolutions for a real time observation of crystallization where a typical dendrite size is $\sim 10 \mu\text{m}$. Such precise imaging may not need relatively wide field of view. A single bunch operation of a Synchrotron source is one of the possible candidates. The parameters for imaging are complementary.

The creation of residual stresses have routinely measured with the scanning x-ray technique [12] which needs a long time operation and it might be observed with time resolved x-ray diffraction made by an ultra-intense coherent x-ray. An x-ray Free Electron Laser [17] might provide such a beam if it can deliver pulses with higher photon energy. Compact ultra short pulse laser driven x-ray sources with a pump-probe technique have also contributed to the real time observation of

phase transitions with ultra fast x-ray diffraction techniques [18]. Such laser driven sources might be also applicable to the imaging with a single shot based operation. Full characterization of melting and solidification of metals is in progress with the technique described here. In addition, these techniques are applicable to the non-metallic materials.

6 Summary

The real time imaging of a laser irradiated metallic molten pool using a Synchrotron facility has been realized. An undulator x-ray source is an almost ideal source for characterizing the macroscopic hydrodynamic behavior of the process. The result is compared with the multi-dimensional fluid simulation. Real time imaging of solidification process has also been realized. We also have made off-line measurement of residual stress distribution. Based on the present achievement, extension of the ultra high brightness x-ray techniques to characterizing the finer and faster components is discussed.

References

1. Von Allmen, M., Blatter, A.: *Laser-Beam Interactions with Materials*, 2nd edn. Springer, Berlin (1995)
2. Daido, H., Nishiuchi, M., Pirozhkov, A.S.: Review of laser-driven ion sources and their applications. *Rep. Prog. Phys.* **75**, 056401 (2012) (71 pages)
3. Daido, H.: Review of soft x-ray laser researches and developments. *Rep. Prog. Phys.* **65**, 1513–1576 (2002)
4. Suckewer, S., Jaegle, P.: X-ray lasers: past, present, future. *Laser Phys. Lett.* **6**, 411–436 (2009)
5. Sakino, Y., Sano, Y., Kim, Y.-C.: Application of laser peening without coating on steel welded joints. *Int. J. Struct. Integr.* **2**, 332–344 (2011)
6. Sano, Y., et al.: Residual stress improvement in metal surface by underwater laser irradiation. *Nucl. Instrum. Methods Phys. Res. B* **121**, 432–436 (1997)
7. Nishimura, A., et al.: Ablation of work hardening layers against stress corrosion cracking of stainless steel by repetitive femtosecond laser pulses. *SPIE Proc.* **5562**, 673–677 (2004)
8. Nishimura, A., et al.: Development of inspection and repair technology for the micro cracks on heat exchange tubes. *J. Jpn. Laser Process. Soc.* **17**, 207–212 (2010)
9. Azuma, H., et al.: Single-shot creation of nanometer-sized silicon tadpoles by ultrahigh-intensity laser. *Jpn. J. Appl. Phys.* **43**, L1172–L1174 (2004)
10. Fujinaga, S., et al.: Direct observation of keyhole behaviour during pulse modulated high-power Nd:YAG laser irradiation. *J. Phys. D: Appl. Phys.* **33**, 492–497 (2000)
11. Fujii, H., Sogabe, N., Nogi, K.: Convection in weld pool under microgravity and terrestrial conditions. *Mater. Sci. Forum* **512**, 301–304 (2006)
12. Yamada, T., et al.: Phenomenological evaluation of laser-irradiated welding processes with a combined use of higher-accuracy experiments and computational science methodologies (3) In-situ observations of welded pool using an intense x-ray beam. In: *Proc. the 12th International Symposium on Laser Precision Microfabrication* (2011). Paper number # 11-055 Tu3-O-7, Att0091

13. Yamashita, S., et al.: Phenomenological evaluation of laser-irradiated welding processes with a combined use of higher-accuracy experiments and computational science methodologies (5) Numerical simulation of the welding processes with a multi-dimensional multi-physics analysis code SPLICE. In: Proc. International Conference on Nuclear Engineering, May 16–19, 2011 (2011). Paper number ICONE19-43939
14. Kou, S., Le, Y.: The effect of quenching on the solidification structure and transformation behaviour of stainless steel welds. *Metall. Trans. A* **13A**, 1141–1152 (1982)
15. Muramatsu, T., et al.: Study on fundamental processes of laser welded metals observed with intense x-ray beams. In: Lee, J., Nam, C.H., Janulewicz, K.A. (eds.) X-Ray Lasers 2010. Springer Proceedings in Physics, vol. 136, pp. 245–255 (2011)
16. Zewail, A.H., Thomas, J.M.: 4D Electron Microscopy. Imperial College Press, London (2009), Chap. 1
17. Tanaka, H.: Next-generation light source gets boost from powerful new analysis technique. RIKEN home page, <http://www.riken.go.jp/engn/r-world/research/results/2010/100922/image/100922.pdf> (September 2010)
18. Rousse, A., Rischel, C., Gauthier, J.-C.: Colloquium: femtosecond x-ray crystallography. *Rev. Mod. Phys.* **73**, 17–31 (2001)

Chapter 13

Generation and Application of Coherent Radiation in the Water Window

L.V. Dao, C. Hall, H.L. Vu, K.B. Dinh, N. Gaffney, E. Balaur, P. Hannaford, and T.A. Smith

Abstract Coherent extreme ultraviolet radiation around the water window region (~ 4.4 nm) is generated by using an infrared driving pulses at 1400 nm, with energy 2.5 mJ and duration 40 fs in a semi-infinite helium gas cell. The beam profile and spatial coherence characteristics of the source in this region are shown to be excellent, enabling this source to be used for coherent diffractive imaging.

1 Introduction

Femtosecond laser-driven high-harmonic generation (HHG) has become an increasingly important source for many applications in time-resolved studies of ultrafast dynamics and in coherent diffractive imaging [1–3]. For biological applications the generation of radiation in the “water window” region (4.4–2.3 nm, or 280–540 eV) is an attractive feature because in this wavelength range the radiation is not absorbed by water and nitrogen while absorption of carbon is strong. Intense ultrashort pulses in the water-window wavelength region would allow the capture of images of live cells in a real environment, preserving structural information that can be lost in the sample’s preparation process for other imaging methods. This soft x-ray radiation can be used to perform various experiments with high spatial and temporal resolution. Thus, light sources in this wavelength

L.V. Dao (✉) · C. Hall · H.L. Vu · K.B. Dinh · N. Gaffney · P. Hannaford
Centre for Atom Optics and Ultrafast Spectroscopy, Swinburne University of Technology,
Melbourne, Australia
e-mail: dvlap@swin.edu.au

E. Balaur
Department of Physics, La Trobe University, Melbourne, Australia

T.A. Smith
School of Chemistry, University of Melbourne, Melbourne, Australia

L.V. Dao · C. Hall · H.L. Vu · K.B. Dinh · N. Gaffney · E. Balaur · P. Hannaford · T.A. Smith
Australian Research Council Centre of Excellence for Coherent X-Ray Science, Melbourne,
Australia

region have been targeted by many researchers including life scientists and physicists.

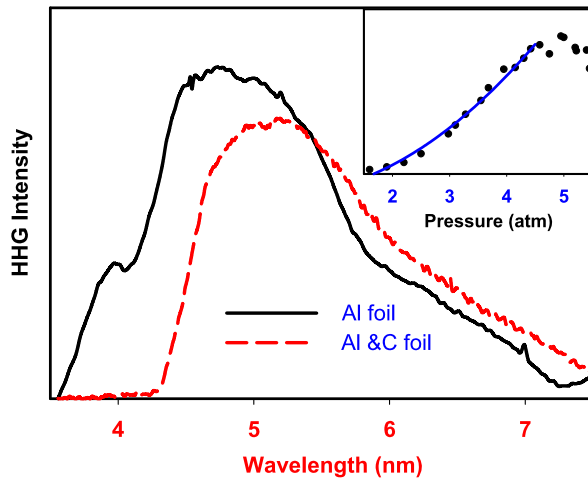
In this paper we report the use of a bismuth triborate (BiB_3O_6 , or BIBO) nonlinear crystal to construct a high power optical parameter amplifier pumped by 8 mJ pulses from a multi-pass Ti:sapphire amplifier at 1 kHz repetition rate. High energy (2.5 mJ) IR pulses at 1400 nm and with short duration (<40 fs) are used for phase-matched generation of radiation of high spatial coherence around the water window region in a semi-infinite cell filled with helium gas. The coherence of the source is studied by measurements of the beam profile and the interference pattern from a Young's double slit. The broadband source is tested for applicability for coherent diffractive imaging.

2 Experiments and Results

The output of a 1 kHz multi-stage, multi-pass, chirped-pulse amplifier system that produces 8 mJ pulses of 30 fs duration and centered at 810 nm is used to pump the OPA system. A collinear OPA scheme is used in our high-energy IR laser system in order to efficiently amplify the OPA signals. One-third of the output of the multistage amplifier (2.5 mJ) pumps a commercial OPA (Quantronix, Palitra), which is designed with a two-stage configuration seeded by a white light continuum. The remaining 5.5 mJ is used to pump the power amplifier stage. In the high power OPA stage we employed a 2-mm thick BIBO crystal with an aperture of $15 \times 15 \text{ mm}^2$, which was placed about 50 cm away from the commercial OPA. The power amplifier OPA stage is seeded by the amplified signal in the commercial OPA whose output is carefully adjusted for a collimated signal beam. The maximum conversion efficiency for the power amplifier stage was about 60 %, producing a total (signal and idler) output of ~ 4 mJ. An IR pulse duration of 40 fs was measured through sum-frequency mixing with a 30 fs fundamental pulse.

The OPA output pulses at 1400 nm are focused by a 300 mm focal length fused silica lens into a 250 mm-long gas cell with a 3 mm-thick fused silica window at the entrance and a 200 μm pinhole at the exit [4]. We use helium gas for HHG in the water window region because of its high ionization energy and because theoretical calculations [5] indicate that it is possible to obtain phase matching for the generation of radiation in the water window region in helium gas using 1400 nm radiation. A high gas pressure (up to 5 atm) is used for generation of radiation around 4.3 nm. A 300 nm-thick aluminum filter with high transmission in the wavelength range <5 nm (~10 % at 4 nm), and a 300 nm-thick silver filter with transmission in the wavelength range 4–12 nm are used to remove the residual fundamental beam. The high harmonic beam passes through a 0.5 mm-wide, 20 mm-high entrance slit of a grazing incidence spectrometer before being dispersed by a 1200 lines/mm diffraction grating and detected by a back-illuminated XUV charge-coupled device (CCD) camera. The far-field profile of the harmonic beam is detected directly by

Fig. 1 XUV HHG spectra from He at 5 atm. The C-edge absorption can be seen (dashed line) when a 150 nm thick C-foil is added. The inset shows the harmonic yield versus the gas pressure: the dots show the experimental data and the line represents the best fit with P^2 where P is the gas pressure

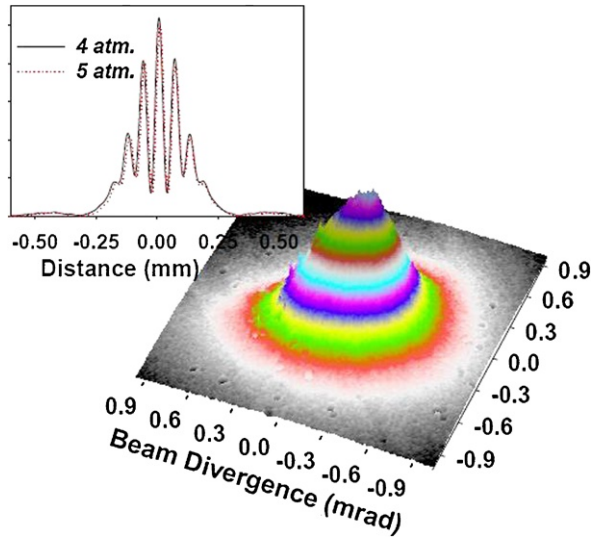


a 13.3×13.3 mm CCD chip of pixel size $13 \times 13 \mu\text{m}$ (PIXIS-XO-1024B, Roper Scientific). For studies of the spatial coherence of the high harmonic beam in more detail a Young double slit (YDS) comprising two parallel slits $4 \mu\text{m}$ wide, $100 \mu\text{m}$ high and slit separation of $20 \mu\text{m}$ is used. The YDS is located 1000 mm from source. The interference fringes are detected by a CCD camera located 800 mm from the slit.

Figure 1 shows the XUV spectrum emitted from helium at 5 atm He pressure with an exposure time of 20 s for each spectrum. The C-edge absorption can be seen (dashed line) when a 150 nm thick C-foil is added. Since the position of the focus of the driving laser beam is close to the exit pinhole of the gas cell the HHG radiation is produced mostly in regions in the gas cell before the focal point along the axis of the fundamental beam. The bandwidth and beam profile of the HHG radiation depend on the gas pressure, the focus position and the diameter of the fundamental beam. The beam profile is remarkably improved for pressures $> 3 \text{ atm}$. The intensity of the IR pulses ($< 5 \times 10^{14} \text{ W/cm}^2$) is adjusted for low ionization of the gas ($\eta < 1 \%$) to generate high harmonic radiation from the neutral atoms. The inset in Fig. 1 shows the total photon number in the spectral range 4–5 nm for different gas pressures where a 300 nm Al foil has been used. The closed circles show the experimental data and the solid line shows a fit based on P^2 . For low pressures ($P < 4 \text{ atm}$), the HHG signal increases quadratically with pressure as is expected for phase-matched HHG emission. For high pressures ($> 5 \text{ atm}$) the phase mismatch is increased because of the high absorption restricting further HHG yield increases.

Figure 2 shows the spatial profile of the HHG beam at a distance of 1800 mm from the source. The beam diameter was measured to be 0.8 mm (FWHM). The almost perfect Gaussian profile of the HHG beam suggests there is no density disturbance due to ionization in the interaction region. The observed dependence of the HHG output on pressure and the observed spatial profile indicate that macroscopic phase matching is satisfied along the propagation axis in our geometrical config-

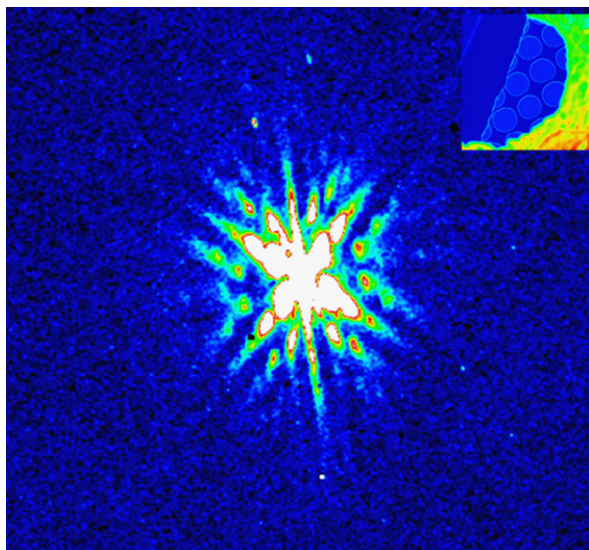
Fig. 2 The beam profile of radiation at a distance of 1800 mm from the source. The inset displays interference fringes of the Young's double slit measurement (YDS). The YDS device consists of two parallel slits of 4 μm in width, 100 μm high and separated by 20 μm



uration. The photon flux around the maximum of the beam profile, measured by the CCD, in the wavelength range 4–5 nm is about 7×10^7 – 10^8 photons/(cm 2 s) when the transmission of the Al foil is assumed to be $\sim 10\%$. To study the spatial coherence of the source in more detail, a YDS is used. The inset in Fig. 2 shows a clear interference pattern resulting from the YDS, which consists of two parallel slits 4 μm wide, 100 μm high and 20 μm separation. The beam diameter at the slit position is ~ 0.5 mm (FWHM) which is much larger than the slit separation. When the gas pressure is high (>3.5 atm) the contrast at the center of the interference pattern is nearly independent of the gas pressure. We note that the YDS was illuminated from a broad wavelength beam (an Al foil was used to filter out the fundamental beam) and therefore the contrast of the fringes is not very high. The interference pattern is dependent on the gas pressure indicating a variation of the harmonic spectrum with pressure. The Gaussian beam profile and high contrast of the YDS interference fringes confirm that the HHG radiation is highly coherent.

The diffraction imaging from a pinholes sample illuminated by a broadband source is shown in Fig. 3. Close inspection reveals that the diffraction pattern is blurred because of the broad band nature of the source (4–5 nm). In the present reconstruction procedure we require that the bandwidth of the source is less than 10 % of the center wavelength and the coherence degree should be >0.9 . New reconstruction procedures need to be developed and also the bandwidth of the source needs to be reduced with a quasi-phase matching configuration. These improvements are under development.

Fig. 3 Diffraction pattern from the pinholes sample illuminated by the source at 4–5 nm. A scanning electron microscope (SEM) image of the sample is shown in the *inset*



References

1. Gagnon, E., et al.: Soft X-ray-driven femtosecond molecular dynamics. *Science* **317**, 1374–1378 (2007)
2. Cavalieri, A.L., et al.: Attosecond spectroscopy in condensed matter. *Nature* **449**, 1029 (2007)
3. Chen, B., et al.: Multiple wavelength diffractive imaging. *Phys. Rev. A* **79**, 023809 (2009)
4. Dao, L.V., et al.: Generation of high flux, highly coherent extreme ultraviolet radiation in a gas cell. *J. Appl. Phys.* **104**, 023105 (2008)
5. Chen, M.-C., et al.: Bright, coherent, ultrafast soft x-ray harmonics spanning the water window from a tabletop light source. *Phys. Rev. Lett.* **105**, 173901 (2010)

Chapter 14

Time-Dependent Simulation of Carbon Illuminated by a High Intensity X-Ray Laser

Alberto G. de la Varga, Pedro Velarde, François de Gaufridy, Manuel Cotelo, David Portillo, and Philippe Zeitoun

Abstract We simulate a biological cell composed of solid density carbon illuminated by a high intensity X-ray laser with a time-dependent model. This first version is a simple model that neglects inverse bremsstrahlung absorption by free electrons, electron conduction or hydrodynamic effects. Atomic data needed for the simulations can be generated with the flexible atomic code (FAC) or the screened hydrogenic model (SHM).

1 Introduction

Taking advantage of the recently developed collisional-radiative module in the code bigbart [1] we have implemented the module `muffinman` to study time-dependent radiation transport in carbon as an approximation to simulate the response of biological tissue.

We expect inverse bremsstrahlung absorption by free electrons, electron conduction or hydrodynamic effects to be negligible. At first hand these assumptions seem reasonable. Due to the non-equilibrium nature of the problem free electrons are born with high energies which, in addition to the high energy photons from the laser pulse, produces low resonant free electron absorption that comes mainly from low energy electrons. The short time scale employed leads in principle to low hydrodynamic and electron conduction effects. The influence of this effects will be studied in future versions in order to check our assumptions.

A.G. de la Varga (✉) · P. Velarde · F. de Gaufridy · M. Cotelo · D. Portillo
Instituto de Fusión Nuclear, Universidad Politécnica de Madrid, José Gutiérrez Abascal 2, 28006
Madrid, Spain
e-mail: agardelavarga@gmail.com

F. de Gaufridy
Institute of Physics, Czech Academy of Sciences, Prague, Czech Republic

P. Zeitoun
Laboratoire d'Optique Appliquée, UMR CNRS/ENSTA ParisTech/Ecole Polytechnique
ParisTech, Chemin de la Hunière, 91671 Palaiseau, France

There is no treatment of escaped or trapped electrons [2], all electrons are considered trapped and contribute to the average free electron energy and collision rates. For the sake of simplicity we assume that free electrons have time for thermalization at a certain calculated thermalization temperature.

Energy exchange involving ions, free electrons and the radiation field is computed in each timestep to check the consistency of the model and to obtain the free electron temperature in the next timestep.

2 Description of the Time-Dependent Radiation Transport Module

The module `muffinman` implements an explicit model that computes the variation in configuration populations and the energy exchange between timesteps. Configurations are connected through all possible collisional and radiative processes. Processes and their inverse considered in `muffinman` are spontaneous emission and resonant photoabsorption (multipole transitions E1, E2 and M1), collisional excitation and collisional de-excitation, radiative recombination and photoionization, collisional ionization and three body recombination, and autoionization and resonant capture.

Spontaneous emission, collisional excitation, radiative recombination, collisional ionization and autoionization rates may be computed with the relativistic atomic code FAC [3] or SHM [4, 5]. Collisional de-excitation, three body recombination and resonant capture are calculated by detailed balance [6]. For transitions due to interaction with the radiative field, resonant photoabsorption and photoionization, formulas from [7] are used.

Once we have computed the transition rates, the system of equations that yields the change in population of configuration α is written as

$$\frac{dn_\alpha}{dt} = -n_\alpha \sum_{\beta \neq \alpha}^N W_{\alpha\beta} + \sum_{\beta \neq \alpha}^N n_\beta W_{\beta\alpha} \quad (\text{s}^{-1}) \quad (1)$$

where n_α is the population of configuration α normalized to unity and $W_{\alpha\beta}$ refers to the transition rate from configuration α to configuration β . The system is solved with an explicit method. Also energy exchange is calculated for each process that produces energy transfer between ions, free electrons and the laser pulse. The variation of energy of each component c due to process γ between configurations α and β with an energy exchange of $\Delta e_{\alpha\beta}^\gamma$ in a timestep Δt is

$$E_c^{n+1} = E_c^n + \sum_{\gamma} \sum_{\beta} \sum_{\alpha} \Delta e_{\alpha\beta}^\gamma W_{\alpha\beta}^\gamma n_\alpha \Delta t \quad (\text{eV}) \quad (2)$$

$$\Delta E_c = E_c^{n+1} - E_c^n \quad (3)$$

where E_c can be the energy of the ions E_{bound} , free electrons E_{free} and laser pulse E_{pulse} . Consistency in energy transfer implies in each timestep

$$\Delta E_{\text{bound}} + \Delta E_{\text{free}} + \Delta E_{\text{pulse}} = 0 \quad (4)$$

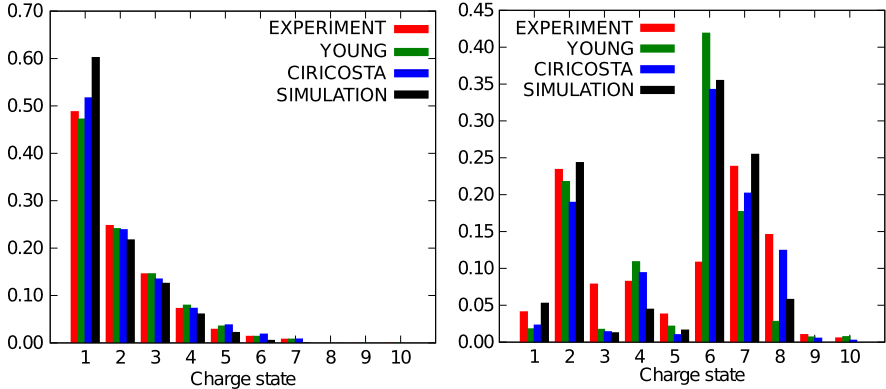


Fig. 1 Charge-state yields in the 800 eV (left) and 1050 eV (right) cases

From the free electron density n_e and the free electron energy density ρ_E we compute the average free electron energy

$$\langle E_{av} \rangle = \frac{\rho_E}{n_e}.$$

Equivalent thermalization temperature is obtained by

$$\frac{3}{2}kT_e = \langle E_{av} \rangle.$$

3 Experimental Benchmark

In order to test the accuracy of the developed module we compared experimental neon charge-state yields measured at LCLS with theoretical calculations [8, 9]. The neon gas (10^{19}) was irradiated at intensities up to 10^{18} W/cm² and photon energies of 800 eV (below the K-edge), 1050 eV (just above the K-edge) and 2000 eV (far above the K-edge).

Here we consider the 800 and 1050 eV cases for comparison with a 0D model. As in the theoretical model in [8] we consider photoionization and autoionization as predominant over collisional processes. This is approximately true at this densities, although collisional ionization may compete with photoionization in the 800 eV case [9].

In Fig. 1 (left) theoretical models correctly reproduce experimental charge-state yields. This is due to the simple absorption mechanism with dominance of valence shell photoionization, with no K-shell vacancies and therefore no autoionization. In Fig. 1 (right) our model performs in the range of the other two theoretical models but none is close to the experimental measurement. Production of Ne^{2+} , Ne^{4+} and Ne^{6+} is mainly due to autoionization. Inner shell photoionization is the main mechanism for Ne^{1+} , Ne^{3+} and Ne^{5+} production, introducing other mechanisms due to

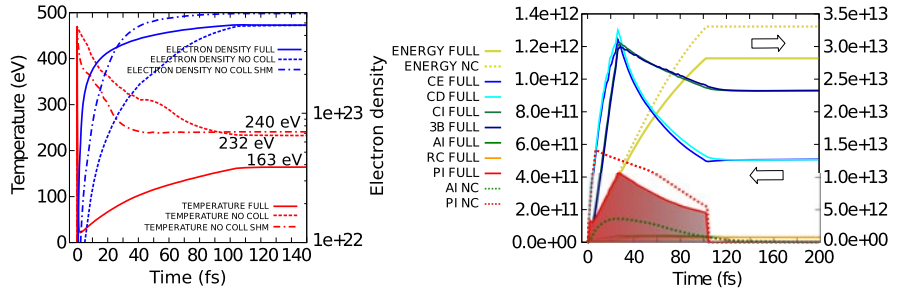


Fig. 2 Temperature, electron density (*left*) and energy exchange (*right*) with free electrons from different processes and total energy absorption in J/m^3

Table 1 Temperatures (eV) after $10^{17} \text{ W}/\text{cm}^2$ and 1 keV photon energy irradiation

FAC	FAC NC	SHM NC	Whittaker et al.
163	232	240	230

inner-shell vacancies not considered in neither of the theoretical models which may explain the discrepancies.

4 High-Intensity X-Ray Simulations

The aim of the developed module is to perform 1D simulations of solid carbon illuminated by ultraintense and ultrashort x-ray pulses as a first approximation to the irradiation of biological tissue.

First we will compare 0D simulations of solid carbon with a SHM model [10]. In their article Whittaker et al. investigated temperatures following from irradiation of 100 fs flat-top pulses at different intensities and photon energies, assuming that after irradiation and before the expansion of the sample, approximately one picosecond, the sample reaches full thermalization. Only photoionization and autoionization were considered in their model.

In Fig. 2 and Table 1 it can be seen that FAC (FULL) and SHM with no collisions (NC) agree quite well with results by Whittaker et al., but when collisional processes are included the temperature reached is lower. This happens because electron density increases rapidly and so collisional ionization competes with photoionization, reducing the photon absorption and hence the energy absorbed by the sample.

In the second selected case at 2 keV and $10^{18} \text{ W}/\text{cm}^2$, see Table 2, we included calculations with a modified SHM model (SHM MOD) as in Whittaker et al., where the Kramer's photoionization was scaled as the inverse square and not the inverse cube. This greatly increases photoionization cross sections far from the ionization potential of a transition, resulting in a great enhancement of the photon absorption leading to high temperatures. Our modified model agrees with their results and FAC and SHM models predict much lower temperatures after irradiation.

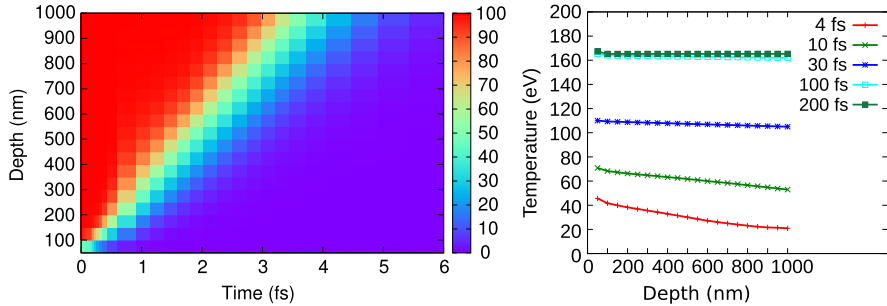


Fig. 3 Absorption (%) and temperature profiles in 1 μm of solid carbon

Table 2 Temperatures (eV) after 10^{18} W/cm^2 and 2 keV photon energy irradiation

FAC	SHM	SHM MOD	SHM MOD NC	Whittaker et al.
192	90	538	584	560

Finally we performed a simulation of a 1 μm carbon layer at $2 \times 10^{16} \text{ W/cm}^2$ and wavelength $\lambda = 13 \text{ nm}$, consistent with $I\lambda^2$ values from FEL experiments [8, 11]. The absorption through the layer, see Fig. 3, decreases to almost zero after less than 10 fs. Temperature profile in the sample needs a few tens of fs to reach uniformity.

Acknowledgements The authors would like to thank the financial support provided by the Spanish Ministerio de Educación y Cultura program no. ENE2009-09837 and also to the European Commission SFINX-LASERLAB-II.

References

1. de la Varga, A.G., et al.: High Energy Density Phys. **7**, 163 (2011)
2. Hau-Riege, S.P., et al.: Phys. Rev. E **69**, 051906 (2004)
3. Gu, M.F.: Can. J. Phys. **86**, 675 (2008)
4. More, R.M.: J. Quant. Spectrosc. Radiat. Transf. **27**, 345 (1982)
5. Faussurier, G., et al.: J. Quant. Spectrosc. Radiat. Transf. **58**, 233 (1997)
6. Salzmann, D.: Atomic Physics in Hot Plasmas. Oxford University Press, New York (1998)
7. Rose, S.J.: High Energy Density Phys. **5**, 23 (2009)
8. Young, L., et al.: Nature **466**, 56 (2010)
9. Cricosta, O., et al.: High Energy Density Phys. **7**, 111 (2011)
10. Whittaker, D.S., et al.: Phys. Plasmas **18**, 013105 (2011)
11. Ackermann, W., et al.: Nat. Photonics **1**, 336 (2007)

Chapter 15

Regenerative Laser Cavity Tuning for Efficient Soft-X-Ray Laser Operation

O. Delmas, K. Cassou, O. Guilbaud, S. Kazamias, S. Daboussi, M. Pittman, O. Neveu, J. Demainly, and D. Ros

Abstract The influence of temporal pump laser profile on the Soft X-ray laser (SXRL) efficiency is investigated in double grazing incidence pumping (DGRIP) transient collisional scheme. We have demonstrated a simple method that allows to produce and control one or several small prepulses and the ASE level of the pump laser beam by modifying the regenerative amplifier parameters. By changing the temporal structure of the pump beam we observed both an increase of the SXRL energy and an improvement of the target lifetime. Measurements made for different configurations are presented and discussed.

1 Introduction

The recent progress made on high intensity lasers and laser-pumped XUV sources allowed the construction of the LASERIX soft-X-ray laser (SXRL) facility at the Paris Sud University. SXRL pulses considered here are generated in a plasma in the transient collisional excitation scheme. For this, the plasma is created by a long laser pulse (100 ps to 1 ns) focused on solid target, which in turn is excited by a short pulse (in the ps range) creating then a population inversion through electrons/ions collisions in the soft-X-ray domain. It has recently been demonstrated on LASERIX that low intensity precursor pulses and a low amount of ASE in a nanosecond range are favourable for XUV signal level and target lifetime [1]. In the present work, we study the effect of the forefront temporal contrast on the SXRL generation by adding

O. Delmas (✉) · K. Cassou · O. Guilbaud · S. Kazamias · S. Daboussi · M. Pittman · O. Neveu · J. Demainly · D. Ros
CLUPS/LASERIX, Université Paris Sud XI, 91405 Orsay Cedex, France
e-mail: olivier.delmas@u-psud.fr

O. Delmas · K. Cassou · O. Guilbaud · S. Kazamias · S. Daboussi · O. Neveu · J. Demainly · D. Ros
LPGP, Bât 210, Université Paris Sud XI, 91405 Orsay Cedex, France

O. Delmas
Amplitude Technologies, 2-4 rue du Bois Chaland, 91090 Lisses, France

precursor pulses by simply tuning the output synchronization of the regenerative amplifier (RGA) of the laser chain.

2 Experimental Set-up

2.1 *Laserix Facility Overview*

The LASERIX facility provides two XUV beamlines. The first is based on High Harmonic Generation in rare gas (Ar, Ne ...) while the second is based on transient collisional SXRL with Ni or Ne like targets (Mo, Ag, Ti). The SXRL is pumped by a 10 Hz–100 TW class Ti:Sa laser with a double pulse structure. The pulse to pulse energy stability of SXRL has been improved by using a “Double Grazing Incidence Pumping” (DGRIP) configuration, where the long pulse is created before amplification in order to produce two pulses within the same laser beam [2] which is more stable and convenient than the classical GRIP configuration [3] which requires the use of two different beams (Fig. 1). A disadvantage of this method is a loss of energy for the long pulse during the compression process which can be estimated to be of about 15 % of the total energy for a typical energy ratio of 70/30 % in favour of the main pulse. Another disadvantage of the DGRIP configuration for LASERIX, which can propose multibeam configurations mainly for pump-probe experiments, lies in the double pulse structure which degrades the temporal resolution for femtosecond IR or XUV based HHG probe.

2.2 *Temporal Pulse Shaping*

The setup used to produce the two following pulses for the DGRIP configuration is illustrated on Fig. 2. After passing through the Offnér stretcher, the beam is split into two parts with an energy ratio control at the input of a Mach-Zehnder interferometer like setup. In one arm, corresponding to the first pulse, the beam passes through a Martinez stretcher in order to increase its spectral phase dispersion [4]. In the other arm, corresponding to that of the main pulse, the beam is sent into a motorized delay line in order to control the temporal delay with respect to the first. The two beams are then recombined in one with a beam splitter which is sent into the RGA. The cavity configuration of the RGA induces a transverse mode filtering which allows a perfect spatial recombination between the two pulses. After three stages of multipass power amplification, the two pulses are injected in the compressor so as to finally obtain a long pulse having a duration fixed by the Martinez stretcher followed by a short pulse only compressed in the 0.5 to 10 ps range.

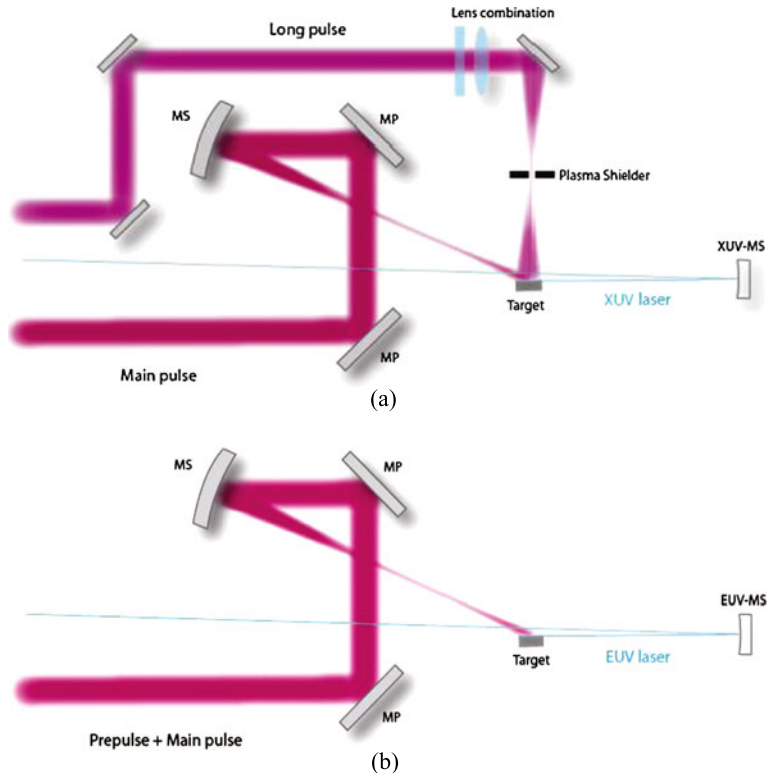


Fig. 1 Experimental set-up; (a) In the GRIP scheme two different beams are focused on the target, the nanosecond pulse (purple) arrives normally to the target surface for plasma generation while the picosecond pulse (red) arrives later at a grazing incidence to pump the plasma [3]; (b) In the DGRIP scheme, the two pulses arrive in the same beam at a grazing incidence on the target [2]

2.3 Regenerative Amplifier Tuning

It is generally admitted that a front nanosecond pedestal or even a prepulse in the temporal profile can change dramatically the SXRL performance [5–7]. In the present approach, we generate prepulses in the RGA of the Ti:Sa front-end laser (Fig. 3) by a fine adjustment of the trigger delay of the output Pockels cell (PK_{OUT}). In the same way, we add one or more round trips after the maximum pulse extraction from the cavity, in order to favour front ASE pedestal, by a coarse delay adjustment of PK_{OUT} . This way, since the synchronization of all the pump lasers remains unchanged with respect to the initial maximum extraction from RGA, the following power amplifiers will increase an ASE signal in that temporal region. By carefully adjusting first the coarse delay for ASE generation then fine delay for prepulses we could evidence strong improvement of the SXRL emission and a non negligible extension of the target lifetime.

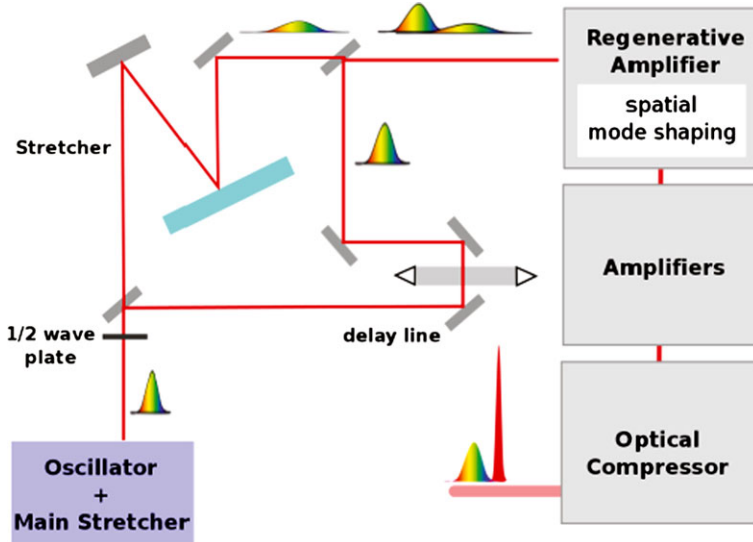


Fig. 2 Scheme of the Mach Zehnder like set up used in the laser driver for the DGRIP configuration. After separation, one part of the beam undergoes a second temporal stretching while the other part passes through a motorized delay line before spatial recombination and injection in the amplification chain

3 SXRL Optimization Experiments

3.1 Lifetime Improvement

In a first approach, we are interested in the improvement of the target lifetime with respect to ASE level by modifying the number of round trips added in the RGA. Three different cases are considered to observe the role played by the ASE level (Fig. 4). In all cases, the single shot SXRL emission is recorded at 10 Hz with a XUV 16 bits camera, and integrated energy is calculated. With no round trips added in the cavity (blue plot), the average integrated XUV energy is around 3000 shots. This configuration shows an unstable energy regime, then a progressive decrease of the signal after 200 shots. When we delay by 2 round trips the pulse extraction (violet plot), the SXRL energy is two times greater. Even if the emission decreases faster, reflecting a higher consumption velocity (Fig. 4(b)), SXRL is still effective over 500 shots. Thus, we are not only able to obtain higher SXRL energy but we can also use the same target position for a greater number of efficient shots. On the contrary, with 3 supplementary round trips (red curve), the target lifetime is distinctly worse than the two previous cases. The SXRL energy drops back to the initial level but rapidly falls after only 150 shots.

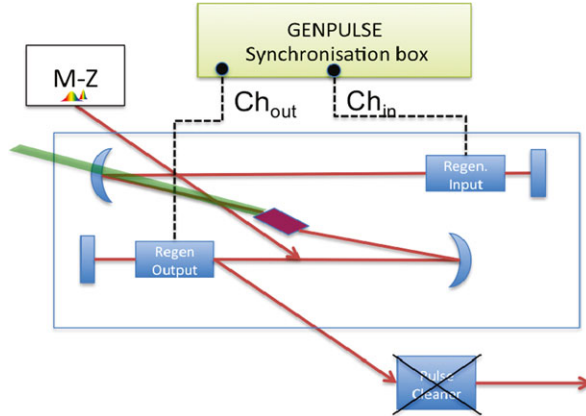


Fig. 3 Regenerative amplifier scheme. After passing through the Mach-Zehnder setup to get the double pulse structure the beam is injected in the RGA. The coarse and the fine adjustments of the pulse extraction delay allow to modify respectively ASE level and small prepulse intensity in the temporal laser profile. For this experiment the pulse cleaner located at the output of the RGA for high contrast pulse generation has to be bypassed in order not to trunk the complex shaped temporal profile

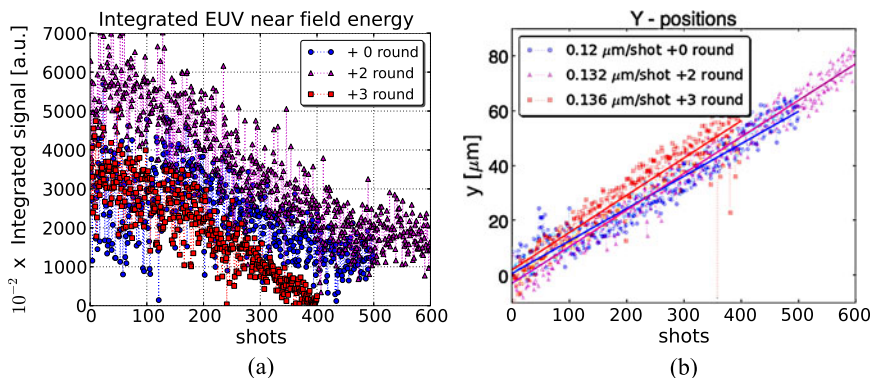


Fig. 4 (a) Integrated EUV near field energy with different number of round trips (RT) added in the RGA from nominal pulse extraction. With 2 RT (violet curve), SXRL energy and target lifetime are improved compared to the nominal RGA configuration (blue curve). With 3 more RT, maximum energy is not higher and the lifetime behaviour is really poor showing no SXRL emission after 400 shots. (b) Evolution of the position of the near-field SXRL emission for different number of added RT. The target consumption increases with the number of RT, while the slope of the penetration into the target increases from the blue curve to the red

3.2 Short Prepulse Effect

The short prepulse comes from a leak from the RGA due to a small amount of polarization induced ellipticity of the laser pulse when passing through the PK during the high voltage slope. The energy level of the short prepulse can be coarsely controlled

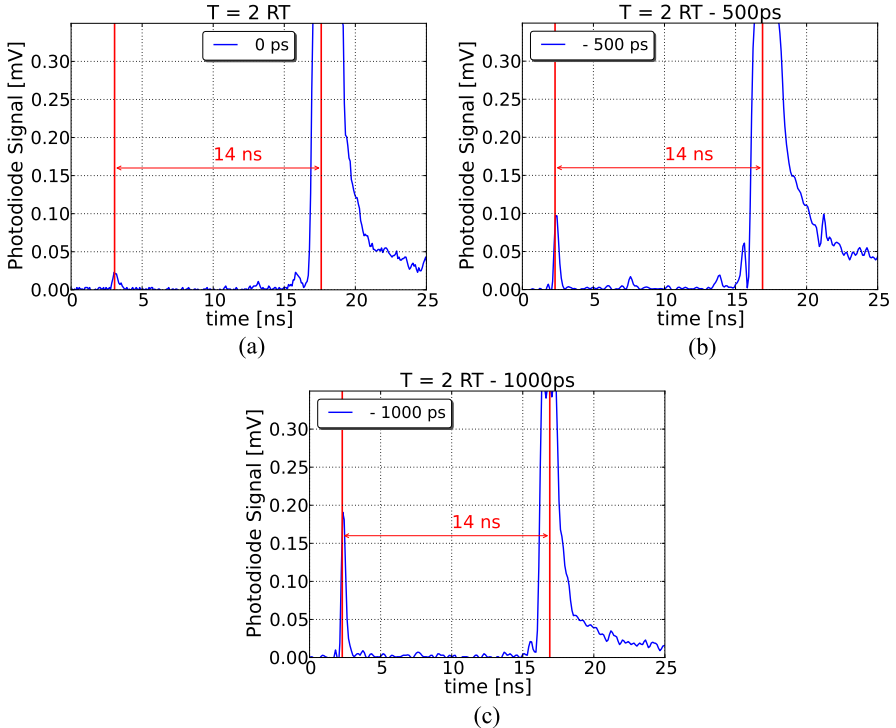


Fig. 5 Fast photodiode measurements of the prepulse intensity for different fine delay adjustments of PK_{OUT} from the temporal position corresponding to two additional passes (RT) in the RGA. The main saturated pulse is composed of both the long plasma pulse of 250 ps followed by the pump pulse compressed down to 3 ps which can not be temporally resolved with this measurement system. (a) $\text{Ch}_{\text{out}} = 2 \text{ RT}$, low prepulse (0.5 % of main pulse). (b) $\text{Ch}_{\text{out}} = 2 \text{ RT} - 500 \text{ ps}$, average prepulse intensity >20 mJ (2 % MP). (c) $\text{Ch}_{\text{out}} = 2 \text{ RT} - 1000 \text{ ps}$, High Prepulse intensity >40 mJ (4 % MP)

by a fine adjustment of PK_{OUT} timing with a precision limited by the intrinsic jitter of the PK trigger. The prepulse exiting the RGA will then be amplified in the following succession of multipass amplifiers.

The prepulses are observed with an ultrafast photodiode (30 ps rising time) associated with a 2.4 GHz oscilloscope. Measurements have been done in three different cases by tuning prepulse intensity by delaying the timing by 500 ps steps. Figure 5 shows that a negligible prepulse of 0.5 % of the main pulse is located 14 ns before the main pulse. This configuration corresponds to the optimal coarse delay for SXRL generation located 2 round trips after the maximum peak of RGA amplification as depicted in the previous section. The round trip duration being of 14 ns, it evidences that prepulse takes place at the round trip preceding the main extraction. We can also observe that the shift of PK triggering by 500 ps increases four times the prepulse energy (b), which doubles once more when adding 500 ps once again (c).

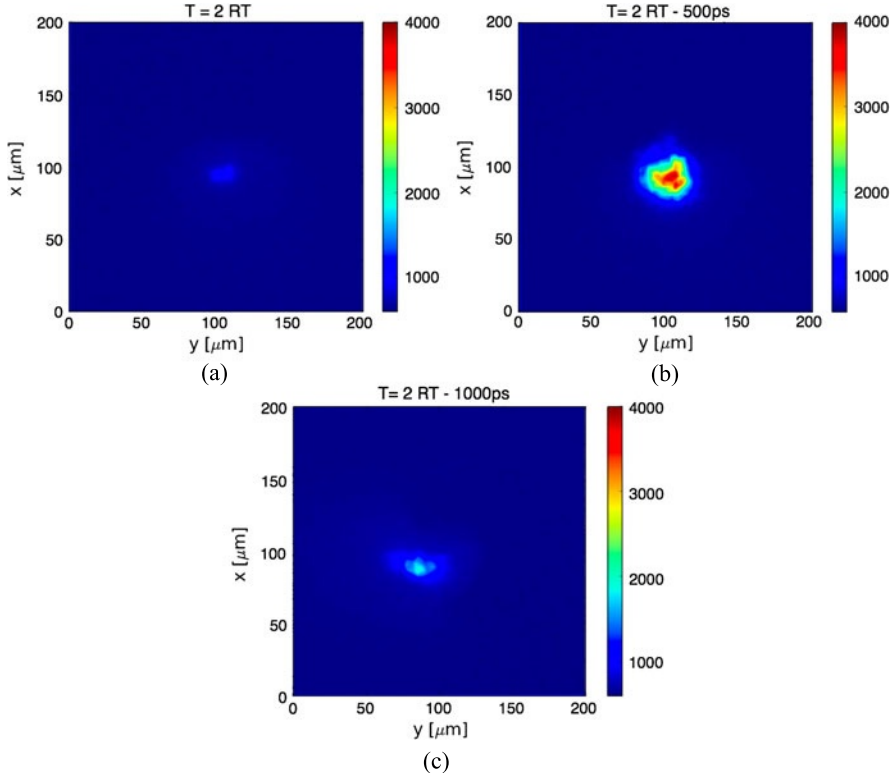


Fig. 6 Integrated SXRL near field profile measured with a 16 bits XUV CCD camera for different fine delays corresponding to the prepulse intensities of Fig. 5 in the configuration corresponding to 2 supplementary round trips in the RGA. (a) Very low prepulse intensity (0.5 % MP). (b) Average prepulse intensity (2 % MP). (c) High prepulse intensity (4 % MP)

Figure 6 shows near field SXRL measurements made for the best ASE configuration described previously (RGA tuned with 2 supplementary round trips with respect to nominal extraction) for the three fine delays of 0.500 ps and 1 ns corresponding to the prepulse levels of Fig. 5. This figure evidences a strong energy enhancement with the presence of an average prepulse (Fig. 5(b)) by comparison with the cases of no (Fig. 5(a)) or intense (Fig. 5(c)) prepulse.

4 Conclusion and Future Work

This empirical approach confirms that SXRL efficiency strongly depends on the pump laser temporal structures in the ten's of nanosecond range. In this paper, we saw that RGA cavity tuning allows control on both ASE level and a picosecond prepulse intensity. By modifying these parameters, we observed an improvement of the SXRL efficiency and a better target lifetime. Interpretations are still in discussion,

but we could reasonably suppose that the small prepulse creates a low preionized plasma in front of the solid target which could increase the main plasma creation and/or its characteristics by the long pulse then increasing the coupling efficiency with the short pump pulse. The ASE role is also discussed, but it could act, like the small prepulse, to prepare the target surface for a better interaction with DGRIP pulses. All these suppositions are yet under theoretical investigation. We are now installing a new system allowing to better control stability of the small prepulse and will soon reproduce these experiments.

In the same frame, we will study a new pumping configuration in which an external Nd:YAG nanosecond laser pulse, synchronized with the CPA laser chain, will be used to produce cold expanded plasma before the main interaction. The advantage of this method would be to keep the possibility to tailor the prepulse structure for SXRL optimization without degrading the contrast of the main laser driver. This configuration would be attractive if an experiment requires a high contrast pump irradiating a sample that is later probed by the SXRL.

References

1. Habib, J., et al.: Opt. Express **20**(9), 10128–10137 (2012)
2. Zimmer, D., et al.: Opt. Lett. **35**(4), 450–452 (2010)
3. Keanan, R., et al.: Phys. Rev. Lett. **94** (2005)
4. Martinez, O.E., et al.: IEEE J. Quantum Electron. **23**, 8 (1987)
5. Janulewicz, K.A., et al.: Phys. Rev. E **82**, 5 (2010)
6. Kim, H.T., et al.: Phys. Rev. A **77**, 2 (2008)
7. Janulewicz, K.A., et al.: Phys. Rev. A **68**, 5 (2003)

Chapter 16

X-Ray Laser Developments at PHELIX

B. Ecker, B. Aurand, D.C. Hochhaus, P. Neumayer, B. Zielbauer, K. Cassou, S. Daboussi, O. Guilbaud, S. Kazamias, T.T.T. Le, E. Oliva, L. Li, H. Zhao, Q. Jin, D. Ros, P. Zeitoun, and T. Kuehl

Abstract We present results of two experimental campaigns dedicated to improve the performance of our Mo XRL source. A first beamtime was dedicated to study the XRL output when the target is pumped with three collinear pulses. The results show that the first pulse can be used to improve the spatial profile of the XRL beam. The second project focused on an injection-seeding experiment utilizing a double-stage XRL setup. Here we were able to characterize the amplifier medium by a temporally resolved measurement of the size of the gain zone. The amplified XRL beam exhibited an increased beam quality of almost two orders of magnitude in brilliance.

B. Ecker · B. Zielbauer
Helmholtz Institute Jena, Helmholtzweg 4, 07743, Jena, Germany

B. Ecker · B. Aurand · T. Kuehl
Johannes-Gutenberg Universität Mainz, Saarstr. 21, 55122, Mainz, Germany

B. Aurand · D.C. Hochhaus · P. Neumayer
ExtreMe Matter Institute EMMI, Planckstr. 1, 64291, Darmstadt, Germany

B. Aurand · B. Zielbauer (✉) · T. Kuehl
GSI Helmholtzzentrum fuer Schwerionenforschung, Planckstr. 1, 64291, Darmstadt, Germany
e-mail: b.zielbauer@gsi.de

K. Cassou · S. Daboussi · O. Guilbaud · S. Kazamias · D. Ros
LASERIX-CLUPS, Université Paris-Sud 11, 91400, Orsay, France

T.T.T. Le · E. Oliva · L. Li · P. Zeitoun
Laboratoire d'Optique Appliquée, 91761 Palaiseau cedex, France

D.C. Hochhaus
Goethe-Universität Frankfurt, 60438 Frankfurt, Germany

H. Zhao · Q. Jin
Institute of Modern Physics, Chinese Academy of Sciences, 73000 Lanzhou, People's Republic of China

1 Motivation

The main motivation for X-ray laser (XRL) research at GSI is to perform spectroscopy experiments on highly-charged heavy-ions stored in the experimental storage ring (ESR) of the GSI accelerator facility. The first experiment of this kind will aim at measuring the $2s_{1/2} - 2p_{1/2}$ transition in Li-like ions. For ions of an atomic number between 50 (Sn) and 92 (U), this transition energy lies between 100 eV and 300 eV [1], which corresponds to wavelengths between 12 nm and 4 nm. Setting up the experiment in a way, that the XRL is counter propagating to the ion bunch, one can exploit the relativistic Doppler effect. This way, the XRL wavelength as seen by the ion bunch will be blue-shifted according to $\lambda' = \lambda \cdot \sqrt{\frac{1-\beta}{1+\beta}}$. Here λ' and λ denote the Doppler-shifted and original wavelength of the XRL, respectively. The velocity β of the ion bunch stored in the ESR can be as high as 0.7. For a Mo XRL of 18.9 nm, changing the ion velocity between 0.4 and 0.7 will correspond to Doppler-shifted wavelengths between 12 nm and 8 nm. This will be sufficient to excite the $2s_{1/2} - 2p_{1/2}$ transition in ions of atomic numbers up to 67 (Li-like Ho). In addition, adjusting the velocity of the ion bunch allows for tuning the otherwise fixed XRL wavelength to resonance with the ionic transition. The precise measurement of this transition energy in high-Z ions will provide a valuable benchmark for QED theories, which aim at modeling the complex electromagnetic interactions within such few-electron systems.

In order to support the spectroscopy experiments with the most suitable XRL source, a number of preparations and developments are required. The XRL pulse energy for this experiment has been estimated to at least 1 μJ . In addition, the XRL beam quality is of concern, since the XRL pulse needs to propagate over approximately ten meters, ensuring good spatial overlap with the ion beam at the same time. Due to radiation safety measures, access to the ESR area during the experiment will not be possible without a significant loss of time. Thus, the complete XRL setup needs to be remote-controlled and support hours of stable XRL operation.

To address these issues, we pursued two different approaches. In a first experimental campaign, we performed multi-parameter scans in order to optimize our conventional Mo XRL source, especially in terms of output energy. Within this context, we examined the influence of a third pumping pulse, which is applied to the target before the conventional double-pulse. This technique has already been studied both theoretically [2] and experimentally. The third pulse has proven to have a significant impact on the minimum pumping energy required for XRL operation [3, 4], on target lifetime [5] and on the size of the gain zone [6].

Our second approach aimed at operating two Mo XRL targets in a seed-amplifier configuration. It has been demonstrated in former experiments that such a setup allows for a significant increase in beam quality [7–9]. In our opinion, this approach is an interesting alternative to high-order harmonic (HH) seeding, where the pulse duration of the seed (usually few tens of fs) is significantly smaller compared to the lifetime of the gain within the amplifier medium (few ps). Several groups already succeeded in demonstrating the amplification of a HH seed in various XRL media [10–14]. However, the spectral and especially the temporal mismatch of the HH seed

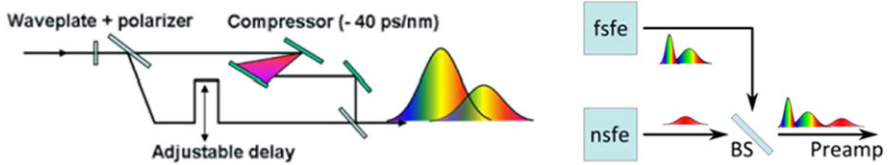


Fig. 1 Left side: Sketch of the Mach-Zehnder interferometer creating the double-pulse. Right side: The combination of both frontends using a beam splitter (BS) leads to three collinear pulses

might ultimately cause constraints in efficiently extracting the energy stored in the amplifying XRL medium [15]. In this paper, we present the results of both beam-times dedicated to the optimization and characterization of our Mo XRL source.

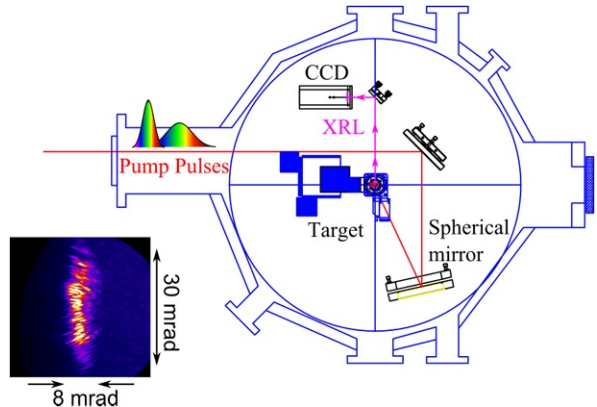
2 The PHELIX Preamplifier System

The PHELIX laser system provides two independent frontends delivering pulses of either nanosecond duration (ns-frontend) or femtosecond duration (fs-frontend). The fs-frontend is based on chirped pulse amplification (CPA). The original ~ 100 fs pulses delivered by the master oscillator are stretched to several nanoseconds before being injected in two consecutive regenerative amplifiers. The fs-frontend delivers pulses of up to 20 mJ at a repetition rate of 10 Hz. Between the stretcher and the first amplifier, a Mach-Zehnder interferometer allows for the creation of a double-pulse structure (left side of Fig. 1). The energy ratio of the two pulses can be varied continuously by use of a wave plate and a polarizer and the timing between the two pulses can be adjusted between 0 ns and 2 ns by a delay stage. One of the two arms of the interferometer provides a pulse compressor, which enables setting up different pulse durations after the final compression stage of the CPA chain.

Due to an upgrade of the timing system of the PHELIX laser within the last year, it is now possible to combine this double-pulse with a third pulse created by the ns-frontend. This delivers ~ 20 mJ pulses at a repetition rate of 0.5 Hz, while the pulse duration can be varied between 1.5 ns and more than 15 ns. This allows for setting up a series of three collinear pulses with variable energy ratios and delays (right side of Fig. 1).

The pulse series is injected into the preamplifier section, providing a total energy of up to 5 J at a repetition rate of one shot in two minutes. Within the preamplifier, a serrated aperture is used to define the size as well as the geometrical shape of the beam. Besides circular beams of various diameters, one can choose an aperture that provides two vertically separated, square beams. This double-beam option, originally intended to support pump-probe experiments, has been used for the double-stage XRL experiment. The experimental results presented in this paper have been performed in the X-ray laboratory of the PHELIX facility. It comprises the final pulse compressor as well as the target chamber. More information on the complete PHELIX system, including the main amplifier and the Petawatt target area, can be found in [16].

Fig. 2 XRL setup utilizing the DGRIP technique. The inset shows a XRL footprint obtained with the optimized parameters: 25 %–75 % energy ratio; delay 250 ps; main pulse duration 3 ps



3 DGRIP Mo XRL Performance

In order to optimize the output of our conventional double-pulse grazing incidence (DGRIP, [17, 18]) Mo XRL source, we performed scans of the most important pump parameters. The simple experimental configuration is shown in Fig. 2. The collinear double-pulse is focused on the target by a spherical mirror. The XRL output is detected by a footprint camera positioned 40 cm away from the target. A flat 45° XUV mirror was used both to align the XRL output on the CCD and to suppress the background of the plasma emission. In addition, Al filters of various thicknesses have been employed.

Two delay scans have been performed for energy ratios of 25 %–75 % and 50 %–50 % (prepulse–main pulse), varying the delay between 150 ps and 500 ps in steps of 50 ps or even 25 ps. For the optimum energy ratio of 25 %–75 % and 250 ps delay, we performed a main pulse duration scan between 2 ps and 5 ps, finding the highest XRL pulse energy at 3 ps. Five consecutive shots have been recorded for each set of parameters at a repetition rate of one shot every two minutes.

The target was irradiated by a total pump energy of 600 mJ, which was focused to a line of 6 mm length and 70 μm width under a GRIP angle of 25°. The pulse durations of 200 ps and 3 ps and the energy ratio of 25 %–75 %, lead to intensities of $3 \times 10^{11} \text{ W/cm}^2$ and $6 \times 10^{13} \text{ W/cm}^2$ for the prepulse and main pulse, respectively. The obtained pulse energies of the XRL output were in the order of several hundreds of nanojoules, corresponding to conversion efficiencies slightly below 10^{-6} . This pulse energy is not sufficient to support the ESR spectroscopy experiment. However, a gain length measurement series showed that the XRL has not been saturated. Setting up the experiment with a line focus length larger than 6 mm may thus allow for achieving higher XRL pulse energies, especially considering that the PHELIX preamplifier was not yet operated at its maximum energy output. Another concern is the non-ideal beam quality of the XRL source. Its divergence in the direction away from the target added up to 8 mrad. In the other direction, the XRL exhibited a significantly larger divergence of 30 mrad. This aspect ratio does not al-

low for an efficient spatial overlap with the ion beam. This issue has been addressed by applying the third pumping pulse.

4 Triple-Pulse Pumping

As described in Sect. 2, the additional pulse of the ns-frontend is combined with the double-pulse before the preamplifier section, to form a series of three collinear pulses. Thus, no change of the setup as depicted in Fig. 2 was necessary for switching from double-pulse pumping (DGRIP) to triple-pulse pumping (TGRIP). Since the two frontends are temporally synchronized, the delay between the double-pulse and the third pulse could easily be varied by use of a Stanford delay generator. In the following, this delay is defined as the time between the maximum of the early third pulse and the maximum of the main pulse.

Starting with the optimized DGRIP parameters concerning the double-pulse, we performed several scans with different durations (1.5 ns, 3 ns and 5 ns) and energies (250 mJ and 500 mJ) of the third pulse. For each energy and pulse duration setting, we varied the delay of the third pulse from 7.5 ns to 0.5 ns in steps of 1 ns. Afterwards, the delay between the double-pulse was varied from the original 250 ps to 500 ps and 700 ps, performing another set of third-pulse delay scans. Again, five consecutive shots for each parameter setting have been measured to increase the quality of the data.

In terms of XRL pulse energy, the optimum conditions were found with the original double-pulse optimized in DGRIP and a 1.5 ns long third pulse of 500 mJ, which resulted in an intensity of $1 \times 10^{11} \text{ W/cm}^2$. The optimum delay of this pulse was confined to a time window between 2 ns and 3 ns. For larger delays (corresponding to an earlier arrival of the third pulse), the XRL output was significantly suppressed. With a delay of 2 ns or 3 ns, the third pulse affected the shape of the XRL output, leading to a symmetric XRL footprint with a divergence of 15 mrad in both directions. The energy of the TGRIP XRL was in the same order of magnitude than the original XRL pulses pumped with two pulses. However, the change in the aspect ratio of the XRL pulse is of interest for the ESR spectroscopy experiments, as it allows for a good spatial overlap between the XRL pulse and the ion beam. For delays smaller than 2 ns we observed the transition back to the original footprint patterns known from the DGRIP scheme.

5 The Double-Stage Mo XRL Experiment

The double-stage XRL experiment has been carried out using the Butterfly configuration [19]. As depicted in Fig. 3(a), it is based on two XRL media that are pumped in the DGRIP scheme, providing both XRL targets with TW excitation. Additionally, DGRIP allows for a very compact and simple injection-seeding setup relying only on two beams and one target. The seed XRL is injected into the amplifying

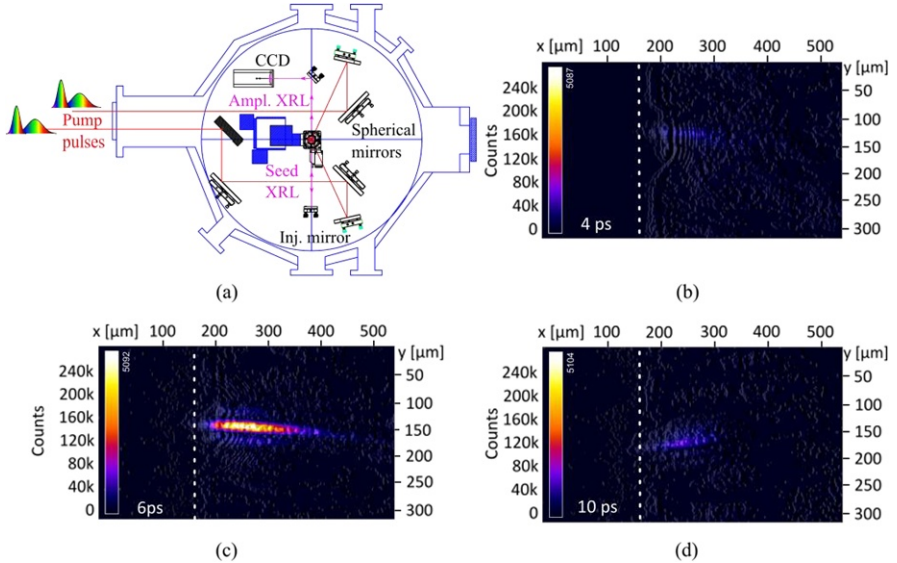


Fig. 3 (a): Sketch of the Butterfly setup. (b-d): Signal of the amplified seed for different delays between the seed and amplifier heating pulse. The *white dashed lines* indicate the target surface

medium by a spherical XUV mirror. A 45° XUV mirror is then used to align the amplified seed to the footprint camera.

The beams are created using the PHELIX double-beam option described in Sect. 2. Each of the beams is carrying an identical double-pulse structure and is focused onto the same Mo slab target under a GRIP angle of 25° , vertically separated by a few millimeters. The size of the line focus providing the seed (amplifier) was $5 \text{ mm} \times 90 \mu\text{m}$ ($2.5 \text{ mm} \times 220 \mu\text{m}$). The pump energy was 300 mJ for each beam, which resulted in an intensity of $8 \times 10^{10} \text{ W/cm}^2$ (prepulse) and $2 \times 10^{13} \text{ W/cm}^2$ (main pulse) for the seed XRL. The amplifier target was irradiated with $7 \times 10^{10} \text{ W/cm}^2$ (prepulse) and $1 \times 10^{13} \text{ W/cm}^2$ (main pulse). The injection mirror had a focal length of 120 mm and was positioned 275 mm away from the target. The resulting spatial coupling of the seed XRL into the amplifier medium was 2 %.

The timing between the two IR beams has been adjusted by a fast rise-time photo diode and a 12 GHz oscilloscope. This method allowed for synchronizing the main pulses of each IR beam within an accuracy of $\pm 15 \text{ ps}$, which is much larger than the lifetime of the gain and the XRL pulse duration. The absolute timing between the two beams is therefore not defined. Only the relative delay, which is set by a motorized delay stage positioned outside the target chamber and provides sub-picosecond resolution, can be interpreted. In order to achieve a simultaneous arrival of the seed XRL and the IR main pulse at the amplifier target, the delay of the two IR main pulses has been set to 1835 ps , corresponding to $2 \times 275 \text{ mm}/c$. This will be referred to as a delay of 0 ps . However, due to the large uncertainty of the synchronization method, this absolute value of the delay is not significant. The

optimum timing had to be found by scanning the delay of the IR main pulses within the 30 ps window. In the following, smaller delays correspond to an earlier arrival time of the seed at the amplifier and vice versa.

Figure 3(b)–(d) depict three exemplary results of a timing scan. The complete measurement series comprises a time window of 12 ps, scanned with 1 ps steps. The data shows the temporal development of the amplifier medium, in terms of size, distance to the target and magnitude of the gain. The scale in Fig. 3(b)–(d) corresponds to the exit plane of the target and has been calibrated using a 50 μm wire attached to the target. In addition to the determination of the lifetime of the gain of the Ni-like Mo XRL to 4 ps FWHM, these results could provide valuable input for hydro simulations. The data obtained at 6 ps (Fig. 3(c)) shows the maximum size of the gain zone, extending more than 200 μm in the direction away from the target. In the perpendicular direction, the size of the gain medium does not vary for different delays and amounts to 25 μm , which is significantly smaller than the width of the line focus (220 μm). This could indicate that the intensity of the IR pulses was not large enough to create a population inversion in the complete amplifier plasma.

The energy of the amplified pulse added up to 90 nJ, which is comparable to the 140 nJ of the seed pulse. The divergence of the amplified beam was 4 mrad \times 0.5 mrad, which is significantly improved compared to the 8 mrad \times 30 mrad of the single XRL-target setup. Hence, the amplification process helped to increase the brilliance of the source by a factor of 80.

6 Conclusions and Outlook

Performing detailed multi-parameter scans, we optimized our single-target Mo XRL source pumped in DGRIP. Adding a third pulse of nanosecond duration before the original double-pulse did not lead to an increase in photon numbers. However, it was possible to improve the quality of the XRL beam with respect to its aspect ratio. This is of interest for the ESR spectroscopy experiments, where a good spatial overlap of the XRL and the ion beam is required.

In addition, we carried out an injection-seeding experiment using the Butterfly configuration. The data allowed for following the temporal development of the gain in terms of its geometrical size, lifetime and magnitude. The amplified XRL exhibited a brilliance 80 times larger compared to the single-target geometry. Further experiments of this kind will aim at determining saturation effects, increasing the spatial coupling efficiency and measuring the spatial coherence of the amplified XRL beam.

References

1. Kim, Y.-K., et al.: Phys. Rev. A **44**, 148 (1991)
2. Janulewicz, K.A., Kim, C.M.: Phys. Rev. E **82**, 056405 (2010)

3. Balmer, J., et al.: In: Sebban, S., et al. (eds.) X-Ray Lasers 2012. Springer Proceedings in Physics, vol. 147. Springer, Cham (2013). Chapter 5 in this book
4. Ursescu, D., et al.: Ag X-ray laser pumped with one long and two short pulses
5. Habib, J., et al.: Opt. Express **20**, 10128–10137 (2012)
6. Cassou, K., et al.: Opt. Lett. **32**, 139–141 (2007)
7. Sebban, S., et al.: Phys. Rev. A **61** (2000)
8. Nishikino, M., et al.: Phys. Rev. A **68**, 1–4 (2003)
9. Tanaka, M., et al.: Opt. Lett. **28**, 1680–1682 (2003)
10. Ditmire, T., et al.: Phys. Rev. A **51**, 6 (1995)
11. Zeitoun, Ph., et al.: Nature **431** (2004)
12. Hasegawa, N., et al.: Phys. Rev. A **76** (2007)
13. Mocek, T., et al.: Phys. Rev. Lett. **95**, 19–22 (2005)
14. Wang, Y., et al.: Nat. Photonics **2**, 94–98 (2008)
15. Zeitoun, P., et al.: Time-dependent Bloch-Maxwell modelling of high harmonic seeding in gas and solid amplifier
16. Bagnoud, V., et al.: Appl. Phys. B **100**, 1 (2010)
17. Zimmer, D., et al.: Opt. Express **13**, 2403 (2008)
18. Ros, D., et al.: Nucl. Instrum. Methods Phys. Res., Sect. A **653**(1), 76–79 (2011)
19. Ecker, B., et al.: In: Proc. SPIE, vol. 8140 (2011). doi:[10.1117/12.897277](https://doi.org/10.1117/12.897277)

Chapter 17

Parabolic Equation and Exact Transparent Boundary Conditions in X-Ray Optics—Application to Waveguides and Whispering Gallery Optics

R.M. Feshchenko and A.V. Popov

Abstract In this paper we report a novel transparent boundary (TBC) condition for the 2D parabolic wave equation in which the dielectric constant is linearly dependent on the transversal coordinate. The proposed condition does not involve special functions and can be a basis for an efficient finite difference approximation.

1 Introduction

Leontovich and Fock introduced the parabolic wave equation (PWE, also known as the Fresnel equation) as applied to radio wave propagation more than half a century ago [1]. It was widely used in oceanic acoustics for modeling sound wave propagation [2, 3]. Further applications have been found in optics, including X-ray and EUV spectral band [4] where it is used to describe the propagation of weakly divergent light beams in inhomogeneous media. However any numerical solution of PWE, for instance by finite difference approximation, requires appropriate truncation conditions as realistic computational domains must be necessarily finite, while the original wave field is sought in the whole space.

In this paper we will be only concerned with the linear 2D parabolic wave equation having the following form:

$$2ik \frac{\partial u}{\partial z} + \frac{\partial^2 u}{\partial x^2} + k^2 \alpha(x, z)u = 0, \quad \alpha(x, z) = \alpha_0(x, z) + axg(z), \quad (1)$$

where x and z are, respectively, longitudinal and transversal coordinates, a is a parameter and $g(z)$ is a real function, $k = 2\pi/\lambda$ is the wave number and $\alpha_0(x, z)$ is a finite arbitrary function. Equation (1) describes, for instance, the propagation of light in a weakly bent X-ray waveguide or optical fiber in a curvilinear system

R.M. Feshchenko (✉)
P.N. Lebedev Physical Institute of RAS, Moscow, Russia
e-mail: rusl@sci.lebedev.ru

A.V. Popov
Pushkov Institute of Terrestrial Magnetism, Ionosphere and Radiowave Propagation, Troitsk,
Russia

of coordinates. Function $\alpha(x, z)$ in this case is a sum of a true dielectric constant $\alpha_0(x, z)$, which, for simplicity, is supposed to vanish at the boundary of the computational domain and beyond it, and an additional linear term resulting from bending and proportional to the curvature $g(z)$.

There are two main types of boundary conditions for parabolic equation (1): transparent boundary conditions (TBCs) [5, 6], and perfectly matched layer (PML) conditions [7]. The TBCs are generally non-local Neumann-to-Dirichlet or Dirichlet-to-Neumann mappings relating the wave field boundary values with its first derivative by x , whereas PMLs are local.

In the case of standard 2D parabolic wave equation in free space ($\alpha = 0$), the TBC now is known for more than 20 years as Baskakov-Popov-Papadakis (BPP) condition [3, 5–8]. A TBC for Eq. (1) with $g(z) = 1$ has been known for a long time as well [6]. However, involving integration of a ratio of Airy functions to obtain the kernel, it is rather complicated and difficult for numerical implementation [9].

In this paper we contrive to obtain a much simpler TBC for the 2D parabolic equation (1) with a linear potential, which does not involve special functions and additional integration, having a kernel explicitly expressed via elementary functions. We also try to preserve as much generality as possible by considering the case when the curvature $g(z)$ is an arbitrary function.

2 Transparent Boundary Condition

Let us consider the parabolic wave equation (1) where function $\alpha_0 = 0$. It can be transformed by introducing a new variable $\varphi(x, z)$:

$$u(x, z) = \varphi(x, z) \exp \left[i \frac{kax}{2} G(z) - i \frac{ka^2}{8} \int_0^z G^2(\xi) d\xi \right], \quad G(z) = \int_0^z g(\xi) d\xi. \quad (2)$$

By substituting (2) into (1) one obtains an equivalent equation for the function φ :

$$2ik \frac{\partial \varphi}{\partial z} + \frac{\partial^2 \varphi}{\partial x^2} + ikaG(z) \frac{\partial \varphi}{\partial x} = 0. \quad (3)$$

The advantage of this equation is independence of its coefficients of x , which allows us to obtain a transparent boundary condition by applying Laplace transform by this variable, which yields

$$\frac{\partial F}{\partial z} = \left[\frac{iw^2}{2k} - \frac{aw}{2} G(z) \right] F - \left[\frac{iw}{2k} - \frac{a}{2} G(z) \right] \varphi_0(z) - \frac{i}{2k} \varphi'_0(z), \quad (4)$$

where $\varphi_0(z) = \varphi(0, z)$, $\varphi'_0(z) = \varphi'_x(0, z)$, w is Laplace variable and $F = F(w, z)$ is the Laplace transform of φ .

We shall assume that the initial wave field $u(x, 0) = 0$ for $x > 0$ —the sources of the wave field are located where $x < 0$. This means that $F(w, 0) = 0$ as well. Now the unique solution of (4) can be written as

$$F = - \int_0^z \exp\left[\frac{iw^2}{2k}(z-\xi) - \frac{aw}{2} \int_\xi^z G(\mu) d\mu\right] \\ \times \left\{ \left(\frac{iw}{2k} - \frac{a}{2} G(\xi) \right) \varphi_0(\xi) + \frac{i}{2k} \varphi'_0(\xi) \right\} d\xi. \quad (5)$$

Applying the inverse Laplace transform to (5) and substituting in (2) we write down the following two equivalent TBCs:

$$u(x_0, z) = -\frac{1}{\pi\sigma} \int_0^z \exp[i\Phi(z, \xi)] \frac{u'_x(x_0, \xi)}{\sqrt{z-\xi}} d\xi \\ + \frac{ik}{2\pi\sigma} \int_0^z \exp[i\Phi(z, \xi)] \frac{u(x_0, \xi)(\bar{G} - G(\xi))}{\sqrt{z-\xi}} d\xi, \quad (6)$$

$$u'_x(x_0, z) + \frac{\sigma a}{4} \int_0^z \exp[i\Phi(z, \xi)] \frac{u'_x(x_0, \xi)(\bar{G} - G(z))}{\sqrt{z-\xi}} d\xi \\ = -\sigma \frac{\partial}{\partial z} \int_0^z \exp[i\Phi(z, \xi)] \frac{u(x_0, \xi)}{\sqrt{z-\xi}} d\xi \\ + \frac{i\sigma ka^2}{8} \int_0^z \exp[i\Phi(z, \xi)] \frac{u(x_0, \xi)G(z, \xi)(\bar{G} - G(z))}{\sqrt{z-\xi}} d\xi \\ + \frac{i\sigma kax_0}{2} g(z) \int_0^z \exp[i\Phi(z, \xi)] \frac{u(x_0, \xi)}{\sqrt{z-\xi}} d\xi, \quad (7)$$

where

$$\Phi(z, \xi) = \frac{kax_0}{2} G(z, \xi) - \frac{ka^2}{8} (z-\xi)[\langle G^2 \rangle - \bar{G}^2], \quad G(z, \xi) = \int_\xi^z g(\tau) d\tau, \quad (8)$$

$$\bar{G} = \frac{1}{z-\xi} \int_\xi^z G(\tau) d\tau, \quad \langle G^2 \rangle = \frac{1}{z-\xi} \int_\xi^z G^2(\tau) d\tau, \quad \sigma = \sqrt{\frac{2k}{\pi i}}. \quad (9)$$

In a waveguide with a constant curvature $g(z) = 1$ we have: $G(z) = z$, $\bar{G} = (z+\xi)/2$, $\langle G^2 \rangle = (z^2 + z\xi + \xi^2)/3$ and $\langle G^2 \rangle - \bar{G}^2 = (z-\xi)^2/12$. After substituting these expressions into (6) and (7) we obtain boundary conditions having the form of convolutions. In the particular case $a = 0$, they are reduced to the ordinary BPP conditions (see [5]).

3 Conclusion

A novel TBC for the parabolic wave equation with a linear dependence of the dielectric susceptibility on the transversal coordinate x and an arbitrary dependence on the longitudinal coordinate z is obtained. It is different from the previously known [6] transparent condition for the constant linear potential. The latter has a kernel that is a complex integral of the logarithmic derivative of an Airy function that can not be expressed through elementary functions. In contrast, the kernels of all integrals in the TBC proposed here are elementary. Even more important is the applicability

of this new TBC to the case of variable curvature of the artificial boundary, including possible change of sign. That fact makes it very promising for the simulation of realistic bent X-ray waveguides and optical fibers.

Acknowledgements This work was supported in part by the basic research program of Russian Academy of Sciences “Femtosecond optics and new optical materials” (subprogram “New optical materials”), and by the Russian Foundation for Basic Research (RFBR) grant No. 10-02-00991-a.

References

1. Fock, V.A.: Electromagnetic Diffraction and Propagation Problems. Pergamon, Tarrytown (1965)
2. Tappert, F.D.: The parabolic approximation method. In: Keller, J.B., Papadakis, J.S. (eds.) Wave Propagation and Underwater Acoustics. Lecture Notes in Physics, vol. 70, pp. 224–287 (1977)
3. Papadakis, J.S.: Exact nonreflecting boundary conditions for parabolic type approximations in underwater acoustics. *J. Comput. Acoust.* **2**, 83–98 (1994)
4. Attwood, D.: Soft X-rays and Extreme Ultraviolet Radiation. Cambridge University Press, Cambridge (1999)
5. Baskakov, V.A., Popov, A.V.: Implementation of transparent boundaries for numerical solution of the Schrodinger equation. *Wave Motion* **14**, 123–128 (1991)
6. Popov, A.V.: Accurate modelling of transparent boundaries in quasi-optics. *Radio Sci.* **31**, 1781–1790 (1996)
7. Berenger, J.: A perfectly matched layer for the absorption of electromagnetic waves. *J. Comput. Phys.* **114**, 185–200 (1994)
8. Yevick, D., Friese, T., Schmidt, F.: A comparison of transparent boundary conditions for the Fresnel equation. *J. Comput. Phys.* **168**, 433–444 (2001)
9. Ehrhardt, M., Mickens, R.E.: Solutions to the discrete Airy equation: application to parabolic equation calculations. *J. Comput. Phys.* **72**, 183–206 (2004)

Chapter 18

Harmonic Generation and Soft-X-Ray Laser with LASERIX: Source Development, Applications and Advanced Diagnosis

Olivier Guilbaud, Sophie Kazamias, Kevin Cassou, Moana Pittman, Sameh Daboussi, Olivier Delmas, Julien Demailly, Olivier Neveu, Chris Pouhe, Boris Vodungbo, Philippe Zeitoun, Lucy Wilson, Greg Tallents, Antonin Dusseix, Gabriel Richet, Aurelie Gense, Bich-Lien Nghiem, Brigitte Cros, Gilles Maynard, and David Ros

Abstract The LASERIX facility has restarted operation in the middle of the year 2010. Since then, important work has been achieved on the XUV sources performance, reliability and stability, which lead to the construction of two beamlines. The first one is based on transient collisional soft X-ray laser. In the second one, the high order harmonic generation process is used to convert infrared laser into coherent XUV radiations. Characteristics and some recent works on both of them will be presented. Besides, a complete setup for pump-probe experiments has been developed and successfully tested. Some examples involving this device and dealing with plasma opacity, radiobiology and nanomagnetism will be presented. We will conclude this paper by a discussion on how application experiments can be turned into valuable diagnostics for XUV sources.

O. Guilbaud (✉) · S. Kazamias · K. Cassou · S. Daboussi · O. Delmas · J. Demailly · O. Neveu · C. Pouhe · A. Dusseix · G. Richet · A. Gense · B.-L. Nghiem · B. Cros · G. Maynard · D. Ros
Laboratoire de Physique des Gaz et Plasma, CNRS-Université Paris Sud, Orsay, France
e-mail: olivier.guilbaud@u-psud.fr

M. Pittman · D. Ros
Centre Laser de l'Université Paris-Sud, Université Paris-Sud, Orsay, France

O. Delmas
Amplitude Technologies, Evry, France

B. Vodungbo · P. Zeitoun
Laboratoire d'Optique Appliquée, ENSTA ParisTech – CNRS – École Polytechnique, Palaiseau, France

L. Wilson · G. Tallents
University of York, York, UK

1 Introduction

As demonstrated by the papers presented during this conference, laser-based soft X-ray sources have now reached a sufficient level of maturity to be considered as valuable and available scientific tools for a large user community. XUV sources are sophisticated systems encompassing both the laser driver, the conditioning optics, the conversion medium, and specific XUV optics. In the Laserix facility two laser-based XUV sources are now in operation: a soft X-ray laser beamline and a high order harmonics beamline. We will briefly present these two devices, not only including some fundamental aspect of the wavelength conversion but also the technical developments on the laser driver and optical systems to achieve higher control on these sources. One particular feature of laser-based sources is their natural synchronization with the infrared laser. They are therefore highly interesting for pump-probe experiments and we will therefore give an overview of activities on this subject with Laserix. Due to their spectral range, specific tools are required to characterise the radiation properties of these sources. Among them, the temporal characterisation is one of the most challenging. As a prospect we will discuss the opportunity of using some ultrafast phenomena as a tool for soft X-ray laser temporal profile reconstruction.

2 Laserix Present Status

All the laser-based XUV sources of the facility are driven by the same high power laser chain. This system is a commercial Titanium-Sapphire laser delivering 800 nm pulses at 10 Hz repetition rate and that can be recompressed to duration as short as 35 fs (confirmed from SPIDER measurements). In a recent laser upgrade, KDP doubling crystals of the Nd-YAG pumping lasers have been replaced by LBO crystals leading to an increase of doubling efficiency and of the output energy before compression from 2 J to 3 J. This change leads also to a significant reduction of warming time and to a global improvement of the laser beam profile. Addition of remote monitoring and control of the laser beam at critical points of the laser chain enables a faster laser preparation. A schematic of the beamline is presented in Fig. 1. The laser output energy is separated into two main beams, with an adjustable energy balance. The first part is directly compressed under vacuum into a picosecond pulse and is used for TCE soft X-ray laser plasma pumping. The second beam can be used directly in order to get a high energy uncompressed (500 ps) pulse, mainly to form the plasma of the TCE soft X-ray laser. A variable part of this uncompressed beam can be sent into an auxiliary compressor and redirected in the high order harmonic beamline or as an auxiliary beam for pump-probe experiments. The harmonic beamline and the soft X-ray laser beamline are in a large extend independent but can also be used together in a same experiment. Since 2009, the Laserix facility provides XUV beamtime for users interested in soft X-ray sources development or in their use for application experiments. As a member of the European Laserlab network, Laserix shall provide four weeks every years of dedicated European beamtime.

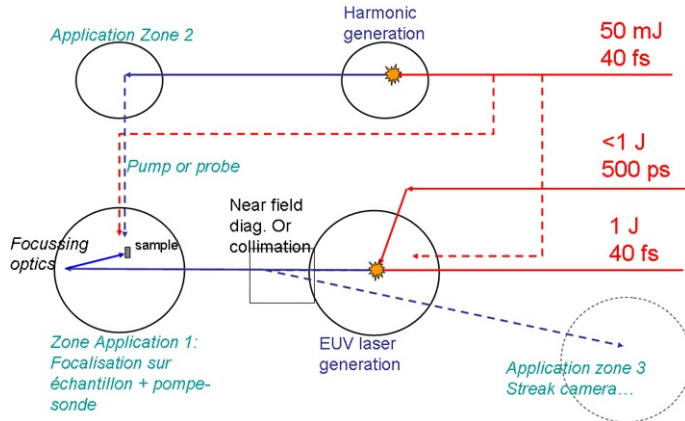


Fig. 1 General view of the XUV beamlines and their possible combinations

3 The Soft X-Ray Laser Beamline

The soft X-ray laser beamline requires most of the infrared laser energy. The soft X-ray laser source relies on the Transient Collisional Excitation (TCE) scheme [1] implemented in a GRIP (Grazing Incidence Pumping) irradiation geometry [2]. In the nominal configuration, the preforming long pulse is focused by a combination of cylindrical lenses in normal incidence compared to the target plane. The short (picosecond) pumping pulse is line-focused on the target by an off-axis spherical mirror with a grazing angle of 17 to 23 degrees on target. The delay between the long and short pulses can be adjusted with a delay line. Efficient lasing has been achieved with Ni-like Molybdenum (18.9 nm) and Ni-like Silver (13.9 nm). However, it has been observed that this scheme is sensitive to beam pointing instability which leads to an unperfect overlap of the two line-foci when the pointing is drifting. Recently a variant of the GRIP scheme has been proposed to overcome this drawback [3, 4]. In the DGRIP configuration, only the beam travelling through the compressor and focused by the spherical mirror is used and supports both long and short pulses. This train of pulses is synthesized between the stretcher and the regenerative amplifier cavity by a Mach-Zendher type device, with adjustable delay and energy balance. A Martinez Stretcher installed in one of the arms of the Mach-Zendher adds an extra chirp to the corresponding pulse. When recompressed by the final compressor, this pulse has a duration of 200 ps and will act as the long pulse of TCE X-ray laser. Beam pointing differences between the two pulses are strongly reduced by the regenerative amplifier cavity leading to an always perfect overlap of the two line-foci on target. Successful operation with Molybdenum, Silver and Ne-like Titanium (32.6 nm) have been achieved. The implementation of low energy prepulses prior to the two main pulses is known to improve the soft X-ray laser output. This has been checked in the case of DGRIP configuration. Moreover, these prepulses also lead to a significant extend of the time a soft X-ray laser can be generated from a same target position [5]. This property is useful for experiments requiring high

photon exposure [4, 6]. Since the last SPIE conference, we have worked on different ways to introduce these prepulses in the DGRIP configuration by playing on the regenerative amplifier properties. Two parameters can be easily modified and lead to dramatic changes: (i) the number of additional round-trip in the regenerative amplifier compared to the optimal extraction time, (ii) the fine coarse delay of the extracting Pockels cell. Parameter (i) enables the generation of a train of low energy pulses separated by the regenerative round-trip time. A train composed of two prepulses has been found to be optimal for Ni-like Mo DGRIP operation. The second parameter (ii) gives a control on the energy levels of the prepulses. An optimum has also been experimentally observed.

The DGRIP multipulses structure will be present in all beams delivered by the laser chain. It has been observed that the presence of the long pulse does not affect the high order harmonic generation in Argon. Thus, the DGRIP configuration may contribute to make seeding experiment with solid target easier. However, the DGRIP approach is not well suited for pump-probe experiments requiring a high contrast in the auxiliary beam. If only single shot operation is required, GRIP configuration will be chosen instead. For experiment requiring both pump-probe approach and important shot accumulation, DGRIP can be used in conjunction with an auxiliary beam frequency-doubled with a LBO crystal and filtered by 400 nm coated mirrors.

4 The High Order Harmonics Beamline

In parallel to the soft X-ray laser, a high order harmonic beamline has been developed. Up to 30 mJ of infrared energy, compressed to 35 fs, are available for high order harmonic generation. A typical setup involves a one meter focal length lens and a gas cell, followed by a transmission grating spectrometer. Absolute measurement with a calibrated photodiode indicates XUV radiation in the nJ range per pulse and per harmonic when argon is used as a generation medium. This standard setup has been recently completed with a Mach-Zendher system placed before the focussing optics. This device is represented in Fig. 2. It enables the obtention of two infrared pulses and, after conversion, two harmonic pulses with variable delay, energy balance and directions. When the two output beams are collinear such a device can be used to probe the gain dynamics of the soft X-ray laser gain in the context of seeding experiments. When a small angle is introduced and the delay is set to zero, harmonic generation in the bissectrice direction of the two IR beams can be observed. This type of experiment may give physical insight in processes involved in some intracavity harmonic generation scheme. The device is designed to be easily switched to two-color harmonic generation experiments.

5 Some Pump-Probe Experiments Examples

The infrared beam feeding the harmonic beamline can also be used as an auxiliary beam for pump-probe experiments and can enter an interaction chamber placed

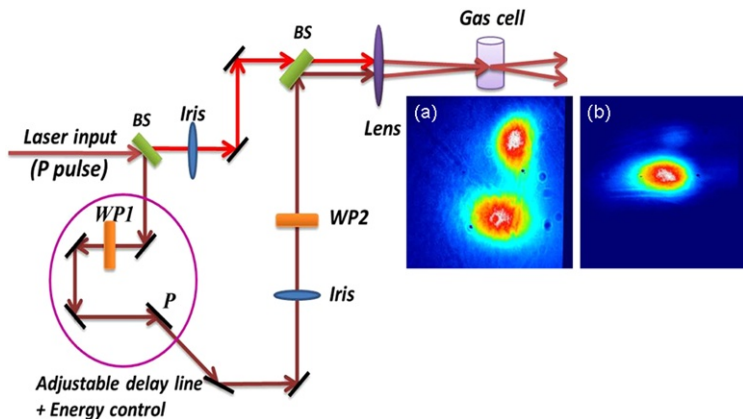


Fig. 2 Principle of the two harmonic pulses generation setup. *Inset:* farfield image of the harmonic beam. The two infrared pulses are quasi-collinear (1 mrad of angular separation) and delayed by 10 ps (*inset (a)*). The angular separation is also observed in the XUV range. For a 0 ps delay (*inset (b)*), on-axis harmonic generation can be observed

after the X-ray laser chamber. The soft X-ray laser is focussed onto a sample by an $f = 300$ mm multilayer spherical mirror, whereas the auxiliary beam is focussed by a short focal lens. The sample holder presented in Fig. 3 is equipped with a BBO crystal for precise timing between the pump and the probe. Besides, a YAG-Cerium crystal is mounted on the holder for XUV focal spot characterisation and spatial overlap checking. The soft X-ray laser beam has been used either as a probe or as a pump. Considering the soft X-ray laser as a pump, the XUV beam can induce permanent or transient changes in a polymer sample (polyvinyl-alcohol). The photoelectrons produced by the XUV photons will recombine and generate free radicals or new chemical species on time scales ranging from picosecond to permanent. This evolution can be followed with a visible light shining through the X-ray laser focal volume and absorbed by the induced species. For a proof-of-principle experiment, a CW He-Ne laser was used as a probing beam. Calculations showed that a one thousands variation of the He-Ne signal can be expected in the tens of nanosecond range following the interaction. A fast photodiode and an oscilloscope are therefore sufficient to record the evolution after the interaction, provided that the signal to noise ratio is high. The first experimental run was unsuccessful but helped us to identify the sources of noise and significant reduction has been achieved.

The soft X-ray laser is also recognized as an interesting probe in the context of hot dense plasmas. Recently we performed a plasma probing experiment in collaboration with the University of York. A sample composed of thin layer (50 nm) of Iron buried in a plastic (Parylene) foil was irradiated and heated by the compressed auxiliary beam in a non-normal incidence geometry and with a P polarisation. The change in opacity at 13.9 nm was followed with a Ni-like Silver X-ray laser shining through the sample. The size of the beam was greater than the heating pulse focal spot in order to get on a same image the transmission in the perturbed and

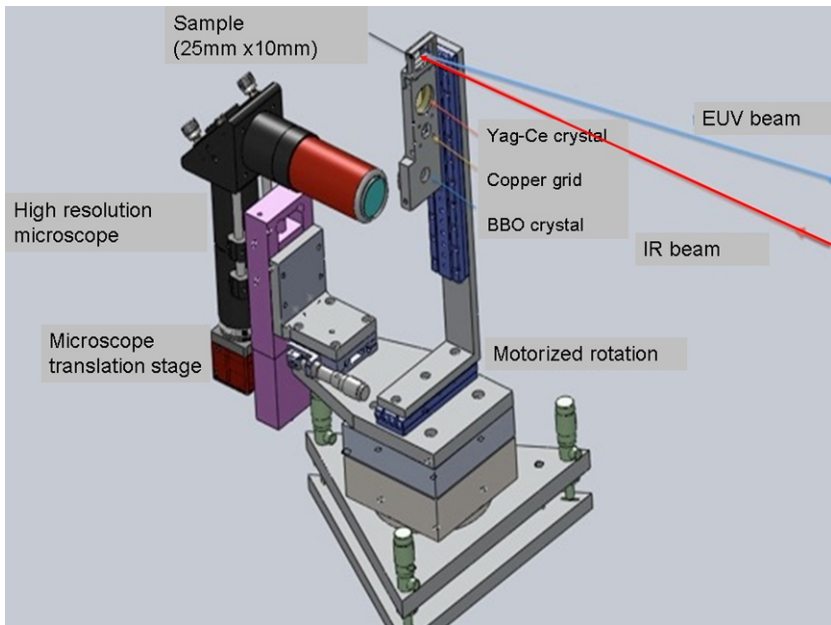


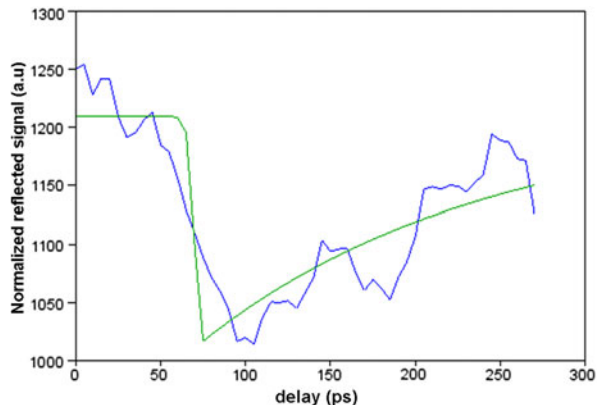
Fig. 3 Schematic of the pump-probe sample manipulator

unperturbed material. This type of experiment may provide important insight in suprathermal electron generation and propagation, heating by return current, and non-local thermal conduction in solid density plasmas.

6 Towards Advanced Soft X-Rays Diagnostics

The determination of soft X-ray laser temporal profile is an important but delicate task. Two techniques have been so far experimented. XUV streak cameras have already provided important results on soft X-ray lasers pulse durations. But their dynamical range is small, their resolution limited to the picosecond range and they are affected by important jitter. The other techniques relies on two color (XUV-IR) ionization of gas, and is in essence a cross-correlation measurement between the IR field (known) and the XUV field (unknown). This techniques potentially offers femtosecond resolution but requires electron spectroscopy in a magnetic bottle spectrometer where ultrahigh vacuum is mandatory. An ideal approach would be to get some sample that, when exposed to a short laser pulse, would experience a fast change in XUV transmission or reflectivity. The measurement of the transmitted/reflected XUV signal has a function of the delay between the short pulse and the XUV pulse would give, after deconvolution, the temporal profile of the XUV pulse. This measurement would be jitter-free, and no ultrahigh vacuum would be required. Finally, by exploiting focussing geometry generating travelling waves, in

Fig. 4 Normalized reflected XUV signal on the magnetic sample as a function of the delay between the heating pulse and the X-ray laser pulse. A fitting curve by a simple convolution model corresponding to a 5 ps X-ray laser duration is superimposed on experimental data



association with XUV imaging optics, it should be possible to get the correlation function in single shot.

It has been demonstrated recently that the XUV reflectivity of a polarised HHG beam on a magnetic sample can change of 20 % on a 100 fs time scale after irradiation by a low energy, femtosecond IR laser pulse [7]. For IR fluence of the order of 1 mJ/cm^2 , this fast change is only transient and the same sample can be used an infinite number of time. In collaboration with LOA, we performed an experiment to assess the interest of such a technique for soft X-ray laser pulse duration estimation. The sample was placed in the pump-probe setup presented in the previous section. The soft X-ray laser was P polarised before the focussing optics by two multilayer mirrors. The angle of incidence on the sample was set to 45° in order to maximise the magneto-optical Kerr effect (MOK). A XUV camera observed the specular reflexion of the XUV beam. A live measurement of the incident XUV energy is given by the photocurrent generated by the XUV beam into the focussing optics. The heating pulse is incident on the sample with a normal angle in order to minimise the time mismatch between the two pulses. It has been frequency doubled in order to remove all the prepulses introduced by the DGRIP setup. A delay scan of the reflectivity is presented in Fig. 4, where each point results from the accumulation of 100 X-ray laser shots. Despite important fluctuations, a deep in reflectivity can be observed at a delay corresponding to the temporal overlap of the two pulses. The experimental trend has been fitted by a model resulting from the convolution of a reflectivity response similar to the one presented in [7] by a XUV pulse of single-sided exponential shape. The best fit leads to a X-ray laser pulse duration of 5 ps (at $1/e$). This results are very preliminary and important work will be needed to improve the signal quality. However, the total signal level experienced during this work might be compatible with the idea of a single shot experiment involving a travelling wave irradiation.

7 Conclusion

In conclusion, we gave in this paper an overview of the work performed with the Laserix facility since the last ICXRL conference. The laser driver is now highly reliable increasing the availability of the XUV sources. Both harmonic and soft X-ray laser beamlines are now in operation, and their use in pump-probe experiments is underway. Investigations of a large variety of phenomena using the soft X-ray sources not only raise hopes of new discoveries but also will catalyse new idea for XUV radiation measurement and manipulation.

Acknowledgements We thank the LPGP and LOA technical and administrative staff for their always efficient help. The support of the Agence Nationale de la Recherche (ANR) is also acknowledged through the project ‘‘jeunes chercheuses et jeunes chercheurs’’ ASOURIX ANR-09-JCJC-0056.

References

1. Nickles, P.V., Shlyaptsev, V.N., Kalachnikov, M., Schnürer, M., Will, I., Sandner, W.: Short pulse x-ray laser at 32.6 nm based on transient gain in Ne-like titanium. *Phys. Rev. Lett.* **78**, 2748–2751 (1997)
2. Keenan, R., Dunn, J., Patel, P.K., Price, D.F., Smith, R.F., Shlyaptsev, V.N.: High-repetition-rate grazing-incidence pumped soft X-ray laser operating at 18.9 nm. *Phys. Rev. Lett.* **94**, 103901 (2005)
3. Zimmer, D., Zielbauer, B., Pittman, M., Guilbaud, O., Habib, J., Kazamias, S., Ros, D., Bagnoud, V., Kuehl, T.: Optimization of a tabletop high-repetition-rate soft X-ray laser pumped in double-pulse single-beam grazing incidence. *Opt. Lett.* **35**, 450–452 (2010)
4. Zielbauer, B., Zimmer, D., Habib, J., Guilbaud, O., Kazamias, S., Pittman, M., Ros, D.: Stable and fully controlled long-time operation of a soft X-ray laser for user application experiments. *Appl. Phys. B* **100**, 731–736 (2010)
5. Habib, J., Guilbaud, O., Zielbauer, B., Zimmer, D., Pittman, M., Kazamias, S., Montet, C., Kuehl, T., Ros, D.: Low energy prepulse for 10 Hz operation of a soft-x-ray laser. *Opt. Express* **20**, 10128–10137 (2012)
6. Capeluto, M.G., Vaschenko, G., Grisham, M., Marconi, M.C., Luduena, S., Pietrasanta, L., Lu, Y., Parkinson, B., Menoni, C.S., Rocca, J.J.: Nanopatterning with interferometric lithography using a compact $\lambda = 46.9$ nm laser. *IEEE Trans. Nanotechnol.* **5**, 3–7 (2006)
7. La-O-Vorakiat, C., Siemens, M., Murnane, M., Kapteyn, H.C., et al.: Ultrafast demagnetization dynamics at the M edges of magnetic elements observed using a tabletop high-harmonic soft x-ray source. *Phys. Rev. Lett.* **103**, 257402 (2009)

Chapter 19

Observation of the Laser-Induced Surface Dynamics Using the Single-Shot Soft X-Ray Laser Probe

N. Hasegawa, Y. Ochi, T. Kawachi, M. Nishikino, M. Ishino, T. Imazono, T. Kaihori, T. Morita, A. Sasaki, K. Terakawa, Y. Minami, M. Baba, T. Tomita, M. Yamamoto, M. Yamagiwa, and T. Suemoto

Abstract We constructed optical laser pump and soft x-ray laser probe system and succeed to obtain the temporal evolution of the soft x-ray images on the laser irradiated Pt surface during the femtosecond laser ablation. The temporal evolution of the reflectivity of the soft x-ray strongly depends on the pump laser fluence, and the apparent ablation threshold was observed. The results were well explained by the molecular dynamics simulations of femtosecond laser ablation process.

1 Introduction

The unique sub-micron scaled structures formed by the irradiation of the femtosecond lasers, such as the ripple and bubble structures [1], are expected to have new material functionalities with low processing cost. In order to precisely control the laser ablation, the detailed observation of the laser ablation dynamics is required. The researches for the ablation dynamics by using the visible laser probe have been reported by several groups. The expansion speed of the ablation front was estimated to be 900 m/s from the result of the interference pattern (Newton ring) between the ablation front and melting front [2]. While the visible laser probe enables the measurement below and around the ablation threshold, it is difficult to observe the dynamics of the laser ablation with generation of the surface plasmas that reflect the visible light. For the direct observation of the femtosecond laser ablation dynamics,

N. Hasegawa · Y. Ochi · T. Kawachi (✉) · M. Nishikino · M. Ishino · T. Imazono · T. Kaihori · T. Morita · A. Sasaki · M. Yamagiwa
Quantum Beam Science Directorate, Japan Atomic Energy Agency, 8-1-7 Umemidai, Kizugawa, Kyoto 619-0215, Japan
e-mail: kawachi.tetsuya@jaea.go.jp

K. Terakawa · Y. Minami · M. Baba · T. Suemoto
Institute of Solid State Physics, The University of Tokyo, 5-1-5 Kashiwanoha, Kashiwa, Chiba 277-8581, Japan

T. Tomita · M. Yamamoto
Department of Ecosystem Engineering, The University of Tokushima, 2-1 Minamijo-Sanjima, Tokushima 770-8506, Japan

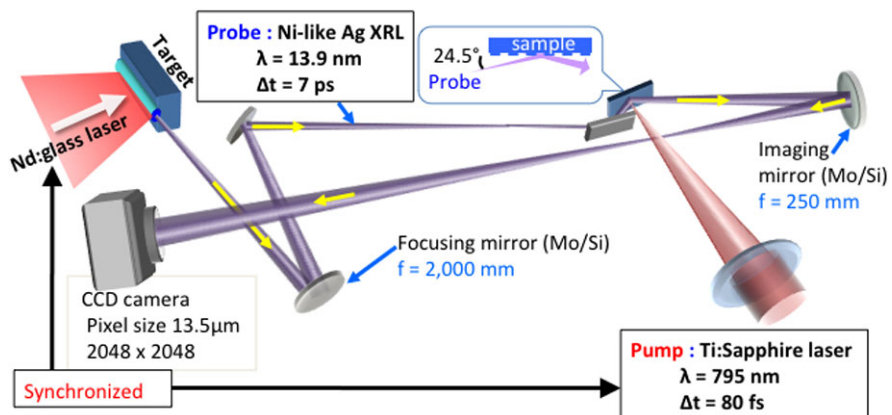


Fig. 1 Single shot x-ray laser probe with optical pump laser system

we propose to use the soft x-ray laser (SXRL) probe that can penetrate the surface plasmas and not penetrate the surface layer. In this study, we observed the temporal evolution of the soft x-ray reflective image of the laser induced metal surface, because the reflectivity of the soft x-ray is not sensitive to the electric state of the surface but quite sensitive to the surface morphology (see Fig. 3).

2 Observation of the Laser-Induced Surface Dynamics Using the Single-Shot Soft X-Ray Laser Probe

The experimental setup is shown in Fig. 1. The Ni-like silver SXRL at the wavelength of 13.9 nm generated by the CPA Nd:glass laser was used for the probe beam. The output energy and duration were 1 μJ and 7 ps, respectively. The SXRL was loosely focused on the sample with the oblique incidence angle of $\theta = 24.5$ deg. The SXRL beam size on the sample was about 1.2 mm (horizontal) and 0.5 mm (vertical). The spatial resolution of the soft x-ray image on the sample surface was measured to be $1.8 \mu\text{m}$ [3]. Ti:Sapphire laser at the central wavelength of 795 nm with the duration of 80 fs was used for the pump source. The spatial profile of the pump laser was Gaussian, and this enables us to discuss the pump fluence dependence at each radial position. The timing jitter between Ti:Sapphire laser and SXRL was measured to be 10 ps in RMS.

We observed the soft x-ray images of the laser induced Pt film (300 nm thickness) for the study of the ablation dynamics. The surface roughness of Pt was measured to be better than 1 nm by atomic force microscope. Figure 2 shows the temporal evolution of the soft x-ray reflective images and the cross sections of the relative reflectivity at various times. Relative reflectivity was obtained under the condition that reflectivity at the non-irradiation area by the pump laser was 1.0. The typical pump laser energy, peak fluence and intensity on the sample surface

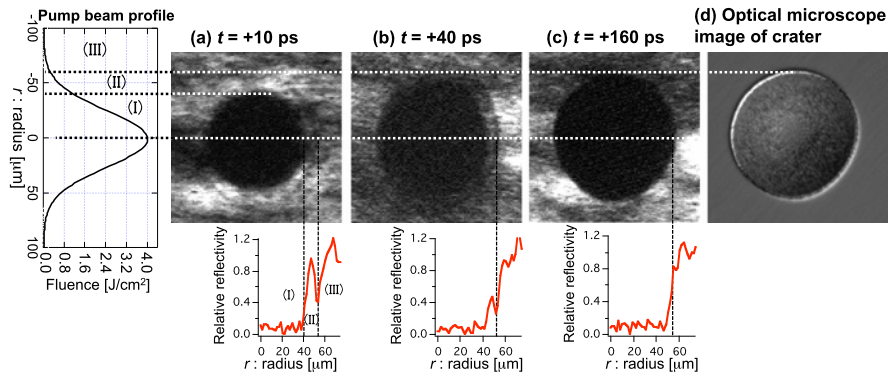


Fig. 2 The soft x-ray reflective images of femtosecond laser induced Pt surface

were $200 \mu\text{J}$, $4 \text{ J}/\text{cm}^2$ and $5 \times 10^{13} \text{ W}/\text{cm}^2$, respectively. In Fig. 2(a), the dark disk appeared at the central part (region I: $r < 40 \mu\text{m}$, $F > 1.0 \text{ J}/\text{cm}^2$) of irradiation area at $t = +10 \text{ ps}$. Here, F and r show the pump laser local fluence and radial position, respectively. Around the dark disk (region II: $40 \mu\text{m} < r < 55 \mu\text{m}$, $0.4 < F < 1.0 \text{ J}/\text{cm}^2$), the reflectivity slightly decreased. Outside of region II (region III: $r > 55 \mu\text{m}$, $F < 0.4 \text{ J}/\text{cm}^2$), reduction of the reflectivity was not observed. At $t = +40 \text{ ps}$, reduction of the reflectivity was observed in region II ($40 \mu\text{m} < r < 55 \mu\text{m}$) compared with that of $t = +10 \text{ ps}$. At $t = +160 \text{ ps}$, the size of the dark disk was equal to that of the bright ring in Fig. 2(d). The bright ring shows the rim structures. From these results, temporal evolution of the reflectivity was not linear function of the pump laser fluence, and the pump fluence at the boundary between the regions II and III leads to the ablation threshold fluence, $F = 0.4 \text{ J}/\text{cm}^2$. More interestingly, thin dark ring was observed at the boundary between the regions II and III at $t = +10 \text{ ps}$ and $+40 \text{ ps}$.

Next, we discuss the origin of the reduction of the soft x-ray reflectivity. The penetration depth of the soft x-ray with the oblique incidence angle of $\theta = 24.5 \text{ deg}$ for the solid Pt is less than 10 nm . Therefore, the reflectivity of the soft x-ray depends on the nanometer scaled surface morphology. We calculated the soft x-ray reflectivity on the several surface conditions. From Fig. 3(a), the reflectivity is quite sensitive to the surface roughness. But the density reduction by the phase transition from solid to liquid is not critically to explain the results. As shown in Fig. 3(b), 20 nm -density transition layer decreases the reflectivity to less than one-third. From these calculations, soft x-ray reflectivity drops occurred mainly due to the nanometer scaled surface roughness and density gradient.

The several ablation processes, the spallation ($F = F_{th}$), homogeneous nucleation ($F = 1.2F_{th}$), fragmentation ($F = 2.8F_{th}$), and vaporization ($F > 2.8F_{th}$), are predicted by the molecular dynamics simulations [4]. Here, F_{th} is the ablation threshold fluence. In vaporization and fragmentation processes, the solid surface is destroyed into gas and clusters just after the laser irradiation. In homogeneous nucleation process, the gas-bubbles are formed in the homogeneous liquid under the

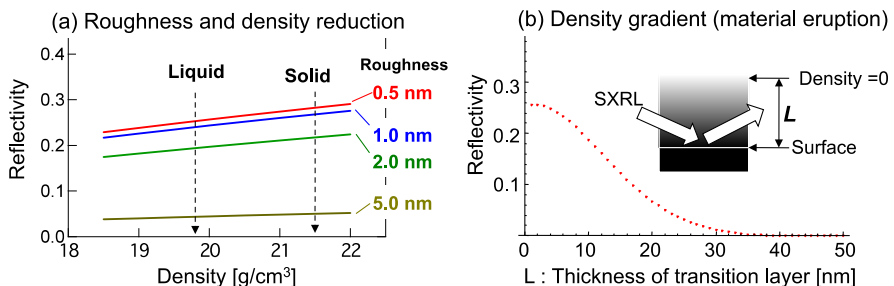


Fig. 3 Soft x-ray reflectivity calculated under the various surface conditions

condition that the pressure of liquid is lower than the saturation vapor pressure. In this case, the smooth surface is retained during dozens of picoseconds. The dependence of the transient surface conditions on the pump fluence well accorded with that of the experimental results in regions I~III. Therefore, the experimental results in the regions I and II are supposed to be equivalent to the vaporization (or fragmentation) and homogeneous nucleation, respectively. Spallation process is the rapid peeling of the solid surface layer induced by the tensile strain. The tensile strain is caused by the compressive pressure wave reflected at the free surface, therefore the spallation is required the solid surface and observed only under the condition that the pump laser fluence close to the ablation threshold. It just explains the thin dark ring observed at the boundary between regions II and III.

3 Summary

We observed that the temporal evolution of the soft x-ray reflectivity after the femtosecond laser irradiation on Pt surface. The results showed strong dependence on the pump laser fluence. In addition, the experimental results well accorded with the ablation process predicted by the molecular dynamics simulations.

References

1. Tomita, T., et al.: Effect of surface roughening on femtosecond laser-induced ripple structures. *Appl. Phys. Lett.* **90**, 153115 (2007)
2. Sokolowski-Tinten, K., et al.: Transient states of matter during short pulse laser ablation. *Phys. Rev. Lett.* **81**, 224–227 (1998)
3. Suemoto, T., et al.: Single-shot picosecond interferometry with one-nanometer resolution for dynamical surface morphology using a soft x-ray laser. *Opt. Express* **18**, 14114–14122 (2010)
4. Perez, D., Lewis, L.J.: Molecular-dynamics study of ablation of solids under femtosecond laser pulses. *Phys. Rev. B* **67**, 184102 (2003)

Chapter 20

Nano-meter Size Modification of Metal Surfaces Induced by Soft X-Ray Laser Single Pulse

Masahiko Ishino, Anatoly Faenov, Momoko Tanaka, Tatiana Pikuz,
Satoshi Tamotsu, Noboru Hasegawa, Masaharu Nishikino, Sergei Starikov,
Vladimir Stegailov, Genry Norman, Vladimir Fortov, Igor Skobelev,
Takeshi Kaihori, and Tetsuya Kawachi

Abstract We show experimentally the possibility of the precise nanometer size surface structuring of metal surfaces induced by ultra low fluencies of picosecond soft x-ray laser single pulse. After irradiation processes, we observed the modified surfaces to understand the interactions between the soft x-ray laser pulses and various materials by a scanning electron microscope. The formations of unique modified structures caused by irradiations of the soft x-ray laser pulses were seen. On Al surface, the formations of conical structures were observed. It was found that on Au surface, the ripple-like structures were formed. The atomistic model of ablation is developed that reveals the ultra-low threshold fluence values of this process. Calculated ablation depth as a function of fluence is in good agreement with the experimental data.

1 Introduction

Laser pulses having short durations have abilities to make high temperature and pressure, excite states of electrons in materials, emit rays, and so on, as the results of interaction with matters. Soft x-ray laser (SXRL) beam is one of attractive x-ray source for scientific studies, because of its features of short wavelength, short pulse duration, and highly spatial coherence. At the Japan Atomic Energy Agency, we have generated the SXRL beam, which has a fully spatial coherence, a short

M. Ishino (✉) · A. Faenov · M. Tanaka · T. Pikuz · N. Hasegawa · M. Nishikino · T. Kaihori ·

T. Kawachi

Quantum Beam Science Directorate, Japan Atomic Energy Agency, Kyoto, Japan

e-mail: ishino.masahiko@jaea.go.jp

A. Faenov · T. Pikuz · S. Starikov · V. Stegailov · G. Norman · V. Fortov · I. Skobelev
Joint Institute for High Temperatures, Russian Academy of Sciences, Moscow, Russia

S. Tamotsu

Division of Natural Science, Faculty, Nara Women's University, Nara, Japan

S. Starikov · V. Stegailov · G. Norman

Moscow Institute of Physics and Technology, Moscow, Russia

wavelength of 13.9 nm and the short duration of 7 ps. When we investigated a characteristic of the focal patterns of SXRL beam by means of color center formation in lithium fluoride (LiF) crystal [1], we found the ablation structures in the central parts of color center [2]. The ablation property appearing on LiF was very unique, because the ablation threshold was much smaller than those obtained with other lasers having longer wavelengths [2, 3].

It is quite interesting in the investigations of surface modifications induced by SXRL pulse irradiations, because understanding of surface modifications induced by laser irradiations is both fundamental and technological applications. The low ablation threshold of materials and formation of peculiar surface structure have possibilities of efficient and unique surface machining. There are still a lot of gaps in the understanding of the ablation mechanisms, especially for ultra short pulse lasers, because the existing experimental data are inconsistent with theoretical predictions. To confirm the appearance of surface modification, we irradiated the focused SXRL pulses to the target surfaces, and to describe the observed modification process, we proposed to use the atomistic model.

2 Experimental Results and Discussion

The SXRL irradiation experiment was carried out by use of the SXRL facility at Japan Atomic Energy Agency. The SXRL pulse was generated from the silver (Ag) plasma mediums using an oscillator-amplifier configuration. Characteristics of the generated SXRL pulse had a wavelength of 13.9 nm, bandwidth of narrower than 10^{-4} , and duration of 7 ps. The SXRL pulse was focused on the target surfaces by using a Mo/Si multilayer coated spherical mirror. A zirconium filter having 0.2 μm thick was placed in front of the spherical mirror to reduce the scattered optical radiations from the laser produced Ag plasmas. The total energy of the SXRL beam on the target surface was calculated to be 48 nJ. Using the LiF detector technique for estimation of the focused SXRL beam properties, we found that the SXRL energy concentration in focusing areas reached about 60 %. And around 40 % of the focusing SXRL beam energy was concentrated in the center of the best focusing spots.

After the SXRL irradiation processes, target surfaces were observed by use of various techniques, such as visible microscope, scanning electron microscope (SEM), and atomic force microscope (AFM). Details of experimental setup are described in previous papers [4].

Figure 1 shows SEM images of the irradiated aluminum (Al) and gold (Au) surfaces after a single shot exposure of the SXRL pulse around the focal points. The modified structures caused by the SXRL pulse irradiation are clearly observed on both targets, and we can confirm that the induced structures have quite different topology. On Al surfaces, it can be confirmed that the conical structures, which observed previous work [4], are formed around the ablated holes, and the relatively area of the conical structures increases by the reduction of the SXRL fluence. On

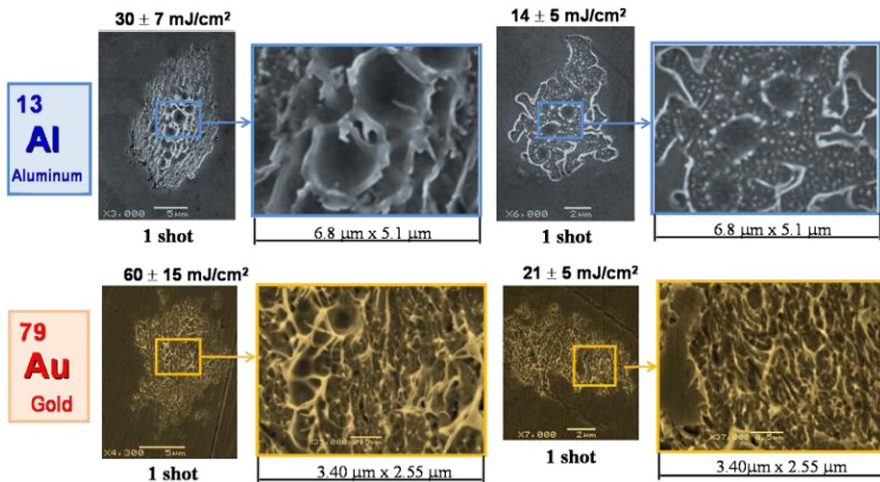


Fig. 1 SEM images of Al and Au surfaces after the SXRL single pulse irradiation

Au surfaces, on the other hand, the ripple-like shallow structures are seen. Areas of modified parts of Au surfaces are essentially smaller than those of Al cases.

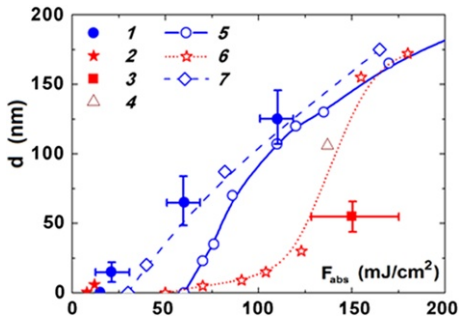
The obtained depths of surface irregularities are 400 nm and 170 nm for Al surfaces with the fluences of $30 \text{ mJ}/\text{cm}^2$ and $14 \text{ mJ}/\text{cm}^2$, respectively [5]. For Au cases, 80 nm and 20 nm of surface irregularities are obtained by the fluences of $60 \text{ mJ}/\text{cm}^2$ and $21 \text{ mJ}/\text{cm}^2$ [6]. With increasing of SXRL fluence on the target surfaces, the depths and height of surface modifications are growth. As the experimental results of interactions between SXRL pulses and metal surfaces with various fluences, the difference type of surface modifications are distinguished, such as (1) at relatively low fluence ($\sim 10\text{--}20 \text{ mJ}/\text{cm}^2$), modified surfaces with nanometer size structures are formed, and (2) at relatively high fluence ($>30\text{--}60 \text{ mJ}/\text{cm}^2$), ablated holes deeper than the attenuation lengths of SXRL beam for metals are confirmed.

To explain the experimental results obtained by the laser pulses with ultra short duration, the atomistic model of ablation was developed [6, 7]. To describe the ablation process near the threshold fluence, we propose the molecular dynamic (MD) model of two-temperature system with electron-temperature-dependent interatomic potential. Figure 2 shows the dependence of modification depth on absorbed laser fluence (F_{abs}). For SXRL pulses, the ablation depth smoothly grows together with F_{abs} , and it is clearly seen that the calculated ablation depth is in a rather good agreement with the experimental data. Our model calculation reveals that the first changes of surface structure are most probable due to the splash of molten gold.

3 Conclusion

We show the possibility of the precise nanometer size modified structures on Al and Au surfaces induced by the irradiation of the focused SXRL single pulse (experi-

Fig. 2 The dependence of modification depth on absorbed fluence (F_{abs}) for gold target: 1—experimental results (this work); 2 and 3—optical pulses; 4—MD calculation result (previous work); 5, 6 and 7—our MD calculation results with different conditions. See for details in Refs. [6, 7]



ment). We also provide the MD model to describe the ablation processes induced by SXRL single pulse irradiations (theory). The results we demonstrated will be important not only for a pursuite of ablation process but also for future application of SXRL beam, such as micromachining.

Acknowledgements This work was partly supported by the Grant-in-Aid for Scientific Research (B) from MEXT, Japan (No. 21360364), the Russian Foundation for Basic Research (Nos. 12-02-0947, 12-08-00666), and the Russian Academy of Science Presidium Program of Basic Research (No. 2). The presentation at conference was supported by Grant-in-Aid for Young Scientists (B) from MEXT, Japan (No. 24710096).

References

1. Faenov, A.Ya., et al.: Opt. Lett. **34**, 941–943 (2009)
2. Faenov, A.Ya., et al.: Appl. Phys. Lett. **94**, 231107 (2009)
3. Inogamov, N.A., et al.: Appl. Phys. A **101**, 87–96 (2010)
4. Ishino, M., et al.: J. Appl. Phys. **109**, 013504 (2011)
5. Ishino, M., et al.: J. Laser Micro Nanoeng. **7**, 147–151 (2012)
6. Norman, G., et al.: J. Appl. Phys. **112**, 013104 (2012)
7. Starikov, S.V., et al.: JETP Lett. **93**, 642–647 (2011)

Chapter 21

Speckle Statistics, Coherence and Polarization of a Collisional Soft X-Ray Laser

K.A. Janulewicz, C.M. Kim, P.V. Nickles, H. Stiel, M. Nishikino, N. Hasegawa, and T. Kawachi

Abstract A simple model of dynamics of a collisional X-ray laser is given applying Maxwell-Bloch equations in a uniform approximation. The main considered parameters include polarization and coherence of the emitted radiation. Speckle pattern, typical for a radiation source of partial coherence, especially, if involving process of the amplified spontaneous emission (ASE), are used as an alternative source of information on the processes occurring in the active medium of an X-ray laser. A level of partial coherence is deduced by statistical analysis of the speckle pattern generated in the output beam of the laser. It is shown that plasma fluctuation and non-Gaussian character of the statistics are needed to reproduce the transverse coherence values reported in the experiment.

1 Introduction

Plasma-based, transient-inversion X-ray lasers work nearly exclusively in the mirrorless arrangement. The main reason for that is short-lived gain with a typical duration between 10 and 15 ps. As a consequence, the amplified spontaneous emission (ASE) is used as the energy extraction mechanism [1]. Present-day X-ray lasers excited by the collisional processes in the grazing incidence pumping geometry (GRIP) or by electron residual energy of the above-threshold-ionization (ATI) in an

K.A. Janulewicz (✉) · C.M. Kim

Advanced Photonics Research Institute, Gwangju Institute of Science and Technology, Gwangju, 500-712, Rep. of Korea

e-mail: kaj@gist.ac.kr

P.V. Nickles

WCU Dept. of Nanobio Materials and Electronics, Gwangju Institute of Science and Technology, Gwangju, 500-712, Rep. of Korea

H. Stiel

Max Born Institute, 12489 Berlin, Germany

M. Nishikino · N. Hasegawa · T. Kawachi

Japan Atomic Energy Agency, 8-1-7 Umemidai, Kizugawa, Kyoto 619-215, Japan

optical field, show exceptionally high (50–80 cm⁻¹) small-signal-gain coefficient [2–4]. This causes them to work even more readily in the ASE regime.

One of the distinguishing effects of ASE-based lasers is presence of speckle (deep and random modulation of the intensity distribution giving a kind of granular structure) in the output beam. This is caused mainly by lack of a mode selecting cavity [5]. For these reasons X-ray lasers seem to be an inherent source of the speckle effect and indeed, randomly distributed hot spots were observed in the experiment [4, 6].

Application perspective was always important in the development of plasma-based X-ray lasers (XRLs). One of the fundamental parameters for using them in practice is coherence. While plasma-based XRLs proved excellent temporal coherence (probably the best among the short-wavelength sources), their spatial coherence is limited. Partial coherence in a plane perpendicular to the propagation direction is frequently quantified by a ratio of the coherence area A_{coh} and the beam cross-section A . This value is typically, for the systems without injection of an external signal and not pumped by fast electric discharge, about one percent [7].

The Young's interferometry is commonly used method of spatial coherence measurement. This is a well-established and simple method but it has some drawbacks when applied to XRLs. The Young's interferometry applied to the plasma-based sources requires removal of a noticeable background of the plasma thermal emission to avoid reduction in the fringes visibility. The principal practical assumption of this measurement scheme is equality of the signals at each of two distant slits. If this is not fulfilled, the correction factor $2\sqrt{I(1)I(2)}/[I(1)I(2)]$ has to be introduced in the formula for the fringes visibility, where $I(1)$ and $I(2)$ denote the intensities at each of the slits. The speckle effect causing randomness of the intensity distribution in the beam pattern precludes exact knowledge of the correction factor. Influence of this effect on the experiment was analyzed and clearly demonstrated in [8]. As a consequence, the Young's interferometry should typically underestimate a spatial coherence level of the plasma-based X-ray lasers. On the other hand, the saturation intensity level of X-ray lasers is about 10¹⁰ W/cm² and at this level of the optical field plasmonic effects on the slit edges can also affect fringes visibility by their modulation [9].

Radiation polarization is another parameter crucial for applications. It is commonly assumed that the beam originating from a spontaneous noise is naturally polarized, i.e. it does not show any preferential direction in the field oscillations. There were totally contradictory reports regarding this aspect. One showed strong *s*-component [10] and another one natural (undefined) polarization [11].

Recently, a simple model for the origin of the speckle structure in the X-ray laser output beam has been proposed [12]. This structure was termed as a speckle-like one and modeled by standard dependencies from coherence and diffraction theories. Description of the effect was done in terms of so-called classic or full developed speckle [13, 14]. It was concluded that the length of the output pulse exceeding the coherence time was responsible for creation of this structure. It was also assumed that the ratio of the pulse length t_p and coherence time t_{coh} was a measure of the modal structure of the emitted radiation. This is in our opinion, taking into account a

very high level of medium inhomogeneity, unnecessarily strong limitation. It tacitly assumes, that an X-ray laser beam shows full spatial coherence and this is not the case in the experimental practice. In fact, in the most general case, separation of the effects of the spatial and temporal coherences is possible, subject to the mutual spectral purity.

In the present contribution we are analyzing, whether the observed and discussed earlier intensity inhomogeneity in the X-ray laser output beam is really a classic speckle structure and undergoes well established statistical rules of the speckle-related phenomena [13–15]. No assumption regarding the coherence state of the beam is introduced. It was attempted to determine whether the speckle structure could be used as a source of reasonable quantitative information on the X-ray laser beam coherence level.

2 The Method

2.1 X-Ray Laser Dynamics

We applied the X-ray laser dynamics model developed and presented in detail in [17]. The model formulated in a uniform approximation describes emission and amplification of the polarized radiation in terms of Maxwell-Bloch equations. Observing build-up of polarization in a single mode, it was found that saturation of the amplification process is responsible for decreasing in the polarization built-up. Polarization achieves nearly completeness before saturation onset, to decrease in the saturated regime to a value slightly above 80 %. It should be stressed that here the well-defined polarization has been considered (one of the P -states different from the natural polarization) and not some specific polarization state. In other words, the polarization state could be different from shot to shot, but it would be always well defined. The build-up of a random, but defined, polarization state with the length of the medium is shown in Fig. 1. In the model it was assumed that the seeding process by spontaneous noise is perfectly random and of uniform distribution. It is seen in Fig. 1 that (in this specific case) elliptic polarization achieves maximum for 3 mm and then is reduced. At a length of 3 mm the gain saturation effect begins. The horizontal axis describes the polarization state by the phase difference between the perpendicular field components. It was tried to verify experimentally the effect observed in simulations. A double-target arrangement was used to generate coherent X-ray radiation at 13.9 nm and those was subsequently analyzed by a membrane/multilayer beam-splitter allowing quantitative distinguishing between the “amount” of s - and p -polarized components in the output radiation. More detailed description of the experiment is given in these proceedings (see [16]). It was found that the p -component of the wave electric field dominated in the emitted radiation. There are some shot-to-shot fluctuations but on a very strong background of the p -component. This clearly suggests elliptical polarization of radiation emitted by the X-ray laser under investigation.

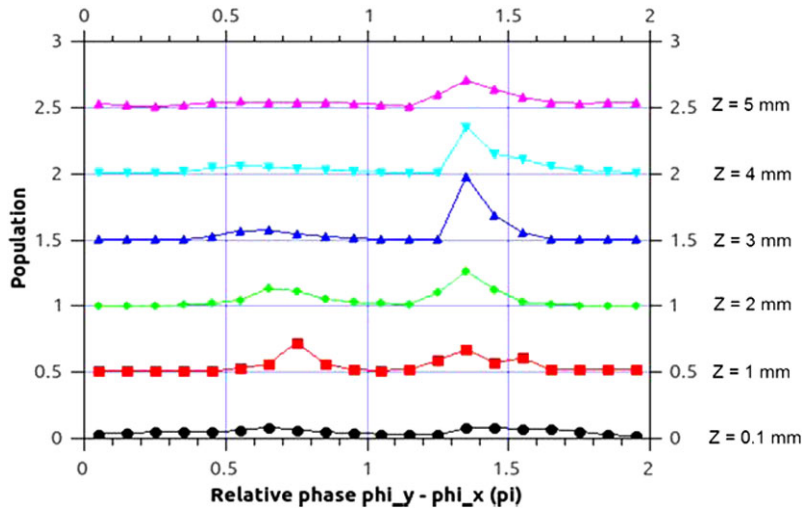


Fig. 1 Development of a defined polarization state with a length of the active medium in the output radiation of a nickel-like silver X-ray laser

Analysis of the amplification process showed also interesting dependence of the gain-narrowing effect on the medium length. The rate of the bandwidth reduction with the length is in the medium beginning noticeably lower than that in the strong amplification (see Fig. 2). The probable reason for that is strong influence of the “noisy” character of the signal within the first few millimeter of propagation. This could explain difficulty faced by Koch [18] to fit its experimental data of short length amplifier with a bandwidth reduction curve based on the rate equations.

2.2 Data Acquisition and Reproducibility

The experimental data processed here were obtained from the far-field images of the output beam of a Ni-like silver soft X-ray laser working at 13.9 nm. The images were recorded during the experiment described in [4]. The observation plane was placed 55 cm from the laser exit. A plasma column of 7 mm in length was obtained by irradiation of a slab target in the typical form of the GRIP geometry (double-pulse scheme with a long pulse incident normally to the target). The total pump laser energy contained in the irradiating laser pulse was equal to 1.5 J. The small-signal-gain coefficient was estimated to be 61 cm^{-1} . More detailed description of the experimental layout as well as measurements of the transverse coherence done in the classic Young’s double-slit arrangement are given in [4]. Visibility of the fringes determined as a function of the slits separation was fitted under the assumption of the uniform circular source by using van Cittert-Zernike (vCZ) theorem. The measurement, with all mentioned earlier limitations, gave an effective incoherent source

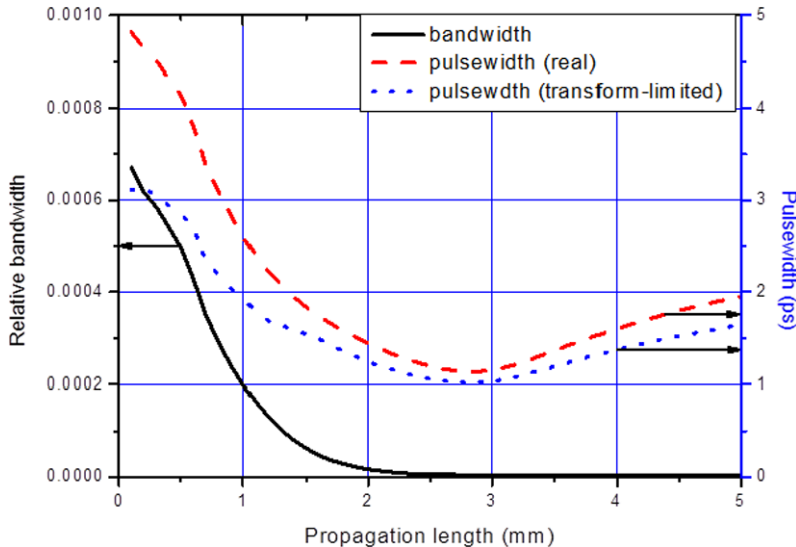


Fig. 2 Band- and pulse-width of the output pulse. Characteristic is that close to the origin (very short medium) the decrease in the bandwidth and the pulse-width are slightly slower in the beginning of the amplification process, in contradiction to the standard rate-equation result [18]

of $6.6 \mu\text{m}$ and a coherence length of L_{coh} of $57 \mu\text{m}$ at a position of 8.4 cm behind the laser exit [4]. Following this, it was estimated that the double-pulse irradiation delivered 3 % of fully coherent photons in a beam of 4 mrad divergence.

X-ray lasers are, due to the character of the processes involved in the generation scheme, very sensitive to small and accidental fluctuation in the laser pulse energy, accuracy of the pump beams overlapping and the focal line parameters. These depend partly on stability of the driving laser system and partly on quality of the medium/target itself. Beam pointing of a pump laser (spatial stability of the emitted beam) is one the most serious deteriorating effects. Generally, a typical reproducibility of XRL output determined by a standard deviation from the mean usually exceeds slightly 20 % and is considered as a good one [19].

On the other hand, it was assumed—what frequently used to be done—that the source is circular and uniform with a very narrow field correlation function justifying the use of the standard analytic formulae resulting from the vCZ theorem [20]. In fact, the beam profile is better described by more realistic distribution function $I(r) = I_0 \cosh^{-2}(r/a)$, approximating well a parabolic function close to its maximum [8, 21].

2.3 Data Processing and Simple Estimates

Using the coherent length value experimentally determined by the Young's interferometry, one can get a coherence volume of $V_{coh} = A_{coh} \times t_{coh} \times c =$

1.97×10^{-6} cm³. Having assumed a typical pulse length of 6 ps and a number of photons in the pulse of 10^{11} , the degeneracy factor δ_c , indicating amount of the indistinguishable (coherent) photons within the coherence volume has been estimated as equal to 8.5×10^{10} . This is a very high value but one has to bear in mind that it was obtained for strongly idealized case of plane wave neglecting dependence of the coherence volume on the position in the considered space (medium). A simple estimate method of XRL spatial coherence assuming an active medium of a cylindrical shape and a less strict definition of the coherence length considered as a distance from the origin over which the coherence degree is not smaller than 0.5 give a simple analytic formula $L_{coh} \cong \lambda L / 4a$ to estimate dimensions of the coherence area [22]. It was concluded that, in the case of the coherence length corresponding to the plasma/XRL width a , the Fresnel number associated with the plasma column should be $N_F = a^2 / \lambda L \cong 1/4$ [22]. These order of magnitude estimates are related only to the main peak of the correlation function. Applying these approximated expressions to the parameters of our XRL (assumed $a = 32$ μm) and a medium length of $L = 7$ mm we got $L_{coh} \cong 0.5$ μm at the source plane. This value is related to the main peak of the correlation function and differs markedly from the value of 2 μm obtained from the experimental far-field (FF) intensity profile by the Fourier transform.

It is well known that in the ideal case of full coherence a laser emits photons in a single mode with a statistics ruled by the Poisson distribution and the relevant probability density (probability density to obtain a given intensity level I within the intensity gap of I , $I + dI$) has negative exponential distribution [13, 14]. The speckle pattern governed by this distribution is called the fully developed speckle. Corresponding distribution for a partially coherent light is given in the form of the gamma distribution, sometimes also called m -distribution [13, 14]

$$p_M(E/\bar{E}) = M^M (E/\bar{E})^{M-1} \exp(-ME/\bar{E}) / \bar{E} \Gamma(M) \quad (1)$$

where M is a number of statistically independent but equally intense (average value) coherence modes in the output radiation. The experimental practice (detectors and the time scale) forces one to use temporally integrated intensity as a variable. Thus, for the sake of consistence we can use E/\bar{E} —the normalized pulse integrated intensity instead of I/\bar{I} for the normalized peak intensity. The beam images recorded in the far-field zone presented in Fig. 3 have been processed to obtain dependence of the probability density on the normalized integrated intensity E/\bar{E} . The histograms of the image intensity level were created with binning including 50 bins. The part of the beam used for the histogram was selected by a rectangular window (Fig. 3), drawn to cover the maximum possible area of the irregular beam spot and minimize contribution from the non-irradiated but noisy vicinity.

The nature of the lasing process in X-ray lasers makes analysis of the speckle structure difficult. Due to mentioned limited reproducibility of the plasma dynamics, X-ray lasers show a significant shot-to-shot fluctuation of the beam position caused by variable deflection on not fully relaxed density gradients. As a consequence, averaging the speckle images as it is recommended in the scattering experiments at a synchrotron [23, 24] is impossible as it leads to artificial beam homogenization and

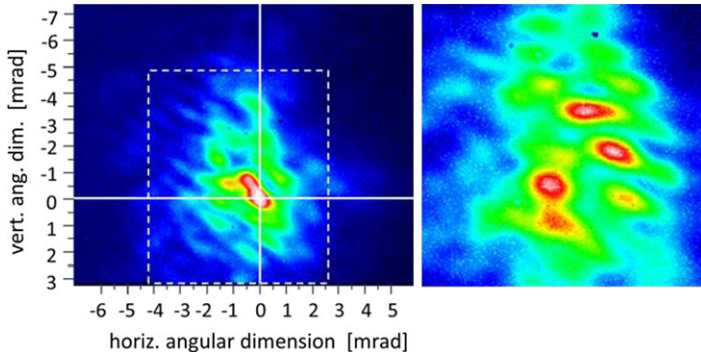


Fig. 3 Far-field image of X-ray laser output recorded at a distance 55 cm from its exit and with the marked area taken to the statistical analysis. The image of the speckle pattern on the *right side* is already equal to the analysis area

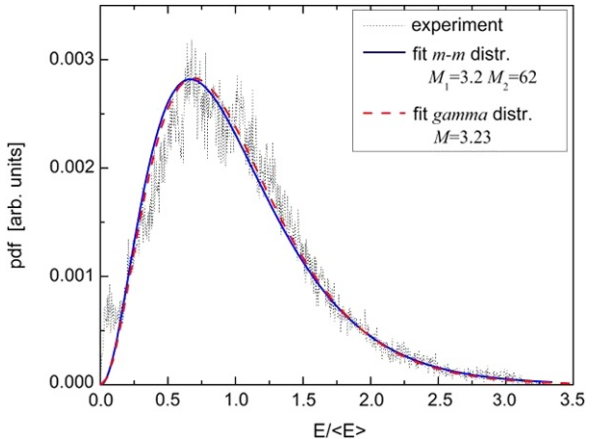
the speckle statistics tends towards the negative exponential distribution equivalent to reduction in the effective number of the contributing modes. By averaging in this way five images from our experiment with the M value between 2.4 and 6.5 we got an effective number of coherence modes $M = 1.6$, that is definitely incorrect. Another procedure realized by averaging statistics of the individual beam images was found, during speckle analysis of a synchrotron beam, to deviate too much from the realistic values [23]. Moreover, the gain area of X-ray lasers is not exactly stable in time [25] and this can result in additional smearing and blurring effects. The detectors integrate the signal within the time gap equal to the pulse length that is typically longer than the coherence time. That means, the integrated intensity (pulse energy) includes a few overlapped (incoherently added) speckle patterns, each corresponding to the time gap equal to the coherence time. All this makes the picture to be very complex and the question arises if the standard statistical tools allow for fast, simple and reasonable estimate of the radiometric features of the observed radiation.

3 Results and Discussion

The far-field images of the beam were recorded independently in five consecutive shots and analyzed using the standard software of the back illuminated CCD camera of Princeton Instruments. The average intensity and corresponding standard deviation were the main output parameters of the statistics. The mean value from this processing was put in Eq. (1) with M as a fitting parameter—the procedure suggested by Goodman as the reasonable one [13].

Dimension of the selected analysis window (area) had limited influence on the output of the statistical procedure. Usually, the M value varied by much less than 10 % as a function of the window area choice. Figure 3 shows an example of such a recorded image with indication of the angular distribution of the intensity and the area from which the data were used. In spite of the local deviations, the best fit gave

Fig. 4 Experimental histogram of the right-side image in Fig. 3 with two possible fits: m distribution and $m-m$ distribution. m -Distribution is a synonym of gamma distribution



$M = 2.4$, which is a very low value. The poor shot-to-shot reproducibility of the X-ray laser was confirmed as within the registered series of shots the derived number of the coherence modes varied between 2.4 and 6.5.

All the above discussed characteristics and experiments confirm that a collisional X-ray laser is a device of limited (partial) spatial coherence. The histograms of the recorded far-field patterns, the obtained values of the mean intensity and the standard deviation allowed for determination of the speckle contrast K_{sp} and the number of modes $1/M = \sigma_E^2 / \bar{E}^2$ involved in creation of the partially developed speckle pattern ($K_{sp} < 1$). It is not surprising that these values are very close to those derived from the fitting process as the experimental value of the mean was used in the fitting process as a fixed parameter. This confirms, however, a high goodness of the fit. It has to be stressed here, that the obtained M values have to be halved when the polarization state of the XRL output radiation is unknown and commonly assumed as natural one (undefined polarization).

From here on, we concentrate on the speckle pattern presented in Fig. 3 (right image) delivering the best fit and relatively low value of M . A contrast value of the speckle $K_{sp} = \sigma_E / \bar{E} = 1 / \sqrt{M}$ equal to 0.56 was estimated from the statistics when M estimated in the fitting procedure was equal to 3.23. This confirms, that the photon statistics is definitely non-Poissonian (in this case the contrast is equal to 1) and one can guess that the presented in Fig. 3 speckle patterns show structures resulting from intensity summing of some finite number of spots (coherent modes). This guess is justified even if Eq. (1) is, in fact, obtained under the assumption that all the contributing statistically independent spots (modes) have the same mean intensity and an uniform phase distribution.

While the second condition is fulfilled in the X-ray laser medium the former one is actually not fulfilled. The active medium is inhomogeneous and the radial density gradient is sufficient to cause radiation to be refracted (bent off the active area in the extreme case) from the axial direction and the modes can partially overlap each other, especially at the end of the medium where the saturation effect is strongest. On the other hand, the gain itself is sufficiently high to cause significant differences

in the group velocities of the photon fluxes traversing the medium areas of different gain [26]. The absolute gain values are extremely high and one can consider two realistic values of the gain coefficient, namely 80 cm^{-1} and 50 cm^{-1} . The corresponding group velocities v_{gr} in a medium with a Gaussian spectral line profile ($\Delta\nu_D = 1 \times 10^{12} \text{ 1/s}$) are equal to $0.735c$ and $0.816c$, respectively. The time delay for two groups of photons amplified in these areas will achieve a value of $\approx 2.3 \text{ ps}$. This is much more than the coherence time of the radiation. Hence the assumption about the constant average intensity of all correlation (coherence) areas is definitely not fulfilled.

All these effects cannot, unfortunately, account for the large discrepancy between the experimental results and the estimates of the transverse coherence length derived from the speckle data. The latter suggest existing up to 30 % of fully coherent photons in the output beam, at least one order more than the experimental data. The field correlation function at the XRL exit indicates multi-mode distribution. Most of the area is weakly correlated but the number of the hot spots is large. The resulting speckle has to be described by other distribution function. It was found, that a bi-statistical process described by gamma-gamma ($m\text{-}m$) distribution fits favorably the experimental speckle statistics (see Fig. 4) and differs negligibly from gamma distribution. However, the number of modes is much larger. Plasma fluctuations cause mode mixing and movement of the source and it results in non-Gaussian character of the beam propagation through the medium. This process is overlapped (modulated) by formation of large-scale modes determined by the medium geometry.

Taking into account that M can be treated as a measure of the ratio A/A_{coh} we can introduce two separate numbers M_1 , M_2 characterizing the multiplicative component processes of the mode formation. Hence one can estimate the value of spatial coherence length $L_{coh} \cong \sqrt{A_{coh}}$ or $L_{coh} \cong \sqrt{A/M}$, where $M = M_1 \times M_2$. Using obtained from the fitting process values $M_1 = 3.2$ and $M_2 = 62$ we obtained a coherence length in the observation plane equal to $263.5 \mu\text{m}$. This value corresponding to 1/14 of the beam diameter is in reasonable agreement with 1/18–1/20 reported in the experiment [8].

4 Conclusion

In summary, it was found that polarization of a slab target collisional X-ray laser is not undefined (natural polarization), but it has a strong p -component fluctuating from shot-to-shot, what indicates tendency to elliptical polarization. This finding is not in perfect agreement with 1D modeling suggesting that the output beam can have well defined, but random polarization state.

Analysis of the speckle pattern in a beam of an X-ray laser stated that these undergo the usual statistics of partially coherent source, i.e. the probability density corresponds to a gamma distribution. However, more exact inspection of the results shows that in general, the coherence level is very seriously overestimated. This results from the plasma inhomogeneity and reasonable agreement with the experimental reports requires implementation of plasma fluctuations and non-Gaussian

statistics of the speckle. The random inhomogeneities of the medium give the probability density described in an accurate way by gamma-gamma (or $m-m$) distribution. As a consequence, the speckle structure has a bi-statistical character and the derived in this way coherence length compares favorably with the values reported in the experiment. Taking into account the drawbacks of the Young's interferometry the speckle analysis can be considered as a simple tool of reasonable estimate of the coherence level from the far-field beam patterns.

Acknowledgements We would like to pay credit to Dr. Hyung Taek Kim for his help in the experimental effort. The work was supported partially by TBP GIST, NCRC and DASAN.

References

- Pert, G.J.: Output characteristics of amplified-spontaneous-emission lasers. *J. Opt. Soc. Am. B* **11**, 1425 (1994)
- Keenan, R., et al.: High-repetition-rate grazing-incidence pumped X-ray laser operating at 18.9 nm. *Phys. Rev. Lett.* **94**, 103901 (2005)
- Luther, B.M., et al.: Saturated high-repetition-rate 18.9-nm tabletop laser in nickel-like molybdenum. *Opt. Lett.* **30**, 165–167 (2005)
- Kim, H.T., et al.: Characteristics of Ni-like silver X-ray laser pumped by single profiled laser pulse. *J. Opt. Soc. Am. B* **25**, B76–B84 (2008)
- Kravis, S.P., Allen, L.: Measurement of the statistics and spatial distribution of pulsed spontaneous emission. *Opt. Commun.* **23**, 289 (1977)
- Nishikino, M., et al.: Characterization of a high-brilliance soft x-ray laser at 13.9 nm by use of an oscillator-amplifier configuration. *Appl. Opt.* **47**, 1129 (2008)
- Lu, P., et al.: Spatial coherence of prepulse-induced neon-like x-ray lasers. *Phys. Rev. A* **58**, 628 (1998)
- Liu, Y., et al.: Spatial coherence measurements of a 13.2 nm transient nickel-like cadmium soft X-ray laser pumped at grazing incidence. *Opt. Express* **14**, 12872–12879 (2006)
- Gan, C.H., Gbur, G., Visser, T.D.: Surface plasmons modulate the spatial coherence of light in Young's interference experiment. *Phys. Rev. Lett.* **98**, 043908 (2007)
- Kawachi, T., et al.: Observation of polarization of the soft X-ray laser line in neonlike germanium ions. *Phys. Rev. Lett.* **75**, 3826 (1995)
- Rus, B., et al.: Demonstration of amplification of a polarized soft-x-ray laser beam in a neon-like germanium plasma. *Phys. Rev. A* **51**, 2316–2327 (1995)
- Gilbaud, O., et al.: Origin of microstructures in picosecond X-ray laser beam. *Europhys. Lett.* **74**, 823–829 (2006)
- Goodman, J.W.: Statistical properties of laser speckle pattern. In: Dainty, J.C. (ed.) *Laser Speckle and Related Phenomena*, 2nd edn. Springer, Berlin (1984)
- Goodman, J.W.: *Speckle Phenomena in Optics: Theory and Applications*. Roberts & Company, Englewood (2006)
- Goodman, J.W.: Speckle with a finite number of steps. *Appl. Opt.* **47**, A111 (2008)
- Kawachi, T., et al.: Source development of novel coherent x-rays and their applications in JAEA. In: Sebban, S., et al. (eds.) *X-Ray Lasers 2012*. Springer Proceedings in Physics, vol. 147. Springer, Cham (2013). Chapter 23 in this book
- Kim, C.M., Lee, J., Janulewicz, K.A.: Coherent amplification of an ultrashort pulse in a high-and swept-gain medium with level degeneracy. *Phys. Rev. Lett.* **104**, 053901 (2010)
- Koch, J.A., et al.: Experimental and theoretical investigation of neonlike selenium x-ray laser spectral linewidths and their variation with amplification. *Phys. Rev. A* **50**, 1877 (1994)

19. Rocca, J.J., et al.: Saturated 13.2 nm high-repetition rate laser in nickel-like cadmium. *Opt. Lett.* **30**, 2581–2583 (2005)
20. Goodman, J.W.: Statistical Optics, Chap. 9.1. A Wiley-Interscience Publication. Wiley, New York (1985)
21. London, R.A., Strauss, M., Rosen, M.D.: Modal analysis of X-ray laser coherence. *Phys. Rev. Lett.* **65**, 563 (1990)
22. Feit, M.D., Fleck, J.A. Jr.: Spatial coherence of laboratory soft x-ray lasers. *Opt. Lett.* **16**, 76 (1991)
23. Abernathy, D.L., et al.: Small-angle X-ray scattering using coherent undulator radiation at the ESRF. *J. Synchrotron Radiat.* **5**, 37–47 (1998)
24. Tsui, O.K.C., Mochrie, S.G.J., Berman, L.E.: Statistical analysis of X-ray speckle at the NSLS. *J. Synchrotron Radiat.* **5**, 30–36 (1998)
25. Pert, G.J.: Optimizing the performance of nickel-like collisionally pumped x-ray lasers. *Phys. Rev. A* **73**, 033809 (2006)
26. Casperson, L., Yariv, A.: Pulse propagation in a high-gain medium. *Phys. Rev. Lett.* **26**, 293 (1971)

Chapter 22

Upscaling of X-Ray Laser Repetition Rate Using an OPCPA Architecture

Fei Jia, Felix Staub, and Jürg Balmer

Abstract We present a novel design of a hybrid amplification chain for pumping a Sn target producing $\sim\mu\text{J}$ coherent soft-X-ray pulses at few-Hz repetition rate. The driver aims to generate multi-joule energy at the central wavelength of 1053 nm and consists of optical-parametric chirped-pulse amplification (OPCPA) combined with diode-pumped Nd:YLF amplifiers. The soft-X-ray laser at the wavelength of 11.9 nm is produced by focusing the infrared beam into a line focus on a solid Sn target. Benefiting from this hybrid pump scheme and grazing-incidence pump geometry (GRIP), such a system has the potential to upscale the repetition rate of soft-X-ray lasers from single shot to the few-Hz region.

1 Introduction

Single-shot X-ray lasers based on collisional-excitation-pumped nickel-like ions have proved to deliver coherent photons with high brilliance and narrow bandwidth. Inspired by recent work on soft-X-ray lasers at few-Hz repetition rate [1] and driven by demands of versatile applications, novel approaches to increase the duty cycle with a more compact and affordable system are currently under study. The optical-parametric chirped-pulse amplification (OPCPA), a nonlinear technique, benefits from high gain ($\sim 10^6$), wide gain bandwidth and absence of issues due to thermal load. Combined with diode-pumped Nd:YLF rods, this hybrid amplification system provides access to deliver pulse energies up to a few Joules at repetition rates of a few Hz with pulse durations of a few ps.

In this work, numerical simulations have been performed to optimize major parameters in OPCPA and Nd:YLF amplification chains. With the pulse energy and duration from the simulations, we intend to exploit the Ni-like Sn 4d-4p laser line at 11.9 nm approaching saturation at a repetition rate of sub-10 Hz.

F. Jia (✉) · F. Staub · J. Balmer

Institute of Applied Physics, University of Bern, Sidlerstrasse 5, 3012 Bern, Switzerland

e-mail: fei.jia@iap.unibe.ch

2 Experimental Setup and Numerical Model

A schematic drawing of the OPCPA/Nd:YLF hybrid driver setup is shown in Fig. 1. A two-stage OPA, consisting of two lithium triborate (LBO) crystals in the pre-amplifier stage and a single crystal in the power-amplifier stage, is pumped by a commercial Q-switched Nd:YAG laser with a total pulse energy of 200 mJ and a pulse duration of 4.1 ns (FWHM) at the central wavelength of 532 nm. The spatial profile of the pump laser is nearly top-hat, whereas the temporal profile is Gaussian-like as naturally obtained from the Q-switched resonator. The pump beam is then separated by a beamsplitter into a ratio of 25 %/75 % for each stage, in order to maximize the pump energy extraction as well as to optimize the energy stability. Collimated with a telescope, the diameter for the two stages is 1.5 mm and 2.25 mm respectively, which corresponds to a peak irradiance of $0.7\text{--}0.8 \text{ GW/cm}^2$. These pump pulses are required to spatio-temporally overlap the stretched signal pulse. Therefore, a double-folded 4-pass stretcher is designed to stretch the signal pulse (initial pulse duration of 180 fs with 7 nm bandwidth (Origami-10)) to 1 ns with a pass-bandwidth of 2.5 nm. The purpose of over-stretching and subsequent major clipping of the signal spectrum is to reduce the gain narrowing effect in Nd:YLF. The output spectrum of the OPCPA has to be adapted into similar gain bandwidth of Nd:YLF (FWHM 1.4 nm). In this case, energy losses due to gain narrowing of an overfilled spectrum can be reduced by the pre-selection of bandwidth before the OPCPA. The few-mJ pulse from the OPA is further amplified by a 2-pass Nd:YLF amplifier and a 4-pass booster amplifier, resulting in a pulse energy of $\sim 2 \text{ J}$.

The major parameters of this hybrid amplification chain are roughly predetermined by simulations. For OPA simulation, a numerical integration of the three coupled wave equations for difference-frequency generation (DFG) in the slowly-varying-envelope approximation is used [2].

3 Results and Discussion

Electronic trigger synchronization and pulse build-up timing of Q-switch commercial pump laser are the main sources of temporal jitter in an OPCPA system. Figure 2(a) shows the measurements of jitter of the pump laser. We propose an alternative compensation method and compare it with the method proposed by Zhang et al. [3] in the same frame of simulation. The major difference in our method is the shifting of one pump pulse a few hundred ps away from the peak of the signal pulse (the dashed line in Fig. 2(b) shows the temporal shift of the pump pulse). Owing to the symmetric profile of the pump pulse, a jitter compensation mechanism is introduced naturally. By tailoring the crystal length in both stages, an optimized stability of signal gain will be achieved, shown in Fig. 2(d) where every line meets at the exit of the crystal. The reconversion-induced minor spatial profile modification will bring benefits in terms of a more homogeneous line focus. The spatio-temporal profile at the OPCPA output is introduced into the Nd:YLF amplifiers, resulting in the final

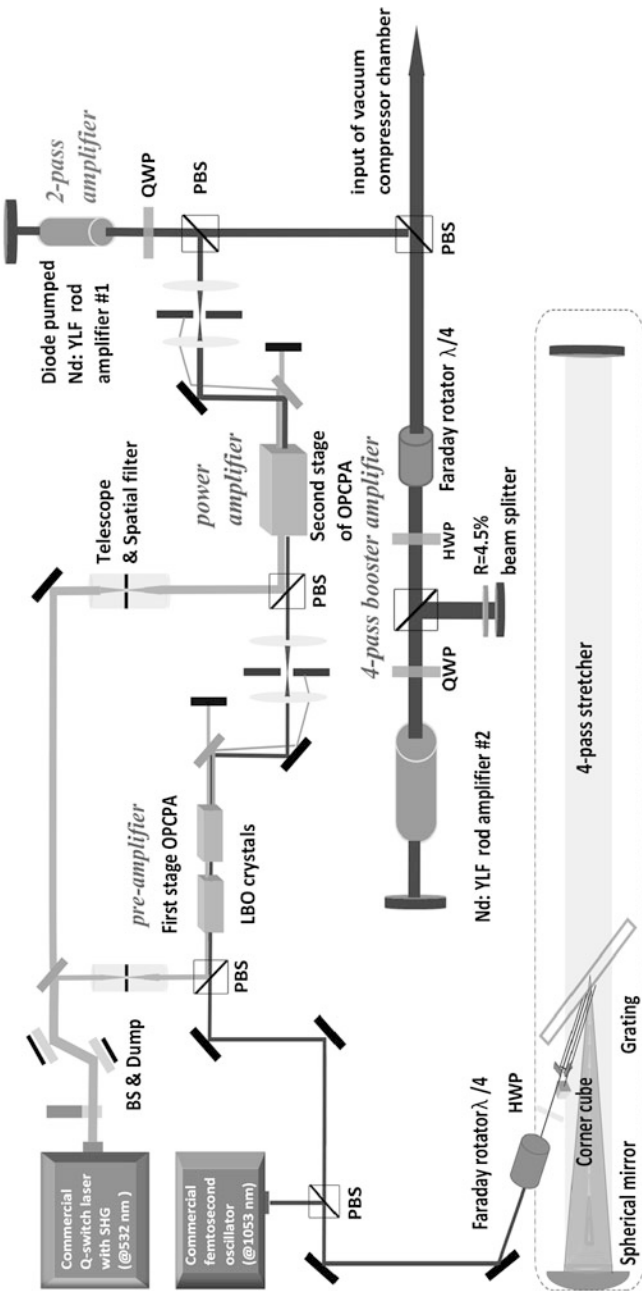


Fig. 1 Experimental setup of the OPCPA/Nd:YLF hybrid amplification system

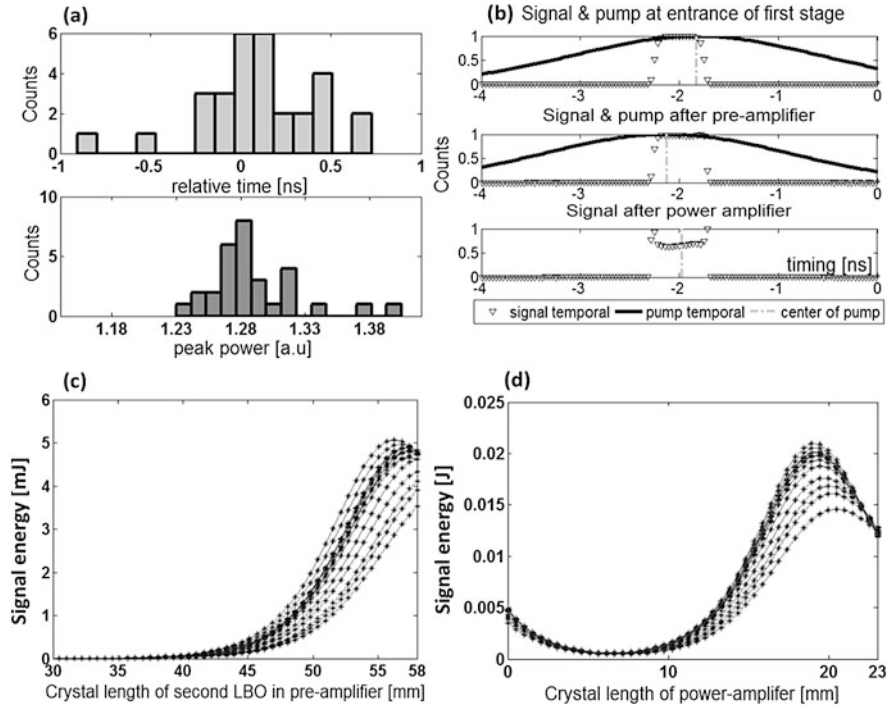


Fig. 2 Jitter compensation simulations. **(a)** Measured temporal jitter with standard deviation (StD) of 0.32 ns, and amplitude jitter StD = 0.036. **(b)** Compensation mechanism, ∇ : signal temporal profile, **(c), (d)** the OPA signal gain simulation with measured jitter values

amplified signal to reach 2 J with a transform-limited pulse duration of 1.8 ps. Based on experiments performed with our single-shot Nd:Glass TW system ('BeAGLE'), such a pump energy is able to saturate the Ni-like Sn 4d-4p (11.9 nm) laser line with a 12-mm line focus [4].

4 Conclusion

A novel tabletop sub-10 Hz coherent soft X-ray laser is under development. The OPCPA technique combined with Nd:YLF amplifiers contribute to upscale the repetition rate from single shot to a few Hz. Simulations demonstrate the feasibility of this hybrid system to deliver 2-J, 1.8-ps pulses at 1053 nm at sub-10-Hz repetition rate. Saturation of the Ni-like Sn 4d-4p laser line (11.9 nm) is expected with this energy in a 12-mm line focus. Numerical models are established for discussion on stability control methods and compression capability.

Acknowledgements This project is funded in part by the Swiss National Science Foundation (Swiss NSF).

References

1. Rocca, J.J., Wang, Y., Larotonda, M.A., Luther, B.M., Berrill, M., Alessi, D.: Opt. Lett. **30**, 2581 (2005)
2. Smith, A.V., Bowers, M.S.: J. Opt. Soc. Am. B **12** (1995)
3. Zhang, S.K., Fujita, M., Yamanaka, M., Nakatsuka, M., Izawa, Y., Yamanaka, C.: Opt. Commun. **184**, 451–455 (2000)
4. Grünig, M., Imesch, C., Staub, F., Balmer, J.E.: Opt. Commun. **282**, 267–271 (2009)

Chapter 23

Source Development of Novel Coherent X-Rays and Their Applications in JAEA

**T. Kawachi, A. Sasaki, M. Nishikino, M. Ishino, N. Hasegawa, T. Imazono,
Y. Ochi, M. Tanaka, A.Y. Faenov, T.A. Pikuz, A. Pirozhkov, T. Esirkepov,
T. Nakamura, M. Kando, S.V. Bulanov, K. Kondo, K. Janulewicz, C.M. Kim,
H. Stiel, G. Norman, T. Suemoto, T. Tomita, K. Namikawa, M. Yamagiwa,
and Y. Kato**

Abstract This paper reviews recent progress in the source development of intense coherent x-rays and the applications in the research fields such as material science and laser processing in Japan Atomic Energy Agency (JAEA). In the source development, the polarization of the fully spatial coherent 13.9 nm soft x-ray laser (SXRL) in the transient collisional excitation (TCE) scheme was investigated experimentally. The result indicated that the SXRL beam was strongly polarized in the direction perpendicular to the target surface. In the alternative schemes toward the

T. Kawachi (✉) · A. Sasaki · M. Nishikino · M. Ishino · N. Hasegawa · T. Imazono · Y. Ochi · M. Tanaka · A.Y. Faenov · T.A. Pikuz · A. Pirozhkov · T. Esirkepov · T. Nakamura · M. Kando · S.V. Bulanov · K. Kondo · M. Yamagiwa · Y. Kato
Quantum Beam Science Directorate, JAEA, 8-1-7 Umemidai, Kizugawa, Kyoto 619-0215, Japan
e-mail: kawachi.tetsuya@jaea.go.jp

A.Y. Faenov · G. Norman
Joint Institute for High Temperatures, Russian Academy of Science, Izhorskaya st. 13 Bd. 2,
Moscow, Russia

K. Janulewicz · C.M. Kim
Advanced Photon Research Institute, GIST, Cheomdan-gwagiro, Buk-gu, Gwangju 500-712,
Republic of Korea

H. Stiel
Max-Born Institute for Nonlinear Optics and Short Pulse Spectroscopy, Max-Born-Strasse 2a,
12489 Berlin, Germany

T. Suemoto
Institute of Solid State Physics (ISSP), University of Tokyo, 5-1-5 Kashiwanoha, Kashiwa, Chiba
277-8581, Japan

T. Tomita
Faculty of Engineering, University of Tokushima, 2-1 Minamijo-Sanjima, Tokushima 770-8506,
Japan

K. Namikawa
Research Institute for Science & Technology, Tokyo University of Science, 2641 Yamazaki,
Noda, Chiba 278-8510, Japan

short wavelength region, intense higher-order harmonics with the photon energy of more than 300 eV was observed from a relativistic plasma generated with the laser intensity higher than 10^{18} W/cm^2 . In the applications of the 13.9 nm TCE laser, we observed temporal evolution of surface distortion of Pt sample pumped by a 80 fs optical pulse by use of x-ray laser interferometer using double Lloyd's mirrors and reflectometer. In the study of SXRL ablation, the melting depth of the substances using single shot SXRL exposure was measured, and the result was quantitatively consistent with the calculated result based upon the spallative ablation model by molecular-dynamics code.

1 Introduction

Several years ago, we have firstly demonstrated fully spatial coherent x-ray laser beam at the wavelength of 13.9 nm by the method of double targets geometry, in which the first gain medium works as the soft x-ray oscillator and the second gain medium works as the soft x-ray amplifier [1]. Now this novel light source with pico-second duration and more than 10^9 coherent photons/pulse is routinely used for the wide variety of research fields such as material science [2], atom and molecular science [3], soft x-ray imaging [4], laser ablation physics and laser processing [5].

In a view point of the source development, one of the most serious limitations so far is the lasing wavelength, and the extension of the lasing wavelength to shorter region is urgent subject. Another important issue is to have deeper understanding of characteristics of x-ray amplifier plasmas, because under the coupling of x-ray seeder with x-ray amplifier, the final beam quality is determined by plasma parameters such as density gradient, homogeneity etc., of the x-ray amplifier plasma. Polarization characteristics is one of the parameters, and the polarization transport in x-ray amplifier is important in the applications of SXRL beam with higher-order harmonics x-ray seeder and double target geometry.

In the applications of the SXRLs, observation of *non-periodic* or *unrepeatable* ultra-fast phenomena such as nano-meter scale deformation of domain structure of substances under the phase transition or surface distortion in laser ablation are quite attractive application in terms of full use of the advantages of plasma x-ray lasers. In order to apply the SXRL beam to this field, we have developed x-ray laser interferometer, which enable us to obtain surface information with 1 nm depth-resolution and 7 ps temporal resolution. On the other hand, the study of SXRL ablation (EUV ablation) has created feasible opportunities for technological breakthrough in the research field of laser surface nano-processing and for fundamental investigations of materials in warm dense matter state. The experimental data obtained through this study can provide good benchmarks for theoretical codes and contribute to understand the laser matter interaction.

In this paper, we describe recent progress in the source development of coherent soft x-rays and the applications in Japan Atomic Energy Agency (JAEA).

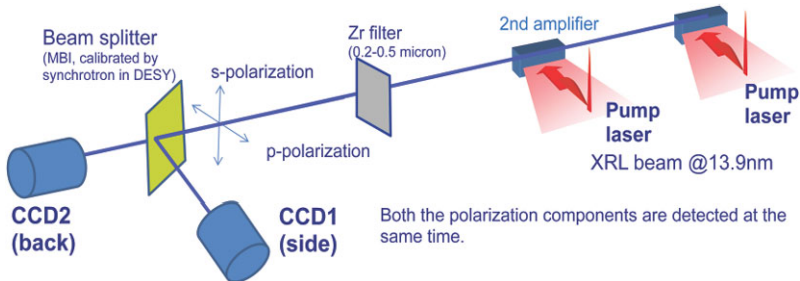


Fig. 1 Experimental-set up for measurement of the polarization

2 Source Development of Novel Coherent X-Rays

2.1 Observation of Polarization of SXRL in Transient Collisional Excitation Scheme

The polarization of plasma x-ray lasers is determined by the summation of plasma anisotropy as the polarization processes such as anisotropic collision, radiation trapping and depolarization processes such as collisional magnetic-sublevel-mixing and localized plasma electric-field. Through polarization measurement, we may obtain the information about the anisotropic feature in plasma and about the polarization transport in x-ray amplifier. The polarization of collisional excitation lasers has been measured for quasi-steady state scheme [6], however there are few reports for transient excitation scheme. Recently concerning with the x-ray amplifier coupled with higher-order harmonics as x-ray seeder, theoretical investigation of polarization transport has been studied, which implies the importance of the information of polarization characteristics of the x-ray amplifier [7]. In order to measure the polarization characteristics of TCE gain medium plasma, we conducted an experiment under the collaboration with APRI-GIST and MBI. Figure 1 is the experimental set-up. The SXRL beam at the wavelength of 13.9 nm passes through a Zr filter to cut visible light and is divided into two polarization components by a Mo/Si multi-layer free-stand soft x-ray beam splitter (BS) fabricated in MBI. The reflectance and transmittance, together with the polarization separation ratio of this BS has been calibrated using synchrotron radiation source. Here *s*- and *p*-polarization component means that the direction of electric field is parallel and perpendicular to the target surface, respectively. We observed the two polarization components at the same time by use of two charged couple devices (CCDs).

We measured the polarization degree, P , $P = (I_p - I_s)/(I_p + I_s)$, for three cases, i.e., XRL from the first target, the second target, and the double target geometry.

Figure 2 shows the experimental result. It was found that the SXRL in the TCE scheme was strongly polarized, $P \sim 0.8$, in the direction perpendicular to the target surface. For the double target case, the tendency was the same however, the polarization degree was slightly lower ($P \sim 0.65$), which might attribute to the gain

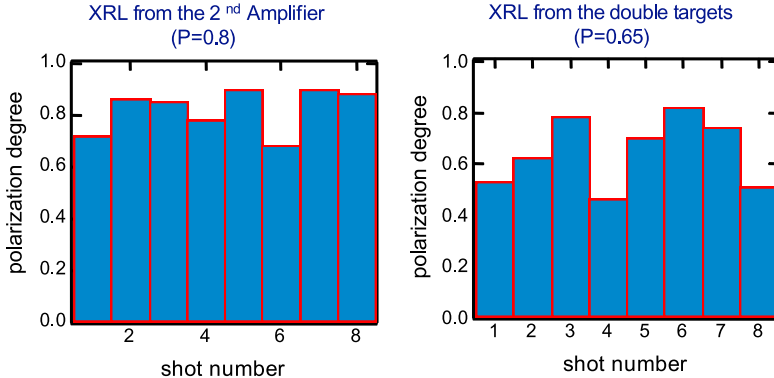


Fig. 2 Measured polarization degree for the second target (*left*), and double target (*right*)

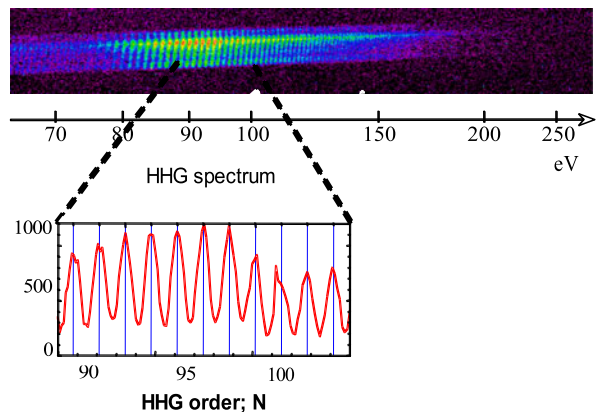
saturation effect. Detailed analysis of the result using ray-trace code is now going on.

2.2 Observation of Higher-Order Harmonics Emission from Relativistic Plasma

In JAEA, several attempts toward shorter wavelength lasing have been studied [8, 9]. Recently higher-order harmonics generation experiment using ultra-intense laser pulse was conducted. A He gas target with the gas density of around 10^{19} cm^{-3} was irradiated by J-KAREN laser which provided 0.4–1 J, 27–40 fs pulse with the focusing intensity of around $4 \times 10^{18} \text{ W/cm}^2$. The charged particles from the He plasma were ejected by the bending magnet, and the x-ray emission from the plasma was observed by grazing incidence spectrometers. Figure 3 shows the spectrum obtained in this experiment. Higher-order harmonics signal up to the order of $N = 180$ were clearly observed. One of the interesting features was that we had even-number order of the harmonics together with the odd-number order. This means this emission is not originated from the atomic HHG. Observation using another spectrometer which covered shorter wavelength region showed that the signal extended to the water-window region.

Present higher-order harmonics is quite different from other coherent sources such as atomic higher-order harmonics, nonlinear Thomson scattering and betatron radiation. We performed 3D PIC (particle-in-cell) simulation to explain the present results. The result of the calculation shows due to the ponder-motive force and Lorentz force induced wake wave and bow wave together with laser-induced modulation generates high density spikes in the plasma. This localized high density regions are collectively oscillated under the laser electric field, resulting in the generation of the higher-order harmonics. Following this model, as the laser intensity is increased, the expected photo energy of higher-order harmonics becomes larger,

Fig. 3 Obtained HHG spectrum. Up to $N = 180$, HHG signal are clearly resolved. The decrease of the signal for the photon energy larger than 200 eV is due to poor efficiency of the spectrograph



and the upper limit of the laser intensity may be determined by radiation damping regime with the laser intensity of around 10^{23} W/cm^2 . This means this scheme can become one of the feasible candidates for generating intense coherent x-ray in 10 keV range.

3 Application of SXRLs

The 13.9 nm laser in JAEA has been used for wide variety of application researches, such as material science, plasma physics, atom and molecular physics, ultrafast soft x-ray imaging and laser processing under the collaborations with universities and other institutes. In these applications, we choose two examples and describe the recent progress: The first one is the development of x-ray laser interferometer for probing surface dynamics, and the second is the study of SXRL ablation of substances.

3.1 X-Ray Laser Interferometer for Probing Surface Dynamics

Schematic figure of the x-ray interferometer is described in Ref. [10]. A Pt sample was pumped by an IR pulse with the Gaussian spatial profile of the spot size of 60 μm , duration of 80 fs, and the peak intensity of $5 \times 10^{13} \text{ W/cm}^2$. The SXRL probe beam illuminated the pumped region, and this probe beam with having the information of the surface deformation, was reflected by the imaging mirror and went to the double Lloyd's mirrors. Here the probe beam was divided into two parts, one had the information of surface deformation and the other was used as the reference, and the two components were merged at the detector (CCD) at the distance of about 5 m. The resolution of this interferometer was tested using a Si sample with several 6 nm-depth grooves on the surface, and the depth and lateral resolution was determined to be 1 nm and 1.5 μm , respectively. Using double time fiducial technique,

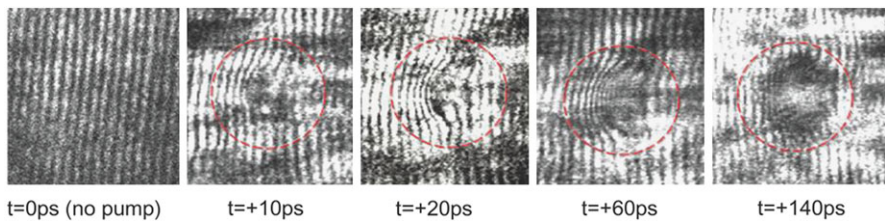


Fig. 4 Temporal evolution of interference patterns of Pt surface pumped by 80 fs-duration Gaussian optical pulse

temporal synchronization of the pumping IR pulse and SXRL probe was achieved to be better than 2 ps.

Figure 4 shows the temporal evolution of the interference pattern as the function of the delay time of the SXRL probe. Our observation shows even in the time of 10 ps, fringe shift can be seen. The absence of the fringe shift in the central portion is due to that the higher fluence of the pump laser (more than 1 J/cm^2) destroys and ionizes the surface in the early time region. This is consistent with observation using soft x-ray reflectometer.

The pumping area may be categorized into 3 areas: (a) The central portion with the fluence larger than 1 J/cm^2 , (b) middle region with 0.4 to 1 J/cm^2 , and (c) outer region with the fluence of around laser ablation threshold. We could see a ring structure in region (c), whose reflectivity was low even in early time region. This temporal behavior of the reflectivity was similar to that of region (a), whereas for region (b) the reflectivity decreased slowly. Detailed analysis using theoretical code will be published elsewhere.

3.2 The Study of SXRL Ablation of Substances

Laser ablation has many technological applications in material processing and nano-structure fabrication. The laser-induce damage of the materials has been intensively studied and its dependence upon the pulse width, the photon energy, and the fluence has come to be understood. Furthermore novel light source in soft x-ray region, i.e., laser-based SXRL and X-FEL, provides new possibility of laser processing, and it is urgent subject to have understanding of the interaction between intense soft x-ray and substances. Recently we found that the threshold fluence value for the ablation of Si and LiF crystal using pico-second duration SXRL pulse was smaller by 2–3 orders magnitude than that of IR and visible laser case. This was qualitatively explained by spallative ablation model: Molecular dynamics simulation shows that SXRL absorption increases temperature of surface layer of the material, and if the heating time is shorter than the heat transport (sonic) time then the temperature growth increases the tensile stress in the material which induces the spallation of the surface layer.

Fig. 5 SEM image of the irradiation area of Aluminum sample under the laser fluence of 30 mJ/cm^2

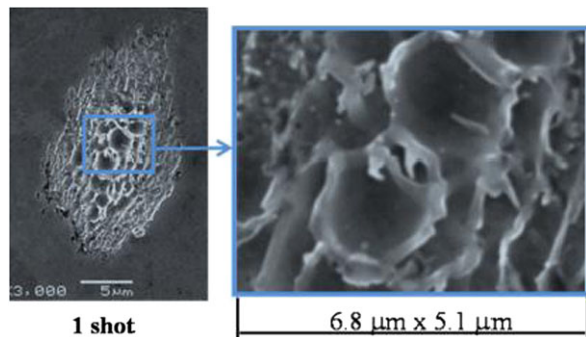
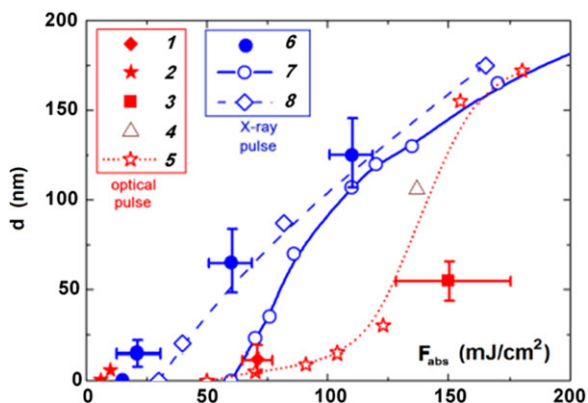


Fig. 6 Fluence dependence of the melting depth of the Au sample. Solid circle is the experimental result and dashed line is the result by molecular dynamics simulation, which is consistent with the experiment



For the quantitative analysis, we measured the depth of melting region of Au and Al in the single-shot SXRL exposure. Figure 5 shows SEM images of typical irradiation area of Al samples. AFM analysis of these irradiation area shows the surface is the mixture of splashed molten metals and hole induced by removed metal from the surface. The measured melting depth of Au is plotted as the function of the fluence in Fig. 6. The blue solid circle and blue dashed line are the present experimental result and the theoretical calculation, respectively. Other experimental result using IR and optical pulse together with the calculation is also added (red marks and lines). Comparison with the present experimental result and the theoretical calculation implies that spallative ablation model is good explanation of the present experimental result.

Acknowledgements This work is partly supported by auspices of Japan Grant-in-Aid for Scientific research, Kiban (B), No. 25289244.

References

1. Tanaka, M., et al.: X-ray laser beam with diffraction-limited divergence generated with two gain media. Opt. Lett. **28**, 1680–1682 (2003)

2. Namikawa, K., et al.: Direct observation of the critical relaxation of polarization clusters in BaTiO₃ using a pulsed x-ray laser technique. *Phys. Rev. Lett.* **103**, 197401 (2009)
3. Namba, S., et al.: Enhancement of double Auger decay probability in Xe clusters irradiated with a SXRL pulse. *Phys. Rev. Lett.* **99**, 043004 (2007)
4. Suemoto, T., et al.: Single-shot picosecond interferometry with one-nanometer resolution for dynamical surface morphology using a soft x-ray laser. *Opt. Express* **18**, 14114 (2010)
5. Faenov, A.Ya., et al.: Low-threshold ablation of dielectrics irradiated by picosecond soft x-ray laser pulses. *Appl. Phys. Lett.* **94**, 231107 (2009)
6. Kawachi, T., et al.: Observation of polarization of the soft x-ray laser line in neonlike germanium ions. *Phys. Rev. Lett.* **75**, 3826–3829 (1995)
7. Kim, C.M., et al.: Pulse buildup from noise and intrinsic polarization of plasma-based x-ray lasers. *Phys. Rev. A* **84**, 013834 (2011)
8. Kando, M., et al.: Demonstration of laser-frequency up-shift by electron-density modulation in a plasma wakefield. *Phys. Rev. Lett.* **99**, 135001 (2007)
9. Kawachi, T., Kato, Y.: Resonant photo-pumping x-ray laser scheme using intense characteristic x-rays for water-window radiation generation. *Phys. Rev. A* **84**, 063848 (2011)
10. Kawachi, T., et al.: Source development and novel applications of laser driven plasma x-ray lasers in JAEA. In: *Proceedings of X-Ray Lasers 2010*. Springer Proceedings in Physics, vol. 136, pp. 15–24 (2010)

Chapter 24

Characterization of Zn X-Ray Laser at PALS Centre, Its Applications in Dense Plasma Probing and Astrophysics

**M. Kozlova, J. Nejdl, M. Krus, J. Prokupek, J. Dostal, B. Rus, A. Klisnick,
L. Meng, F. Tissandier, C. Stehlé, R. Lefevre, U. Chaulagain, N. Champion,
P. Barroso, F. Reix, P. Jagourel, J. Larour, F. Delmotte, C. Constancias,
F. Suzuki-Vidal, and O. Acef**

Abstract This report presents the results from experiments at PALS Centre using a Zn X-ray laser with the pulse length of 0.15 ns and the wavelength of 21.2 nm, working in single or double pass regime with the output energy of 0.4 mJ or 4 mJ per pulse, respectively. The current X-ray laser was experimentally examined to obtain its temporal coherence and spectral width using a path-difference interferometer.

M. Kozlova (✉) · J. Nejdl · M. Krus · J. Prokupek · J. Dostal · B. Rus
IoP/PALS Center, Prague, Czech Republic
e-mail: kozlova@fzu.cz

A. Klisnick · L. Meng
ISMO, Uni. Paris Sud, Paris, France

F. Tissandier
LOA, Ecole Polytechnique, CNRS, Paris, France

C. Stehlé · R. Lefevre · U. Chaulagain · N. Champion
Lerma, Observatoire de Paris, UPMC, CNRS, Paris, France

P. Barroso · F. Reix · P. Jagourel
GEPI, Observatoire de Paris, Univ. Paris-Diderot, CNRS, Paris, France

J. Larour
LPP, Ecole Polytechnique, UPMC, CNRS, Palaiseau, France

F. Delmotte
LCF, Institut d'Optique, CNRS, PXI, Palaiseau, France

C. Constancias
CEA-LETI, Grenoble, France

F. Suzuki-Vidal
Imperial College, London, UK

O. Acef
SYRTE, Observatoire de Paris, UPMC, CNRS, LNE, Paris, France

The double pass regime shows that QSS plasma based source-amplifier is promising for “short” fs soft X-ray pulses. The X-ray laser is commonly used for user’s experiments. Its advantages can be shown in applications such as probing of dense plasmas (up to $2.5 \times 10^{24} \text{ cm}^{-3}$) or single shot experiments (4×10^{14} photons/pulse). The simple technique based on Talbot effect was used to obtain the gradients of electron densities of line plasmas produced under conditions corresponding to XRL’s amplifiers operating in TCE and QSS regime. To investigate radiative shock wave in laboratory is challenging in aspects of the optimization of experimental parameters. Due to the high electron density (10^{22} cm^{-3}) produced in the gas medium propagated by the shock wave, the velocity of the shock wave, and the absorption losses on optical elements, it is necessary to use the energetic single shot probe.

1 Introduction

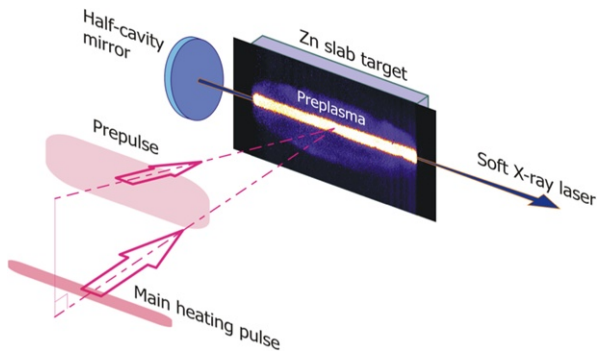
Coherent and high-brightness radiation sources at very short wavelengths are a tool of significant interest in future studies of dense and/or highly ionized plasmas. Among the prospects offered by these sources, there are both novel plasma-probing techniques able to access extremely high densities and provide nanometer spatial resolution, as well as new ways of generation of extremely dense and highly ionized plasmas, previously inaccessible in laboratory conditions. This report describes the XRL, which was implemented with a goal to produce as great amount of energy as possible near the wavelength of 20 nm, use the energetic XRL for imaging, and to probe dense plasmas.

2 Characteristics of Ne-Like Zn X-Ray Laser at PALS Centre

Over past decade, the most energetic XRL is delivered at Prague Asterix Laser System (PALS) Centre [1]. The pumping iodine laser emitting at $1.3 \mu\text{m}$ has total energy about 1 kJ. The pumping beam is split into two beams, prepulse and main pulse, and this sequential generation of the XRL (see Fig. 1) can provide output energies up to 10 mJ.

Several pumping schemes were examined to generate the XRL (Ne-like Fe, Zn, Se and Ni-like Ag), but the most robust and the most emitting schema is Ne-like Zinc. The population inversion is produced between $2p^5 3p$ and $2p^5 3s$ fine-structure levels of Ne-like ions, through electron collisional excitation from the Ne-like ground state $2p^6$. The inversion is maintained by strong radiative dipole decay from the $3s$ levels back to the ground state while the upper $3p$ levels are metastable with respect to this process. Under appropriate plasma conditions, the strongest population inversion is generated (due to the highest monopole electron excitation rate from the ground) for the transition $(2p_{1/2}^5 3p_{1/2})J = 0 \rightarrow (2p_{1/2}^5 3s_{1/2})J = 1$, corresponding in Ne-like zinc to the wavelength of 21.22 nm. The intensity and beam profile emitted by this type of XRL strongly depends on the density profile of the

Fig. 1 Sequential pumping of the XRL amplifier, where the typical ratio of the prepulse ($<10^{11} \text{ W cm}^{-2}$) and the main pulse ($\sim 10^{13} \text{ W cm}^{-2}$) is about 10^{-3} . Half-cavity mirror is placed on one side of the Zn slab target to boosts output energy

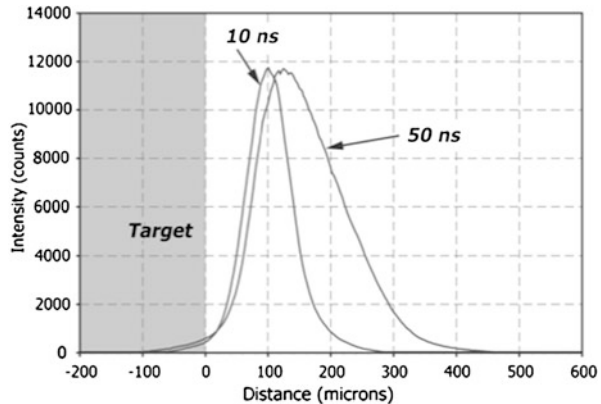


amplifying plasma, as the largest population inversion on the $J = 0-1$ transition occurs at high electron densities. To reduce density gradients in the plasma ablated by a laser from a massive slab target, a technique, consisting of applying a prepulse typically a few nanoseconds prior the main heating pulse, is employed [2–4]. The parameters of the prepulse relative to the main pulse are one of the key features determining the functionality of the XRL and characteristics of the emitted beam. Two configurations where a weak prepulse is applied 10 ns or 50 ns ahead of the main pulse will be discussed. The prepulse is delivered and focused separately to produce a wide pre-plasma column into which the main pulse, focused much more tightly, is coupled (see Fig. 1). The configuration where the prepulse is 10 ns ahead can be operated in single or double-pass regime. The typical value of energy (double-pass regime) is 4 mJ with peak power 40 MW and with 3×10^{14} photons per pulse. The 10 ns configuration is the most stable and robust, and at PALS is provided as the user beamline. In order to increase the energetic output of the XRL, the longer prepulse delays were investigated. The best results were observed for 50 ns prepulse delay operated in double-pass regime. This was studied by the streak camera and near-field measurements. While the streak camera records indicate comparable kinetics of the excited levels for both regimes, from the near-field data, it is found out that the 50 ns prepulse delay can generate $2\times$ larger (in the direction perpendicular to the target) amplification region than in 10 ns regime (see Fig. 2). Therefore the energy measured for 50 ns prepulse delay is 10 mJ with peak power 100 MW and with 1.2×10^{15} photons per pulse.

3 Further Characterization of the Ne-Like Zn X-Ray Laser

Using the Zn XRL as the user beamline requires a detailed characterization of its output parameters such as the energy, the pulse length etc. In addition to routine monitoring parameters, the spectral profile and linewidth were explored. The bandwidth of the Zn XRL is extremely narrow, about 10^{-4} , therefore direct measurement is beyond capabilities of existing spectrometers in XUV range. Hence, the wavefront-splitting interferometer [5, 6] was used to measure temporal coherence

Fig. 2 Near-field profiles in the direction perpendicular to the target (integrated over lateral FWHM width) for the 10 ns and 50 ns pumping configurations



of the source from which the spectral linewidth is inferred. The experimental setup is shown in Fig. 3. The XRL beam, operated in double-pass regime (better spatial coherence expected), was send either to the footprint to monitor spatial intensity distribution and alignment, or to the interferometer. The direct light from the plasma was blocked by Al filter after multilayer mirror.

Two sets of data were acquired for the distance between the source and the interferometer (5 m and 7 m). The distance of the interferometer and the camera was, in both cases, 1.5 m and the tilt of the camera was 35 degrees.

The spectral linewidth ($\Delta\lambda$) is given by

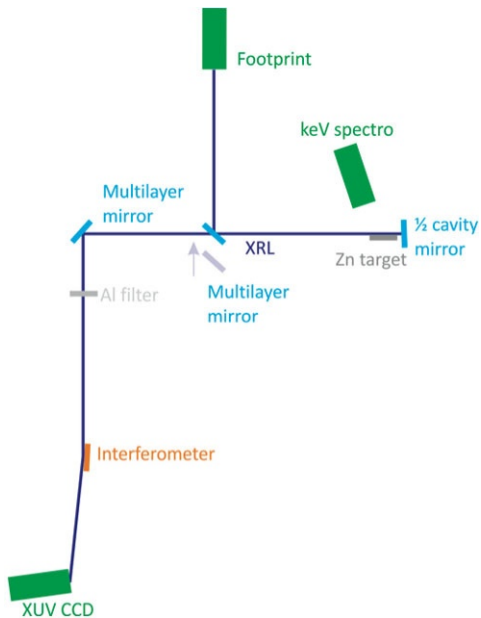
$$\Delta\lambda = \frac{\lambda^2}{c} \Delta\nu \quad (1)$$

where λ is XRL wavelength. The coherence time ($\Delta\nu$) can be measured by the variation of the path difference between dihedron mirrors. This measurement resulted in 0.7 ps and 1 ps for distance of 5 m and 7 m, respectively. According to Eq. (1), the corresponding spectral linewidths are 11.3 mA and 7.7 mA. The measured data of the coherence time leading to a Fourier transform limit of the duration below 1 ps, which is much smaller than duration of the duration of the SXRL and potentially it indicates the possibility of the amplification of sub-picosecond duration [7].

4 The Zn X-Ray Laser as a Powerful Tool to Probe Dense Plasmas

Because of natural constraint, the electromagnetic radiation can propagate through the plasma only if the electron density does not reach the critical density that scales as λ^{-2} . Therefore, one is obliged to use the short-wavelength probe in order to investigate the region close to the critical density for VIS or UV laser light where a lot of interesting phenomena occur. Besides the wavelength criterion, the probe beam must be bright enough to overcome the thermal radiation of the investigated

Fig. 3 The sketch of the experimental scheme. The XRL beam is either sent to footprint or to the interferometer



plasma. Therefore the most suitable plasmatic sources for dense plasma probing are X-ray K-alpha radiation sources, or X-ray lasers [8] emitting in soft X-ray or extreme ultra-violet range [9].

4.1 Deflectometry of the Dense Plasmas

This paper introduces a new simple deflectometric technique that enables to resolve the gradients in both directions of the projection plane using the deformation of the Talbot pattern of a single 2D grating. The simplicity and low demands on spatial coherence of the probing beam enables the use of this method in complex experiments where the previous techniques would not be acceptable. The probing technique is based on a modification of the Talbot reconstruction of the 2D grating, caused by density gradients in the probed plasma. The suggested experimental setup is a simple modification of the setup used for X-ray laser backlighting [10]. The plasma is imaged on a CCD camera with sufficiently high magnification, so that good spatial resolution is achieved. The pinhole is placed in the position of the probing source image in order to eliminate most of the plasma self-emission and enhance the signal-to-noise ratio. The size of the pinhole must be set as a compromise between this ratio and maximum detectable wave-front tilt (maximum detectable density gradient). The 2D grating is placed between the pinhole and CCD so it has its first Talbot sub-plane (or plane) on the CCD. The simplified experimental setup is shown in Fig. 4.

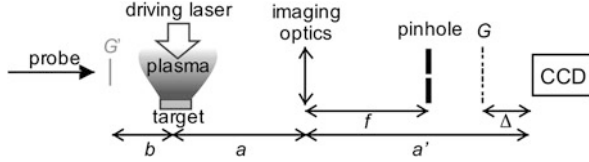


Fig. 4 Experimental setup of the density gradient measurement. a is a object distance, a' is the image distance, f denotes focal length of the imaging element, Δ is the distance between 2D grating and CCD. G' denotes the virtual image of grating G that is placed at a distance b in front of the probed plasma

The beam of the Ne-like zinc X-ray laser emitting at 21.2 nm [1] was used as a probe beam, operating in the single pass regime with the 150 ps (FWHM) pulses of 0.4 mJ estimated energy in a pulse. The Mo-Si multi-layer spherical mirror with $f = 300$ mm was used to image the plasma on back-illuminated X-ray CCD with magnification factor $M = 5.5$. The pinhole of the diameter of 0.5 mm was put to the image of the XRL source in order to reduce the signal of plasma self-emission [10]. The XRL source was 2800 mm from the imaging mirror. Then the 100 μm -period laser-drilled 2D grating made of 5 μm thick steel sheet was placed to the distance $\Delta = 980$ mm from the CCD, i.e. the higher sensitivity and worse spatial resolution configuration for the first Talbot sub-plane ($q = 1$) was used. The plasma was created by the focusing sequence of two pulses in order to create similar plasma conditions on solid target as with XRL sequence. The linear plasma was created by 80 J@250 ps pulse of 1.3 μm laser by pair of cylindrical and spherical lenses with focal lengths of 6 m and 1.2 m, respectively, into the 150 μm -wide and 1.5 mm-long line, overfilling the 1 mm-wide slab in order to produce uniform irradiation on the target with intensity of $4 \times 10^{13} \text{ W cm}^{-2}$. The plasmas created by irradiation of Zn, Fe, and Au slabs were investigated. The recorded pattern $\Phi(x, y)$ is related to density gradient ∇n via the formula

$$\int_0^L \nabla n(x, y, z) dz = \Phi(x, y) \quad (2)$$

where L is the length of plasma. If plasma is regarded as uniform in probing direction, Eq. (2) can be simplified to $L \nabla n(x, y) = \Phi(x, y)$ and supposing $n_e \ll n_c$ the relation $\nabla n_e(x, y) = -2n_c \Phi(x, y)/L$ could be employed. The recorded patterns and evaluated electron density gradient maps for Zn are shown in Fig. 5, for Fe in Fig. 6 and for Au in Fig. 7. All presented plasmas were probe 0.3 ns after auxiliary main pulse arrived to the target.

4.2 XUV Probing of the Laser Driven Radiative Shocks

Using high-energy lasers, the radiative shocks can be produced in gases. For instance, the laser intensity about $10^{14} \text{ W cm}^{-2}$ permits to generate shocks propagating at $\sim 50 \text{ km s}^{-1}$ in gases at low pressure and to produce interesting phenomena

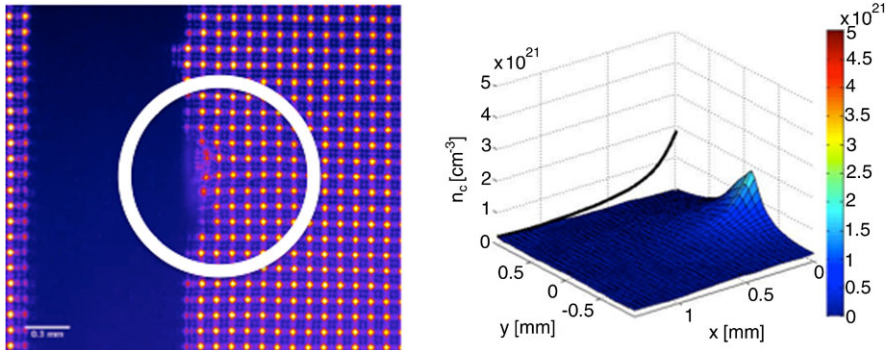


Fig. 5 The example of recorded pattern (left) of the Zn plasma created on 1 mm solid target by sequence of prepulse ($I = 4 \times 10^{10} \text{ W cm}^{-2}$) and main pulse ($I = 4 \times 10^{13} \text{ W cm}^{-2}$), where the prepulse is 10 ns ahead to main pulse, and the corresponding electron density map (right)

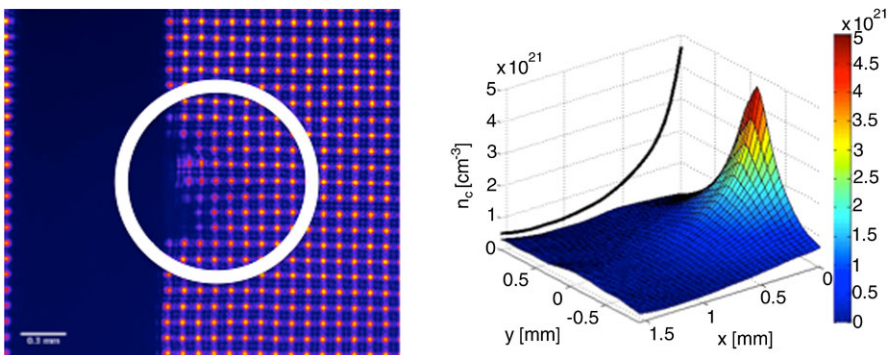


Fig. 6 The example of recorded pattern (left) of the Fe plasma created on 1 mm solid target by sequence of prepulse ($I = 4 \times 10^{10} \text{ W cm}^{-2}$) and main pulse ($I = 4 \times 10^{13} \text{ W cm}^{-2}$), where the prepulse is 10 ns ahead to main pulse, and the corresponding electron density map (right)

like ionization wave, also called radiative precursor [11]. In such environment, the electron density may be up to 10^{23} cm^{-3} and thus is difficult to probe it using long wavelength light such as VIS. To be able to probe electron densities close to critical density, the critical density of probe must be $10\times$ higher than the investigated electron density. The critical density of the Zn XRL is about 10^{24} cm^{-3} , which makes it a very promising tool for investigation. Although, all the requirements on the probing beam is fulfilled, the X-ray shadowgraphy is a very delicate and requires a high quality of all used components such as filters, mirrors, windows or membrane of closing the gaseous targets. Recent experiments performed at PALS laser facility in 2010 and 2011 reveal the critical optical elements, which are necessary for such study. In Fig. 8 is schematically shown the experimental setup.

Probe beam enters and exits the gaseous target through membranes which must be transparent enough, to do not absorb all XRL signal, and sturdy enough to with-

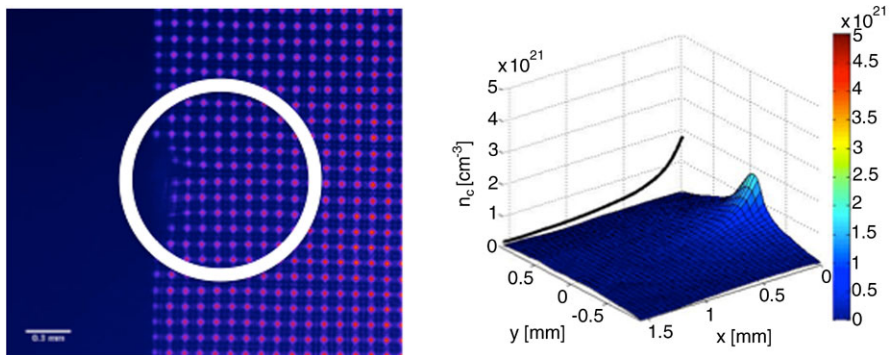


Fig. 7 The example of recorded pattern (*left*) of the Au plasma created on 1 mm solid target by sequence of prepulse ($I = 4 \times 10^{10} \text{ W cm}^{-2}$) and main pulse ($I = 4 \times 10^{13} \text{ W cm}^{-2}$), where the prepulse is 10 ns ahead to main pulse, and the corresponding electron density map (*right*)

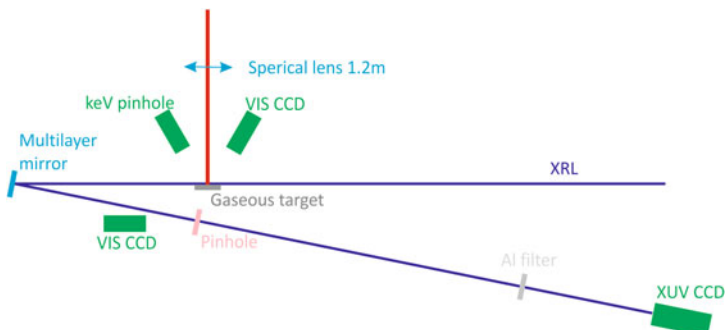


Fig. 8 The experimental schema. The auxiliary beam @1.3 micron is focused on Au/CH piston and launches the shock. 20 ns after the shock start propagating is investigated by XRL. The modifications of transmissivity are imaged on the CCD with magnification 5.5

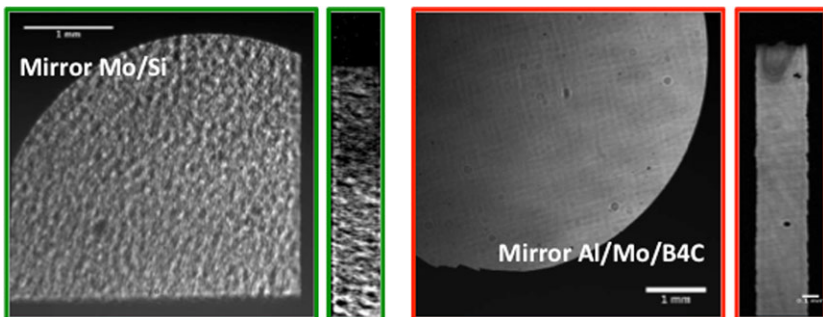


Fig. 9 The image of XRL reflected by Mo/Si multilayer mirror (*left*), Al/Mo/B4C multilayer mirror (*right*) and corresponding images of shock waves

stand a difference of pressure of 0.5 bar (inside the target) and 0 bar outside, without leakage. In order to have the smallest energetic losses, the Si₃N₄ membrane was used ($T = 0.017$ @21.2 nm). The imaging mirror must have a good and uniform reflectivity at given wavelength. In Fig. 9, there are shown two examples of imaging mirrors and corresponding shadowgrams of the shocks. On left part (see in Fig. 9) the front of the shock wave is almost not distinguishable due to strong perturbations coming from Mo/Si mirror. To enhance the mirror quality the new Al/Mo/B4C multilayer mirror was used [12]. The difference is obvious, see in Fig. 9 (right).

5 Conclusion

At conclusion, the work at PALS facility over past decade, led us to provide the most energetic X-ray source as standard user beamline, delivering up to 10 mJ. Beside the standard characteristics of the XRL beam, the linewidth measurement was done and it indicates the possibility of amplification of pulses below 1 picosecond. These results are in good agreement with calculations. It was shown that the Zinc X-ray laser is powerful tool to probe dense plasmas. The electron densities of various elements were measured by deflectometry technique. The results will be used as benchmark data for ARWEN code. Also the XRL beam was used to investigate the radiative shock waves. The critical elements of the experimental setup are the optical components. The dramatic improvement in the pattern contrast was presented.

Acknowledgements This work was partially supported by the by the Czech Ministry of Education, Youth and Sports (projects 7E08099 and 7E09092), and from the European Union (EU) Seventh Framework Programme (LASERLAB-EUROPE, grant agreement 228334).

References

1. Rus, B., et al.: Phys. Rev. A **66**, 063806 (2002)
2. Nilsen, J., et al.: Phys. Rev. A **48** (1993)
3. Cairns, G.F., et al.: In: Proc. 4th Int. Coll. on X-Ray Lasers, vol. 332, p. 289 (1994)
4. Rus, B., et al.: In: Proc. 4th Int. Coll. on X-Ray Lasers, vol. 332, p. 152 (1994)
5. Klisnick, A., et al.: JQSRT **99** (2006)
6. Guilbaud, O., et al.: EPJD **40** (2006)
7. Meng, L., et al.: In: These proceedings
8. Tallents, G.J., et al.: Laser Part. Beams **20**, 201–209 (2002)
9. Nejdl, J., et al.: Plasma Phys. **17** (2010)
10. Kozlová, M., et al.: In: Springer Proceedings in Physics, vol. 130, p. 417 (2009)
11. Stehle, Ch., et al.: Opt. Commun. **285** (2012)
12. Meltschakov, et al.: Proc. SPIE **8168** (2011)

Chapter 25

Development of High Reflective Multilayer Mirrors at “Water Window” Wavelengths in IPOE

Haochuan Li, Jingtiao Zhu, and Zhanshan Wang

Abstract Some X-ray sources for laboratory near “water window” wavelengths have been developed. High reflective multilayer mirrors are required. In this wavelength region, Cr/Sc, Cr/Ti, Cr/V and Cr/C are promising for high reflective multilayer mirror. The layer thickness is typically about 1.0 nm. We have deposited Cr/C and Cr/Sc multilayers for $\lambda = 4.48$ nm and reflectance of 15.2 % was obtained for Cr/C at near normal incidence. We also show that the interface of Cr/Ti multilayers can be significantly improved by inserting B₄C as diffusion barrier layer. In this report, high-reflective multilayer mirrors with and without barrier layer were deposited by using magnetron sputtering method. The reflective properties of the multilayer mirror were measured by using synchrotron radiation.

1 Introduction

Multilayer-based reflective optics in the extreme ultraviolet and soft x-ray region has tremendously progressed in the past three decades, which has been widely used in EUV lithography, x-ray astronomy, soft x-ray microscopy and synchrotron radiation instruments [1]. In the “water window” wavelength ($2.3 \text{ nm} < \lambda < 4.3 \text{ nm}$), great opportunities emerge in microscopy of biological samples with both high contrast and high resolution [2]. High reflective coatings are needed for laboratory “water window” light source.

In the “water window” wavelengths, C, Sc, Ti, V are suitable spacing layer material near their respective absorption edges. State-of-the-art Cr/C [3] and Cr/Sc [4] multilayers have near-normal reflectance of about 13% and 20% respectively. Ti-based [5] and V-based [6] multilayers are still under-developed with reflectance of 2 %-3 %.

In this paper, we present the development of ultra-thin multilayers near “water window”. Cr/C and Cr/Sc multilayers were prepared for $\lambda = 4.48$ nm and measured at BESSY II. Reflectance of 15.2 % was obtained for the Cr/C one. Cr/Ti multilayers

H. Li · J. Zhu (✉) · Z. Wang

Institute of Precision Optical Engineering (IPOE), Physics Department, Tongji University,
Shanghai 200092, China
e-mail: jzhu@tongji.edu.cn

for $\lambda = 2.73$ nm were studied by introducing B₄C at interfaces. The effect of B₄C thickness and interface symmetry were investigated. The hard x-ray ($\lambda = 0.154$ nm) reflectance were found 8 times higher after introducing 0.13 nm B₄C at both interfaces.

2 Experimental Details

All the multilayers were deposited by an ultrahigh vacuum direct current magnetron sputtering system. Base pressure was below 5.0×10^{-5} Pa. The sputter gas was argon at a constant pressure of 1.0 mTorr (0.13 Pa). All multilayers were deposited onto sliced polished silicon (100) wafer.

Grazing-incidence X-ray reflectance (XRR) measurements were made in the θ - 2θ geometry using a 4-circle x-ray diffractometer having a sealed-tube Cu source and a Si (220) crystal monochromator tuned to the Cu K- α line ($\lambda = 0.154$ nm, E = 8.05 keV). The angular divergence of this system is estimated to be $\sim 0.007^\circ$. Near-normal incidence soft x-ray reflectance measurements for Cr/C and Cr/Sc were made on beam line UE56/2-PGM-1 at BESSY-II synchrotron radiation.

3 Results and Discussion

3.1 Cr/C and Cr/Sc Multilayers

Cr/C and Cr/Sc multilayers were designed as near-normal incidence reflective mirror with period D = 2.26 nm, thickness ratio (C layer thickness to period) $\Gamma = 0.55$ and bilayer number N = 300. After deposition, XRR measurements were performed. The results are shown in Fig. 1(a). Both curves show sharp and intense Bragg peaks up to 4° of grazing incidence angle, which indicate sharp interfaces with small roughness or interdiffusion. The reflectance were measured at synchrotron radiation (SR) facility and shown in Fig. 1(b). Cr/C multilayer has a reflectance as high as 15.2 %, while Cr/Sc has only 7.5 %. The less reflectance of Cr/Sc is due to smaller optical contrast at this wavelength than Cr/C.

3.2 Cr/Ti Multilayers

We have deposited 4 sets of Cr/Ti multilayers. Firstly, four pieces of pure Cr/Ti multilayers with $\Gamma = 0.45$, N = 50 were prepared as reference samples and the periods of the multilayers were in the range of 1.37–1.66 nm. Then, other three sets had the same deposition time of Cr and Ti with the 1.37-nm-thick pure Cr/Ti

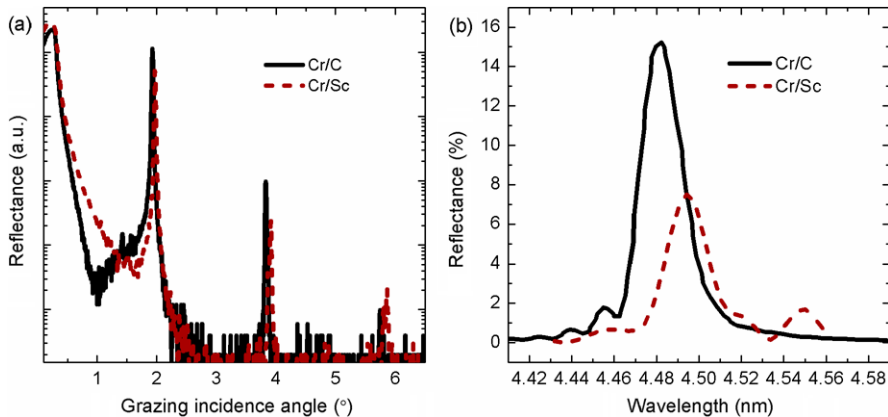


Fig. 1 XRR (a) and SR (b) measurements of Cr/C and Cr/Sc multilayers

multilayer, but they had B₄C diffusion barrier layer inserting at the Cr-on-Ti or Ti-on-Cr or both interfaces. Each set had five samples with nominal B₄C thickness of 0.08, 0.13, 0.18, 0.22, 0.27 nm.

The four sets of multilayers were measured by XRR. Only the first order peaks can be observed as the periods are ultra-short. Thus we plotted the peak intensities versus peak positions of all the samples in Fig. 2(a). For three sets with B₄C barrier layer, points on the left (low angle) side represent multilayers with thicker B₄C as the Cr and Ti layer thicknesses are identical to each other. Inserting B₄C on either interface would improve multilayer quality, and the best performance was achieved by inserting B₄C at both interfaces. Inserting B₄C at Cr-on-Ti interface gives more reflectance than at Ti-on-Cr interface. Comparing samples with different B₄C thickness, we have found that B₄C of 0.13 nm thick provide reflectance improvement as good as thicker ones. Considering that thicker B₄C will reduce theoretic reflectance, 0.13 nm B₄C layer will be inserted at both interfaces.

Basing on the preliminary results, two pieces of Cr/Ti multilayers with N = 600 were deposited for $\lambda = 2.73$ nm, one with 0.13 nm B₄C barrier layer on both interfaces, the other without barrier layer. The XRR measurement results are shown in Fig. 2(b). The peak reflectance of the Cr/Ti multilayer with B₄C barrier is 8 times higher than the one without barrier layer. Such great improvement in hard x-ray reflectance exhibits the effect of B₄C barrier layer, and also predicts improvement in soft x-ray reflectance at $\lambda = 2.73$ nm.

4 Conclusion

Cr/C and Cr/Sc multilayers for $\lambda = 4.48$ nm were deposited and reflectance of 15.2 % was obtained for the Cr/C one. The B₄C diffusion barrier layer inserting into Cr/Ti multilayers were investigated, and the best barrier layer thickness is 0.13 nm.

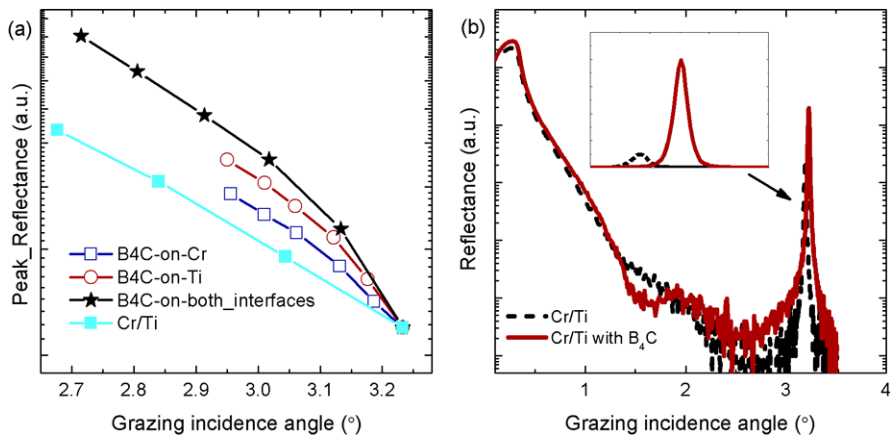


Fig. 2 (a) First order peak reflectance versus peak position plot of the four sets of $N = 50$ Cr/Ti multilayers with or without B₄C barrier layer. (b) XRR curves (log scale) of $N = 600$ Cr/Ti multilayers with or without B₄C barrier layer, the *inset* shows the linear scale zoom of first order peak

After introducing 0.13 nm B₄C in both interfaces, an 8 times improvement of reflectance at 8.05 keV was observed.

Acknowledgements We are indebted to Dr. Franz Schäfers at BESSY-II, and Mingqi Cui at BSRF for their kindly help in synchrotron radiation measurements.

References

1. Schäfers, F.: Multilayers for the EUV/soft X-ray range. *Physica B* **283**, 119–124 (2000)
2. Hoover, R.B., Shealy, D.L., Brinkley, B.R., Baker, P.C., Barbee, T.W. Jr., Walker, A.B.C. Jr.: Development of the water window imaging x-ray microscope utilizing normal-incidence multilayer optics. *Opt. Eng.* **30**, 1086–1093 (1991)
3. Andreev, S.S., Mertins, H.C., Platonov, Y.Y., Salashchenko, N.N., Schaefers, F., Shamov, E.A., Shmaenok, L.A.: Multilayer dispersion optics for X-ray radiation. *Nucl. Instrum. Methods Phys. Res., Sect. A* **448**, 133–141 (2000)
4. Eriksson, F., Ghafoor, N., Schäfers, F., Gullikson, M., Aouadi, S., Rohde, S., Hultman, L., Birch, J.: Atomic scale interface engineering by modulated ion-assisted deposition applied to soft x-ray multilayer optics. *Appl. Opt.* **47**, 4196–4204 (2008)
5. Ghafoor, N., Persson, O.A., Birch, J., Eriksson, F., Schäfers, F.: Interface engineered ultra-short period Cr-Ti multilayers as high reflectance mirrors and polarizers for soft x rays of $\lambda = 2.74$ nm wavelength. *Appl. Opt.* **45**, 137–143 (2006)
6. Eriksson, F., Ghafoor, N., Schäfers, F., Gullikson, M., Birch, J.: Interface engineering of short-period Ni/V multilayer X-ray mirrors. *Thin Solid Films* **500**, 84–95 (2006)

Chapter 26

Time Resolved Holography Scheme Using a Table Top Soft X-Ray Laser

E.B. Malm, N.C. Monserud, P.W. Wachulak, C. Brown, W. Chao,
E. Anderson, H. Xu, C.P. Hains, G. Balakrishnan, C.S. Menoni, J.J. Rocca,
and M.C. Marconi

Abstract We demonstrate a versatile table-top holography setup capable of acquiring single-shot soft X-ray holograms with a 10–90 % knife edge spatial resolution of 170 ± 26 nm and 1 ns temporal resolution. A Fresnel zone plate is used to create the reference wave as well as to illuminate the sample in a Fourier transform holography scheme. A 100 μm in diameter central opening in the zone plate allows the incident beam to pass through and directly illuminate the object. A pinhole is located in the sample mask allowing the first order from the zone plate to pass while blocking the higher orders. This setup can be used to enhance edges for conventional single-shot soft X-ray holography imaging.

1 Introduction

X-ray imaging promises to provide nanometer spatial and femtosecond temporal resolutions [1]. So far, a major limitation preventing X-ray imaging from becoming more prevalent is that much of X-ray imaging research is conducted at limited-access free electron lasers (XFELs) or synchrotron sources [2–5]. Recently, table-top sources have shown the ability to provide the coherence and intensity required for X-ray imaging [6–10]. As table-top soft X-ray lasers become more available, experimental setups need to be developed in order to image specimens in other areas of science.

E.B. Malm · N.C. Monserud · C. Brown · C.S. Menoni · J.J. Rocca · M.C. Marconi (✉)
Department of Electrical Engineering, Colorado State University and Engineering Research
Center for Extreme Ultraviolet Science and Technology, Fort Collins, CO 80523, USA
e-mail: marconi@engr.colostate.edu

H. Xu · C.P. Hains · G. Balakrishnan
Department of Electrical Engineering, University of New Mexico and Center for High
Technology Materials, Albuquerque, NM 87106, USA

P.W. Wachulak
Institute of Optoelectronics, Military University of Technology, Warsaw, Poland

W. Chao · E. Anderson
Center for X-Ray Optics, Lawrence Berkeley National Lab, Berkeley, CA 94720, USA

In this paper we describe a Fourier transform holography (FTH) setup similar to the one described by McNulty [4]. It utilizes FTH for soft X-ray imaging. A Fresnel zone plate is used to create the reference wave while transmitting the beam directly to illuminate the object creating the object wave. The interference between these two waves allows for direct reconstruction of the sample with a simple two-dimensional Fourier transform applied to the detected intensity. Previous work has used the diffracted field from the zones of a Fresnel zone plate to illuminate the object. This experiment allows the incident beam to pass directly through a central opening in the zone plate. The central opening allows for a more intense and uniform illumination of the sample and provides single-shot nanometer-scale reconstructions.

2 Soft X-Ray Laser

The coherent soft X-ray beam is produced from a table-top discharge-pumped laser emitting at a wavelength of 46.9 nm [11]. The high-gain lasing medium is Ne-like argon plasma. The 46.9 nm wavelength light used for illumination is produced by a table-top discharge pumped capillary Ne-like Ar laser. This compact laser when operated with a 27 cm long capillary produces ~ 0.3 mJ pulses at a repetition rate of 1 Hz. The laser fits on an optical table occupying a 1×0.5 m² footprint. The EUV laser has a high temporal coherence with a fractional spectral bandwidth of $\Delta\lambda/\lambda \approx 3\text{--}4 \times 10^{-5}$ [12], which corresponds to a coherence length of $l_c \approx 750$ μm . The beam is also highly spatially coherent. The spatial coherence radius in the position where the hologram was recorded was approximately 500 μm for a capillary length of 27 cm and become fully coherent as the capillary was lengthened to 36 cm [13].

3 Experimental Setup

Figure 1 shows a diagram of the experimental setup. The laser pulse reflects off a Mo/Si multilayer mirror at 45° incidence angle (not shown in the figure). The mirror allows a precise alignment of the laser beam in the optical axis of the hologram recording setup and simultaneously provides extra spectral filtering to the illumination. The pulse then illuminates a Fresnel zone plate which produces a reference wave focusing in the 400 nm pinhole made in the sample substrate and at the same time allows the beam to directly illuminate the sample with its 100 μm central opening. A pinhole in the sample mask allows for the first order from the zone plate to pass while filtering out the higher orders. The sample is placed in the first order focal plane of the zone plate which is approximately 1 mm away from the zone plate. The sample is located 5.5 cm from an X-ray back illuminated charge coupled device (CCD) camera from Andor. The CCD has 2048×2048 pixels with a square pixel size of 13.5×13.5 μm^2 . This setup allows for single-shot time-resolved holograms with real-time detection and reconstruction.

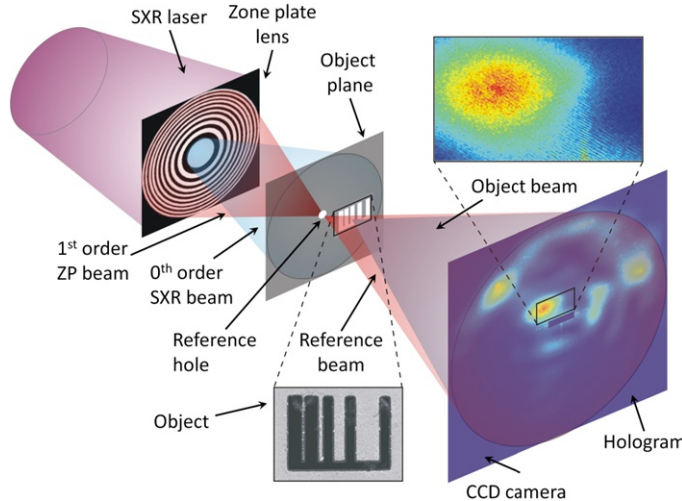


Fig. 1 The Fresnel zone plate creates both the reference and the object waves necessary for FTH. The first order from the zone plate passes through a pinhole in the mask. The 100 μm in diameter central opening in the zone plate allows for the incident light to illuminate the object creating the object wave. The object and reference waves interfere on the CCD

4 Experimental Results

Experiments in the past have used zone plates with all the zones to image samples with X-rays [4]. This previous work used diffracted light through the zones to illuminate the object which might produce a complicated illumination pattern in the sample plane. In the experiment described herein a 100 μm in diameter central opening was created in the zone plate that was used to illuminate the sample. To show the advantage of using a central opening instead of a zone plate with all the zones, we performed a comparison in reconstruction quality for the two cases.

The sample was a series of elbow-shaped apertures made in a 200 nm thick Si_3N_4 membrane with a 200 nm layer of gold deposited on top. The sample was then milled using a focused ion beam (FIB). The slits' widths in this sample vary from 2 μm , 1 μm , 0.5 μm and finally to 0.25 μm in the smallest elbow test pattern. A scanning electron micrograph (SEM) image of the sample is shown in Fig. 2a. Figure 2b was obtained using a zone plate with 100 μm in diameter central block with a zone plate outer zone width of 120 nm.

The reconstruction clearly shows that the sample is illuminated with a distorted wavefront which is less than ideal for imaging purposes. Figure 2c shows the effect of illuminating the object directly with an opening in the zone plate. The bottom section of the sample, indicated with the red dashed line, was illuminated with the opening while the remaining parts were illuminated with the diffracted field from the zone plate. The central opening provides a more intense and uniform field making it more advantageous for imaging. This setup is capable of imaging large samples with

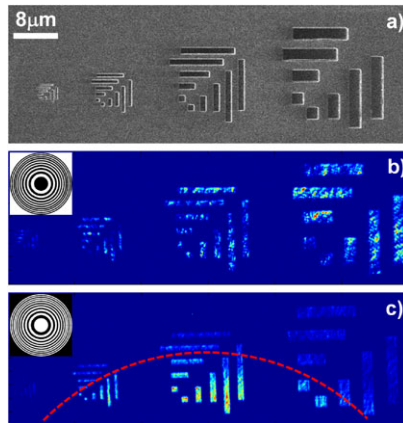


Fig. 2 (a) An SEM image of the sample. (b) The reconstruction using a Fresnel zone plate with a 100 μm in diameter central block. The *inset* in (b) shows a diagram of the zone plate used with a central block. (c) A reconstruction using a Fresnel zone plate with a $D = 100 \mu\text{m}$ central opening. The *inset* in (c) shows a diagram of a zone plate with a central opening. The *bottom section* of (c) is directly illuminated with the incident beam (*red dashed line*), while (b) is illuminated by the diffraction through the zone plate entirely

nanometer-scale resolution. The only limitation to the sample size is determined by the central opening of the zone plate which in this case is 100 μm in diameter.

5 Edge Enhancement

To show the versatility of this setup, it is possible to enhance different features of the sample by repositioning the zone plate relatively to the reference hole. In this experiment the sample was fabricated on a 200 nm of Si_3N_4 with 200 nm of gold deposited on top. A FIB was used to create the four pillar design into the membrane. The sample contains four pillars with a height of 10 μm and of varying widths. The pillar widths are 4 μm , 2 μm , 1 μm and 0.5 μm . An SEM of the pillar sample is shown in Fig. 3a.

The image also shows that the sample is contaminated with several small particles. The contamination appears semi-transparent making it difficult to determine its extent with an SEM. In order to see the contamination more clearly, the image contrast was adjusted and is shown in Fig. 3b. As a comparison, Fig. 3c shows the reconstruction of the sample using the optical setup shown above, and the two images agree well with each other. The small differences between the SEM image and the soft X-ray image could be attributed to the different scattering properties between electrons and X-ray photons. While Fig. 3c shows the capability to image samples with a single-shot, Fig. 3d shows the ability of this setup to optically enhance edges. By adjusting the focal spot location it is possible to increase the amount of light

Fig. 3 (a) An SEM image of the pillar sample. (b) An SEM image with the contrast adjusted to show the contamination more clearly. (c) A reconstruction from a single-shot hologram. (d) A single-shot reconstruction showing the edge enhancement by readjusting the zone plate focal position

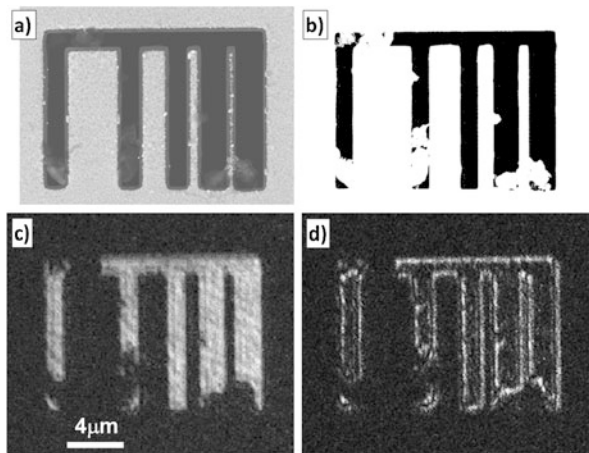
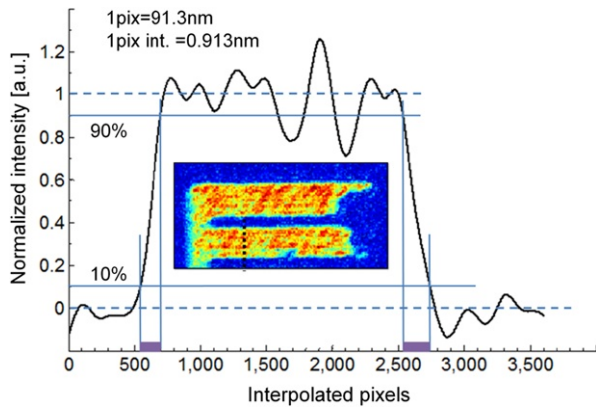


Fig. 4 A knife edge cut from the single-shot reconstruction from Fig. 3c. The resolution obtained is 170 ± 26 nm



at high diffracted angles which would enhance the signal in the hologram corresponding to high spatial frequencies. This annular illumination results in an edge enhanced reconstruction, and the adjustment allows for edge enhancement without any post processing of the reconstruction. A typical example of this illumination effect is shown in the reconstruction in Fig. 3d.

To make a first assessment of the spatial resolution we utilized the knife edge method [14]. A characteristic knife edge cut along the reconstruction in Fig. 3c is shown in Fig. 4. Performing these cuts in different regions of the image gives different values for the 10–90 % intensity transition. We performed a statistical study to obtain a resolution of 170 ± 26 nm from a single-shot hologram based on 12 measurements. The theoretical diffraction limit for the zone plate used in this experiment with a 100 μm in diameter central opening was numerically calculated to be 150 nm, a little larger than for a full zone plate equal to 122 nm.

6 Conclusion

In conclusion, we have demonstrated a soft X-ray optical system capable of acquiring single-shot holograms with a resolution of 170 ± 26 nm. Also, optical edge enhancement can be easily implemented by repositioning the zone plate relative to the sample. This work has shown that having a central opening in the zone plate for direct illumination of the sample is advantageous to illumination with the diffracted field through the zone plate.

Acknowledgements This research was sponsored by the Defense Threat Reduction Agency-Joint Science and Technology Office for Chemical and Biological Defense (Grant no. HDTRA1-10-1-0070) and the NSF ERC Center for Extreme Ultraviolet Science and Technology, NSF Award No. EEC-0310717.

References

1. Gunther, C.M., et al.: Sequential femtosecond X-ray imaging. *Nat. Photonics* **5**, 99–102 (2011)
2. Chapman, H., et al.: Femtosecond diffractive imaging with a soft-X-ray free electron laser. *Nat. Phys.* **2**, 839–843 (2006)
3. Chapman, H., et al.: Femtosecond time-delay X-ray holography. *Nature* **448**, 676–679 (2007)
4. McNulty, I., et al.: High-resolution imaging by Fourier transform X-ray holography. *Science* **256**, 1009–1012 (1992)
5. Schlotter, W.F., et al.: Multiple reference Fourier transform holography with soft X rays. *Appl. Phys. Lett.* **89**, 163112 (2006)
6. Gauthier, D., et al.: Single-shot femtosecond X-ray holography using extended references. *Phys. Rev. Lett.* **105**, 093901 (2010)
7. Sandberg, R.L., et al.: Tabletop soft-x-ray Fourier transform holography with 50 nm resolution. *Opt. Lett.* **34**, 1618–1620 (2009)
8. Kim, H.T., et al.: Single shot nanometer scale imaging with laser-driven x-ray laser. *Appl. Phys. Lett.* **98**, 121105 (2011)
9. Carbajo, S., et al.: Sequential single shot imaging of nanoscale dynamic interactions with a table top soft X-ray laser. *Opt. Lett.* **37**, 2994–2996 (2012)
10. Brewer, C.A., et al.: Single-shot extreme ultraviolet laser imaging of nanostructures with wavelength resolution. *Opt. Lett.* **33**, 518–520 (2008)
11. Benware, B.R., et al.: Demonstration of a high average power tabletop soft X-ray laser. *Phys. Rev. Lett.* **81**, 5804–5807 (1998)
12. Urbanski, L., et al.: Spectral linewidth of a Ne-like Ar capillary discharge soft-x-ray laser and its dependence on amplification beyond gain saturation. *Phys. Rev. A* **85**, 033837 (2012)
13. Liu, Y., et al.: Achievement of essentially full spatial coherence in a high-average-power soft-x-ray laser. *Phys. Rev. A* **63**, 033802 (2001)
14. Heck, J.M., et al.: Resolution determination in X-ray microscopy: an analysis of the effects of partial coherence and illumination spectrum. *J. X-Ray Sci. Technol. (Paris)* **8**, 95–104 (1998)

Chapter 27

Plasma Homogenization for Overcoming Refractive Losses in X-Ray Lasers

Leili Masoudnia and Davide Bleiner

Abstract Refractive losses along laser-produced plasmas used as gain media are caused by density gradients. The pump pulse is thus deflected from the high gain region and the short wavelength signal steers-away causing loss of collimation. Hollow cylinders used as targets make the plasma homogeneous and can mitigate refractive losses by means of waveguiding.

1 Introduction

Profiles of the electron-density in laser-produced plasmas used as gain media lead to a deflection of the pump pulse up to a turning point. The generated short-wave also steers-away during propagation along the plasma column causing loss of collimation and illumination quality. The prepulse technique was shown to mitigate the refraction problem [1] as well as original target designs [2–5]. Refraction is thus an important effect limiting the gain. To begin with, the refractive losses in a planar target are discussed. Then at original target design to produce plasma homogenization was studied; besides, a computational study with a hydro-code for planar and hollow cylindrical target is presented which includes a ray tracing modeling based on the Eikonal theory of the trajectory-equation.

2 Refractive Losses in a Planar Target

Figure 1 shows the electron density distribution before and after delivering of the main pump pulse on a planar target. The onset of a density gradient deflects the pump pulse up to a turning point, causing loss of efficiency.

L. Masoudnia (✉) · D. Bleiner

Institute of Applied Physics, University of Bern, Sidlerstrasse 5, 3012, Bern, Switzerland
e-mail: leili.masoudnia@iap.unibe.ch

D. Bleiner

e-mail: bleiner@iap.unibe.ch

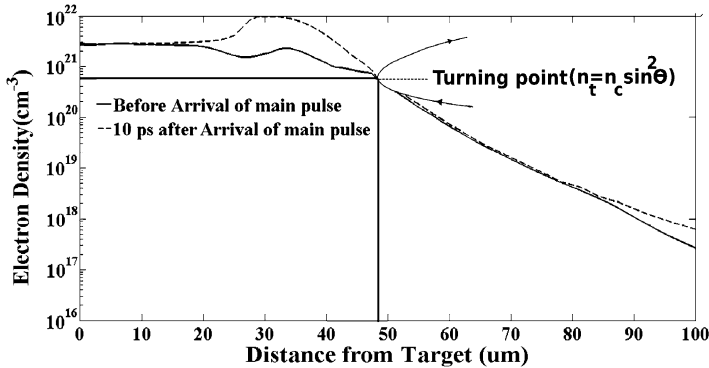


Fig. 1 Electron density distribution before and after delivery of the main pump pulse with the hydro code. The pump is reflected already at $\simeq 56\%$ of the maximum penetration depth ($n_c = 1.1 \times 10^{21}$)

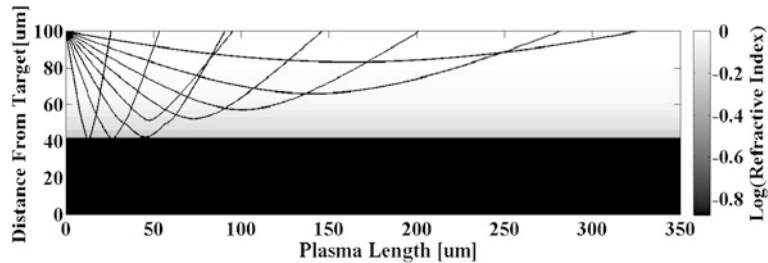


Fig. 2 Trajectory of the pump pulse considering the density profile before the main pulse for the irradiation angle in the range 10° to 80°

Figure 2 shows pump pulse trajectory as a function of irradiation angle. With the smaller angle one notes a longer active volume, that for 49° angle gives a penetration depth of $48\text{ }\mu\text{m}$ (Fig. 1). A longer and shallower active volume has a higher gain-length product for saturation.

The trajectory of the short-wavelength signal is shown on Fig. 3. At a distance larger than $55\text{ }\mu\text{m}$, the output divergence is approx. 6 mrad , which is in agreement with our experimental studies [6]. The observations point at one common solution; i.e., plasma homogenization is required [7].

3 Plasma Confinement for Signal Waveguide

Using hollow targets confines the plasma and acts as a signal waveguide. Figure 4 shows the two counter-propagating fronts toward the center at 1 ns . These merge at 1.7 ns and create a concave density profile. At 5 ns the profile evolves into a convex. Figure 5 shows that using the hollow cylindrical target can effectively overcome the refraction problem of X-ray lasers.

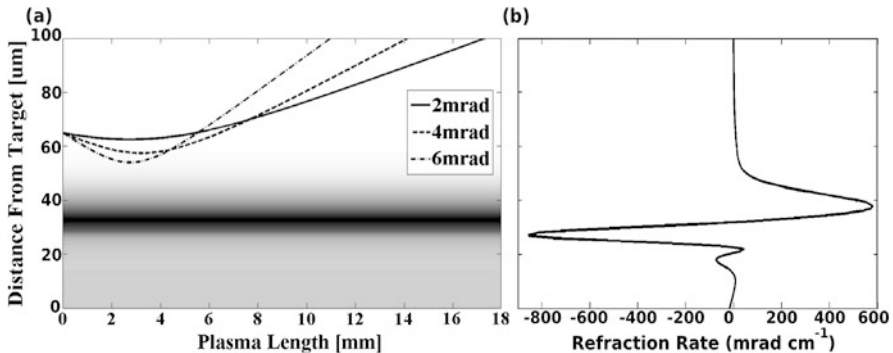


Fig. 3 Short-wavelength signal trajectory along the plasma gain medium (a), and refraction rate as a function of distance from the target (b)

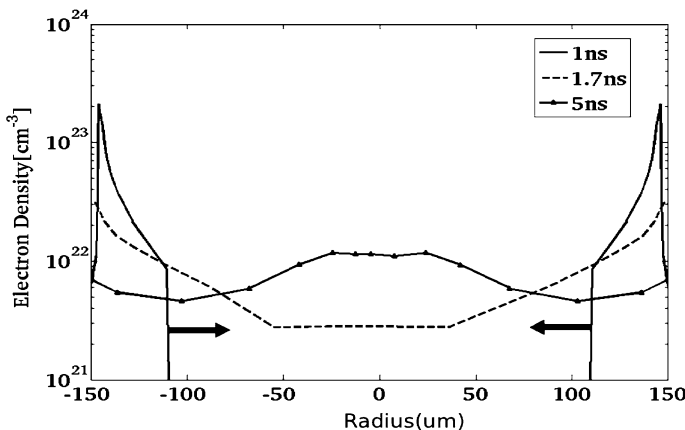


Fig. 4 Temporal and spatial evolution of the electron density profile for hollow cylinder target. The profile tends to self-homogenize

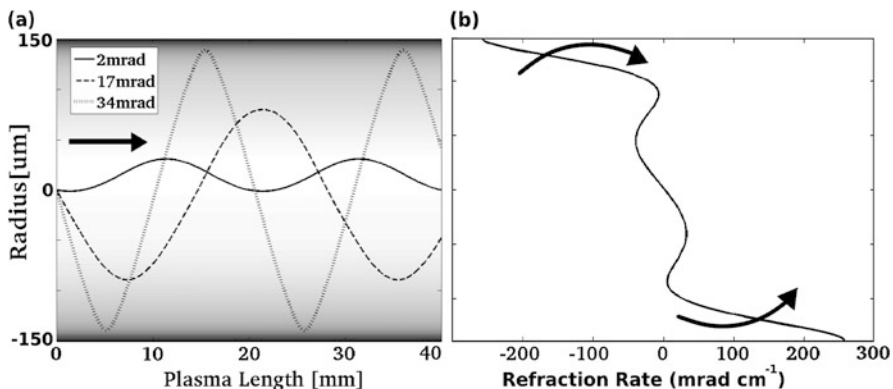


Fig. 5 Short-wavelength signal trajectory inside the hollow cylindrical target (a), and refraction rate as a function of radius (b)

4 Conclusions

Ray trajectory for the IR pump pulse and short-wavelength signal for planar target showed that at the smaller grazing angle a longer active volume is excited. Therefore, a maximum gain-length product was achieved, if refraction would not limit the performance. Ray trajectory for the X-ray signal in hollow targets is presented, and it is shown that it can effectively mitigate refractive losses.

Acknowledgements The present work was supported by the Swiss National Science Foundation under the grant number PP00P2-133564/1.

References

1. Nilsen, J., MacGowan, B.J., Da Silva, L.B., Moreno, J.C.: Phys. Rev. A **48**(6), 4682–4685 (1993)
2. Lewis, C.L.S., et al.: Opt. Commun. **91**, 71–76 (1992)
3. Lunney, J.G.: Appl. Phys. Lett. **48**, 891 (1986)
4. Daido, H., Murai, K., Kodama, R., Yuan, G.: J. Appl. Phys. B **62**, 129–133 (1996)
5. Soom, B., Ellenberger, U., Weber, R., Balmer, J.E.: Opt. Commun. **84**, 23 (1991)
6. Ruiz-Lopez, M., Staub, F., Bleiner, D.: In: Sebban, S., et al. (eds.) X-Ray Lasers 2012. Springer Proceedings in Physics, vol. 147. Springer, Cham (2013). Chapter 36 in this book
7. Masoudnia, L., Bleiner, D.: Laser Phys. **23**, 056003 (2013)

Chapter 28

Temporal Coherence and Spectral Linewidth of Neon-Like XUV Lasers Pumped in the Quasi-steady State Regime

**L. Meng, A. Klisnick, M. Kozlova, K. Bohacek, M. Krus, J. Prokupek,
L. Urbanski, M.C. Marconi, M. Berrill, J.J. Rocca, O. Guilbaud, F. Tissandier,
S. Sebban, P. Zeitoun, A. Calisti, S. Ferri, C. Mossé, and B. Talin**

Abstract We report recent experimental progress in the characterization of the temporal coherence and related spectral linewidth of plasma-based soft X-ray lasers (SXRL). New measurements were carried out with two types of SXRLs pumped in the quasi-steady state (QSS) regime, in a capillary-discharge plasma and in a laser-produced plasma. We describe the main results obtained from both experiments and compare them to dedicated numerical simulations. We discuss the results in the context of the possibility to achieve XUV lasers with pulse duration below 1 picosecond.

1 Introduction

The progress of collisional soft X-ray lasers (SXRL), generated by quasi-steady state [1] or transient pumping in solid target plasmas [2], optical-field-ionization in gaseous targets [3], and capillary discharges [4], have opened the way to compact devices and new prospects for various applications. This requires a detailed

L. Meng (✉) · A. Klisnick
ISMO, CNRS-Université Paris-Sud, Orsay, France
e-mail: limin.meng@u-psud.fr

M. Kozlova · K. Bohacek · M. Krus · J. Prokupek
Institute of Physics of ASCR, Prague, Czech Republic

L. Urbanski · M.C. Marconi · M. Berrill · J.J. Rocca
NSF-ERC for EUV Science and Technology, Colorado State University, Fort Collins, USA

O. Guilbaud
LPGP, CNRS-Université Paris-Sud, Orsay, France

F. Tissandier · S. Sebban · P. Zeitoun
LOA, ENSTA, Palaiseau, France

A. Calisti · S. Ferri · C. Mossé · B. Talin
PIIM, CNRS-Aix-Marseille Université, Marseille, France

characterization of their output parameters, like the energy per pulse, duration etc. The spectral linewidth $\Delta\lambda$, or the coherence time τ_c are also very important parameters, since they determine the shortest pulse duration (Fourier-transform limit τ_{FL}) that can be achieved (in a linear amplification regime), through the relation: $\tau_{FL} = \alpha \frac{\lambda^2}{\Delta\lambda} = \beta \tau_c$, where α and β are numerical factors depending on the particular shape of the line profile. The spectral width of the SXRL line results from the complex combination of several processes, namely the contribution of homogeneous (natural and collisional) and inhomogeneous (Doppler) broadenings of the intrinsic profile, followed by gain narrowing with amplification of the line along the plasma length [5]. When inhomogeneous broadening is the dominant cause of broadening the line can be rebroadened when the laser reaches saturation [6].

The purpose of our work is to characterize experimentally the spectral behavior of existing collisional excitation SXRLs, and to evaluate their potential to support the amplification of pulses with duration below 1 ps. Over the recent years, our previous studies were devoted to short pulse (femtosecond to picosecond) pumped systems, in which the duration of the SXRL pulse is of the same order of magnitude as the coherence time. At LOA-Palaiseau (France), a coherence time of ~ 5 ps was measured in a Ni-like Kr laser generated at 32.8 nm from an optical-field ionized plasma [7]. At Colorado State University (USA), a shorter coherence time of ~ 1 ps was measured in a Ni-like Mo laser ($\lambda = 18.9$ nm) pumped in the transient regime with a grazing incidence irradiation geometry [8]. Here in the present paper, we present new measurements that were carried out with two types of neon-like SXRLs, pumped in the quasi-steady state (QSS), long pulse (100 ps to nanosecond) regime: the capillary-discharge argon laser generated at CSU (USA) [9, 10], and the Ne-like Zn laser generated at PALS (Czech Republic) [1]. These sources differ from the previous ones by several aspects, among which a higher ionic temperature leading to a larger contribution of Doppler broadening of the laser lines.

We used a variable path-difference, wavefront-division interferometer, which was specifically designed to measure the temporal coherence of the source. This interferometer, described in [11], is composed of two dihedrons, tilted towards each other with a small angle. The incoming beam is separated into two beamlets that slightly converge towards each other after reflection on the dihedrons. In their overlapping region, interference fringes can be recorded using a XUV CCD camera. One of the dihedrons can be accurately translated vertically in order to introduce a path difference between the interfering beams. By following the evolution of the fringe visibility as a function of the delay with successive shots performed in identical conditions, it is possible to measure the coherence time of the pulse, and to infer the spectral width of the line through a Fourier transform.

2 Capillary-Discharge Ne-Like Ar Laser

Capillary discharge XUV lasers are the highest average power tabletop source of coherent soft-x-ray radiation [9, 12] up to date. The capillary discharge Ne-like Ar

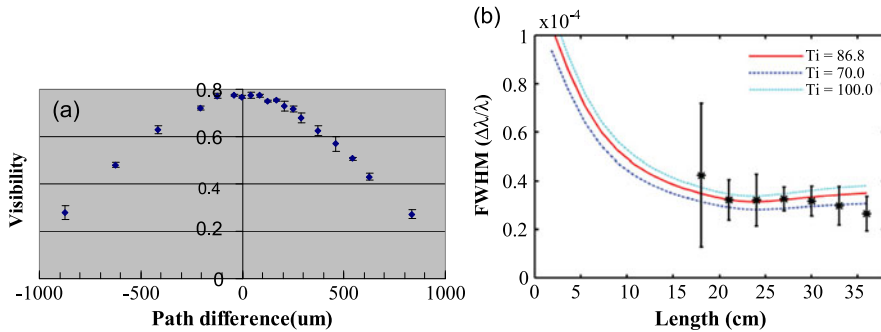


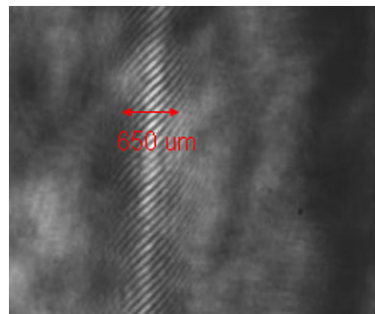
Fig. 1 (a) Example of a measured visibility curve; (b) Measured spectral width as a function of amplifier length. The *black points* with *error bars* stand for experimental data, and the three *curves* show the simulation results for different temperatures [10]

laser operating at $\lambda = 46.9$ nm (3p-3s $J = 0-1$ line), was first demonstrated in 1994 [4] and has been widely characterized [13–17]. However, the spectral linewidth and the temporal coherence, which are important parameters in applications such as interferometry [18] and large area nanopatterning [19], remained to be measured. Capillary discharge plasmas are characterized by a low electron density ($N_e \sim 2 \times 10^{18} \text{ cm}^{-3}$) and a relatively high ionic temperature ($kT_i \sim 100 \text{ eV}$). The Doppler effect is thus expected to be the dominant cause of broadening of the laser line. The Ne-like Ar laser is thus an appropriate system to study the possible existence of saturation rebroadening predicted in highly inhomogeneous line profiles [20]. This is achieved by measuring the linewidth evolution with the plasma column length.

The experiment was performed at CSU (USA). The experimental setup and the results obtained are presented in more detail in [10] as well as in a companion paper (see [21]). Figure 1(a) shows an example of the measured variation of the fringe visibility with the path difference. The coherence time is defined as the delay at which the visibility is decreased by $1/e$ of its maximum. We find that the experimental data fit very well to a Gaussian curve. The corresponding spectral profile, inferred by a Fourier transform of the visibility curve, is also Gaussian. The linewidth is defined as the FWHM of the spectral profile.

The measured variation of the spectral bandwidth as a function of the plasma length is shown in Fig. 1(b). One can see that the bandwidth decreases slowly, while no rebroadening of the line is apparent for the longest lengths, although the laser is operated at saturation. The experimental data are compared to the predictions of numerical simulations, performed at CSU, that compute the line propagation along the amplifier axis taking into account gain saturation and refraction losses. One can see that these calculations predict a weak rebroadening of the line beyond $L \sim 24 \text{ cm}$. However this effect is small compared to our experimental error bars. For the longest plasma length, the typical coherence time τ_c is 2.3 ps, corresponding to a Fourier limit pulse duration τ_{FL} of 1.9 ps, which are both much shorter than the duration of the SXRL pulse (1.2–1.8 ns).

Fig. 2 Portion of the interferogram detected with the Ne-like Zn laser at 21.2 nm



3 Laser-Based Ne-Like Zn Laser

More recently we carried out a temporal coherence measurement of the Ne-like Zn laser, emitting at 21.2 nm (3p-3s $J = 0-1$ line, as above). This SXRL is generated at the PALS (Prague, Czech Republic) laser facility and was used for several applications [22]. The lasing plasma is pumped by a succession of a low-energy prepulse and high-energy main pulse, both ~ 300 ps in duration, delivered by an iodine pump laser ($\lambda = 1.315$ μm). After double-pass amplification in a 3-cm zinc plasma column, the 21.2 nm pulse reaches saturation with a typical energy of ~ 1 mJ per pulse or more [1].

Although lasing is obtained on the same Ne-like 3p-3s transition as for the capillary discharge laser discussed above, the plasma conditions in the gain zone are markedly different. Here the electron density is typically $\times 100$ times higher ($N_e \sim 2-5 \times 10^{20}$ cm $^{-3}$), while the ionic temperature is only twice as high ($kT_i \sim 150-200$ eV). As a result, in Ne-like Zn, both collisional and Doppler broadenings contribute at the same level, as will be shown below.

The interferometer was implemented along the 21.2 nm beam path, at a distance of ~ 5.5 meters from the source. Figure 2 shows a typical example of a single-shot interferogram, when the path-difference between the interfering beams was close to zero. The size of the overlapping region, where fringes are apparent, is ~ 650 μm. This is slightly larger than the spatial coherence of the beam at the interferometer position, so that the fringe visibility is relatively low, of the order of 30 %. The distance from the source was increased by ~ 1.5 m in a second series of measurements, but the fringe visibility was not significantly improved. Another difficulty was the limited number of shots available in a data set, due to the low repetition rate of the laser (2 shots per hour). Two series of data, where the path difference was varied from -300 μm to $+300$ μm, were obtained for the two different distances from the source mentioned above. They led to slightly different, although consistent values for the coherence time of the 21.2 nm laser, namely $\tau_c = 1$ ps and 0.7 ps for the 5.5 m and 7 m distance respectively. The corresponding spectral linewidth are 11.3 mÅ and 7.7 mÅ respectively.

The measured $\Delta\lambda$ values were compared to the predictions of numerical simulations, using the PPP lineshape code [23] to calculate the intrinsic broadening, and a 1D-radiative transfer code [24] that computes the amplified profile, taking into

account saturation. The plasma conditions in the gain zone are not known precisely, but estimated as $N_e \sim 2\text{--}5 \times 10^{20} \text{ cm}^{-3}$, $kT_e = 200\text{--}300 \text{ eV}$; $kT_i = 150\text{--}200 \text{ eV}$. A small-signal gain coefficient of 7 cm^{-1} was considered. We find that within this parameter range, the amplified linewidth of the 21.2 nm laser varies between 7.4 and $10.6 \text{ m}\text{\AA}$, in good agreement with our measurements. The contribution of the collisional broadening to the intrinsic line profile ranges from 11 to $24 \text{ m}\text{\AA}$, whereas the Doppler one is of the order of $25 \text{ m}\text{\AA}$.

Finally the measured τ_c values were used to estimate the corresponding Fourier-transform limit τ_{FL} , which is the shortest duration that could be reached if the 21.2 nm was fully temporally coherent. From the definition recalled in Sect. 1, and considering a Gaussian shape, we find that τ_{FL} is below 1 ps for both measurements, namely 0.6 and 0.7 ps. This is the shortest value ever measured for a plasma-based SXRL and this confirms the high potential of the Zn quasi-steady state laser for the generation of femtosecond amplified pulses, through seeding with high-harmonic radiation.

4 Conclusion

We have measured the temporal coherence and spectral width of two Ne-like soft X-ray lasers pumped in the quasi-steady state regime with two distinct techniques, leading to different plasma conditions and spectral characteristics.

The Ne-like Ar, capillary-discharge pumped laser exhibits a spectral width that decreases slowly as the plasma length increases, as a result of gain narrowing. The small saturation rebroadening, predicted by numerical simulations, was not observed and could be beyond our experimental accuracy. The measured coherence time is $\sim 2 \text{ ps}$, much shorter than the pulse duration of 1.2–1.8 ns. For the laser-pumped Ne-like Zn laser, the measured coherence time is shorter (0.7–1 ps), leading for the first time to a Fourier-transform limit duration that lies below 1 ps.

In both cases, the inferred values for the spectral width of the laser line are in good quantitative agreement with the predictions of numerical simulations. Finally since the measured coherence times are in both cases much smaller than the duration of the SXRL pulse, picosecond (or potentially sub picosecond) durations could be reached through seeding with femtosecond high-order harmonic radiation.

References

1. Rus, B., et al.: Multimillijoule, highly coherent x-ray laser at 21 nm operating in deep saturation through double-pass amplification. *Phys. Rev. A* **66**, 063806 (2002)
2. Wang, Y., et al.: High-brightness injection-seeded soft-X-ray-laser amplifier using a solid target. *Phys. Rev. Lett.* **97**, 123901 (2006)
3. Zeitoun, Ph., et al.: A high-intensity highly coherent soft X-ray femtosecond laser seeded by a high harmonic beam. *Nature* **431**, 426 (2004)

4. Rocca, J.J., et al.: Demonstration of a discharge pumped table-top soft-X-ray laser. *Phys. Rev. Lett.* **73**, 2192 (1994)
5. Koch, J.A., et al.: Experimental and theoretical investigation of neonlike selenium x-ray laser spectral linewidths and their variation with amplification. *Phys. Rev. A* **50**, 1877 (1994)
6. Pert, G.J.: Output characteristics of amplified-stimulated-emission lasers. *J. Opt. Soc. Am. B* **11**, 1425 (1994)
7. Tissandier, F., et al.: Observation of spectral gain narrowing in a high-order harmonic seeded soft-x-ray amplifier. *Phys. Rev. A* **81**, 063833 (2010)
8. Meng, L., et al.: Temporal coherence and spectral linewidth of an injection-seeded transient collisional soft x-ray laser. *Opt. Express* **19**, 12087 (2011)
9. Benware, B., et al.: Demonstration of a high average power tabletop soft X-ray laser. *Phys. Rev. Lett.* **81**, 5804 (1998)
10. Urbanski, L., et al.: Spectral linewidth of a Ne-like Ar capillary discharge soft-x-ray laser and its dependence on amplification beyond gain saturation. *Phys. Rev. A* **85**, 033837 (2012)
11. Guilbaud, O., et al.: Longitudinal coherence and spectral profile of a nickel-like silver transient soft X-ray laser. *Eur. Phys. J. D* **40**, 125 (2006)
12. Macchietto, C.D., et al.: Generation of millijoule-level soft-x-ray laser pulses at a 4-Hz repetition rate in a highly saturated tabletop capillary discharge amplifier. *Opt. Lett.* **24**, 1115 (1999)
13. Tomassetti, G.A., et al.: Toward a full optimization of a highly saturated soft-X-ray laser beam produced in extremely long capillary discharge amplifiers. *Opt. Commun.* **231**, 403 (2004)
14. Heinbuch, S., et al.: Demonstration of a desk-top size high repetition rate soft x-ray laser. *Opt. Express* **13**, 4050 (2005)
15. Le Pape, S., et al.: Electromagnetic-field distribution measurements in the soft X-ray range: full characterization of a soft X-ray laser beam. *Phys. Rev. Lett.* **88**, 183901 (2002)
16. Marconi, M.C., et al.: Measurement of the spatial coherence buildup in a discharge pumped table-top soft X-ray laser. *Phys. Rev. Lett.* **79**, 2799 (1997)
17. Liu, Y., et al.: Achievement of essentially full spatial coherence in a high-average-power soft-x-ray laser. *Phys. Rev. A* **63**, 033802 (2001)
18. Brewer, C.A., et al.: Single-shot extreme ultraviolet laser imaging of nanostructures with wavelength resolution. *Opt. Lett.* **33**, 518 (2008)
19. Wachulak, P.W., et al.: Patterning of nano-scale arrays by table-top extreme ultraviolet laser interferometric lithography. *Opt. Express* **15**, 3465 (2007)
20. Koch, J.A., et al.: Collisional redistribution effects on x-ray laser saturation behavior. In: AIP Conf. Proc., vol. 332, pp. 574–578. AIP, New York (1994)
21. Urbanski, L., et al.: Spectral linewidth measurement of a Ne-like Ar capillary discharge soft x-ray laser. In: Sebban, S., et al. (eds.) *X-Ray Lasers 2012*. Springer Proceedings in Physics, vol. 147. Springer, Cham (2013). Chapter 41 in this book
22. Mocek, T., et al.: Plasma-based X-ray laser at 21 nm for multidisciplinary applications. *Eur. Phys. J. D* **54**, 439–444 (2009)
23. Calisti, A., et al.: Model for the line shapes of complex ions in hot and dense plasmas. *Phys. Rev. A* **42**, 5433 (1990)
24. Guilbaud, O., et al.: Fourier-limited seeded soft x-ray laser pulse. *Opt. Lett.* **35**, 1326 (2010)

Chapter 29

Spectral Broadening of Ni-Like XUV Laser Lines

L. Meng, A. Calisti, S. Ferri, C. Mossé, B. Talin, D. Benredjem, O. Guilbaud, and A. Klisnick

Abstract We have used the PPP lineshape code to calculate the intrinsic (i.e. before amplification) line profile of the Mo XUV laser over an extended range of plasma densities and temperatures, chosen to cover conditions for collisional excitation pumping in the transient and quasi-steady state regimes. The calculated profiles were then used to simulate the amplified line profile, using a detailed 1D-radiative transfer code, taking into account the effect of saturation. We discuss the possibility to achieve a gain bandwidth that would support pulse amplification below 1 ps.

1 Introduction

The demonstration of seeded, plasma-based XUV lasers with high-order harmonic radiation has opened new and promising prospects for both these sources towards higher peak brightness and output energies. Compared to the usual amplified spontaneous emission (ASE) mode, the optical quality of the seeded output beams is dramatically improved, with a smaller divergence and a higher degree of spatial coherence [1, 2]. The degree of temporal coherence was also observed to be improved by the seeding operation [3], but the measured coherence time was of ~ 1 ps thereby limiting the shortest duration accessible to a similar value [4]. A challenging goal is to extend the pulse duration of seeded XUV lasers to the femtosecond range, since this would considerably enhance the potential of these sources to application fields

L. Meng (✉) · A. Klisnick
ISMO, CNRS-Université Paris-Sud, Orsay, France
e-mail: limin.meng@u-psud.fr

A. Calisti · S. Ferri · C. Mossé · B. Talin
PIIM, CNRS-Aix-Marseille Université, Marseille, France

D. Benredjem
LAC, CNRS-Université Paris-Sud, Orsay, France

O. Guilbaud
LPGP, CNRS-Université Paris-Sud, Orsay, France

like ultrafast coherent imaging or interaction with matter at high XUV intensities. This will require significant enlargement of the XUV laser spectral bandwidth.

The main purpose of the work described in this paper was to determine the main plasma parameters that could be used in the experiment to reach the desired bandwidth. We have used the PPP lineshape code [5] to calculate the respective contributions of the broadening processes that affect the intrinsic spectral profile of the 4d–4p ($J = 0–1$) lasing line in Ni-like Mo. Our study cover an extended range of plasma temperatures and densities over which collisional excitation pumping of these ions can be induced. We consider two different pumping regimes: (i) the transient pumping regime, which relies on a picosecond pump laser pulse, leading to plasmas with relatively low ionic temperatures; (ii) the quasi-steady state (QSS) regime, in which the ionic temperature is higher due to a longer (few 100 ps) pump pulse and more efficient electron-ion thermalization. The calculated intrinsic line profiles were then used to simulate the amplified line profile, using a detailed 1D-radiative transfer code [6], taking into account the effect of saturation. We discuss the possibility to achieve a gain bandwidth that would support pulse amplification below 1 ps.

2 Calculation of the Intrinsic Line Profile

The PPP code is a multi-electron radiator line broadening code [5, 7], which includes natural and Doppler broadening, as well as (electronic) collisional broadening using the classical impact approximation. The effect of ions was treated using the static approximation. Figure 1 shows the computed overall FWHM linewidth $\Delta\nu$ plotted as a function of the electron density, for ionic temperatures of 20 eV (transient pumping, left graph) and 200 eV (QSS pumping, right graph) respectively. In both cases the electron temperature was taken as 200 eV. The overall linewidth was inferred from the calculated spectral profile, which was first fitted with a Voigt profile. The individual contributions of the thermal Doppler component (independent of N_e) and of the (electron) collisional component are also shown in Fig. 1.

It can be seen that the respective weight of collisional versus Doppler broadening varies considerably over the considered N_e range. At high N_e the collisional broadening component dominates in both cases, while the linewidth increases with N_e , although less than proportionally. In the transient pumping case the collisional broadening is always larger than the Doppler one, except for $N_e < 8 \times 10^{19} \text{ cm}^{-3}$. In the QSS pumping case the Doppler broadening starts to dominate for densities below $\sim 3 \times 10^{20} \text{ cm}^{-3}$.

It should be noted that the Doppler broadening is calculated here in the free-particle limit, assuming that the velocity of ion emitters does not change over the radiative lifetime. A more recent investigation, involving molecular dynamics simulations, shows that this approximation can be inappropriate in our conditions, where ionic correlation effects cannot be neglected. This aspect is discussed in a companion paper [7]. The inclusion of these effects in a line-transfer model used to calculate the amplified line profile is not straightforward. Thus for the discussion below, we consider the usual free-particle limit Doppler broadening only.

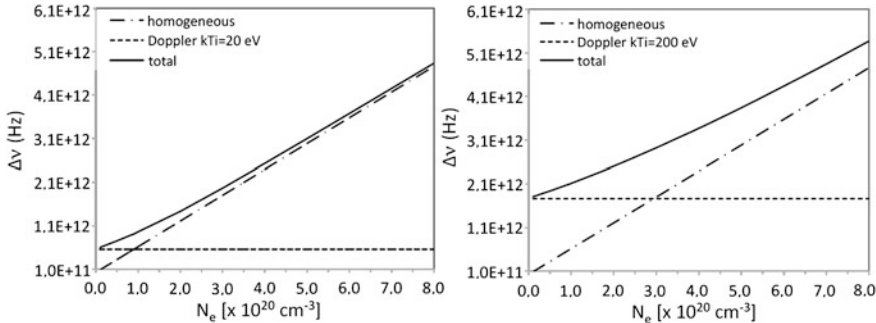


Fig. 1 Calculated intrinsic linewidth (FWHM) as a function of N_e , for 2 pumping regimes: (left) transient pumping ($kT_i = 20$ eV); (right) QSS pumping ($kT_i = 200$ eV). In both cases $kT_e = 200$ eV. Individual Doppler and collisional broadening components are also shown

3 Amplified Line Profile and Fourier-Transform Limit Duration

The calculated intrinsic linewidths were then used to calculate the amplified profile, using a 1D-line transfer code [6]. This code describes the frequency-dependent amplification of the laser line intensity, taking into account the homogeneous (natural and collisional broadening) and inhomogeneous (thermal Doppler frequency shifts) components of the spectral profile, while allowing for gain saturation. A small-signal gain coefficient of 70 cm^{-1} and a plasma length of 7 mm were considered.

Figure 2 shows the evolution of the spectral linewidth as a function of amplification length, calculated in three distinct cases, corresponding to different plasma conditions: (a) $N_e = 8 \times 10^{20}\text{ cm}^{-3}$, $kT_i = 20$ eV (homogeneous profile); (b) $N_e = 2 \times 10^{19}\text{ cm}^{-3}$, $kT_i = 200$ eV (inhomogeneous profile); (c) $N_e = 3 \times 10^{20}\text{ cm}^{-3}$, $kT_i = 200$ eV (mixed profile). As expected, saturation rebroadening is observed only in the inhomogeneous case (b), while the output linewidth recovers $\sim 2/3$ of its intrinsic value for $L = 7$ mm. It should be noted that in all cases (even in the homogeneous case (a)), the amplified line profile tends to a Gaussian shape.

The Fourier-transform limit duration τ_{FL} , i.e. the shortest pulse that could be extracted from the plasma (in a linear amplification regime), is related to the spectral linewidth $\Delta\lambda$ as: $\tau_{FL} = \kappa \frac{\lambda^2}{\Delta\lambda}$, where κ is a numerical factor depending on the particular shape of the line profile (here $\kappa = 1.5 \times 10^{-9}$ for a Gaussian profile). In the three above cases we find that τ_{FL} is below 1 ps, namely (a) $\tau_{FL} = 450$ fs; (b) $\tau_{FL} = 380$ fs; (c) $\tau_{FL} = 650$ fs. The shortest duration is obtained for the strongly inhomogeneous case (b), due to the linewidth rebroadening at saturation. However ionic correlation effects, discussed in [7], were found to be significant in these plasma conditions. As a result, collisional cross-relaxation is efficient and tends to homogenize the profile, preventing the rebroadening behavior.

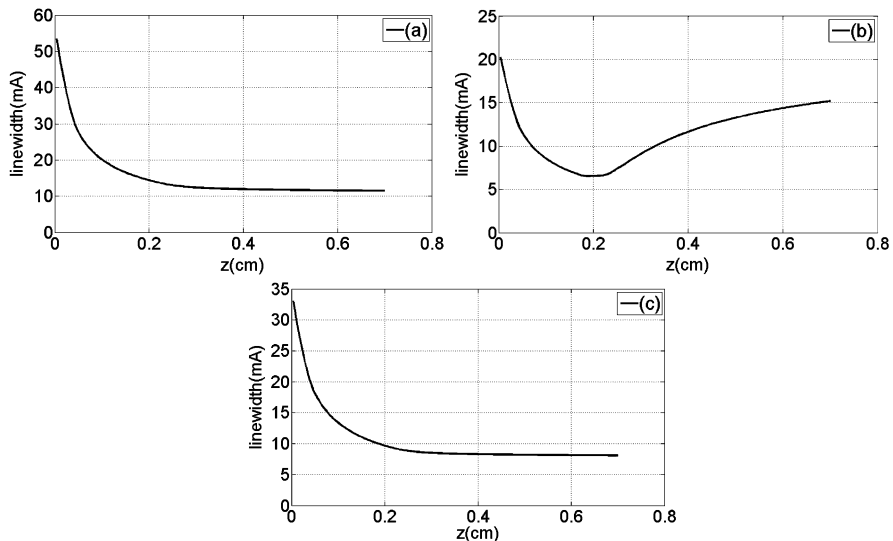


Fig. 2 Calculated amplified linewidth (FWHM) as a function of plasma length for three different plasma conditions, corresponding to different types of profile (see text): (a) homogeneous; (b) inhomogeneous; (c) mixed

References

1. Tissandier, F., et al.: Phys. Rev. A **81**, 063833 (2010)
2. Berrill, M., et al.: Opt. Lett. **35**, 2317 (2010)
3. Meng, L.M., et al.: Opt. Express **19**, 12087 (2011)
4. Wang, Y., et al.: Phys. Rev. A **79**, 023810 (2009)
5. Calisti, A., et al.: Phys. Rev. A **42**, 5433 (1990)
6. Guilbaud, O., et al.: Opt. Lett. **35**, 1326 (2010)
7. Calisti, A., et al.: Study of particle correlation effects on line profiles of Ni-like collisional XUV laser amplifiers. In: Sebban, S., et al. (eds.) X-Ray Lasers 2012. Springer Proceedings in Physics, vol. 147. Springer, Cham (2013). Chapter 9 in this book

Chapter 30

Visualization of Rapid Dynamic Interactions by Flash Soft X-Ray Microscopy

C.S. Menoni, S. Carbajo, I.D. Howlett, W. Chao, E.H. Anderson,
A.V. Vinogradov, I.A. Artyukov, K. Buchanan, M.C. Marconi, and J.J. Rocca

Abstract We demonstrate sequential single-shot real space imaging using a compact soft x-ray (SXR) microscope. A sequence of real space flash images acquired with a table-top SXR laser was used to follow and record the motion of a rapidly oscillating magnetic nanoprobe tip and detect nanoscale dynamic interactions. Changes of tens of nm in the oscillation amplitude were detected when the nanoprobe was made to interact with stray fields from a magnetic sample. Modeling of this interaction confirms the results of the experiments. The ability of compact SXR microscopes to freeze dynamics open up the pathway to investigate the dynamics of a variety of processes that include the motion on nanodevices and potentially nonrecurrent phenomena.

1 Introduction

Time resolved x-ray imaging is a powerful technique to record dynamic interactions at the nanoscale. Stroboscopic pump and probe imaging techniques using synchrotron illumination have been extensively used to monitor dynamics of magnetic materials [1–3]. These experiments have been successful at probing dynamic processes that can be held unaltered over minutes or hours, the time it takes to average

C.S. Menoni (✉) · S. Carbajo · I.D. Howlett · W. Chao · E.H. Anderson · M.C. Marconi ·
J.J. Rocca

NSF ERC for Extreme Ultraviolet Science and Technology, Department of Electrical & Computer Engineering, Colorado State University, Fort Collins, CO 80523, USA
e-mail: carmen.menoni@colostate.edu

W. Chao · E.H. Anderson
NSF ERC for Extreme Ultraviolet Science and Technology and Center for X-ray Optics, LBNL, Berkeley, CA 94720, USA

A.V. Vinogradov · I.A. Artyukov
P.N. Lebedev Physical Institute, Moscow, Russia

K. Buchanan
Physics Department, Colorado State University, Fort Collins, CO 80523, USA

several million of events before moving to the next time delay. There are, however, other material processes such as twinning [4] and nanoscale ablation [5] that are statistically reproducible but individually nonrecurring which can only be imaged using flash illumination. SXR single shot imaging has been demonstrated [6–10]. As of today dynamic SXR imaging has only been realized in holographic and coherent diffractive imaging geometries which require extensive post-image processing [11, 12] using free electron lasers. Electron microscopes have also the ability to follow dynamics at the nanoscale [13–16]. Femtosecond temporal and picometer spatial resolution can be obtained using a scanning imaging configuration similar to photon-based stroboscopic pump and probe, that uses a few electrons per pulse at the expense of long image acquisition times [13, 14]. Single-shot full field imaging instead uses a large number of electrons per pulse, thus the spatial and temporal resolution are limited by space charge effects to 10's of nanometers and 10's of nanoseconds respectively [15, 16]. Electron beams are also affected by the presence of electric and magnetic fields. These constraints do not apply to x-ray microscopes.

Soft x-ray microscopes owe their ability to render real-space images with nanoscale resolution to the use of tailored diffractive optics. Advances in the fabrication of zone plate nanostructures have been instrumental in achieving 12 nm spatial resolution [17]. In turn, the use of bright table-top SXR lasers for illumination give SXR microscopes the capability to acquire single-shot real-space images in a non-destructive way [6]. We demonstrate the recording of nanoscale dynamic interactions using a compact SXR microscope. A sequence of single-shot real-space SXR captured the interaction of a magnetic cantilever tip and a magnetic sample. Analysis of the time-sequenced images revealed an increase in the amplitude of the tip oscillation of a few tens of nm due to the magnetic interaction. These results open new opportunities in material science and nanotechnology, such as the characterization of rapid motion in micro/nano-electro-mechanical devices, and the study of fast non-periodic nanoscale processes in materials, such as the propagation of twins and nanoablation related events. Both these and other laser-initiated phenomena can be accurately synchronized with SXR laser probe pulses by using the same laser driver.

2 Experimental Details and Results

Sequential table-top SXR imaging was implemented using a compact microscope that combines illumination from a desk-top size SXR capillary discharge laser with reflective and diffractive optics [18]. The laser emits pulses of 1.5 ns duration at a wavelength of 46.9 nm (26.5 eV), with a spectral bandwidth of $\Delta\lambda/\lambda = 3.5 \times 10^{-5}$ [19, 20]. A capillary length of 22 cm was selected to obtain pulses of 10 μJ energy, equivalent to 2.4×10^{12} photons/pulse and to maintain the spatial coherence of the laser beam relatively low to minimize coherence effects on the image. The microscope uses a Schwarzschild condenser and a zone plate objective. The Schwarzschild primary convex mirror, 10.8 mm in diameter, and the secondary concave mirror, 50 mm in diameter, are coated with Sc/Si multilayers that result in

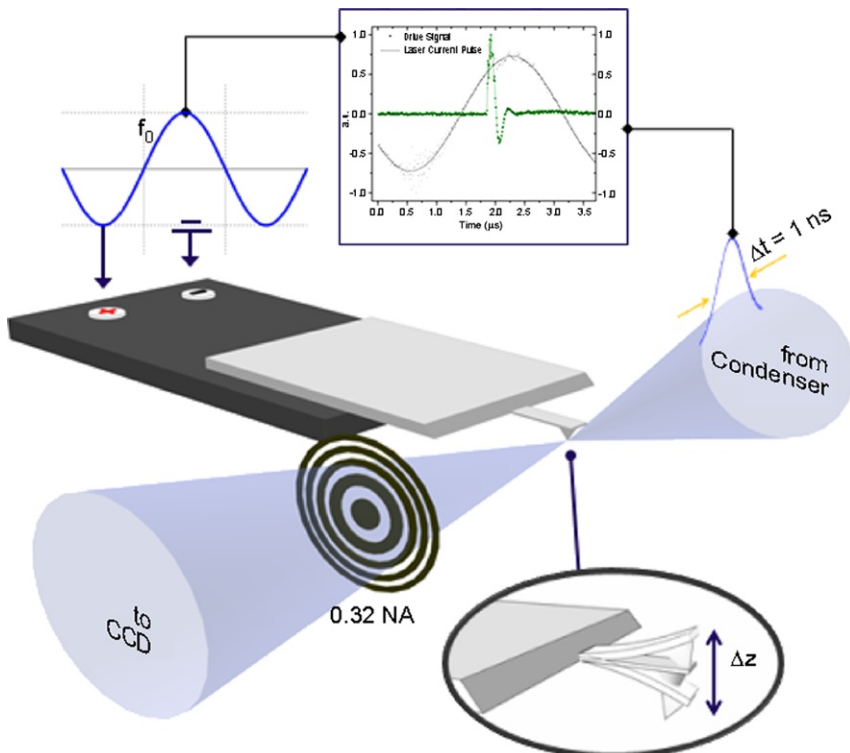


Fig. 1 Schematic of the set up used to implement single shot imaging with a transmission SXR microscope. The object is a commercially available cantilever tip. The tip was driven by a sinusoidal voltage signal of frequency equal to the tip's resonance frequency

a throughput of 16 % at $\lambda = 46.9 \text{ nm}$ and a numerical aperture of 0.18 NA [21]. The objective is a freestanding zone plate with $500 \mu\text{m}$ diameter, numerical aperture 0.32 NA, and a focal length $f = 740 \mu\text{m}$ at $\lambda = 46.9 \text{ nm}$. Its efficiency is 10 % in first order [22]. Sequential single shot images were captured by a back-illuminated array detector with 2048×2048 pixels of $13.5 \mu\text{m}$ size. The detector was cooled to -15°C to minimize thermal noise. We have previously shown through static imaging of gratings with different period that the combination of a 0.32 NA objective zone plate with illumination from the 46.9 nm laser yields images with a spatial resolution of 54 nm [6].

Two commercially available nanoprobe tips were used in the experiments: a high-aspect ratio Si tip and a Co-alloy coated standard magnetic tip that was magnetized along the tip axis prior to use. The former consisted of a cone shaped tip with a nominal radius of 20 nm, a nominal spring constant of 40 N/m, and a resonance frequency of 318.6 kHz. The magnetic nanoprobe had a cone shaped tip radius of 40 nm, a nominal spring constant of 0.7 N/m, and a resonance frequency of 65.2 kHz. Each tip was clamped onto a rectangular bimorph actuator driven by a sinusoidal voltage signal (Fig. 1). The 1:1 array of $10 \mu\text{m} \times 2 \mu\text{m} \times 40 \text{ nm}$ magnetic

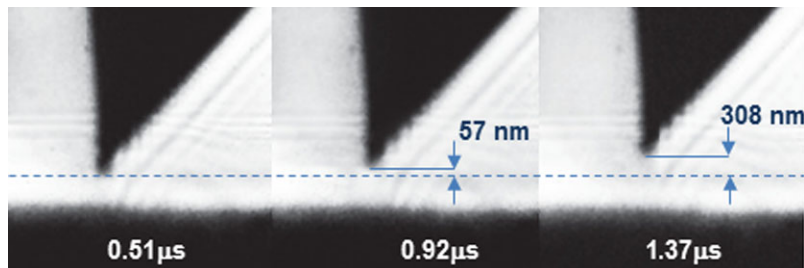


Fig. 2 Sequence of single-shot SXR images of the nanoprobe tip freeze the dynamics of the tip oscillation. The tip moves 57 nm in 0.41 μ s

strips was fabricated by means of standard UV photolithography in conjunction with lift-off process in a 40 nm thick Permalloy film with composition of Ni/Fe 81:19 wt% that was deposited onto a photoresist-patterned Si wafer by DC magnetron sputtering.

Images were acquired by triggering the laser at different times with respect to the tip driving signal. Figure 2 shows a sequence of images taken at different times in the oscillation of the tip. Each image was analyzed using a procedure that consisted of: (1) background-histogram equalization; (2) localization of the tip extremum through a gradient map; (3) plotting of the image intensity profile along a vertical row of pixels containing the tip axis. This intensity profile consists of dark regions at the location of the tip and surface respectively and a clear region in between (Fig. 2). (4) The tip-to-surface separation was determined as the full-width-at-half-maximum of the intensity profile. A set of over 100 sequential images were captured to map the entire period of the tip oscillation. Averaging of five independent sets of tip trajectories traces over a period allowed us to calculate the mean tip-to-sample distance with an uncertainty of ± 3 nm corresponding to one standard deviation. Finally, sequences of images of the nanoprobe tip dynamics were assembled into motion picture by sequencing the SXR images in temporal order [23].

We have used the SXR flash imaging capabilities to record nanoscale dynamic interactions. We exploited the immunity of photons to electrostatic and magnetostatic fields to record the interaction of the magnetic nanoprobe tip with the stray magnetic fields created by the magnetized Permalloy microstrip (Fig. 3a). This type of interaction is what occurs in a magnetic force microscope. From a sequence of single shot SXR images, the motion of the magnetic nanoprobe tip was reconstructed when placed in a region between the strips and above the edge of a strip (Fig. 3). For a given sign of the Permalloy strip remnant field, an increase in the amplitude of the oscillation of (40 ± 3) nm and (30 ± 3) nm were measured. Reversing the direction of the remnant field caused the tip amplitude to decrease (Fig. 3c).

The amplitude changes in the magnetic tip oscillation caused by the interaction with the Permalloy microstrips were modeled assuming the tip to be a perturbed harmonic oscillator in the presence of a magnetic dipole-dipole force. The force gradients were calculated using established values of magnetization of 8×10^5 A/m

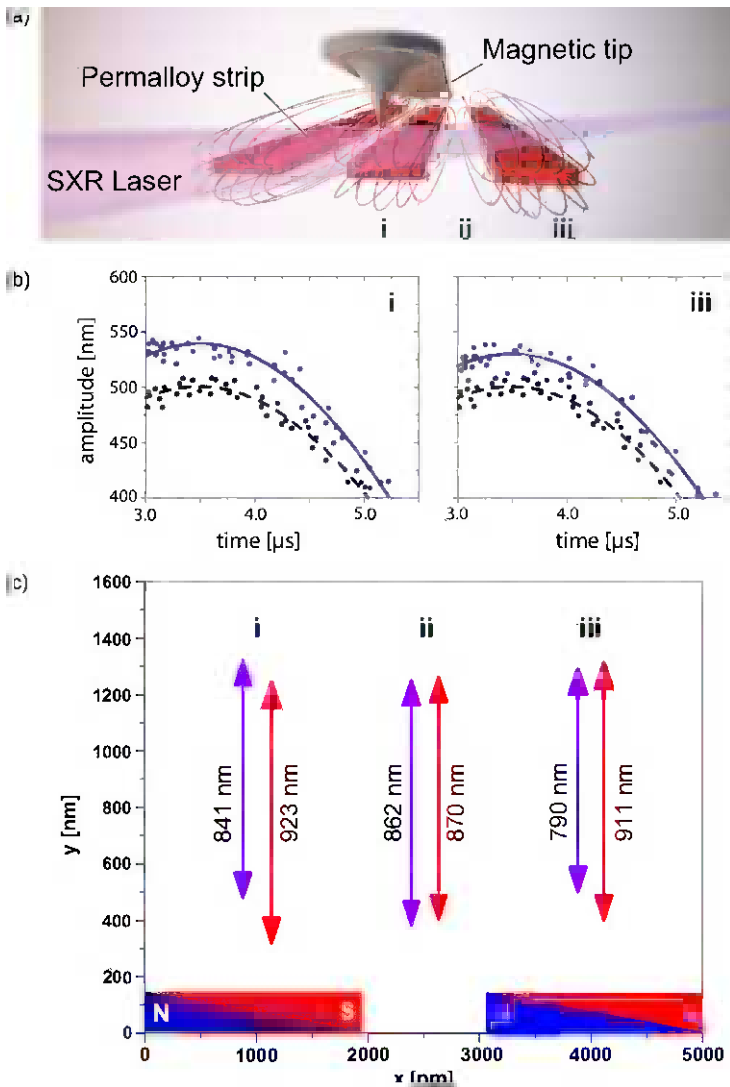


Fig. 3 (a) Schematic rendering of the geometry used to interrogate the magnetic interaction of the magnetized nanoprobe tip and magnetized patterned Permalloy sample. (b) Tip motion reconstructed from the single shot SXR images for locations of the tip above the edge of a microstrip (*i* and *iii*) and in between two microstrips (*ii*). (c) The amplitude of the tip corresponding to the locations indicated by *i*, *ii*, and *iii* is shown for two possible orientations of the remnant field, showing an increase in the amplitude and a decrease compared to the unperturbed oscillation when the direction of the magnetization is changed

and 14×10^5 for Permalloy and Co-alloy which, for the volumes under consideration, result in magnetic moments of $4.1 \times 10^{-17} \text{ A m}^2$ and $6.4 \times 10^{-13} \text{ A m}^2$ for the tip and microstrips respectively. The magnetic force fields effectively change

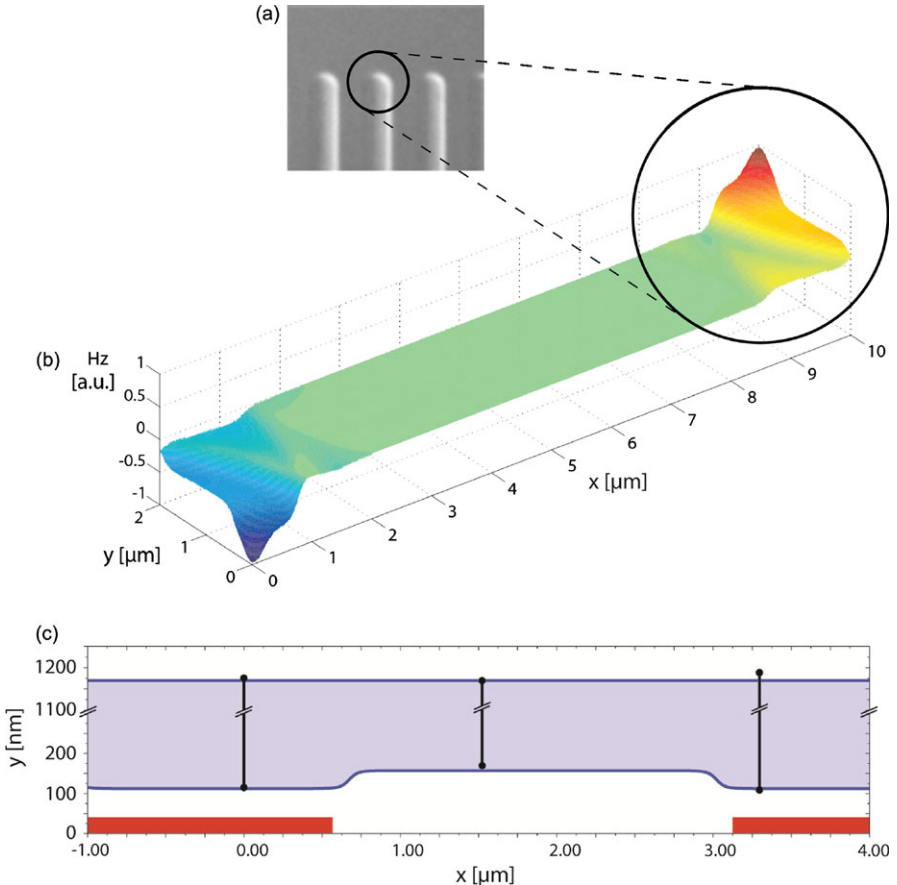


Fig. 4 (a) Photograph of the patterned Permalloy strips. (b) Map of the z-component of the magnetic field strength (Hz) present at $z = 150$ nm from the surface of a single $10\text{ }\mu\text{m} \times 2\text{ }\mu\text{m} \times 40\text{ nm}$ Permalloy strip in remanence along the x direction. The model shows large magnetic strength on the edges of the Permalloy microstrip. Fields calculated using Object Oriented Micro Magnetic Framework (OOMMF) [24]. (c) Calculated amplitude of the tip oscillation for different locations of the tip above or in between the microstrips. The black dots are the maxima and minima of the tip oscillation obtained from the reconstruction of the tip motion shown in Fig. 3b

the restoring force of the oscillating magnetic tip through the addition of a term that is proportional to the magnetic force gradient. A change in the restoring force constant modifies the tip's resonant frequency. When driving the tip at a fixed frequency, a small change in the restoring force varies the amplitude and phase of the tip oscillation. Figure 4 shows the variation of the z-component of the magnetic field calculated at 150 nm above the surface of the microstrip where the tip is located are significant at the edges of the microstrip. The results of the model are shown in Fig. 4c. The model predicts changes in the amplitude of the tip oscillation of tens of nanometers, which is in very good agreement with the experimental results.

3 Conclusions and Outlook

In conclusion we have directly visualized nanoscale phenomena with a table-top microscope using bright flashes from a compact SXR laser. We have recorded single-shot real-space images that mapped the motion of a magnetic nanoprobe tip and its interaction with a magnetic sample. The ability to visualize nanoscale motion on a table top will impact the development of nano-electro-mechanical devices. Moreover, the use of a similar SXR microscope in a reflection configuration [25] will allow to visualize nanoscale material surface dynamics such as laser ablation, nanomachining and the study of material dislocation dynamics, nucleation and growth. Furthermore, our table-top SXR laser dynamic imaging technique is readily scalable in wavelength and temporal resolution. The recent advances in saturated table-top SXR laser sources, that now provide picosecond pulses with energies $> 10 \mu\text{J}$ per pulse at 13.9 nm [26], will open the possibility to visualize ultrafast dynamics with a few tens of nanometer spatial resolution and picosecond time resolution. Further advances in injection-seeding table-top SXR lasers that are expected to produce high energy femtosecond pulses will make it possible to extend this technique to the femtosecond range [27].

Acknowledgements Work supported by the NSF ERC for Extreme Ultraviolet Science and Technology under NSF Award EEC-0310717 using equipment developed under NSF Award MRI-ARRA 09-561, and by the Chemical Sciences, Geosciences and Biosciences Division, Office of Basic Energy Sciences, U.S. Department of Energy. K.S.B. was also supported by NSF award number 0907706.

References

1. Ade, H., et al.: Near-edge X-ray absorption fine-structure microscopy of organic and magnetic materials. *Nat. Mater.* **8**(4), 281–290 (2009)
2. Stoll, H., et al.: High-resolution imaging of fast magnetization dynamics in magnetic nanostructures. *Appl. Phys. Lett.* **84**(17), 3328–3330 (2004)
3. Kammerer, M., et al.: Magnetic vortex core reversal by excitation of spin waves. *Nat. Commun.* **2**, 279–284 (2011)
4. Capolungo, L., et al.: Nucleation and growth of twins in Zr: a statistical study. *Acta Mater.* **57**(20), 6047–6056 (2009)
5. Vaschenko, G., et al.: Nanometer-scale ablation with a table-top soft x-ray laser. *Opt. Lett.* **31**(24), 3615–3617 (2006)
6. Brewer, C.A., et al.: Single-shot extreme ultraviolet laser imaging of nanostructures with wavelength resolution. *Opt. Lett.* **33**(5), 518–520 (2008)
7. Chapman, H.N., et al.: Femtosecond diffractive imaging with a soft-X-ray free-electron laser. *Nat. Phys.* **2**(12), 839–843 (2006)
8. Chou, M.-C., et al.: Single-shot soft-x-ray digital holographic microscopy with an adjustable field of view and magnification. *Opt. Lett.* **34**(5), 623–625 (2009)
9. Kim, H.T., et al.: Single-shot nanometer-scale holographic imaging with laser-driven x-ray laser. *Appl. Phys. Lett.* **98**(12), 121105 (2011)
10. Ravasio, A., et al.: Single-shot diffractive imaging with a table-top femtosecond soft X-ray laser-harmonics source. *Phys. Rev. Lett.* **103**(2), 028104 (2009)

11. Barty, A., et al.: Ultrafast single-shot diffraction imaging of nanoscale dynamics. *Nat. Photonics* **2**(7), 415–419 (2008)
12. Gunther, C.M., et al.: Sequential femtosecond X-ray imaging. *Nat. Photonics* **5**(2), 99–102 (2011)
13. Zewail, A.H.: Four-dimensional electron microscopy. *Science* **328**(5975), 187–193 (2010)
14. Flannigan, D.J., et al.: Nanomechanical motions of cantilevers: direct imaging in real space and time with 4D electron microscopy. *Nano Lett.* **9**(2), 875–881 (2009)
15. Taheri, M.L., et al.: Laser-based in situ techniques: novel methods for generating extreme conditions in TEM samples. *Microsc. Res. Tech.* **72**(3), 122–130 (2009)
16. Kim, J.S., et al.: Imaging of transient structures using nanosecond in situ TEM. *Science* **321**(5895), 1472–1475 (2008)
17. Chao, W., et al.: Demonstration of 12 nm resolution Fresnel zone plate lens based soft X-ray microscopy. *Opt. Express* **17**(20), 17669–17677 (2009)
18. Vaschenko, G., et al.: Nanoimaging with a compact extreme-ultraviolet laser. *Opt. Lett.* **30**(16), 2095–2097 (2005)
19. Heinbuch, S., et al.: Demonstration of a desk-top size high repetition rate soft x-ray laser. *Opt. Express* **13**(11), 4050–4055 (2005)
20. Urbanski, L., et al.: Spectral linewidth of a Ne-like Ar capillary discharge soft-x-ray laser and its dependence on amplification beyond gain saturation. *Phys. Rev. A* **85**(3), 033837 (2012)
21. Artioukov, I.A., et al.: Schwarzschild soft-x-ray microscope for imaging of nonradiating objects. *Opt. Lett.* **20**(24), 2451–2453 (1995)
22. Anderson, E.H.: Specialized electron beam nanolithography for EUV and X-ray diffractive optics. *IEEE J. Quantum Electron.* **42**(1), 27–35 (2006)
23. Carbajo, S., et al.: Sequential single-shot imaging of nanoscale dynamic interactions with a table-top soft x-ray laser. *Opt. Lett.* **37**(14), 2994–2996 (2012)
24. NIST: Available from <http://math.nist.gov/oommf/>
25. Brizuela, F., et al.: Reflection mode imaging with nanoscale resolution using a compact extreme ultraviolet laser. *Opt. Express* **13**(11), 3983–3988 (2005)
26. Martz, D.H., et al.: High-energy 13.9 nm table-top soft-x-ray laser at 2.5 Hz repetition rate excited by a slab-pumped Ti:sapphire laser. *Opt. Lett.* **35**(10), 1632–1634 (2010)
27. Wang, Y., et al.: Phase-coherent, injection-seeded, table-top soft-X-ray lasers at 18.9 nm and 13.9 nm. *Nat. Photonics* **2**(2), 94–98 (2008)

Chapter 31

Using the X-FEL to Understand X-Ray Thomson Scattering for Partially Ionized Plasmas

Joseph Nilsen, Walter R. Johnson, and K.T. Cheng

Abstract For the last decade numerous researchers have been trying to develop experimental techniques to use X-ray Thomson scattering as a method to measure the temperature, electron density, and ionization state of high energy density plasmas such as those used in inertial confinement fusion. X-ray laser sources have always been of interest because of the need to have a bright monochromatic X-ray source to overcome plasma emission and eliminate other lines in the background that complicate the analysis. With the advent of the X-ray free electron laser (X-FEL) at the SLAC Linac Coherent Light Source (LCLS) we now have such a source available in the keV regime. Other X-FEL sources are being built in Germany and around the world. One challenge with X-ray Thomson scattering experiments is understanding how to model the scattering for partially ionized plasmas. Most Thomson scattering codes used to model experimental data greatly simplify or neglect the contributions of the bound electrons to the scattered intensity. In this work we take the existing models of Thomson scattering that include elastic ion-ion scattering and the electron-electron plasmon scattering and add the contribution of the bound electrons in the partially ionized plasmas. Except for hydrogen plasmas almost every plasma that is studied today has bound electrons and it is important to understand their contribution to the Thomson scattering, especially as new X-ray sources such as the X-FEL will allow us to study much higher Z plasmas. Currently most experiments have looked at hydrogen or beryllium. We will first look at the bound electron contributions to beryllium by analyzing existing experimental data. We then consider several higher Z materials such as Cr and predict the existence of additional peaks in the scattering spectrum that requires new computational tools to understand. For a Sn plasma we show that the bound contributions changes the shape of the scattered spectrum in a way that would change the plasma temperature and density inferred by the experiment.

J. Nilsen (✉) · K.T. Cheng

Lawrence Livermore National Laboratory, Livermore, CA 94551, USA
e-mail: nilsen1@lbl.gov

W.R. Johnson
University of Notre Dame, Notre Dame, IN 46556, USA

1 Introduction

Thomson scattering of X-rays is being developed as an important diagnostic technique to measure temperatures, densities, and ionization balance in warm dense plasmas. Glenzer and Redmer [1] have reviewed the underlying theory of Thomson scattering being used in experiments.

In this work we start with the theoretical model proposed by Gregori et al. [2] but with one important difference. We evaluate the Thomson-scattering dynamic structure function using parameters taken from our own average-atom code [3, 4]. The average-atom model is a quantum mechanical version of the temperature-dependent Thomas-Fermi model of plasma developed years ago by Feynman et al. and is described in Ref. [5]. It consists of a single ion of charge Z with a total of Z free and bound electrons in a Wigner-Seitz cell that is embedded in a uniform “jellium sea” of free electrons whose charge is balanced by a uniform positive background. This model enables us to consider the contributions from the bound electrons in a self-consistent way for any ion. Other approaches such as Gregori’s includes hydrogenic wavefunctions with screening factors to approximate the contribution from the bound electrons for a limited number of materials.

In this paper we look first look at the bound electron contributions to beryllium by analyzing existing experimental data. We then consider several higher Z materials such as Cr and predict the existence of additional peaks in the scattering spectrum that requires new computational tools to understand. For a Sn plasma we show that the contributions from the bound electrons can change the shape of the scattered spectrum in a way that would change the plasma temperature and density inferred by the experiment.

2 Validating the Average-Atom Code for Be Experiments

Numerous experiments have been done to look at Thomson scattering for low- Z materials such as hydrogen and beryllium. We examine one particular experiment [6] done at the Omega laser facility that looked at Thomson scattering in the forward scattering direction (40 degrees) off solid Be with a Cl Ly- α source at 2963 eV. Figure 1 shows the measured spectrum as the noisy dotted line. An electron temperature of 18 eV, ion temperature of 2.1 eV, and density of 1.647 g/cc is used in the average-atom model to give an electron density of 1.8×10^{23} per cc, in agreement with the analysis in Ref. [6]. The dashed line shows the experimental source function from the Cl Ly- α line. Because of satellite structure we approximate the source by 3 lines: a Cl Ly- α line at 2963 eV with amplitude 1 and two satellites at 2934 and 2946 eV with relative amplitudes of 0.075 and 0.037 respectively. Using the 3 weighted lines to do the Thomson scattering calculation, we calculate the scattering amplitude for Thomson scattering (solid line) and compare against the experimental data (dotted line). We observe excellent agreement within the experimental noise. Contributions from the bound 1s electrons have a threshold at 2876 eV that are beyond the range of the data shown in the figure.

Fig. 1 Intensity vs photon energy for scattering of a Cl Ly- α X-ray off Be at 40°. Dotted line is experimental data (see Ref. [6]) while solid line is calculation for an electron temperature of 18 eV. The dashed line shows the Cl X-ray source

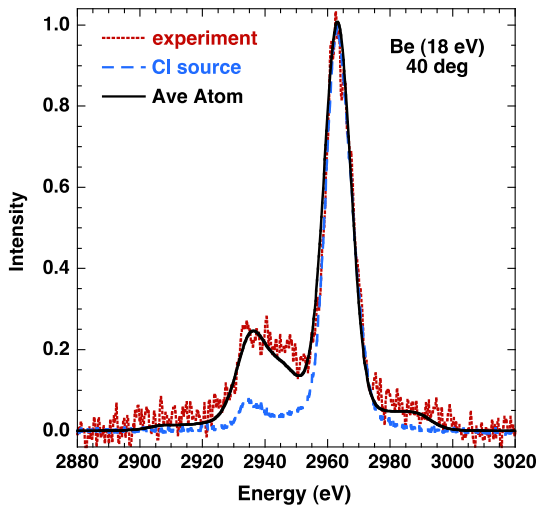
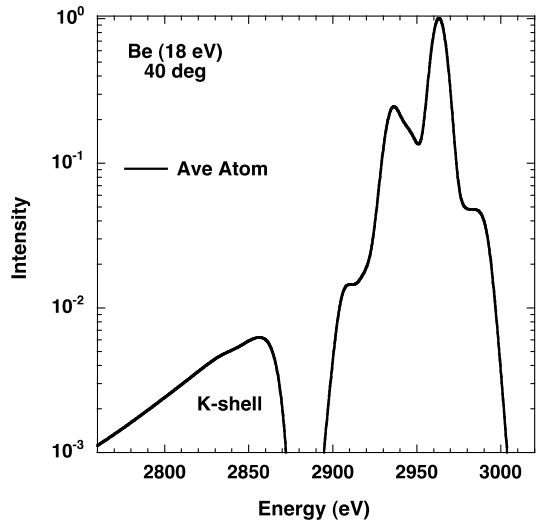
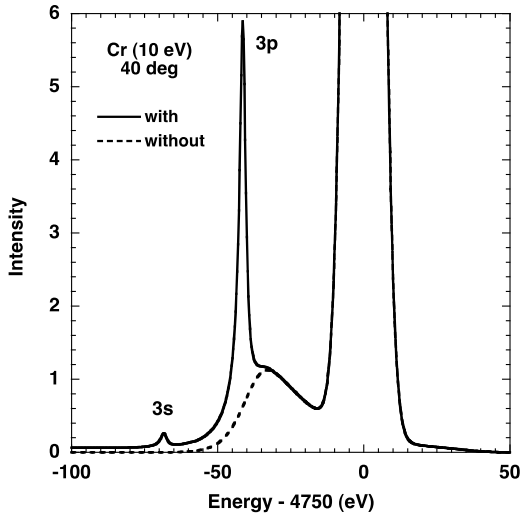


Fig. 2 Intensity vs photon energy for calculation of scattering of a Cl Ly- α X-ray off Be at 40° for an electron temperature of 18 eV. The contribution from the K-shell bound electrons is shown



For Be under the conditions just described the L-shell is completely stripped but the K-shell is 97 % occupied. The average-atom code has $Z_f = 1.647$ for the number of free electrons in the jellium sea outside the Wigner-Seitz cell. The binding energy of the K-shell electron is 86.8 eV which means the threshold for seeing the bound state contribution should begin at $2963 - 86.8 = 2876.2$ eV. To understand the contributions of the bound K-shell electrons to the Thomson scattering we expand the energy scale in Fig. 1 and re-plot it on a log-scale looking just at the average-atom calculation. In Fig. 2 we observe a K-shell contribution that is about 40 times weaker than the low-energy plasmon peak so it would be very difficult to observe in a laser-plasma experiment given the experimental noise.

Fig. 3 Intensity vs photon energy for calculation of scattering of a 4750 eV X-ray line off 10 eV Cr at 40°. The case where the 3p and 3s bound electron contributions are included is shown by solid line

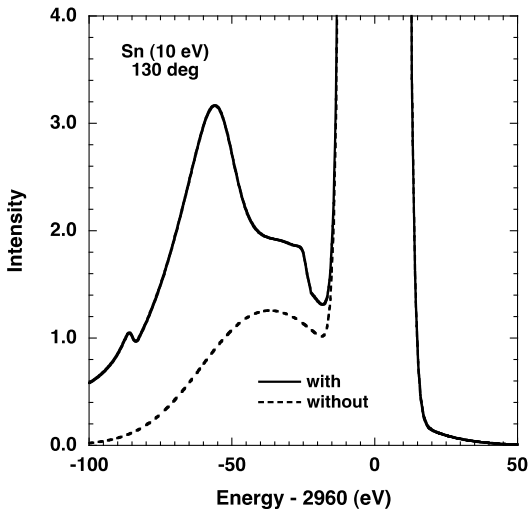


3 Modeling Cr and Sn Experiments

If we now consider higher-Z materials such as Cr and Sn at an electron temperature of 10 eV the bound state contribution can be very important. Following Refs. [4, 6] an ion/electron temperature ratio of 0.1 is assumed to reduce the central elastic scattering peak. The average-atom code predicts that solid density Cr (7.19 g/cc) heated to 10 eV has 6.2 continuum electrons in the Wigner-Seitz cell. This makes it a closed Ar-like core with nearly fully occupied 3s and 3p subshells with binding energies of 57.7 and 30.7 eV, respectively. The code predicts $Z_f = 2.92$ and an electron density of 2.4×10^{23} per cc. Figure 3 shows the scattered intensity versus photon energy for calculations done with (solid line) and without (dashed line) the contribution of the bound electrons for a 4750 eV X-ray source scattered at 40° off the Cr. Without the bound electrons we predict the central elastic scattering peak and the plasmon peaks. When we include the effect of the bound electrons we predict a very strong scattering peak that is downshifted about 40 eV from the central elastic peak due to the 3p electrons and a weaker 3s peak.

For solid density Sn (7.3 g/cc) at 10 eV we look at the case of the 2960 eV X-ray source scattering in the backward direction at 130°. The average-atom code predicts that warm dense Sn has 4.4 continuum electrons with an average occupation of 8.8 for the 4d electrons and 0.8 for the 5s electrons outside a closed Kr-like core with all the lower orbital subshells fully occupied. We predict $Z_f = 3.37$ which gives an electron density of 1.25×10^{23} per cc. The binding energies of the 4d and 5s electrons are 22.4 and 2.14 eV, respectively, which means the effect of the 5s electron will be hidden under the elastic scattering peak. Figure 4 plots the scattering intensity versus photon energy for calculations done with (solid line) and without (dashed line) the contribution of the bound electrons. For backward scattering the scattering is no longer in the collective regime and the distinct plasmon peaks are replaced by a broader scattering structure. The contribution from the bound 4d electrons is now an

Fig. 4 Intensity vs photon energy for calculation of scattering of a 2960 eV X-ray line off Sn at 130° for an electron temperature of 10 eV. The strong contribution from the 4d bound electrons are apparent for the case where the bound electrons are included (solid line) when compared with case without bound electrons (dashed line)



additional large broad feature that lies on top of the Thomson scattering and would make it easy to misinterpret the spectrum if one did not understand the contribution of the bound electrons.

4 Conclusions

The availability of bright monochromatic X-ray line sources from X-ray free electron laser facilities opens up many new possibilities to use Thomson scattering as an important diagnostics technique to measure the temperatures, densities, and ionization balance in warm dense plasmas.

Current attempts to model Thomson scattering tend to use very simplified models, if anything, to model the effect of the bound electrons on the measured scattered intensity. Our approach here is to evaluate the Thomson-scattering dynamic structure function using parameters taken from our own average-atom code [3, 4]. This model enables us to consider contributions from the bound electrons in a self-consistent way for any ion.

In this paper we validate our average-atom based Thomson scattering code by comparing our model against existing experimental data for Be near solid density and temperature near 18 eV. For solid density Cr at 10 eV we predict the existence of additional peaks in the scattering spectrum that requires new computational tools to understand. We also analyze solid density Sn at 10 eV and show that the contributions from the bound electrons can change the shape of the scattered spectrum in a way that would change the plasma temperature and density inferred by the experiment.

Acknowledgements This work was performed under the auspices of the U.S. Department of Energy by Lawrence Livermore National Laboratory under Contract DE-AC52-07NA27344.

References

1. Glenzer, S.H., Redmer, R.: Rev. Mod. Phys. **81**, 1625 (2009)
2. Gregori, G., Glenzer, S.H., Rozmus, W., Lee, R.W., Landen, O.L.: Phys. Rev. E **67**, 026412 (2003)
3. Johnson, W.R., Guet, C., Bertsch, G.F.: J. Quant. Spectrosc. Radiat. Transf. **99**, 327–340 (2006)
4. Johnson, W.R., Nilsen, J., Cheng, K.T.: Thomson scattering in the average-atom approximation. Phys. Rev. E **86**, 036410 (2012)
5. Feynman, R.P., Metropolis, N., Teller, E.: Phys. Rev. **75**, 1561 (1949)
6. Döppner, T., et al.: HEDP **5**, 182 (2009)

Chapter 32

Development of Soft X-Ray Microscopy Using Fresnel Zone Plate for Observation of Laser-Induced Surface Dynamics

M. Nishikino, M. Baba, T. Suemoto, N. Hasegawa, M. Ishino, T. Kaihori, T. Kawachi, and M. Yamagiwa

Abstract X-ray reflective microscope in EUV region has been tried with a Fresnel zone plate (FZP). FZP with an outermost zone width of $0.28\text{ }\mu\text{m}$ and thickness of 250 nm is used as an objective lens. The focal length of FZP is 10 mm at the wavelength of 13.9 nm. Image of a test object has been taken, and the spatial resolution of the measured image is estimated to be less than $1\text{ }\mu\text{m}$ in the case of the magnification of 20.

1 Introduction

The dynamical processes of the ultra-short pulse laser induced surface modifications such as laser ablation come to attract much attention for the micro processing [1, 2]. The understanding of the dynamics of the laser ablation process is important for the accuracy and control of the femtosecond laser processing technique. However, the dynamics of the femtosecond laser ablation is still not clear. Several studies on the time-resolved imaging of femtosecond laser ablation process have been performed on various materials. We have developed the femto-second laser pump and soft x-ray laser interferometer system in order to observe the dynamical processes of the femto-second laser ablation. By using this system, we succeed to obtain surface expansion of the laser induced Platinum (Pt) surface in the early stage [3–5]. It is necessary for the observation of detailed laser ablation to develop the measurement technique with high spatial resolution. An x-ray microscopy technique has expanded in the various fields due to its capability of nondestructive, high resolution and highly sensitivity analysis [6, 7]. The x-ray microscopy with high spatial resolution has been developed for mainly x-ray transmitted samples. In the case of

M. Nishikino · N. Hasegawa · M. Ishino · T. Kaihori · T. Kawachi (✉) · M. Yamagiwa
Quantum Beam Science Directorate, Japan Atomic Energy Agency, 8-1-7 Umemidai, Kizugawa,
Kyoto 619-0215, Japan
e-mail: kawachi.tetsuya@jaea.go.jp

M. Baba · T. Suemoto
The Institute for Solid State Physics, University of Tokyo, 5-1-5 Kashiwanoha, Kashiwa, Chiba
277-8581, Japan

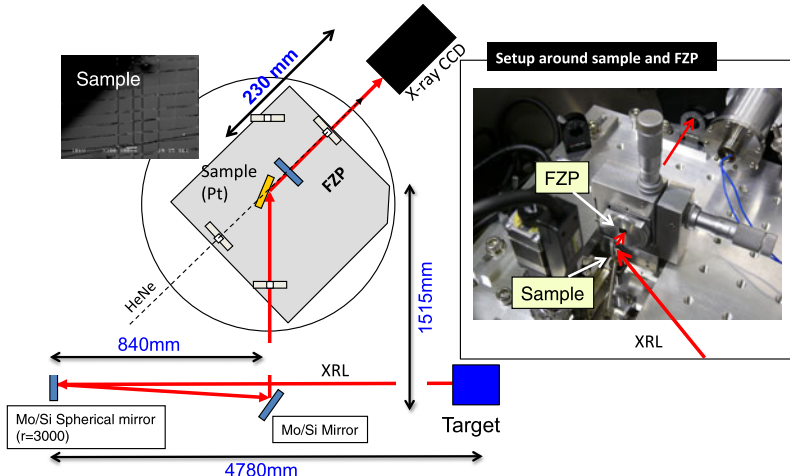


Fig. 1 Schematic view of the experimental setup

the measurement of the opaque sample surface, we can use the refraction type of the x-ray microscopy. Recently, the refraction type of x-ray microscopy with high resolution is developed for the technique of the mask defects in the EUV lithography [8]. However, the decrease in the spatial resolution caused by the deference of focal depth is seemed to be a problem. In this study we have developed the proto-type reflected soft x-ray microscopy with a practical level resolution using the Fresnel zone plate.

2 Experimental Setup and Results

A schematic view of the experimental setup for proto-type refracted x-ray microscopy is shown in Fig. 1. The experiment has been performed at JAEA plasma x-ray laser (XRL) beam lines. A highly coherent XRL at a wavelength of 13.9 nm was generated by the oscillator-amplifier configuration with two targets. The output energy of the XRL beam was about 0.1 μ J, corresponding to a flux of about 10^{10} photons/pulse. The pulse width of the XRL was about 7 ps. The distance between the FZP and the CCD camera is 230 mm in the case of magnification of 20. The image of the test pattern was measured with the CCD camera. The FZP contains a poly(methylmethacrylate) (PMMA) zone on a 0.75×0.75 mm² silicon nitride (SiN) membrane with a thickness of 50 nm. The diameter of the FZP was 0.5 mm, and the total zone number and outermost zone width were 450 and 280 nm, respectively. The focal length was 10 mm for a λ of 13.9 nm. The theoretical resolution was 680 nm. We have obtained the single shot image of the grid on the sample surface.

Figure 2(a) shows single-shot images and spatial profiles of the test pattern in the different focal position. The spatial resolution is about 1 μ m and keeps for about 160 μ m on the sample in the horizontal direction. In the case of few photon numbers

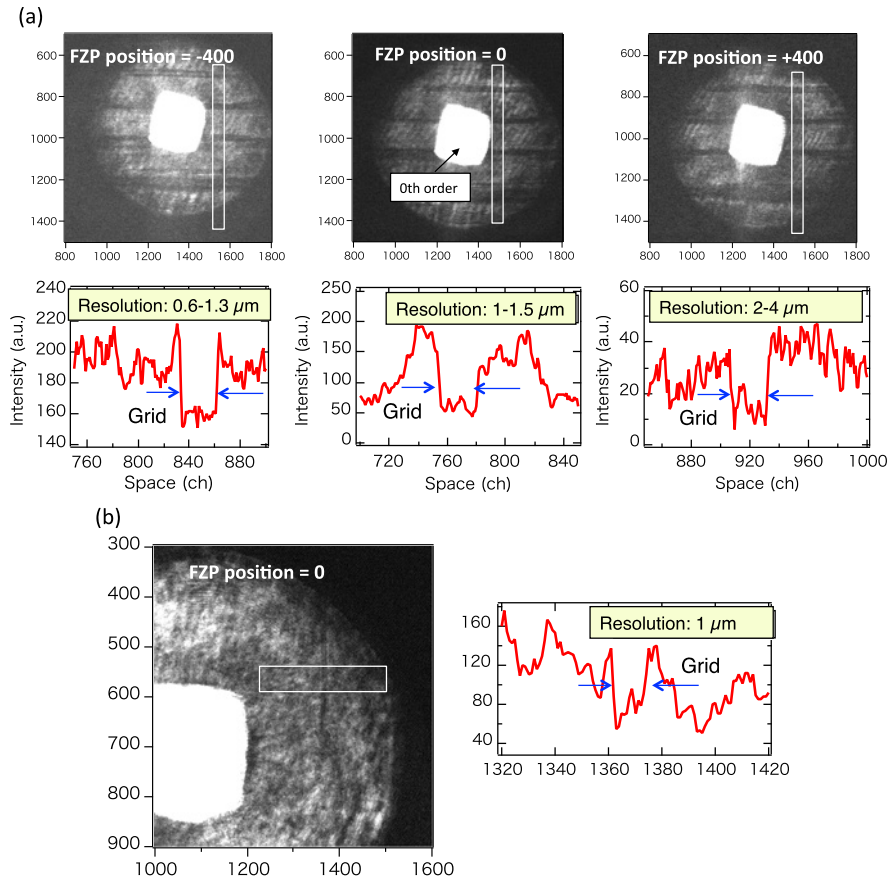


Fig. 2 Single shot x-ray image of test pattern. **(a)** The horizontal grid image. **(b)** The vertical grid image

in the single-shot image, it becomes a high spatial resolution by the data accumulation of x-ray images. Figure 2(b) shows single-shot images and spatial profiles of the test pattern in the vertical direction. The spatial resolution on sample is about 2.6 μm , because of a grazing incidence in the reflected x-ray microscopy system. In this experiment, the spatial resolution by the limitation of the CCD pixel size and the magnification was demonstrated over whole region of the sample surface.

3 Summary

We have developed the reflective x-ray microscopy and observed the surface groove of test pattern. The spatial resolution is evaluated about 1 μm in vertical and about 3 μm in horizontal direction, respectively. In future, the spatial resolution will be

improved by increasing the magnification, and the XRL pump-probe system can be upgraded to have higher spatial resolution of 1 nm in depth and 100 nm in lateral space by combining the reflective x-ray microscopy.

Acknowledgements This work was partly supported by a Grant-in-Aid for Young Scientist (B) No. 24710096 from the Japan Society for the Promotion of Science. The authors are grateful to the staff of the x-ray laser application group for their technical support.

References

1. Korte, F., et al.: *Appl. Phys. A* **79**, 879 (2004) (2010)
2. Perieira, A., et al.: *Appl. Phys. A* **79**, 1443 (2004)
3. Suemoto, T., et al.: *Opt. Express* **18**, 14114 (2010)
4. Ochi, Y., et al.: *Jpn. J. Appl. Phys.* **51**, 016601 (2012)
5. Hasegawa, N., et al.: Observation of the laser-induced surface dynamics using the single-shot soft x-ray laser probe. In: Sebban, S., et al. (eds.) *X-Ray Lasers 2012*. Springer Proceedings in Physics, vol. 147. Springer, Cham (2013). Chapter 19 in this book
6. Schmahl, G., Rudolph, D. (eds.): *X-Ray Microscopy*. Springer, Berlin (1984)
7. Atwood, D.T.: *Soft X-Rays and Extreme Ultraviolet Radiation: Principles and Applications*. Cambridge University Press, Cambridge (1999). Chapter 9
8. Brizuela, F., et al.: *Opt. Lett.* **34**, 271 (2009)

Chapter 33

0.27 GW Soft X-Ray Pulse Using a Plasma-Based Amplification Chain

E. Oliva, M. Fajardo, P. Velarde, D. Ros, S. Sebban, and P. Zeitoun

Abstract Seeding plasma-based soft-x-ray lasers (PBSXRL) with high order harmonics (HOH) has been demonstrated in plasmas created from gas targets (Zeitoun et al. in *Nature* 431:426, 2004) and solid targets (Wang et al. in *Nat. Photonics* 2:94, 2008), obtaining 1 μ J, 1 ps pulses. Reaching multi-microJoule, hundreds of fs regime is the ultimate goal. Recent papers (Oliva et al. in *Opt. Lett.* 34(17):2640–2642, 2009; *Phys. Rev. E* 82(5):056408, 2010) showed that increasing the width (up to 1 mm) of the plasma increases the amplification surface and improves the gain zone properties. Up to 20 μ J could be extracted when seeding but the temporal duration and profile was not studied. Simulations show that the HOH is weakly amplified whereas most of the energy is within a long (several picoseconds) wake induced by the HOH (Al'miev et al. in *Phys. Rev. Lett.* 99(12):123902, 2007; Kim et al. in *Phys. Rev. Lett.* 104:053901, 2010). Amplified Spontaneous Emission (ASE) is also present in the output beam. Using the 1D Maxwell-Bloch code *DeepOne* (Oliva et al. in *Phys. Rev. A* 84(1):013811, 2011) we will show that fully coherent, wake and ASE-suppressed, 21.6 μ J, 80 fs pulse can be obtained when optimizing at the same time both the seed and the plasma conditions.

E. Oliva (✉) · S. Sebban · P. Zeitoun
Laboratoire d'Optique Appliquée, ENSTA ParisTech, École Polytechnique ParisTech, CNRS,
UMR 7639, Palaiseau, France
e-mail: eduardo.oliva@ensta-paristech.fr

M. Fajardo
Centro de Física dos Plasmas, Instituto Superior Técnico, Lisbon, Portugal

P. Velarde
Instituto de Fusión Nuclear, Universidad Politécnica de Madrid, Madrid, Spain

D. Ros
CLUPS, EA4127, Bat 106, Université Paris-Sud, 91405 Orsay, France

1 Introduction

The emergence of free-electron lasers (FEL) emitting in soft X-rays (30 eV–1 keV) and hard X-rays (energy greater than 1 keV) [9] is making astonishing advances in time-resolved X-ray Science [3, 8]. Plasma based seeded soft X-ray lasers [14, 15] are table-top sources that deliver several hundreds nanoJoules with optimal spatial properties as they are fully coherent [14] and aberration-free [4]. However, current and future applications need pulses of hundred femtosecond or shorter. In addition to this, time-dependent Maxwell-Bloch models show that the output beam consists of amplified spontaneous emission (ASE), weakly amplified HOH and a wake field with a complex structure (Rabi oscillations and coherent decay) [1, 6].

In this article, using our time-dependent Maxwell-Bloch code *DeepOne*, we will study the seeding and amplification of high order harmonics (HOH) inside plasma-based amplifiers. We will show that adjusting HOH duration and energy to some values given by plasma hydrodynamics leads to a single component pulse of 1.5 μJ, 140 fs. The amplifier required is a 2.5 mm long, 100 μm wide plasma. The energy of the amplified pulse can be enhanced by increasing the width (i.e. the amplification surface) of the plasma [10, 11]. Nevertheless, to keep the duration of the HOH along the amplifier and avoid the creation of strong ASE and wake, it is necessary to seed at high intensity. Among other possible sources, we selected as seeding source a 100 μm wide plasma amplifier seeded by HOH as described above. We simulated the full pre-amplifier main-amplifier chain, demonstrating that it is possible to obtain a 21.6 μJ, 80 fs single pulse when seeding carefully a 1 mm wide, 2 mm long plasma with a 100 μm wide, 2.5 mm long plasma.

2 Maxwell-Bloch Equations

Amplification of the HOH through a plasma is a multiscale phenomenon involving different physical processes: temporal variation of the envelop of the HOH electric field (tens of femtoseconds), plasma response to this electric field (tens of picoseconds) and plasma hydrodynamics (hundreds of picoseconds to nanoseconds). Maxwell-Bloch type equations (Eqs. (1), (2), (3) and (4)) take into account the first two processes whereas hydrodynamic data is used as an input [12]:

$$\frac{\partial E}{\partial \zeta} = \frac{i\omega_0}{2c} \left[\mu_0 c^2 P - \left(\frac{\omega_p}{\omega_0} \right)^2 E \right] \quad (1)$$

$$\frac{\partial P}{\partial \tau} = \Gamma - \gamma P - \frac{iz_{21}^2}{\hbar} E(N_2 - N_1) \quad (2)$$

$$\frac{\partial N_2}{\partial \tau} = \sum_k C_{k2} N_k + \text{Imag}(E^* P) \frac{1}{2\hbar} \quad (3)$$

$$\frac{\partial N_1}{\partial \tau} = \sum_k C_{k1} N_k - \text{Imag}(E^* P) \frac{1}{2\hbar} \quad (4)$$

Equation (1) is deduced from Maxwell wave equation for the electric field. It describes the propagation, amplification by the polarization density P and damping by the free electron current of the envelope of the electric field. ω_p and ω_0 are respectively the plasma frequency and the electric field frequency. To simplify the equations we use the coordinate change $\tau = t - \frac{z}{c}$, the so-called reduced time (i.e. the referential frame of the photon), and define $\xi = ct\tau$.

The rest of equations are deduced from Bloch equations. Equation (2) gives the temporal evolution of the polarization [7, 13], where γ is the depolarization rate, which we take to be proportional to the electron-ion collision frequency [7] and N_2, N_1 are respectively the population of the upper and lower level of the transition. z_{21} is the dipole matrix element. To model the spontaneous emission, we have added a stochastic source term, Γ . This term is a random variable with vanishing correlation function, properly normalized to obtain the expected Lorenzian lasing line profile [2, 7].

Finally, the populations of the levels involved on the lasing transition are computed using the standard rate equations coupled with the electric field (Eqs. (3), (4)). The populations of the levels involved on the transition are coupled with collisional (de)excitation and radiative deexcitation rates included in the C_{ij} coefficients and with the soft X-ray laser electric field through polarization density. We have modeled the $2p^53s J = 1 \rightarrow 2p^53p J = 0$ transition in Ne-like Zinc, situated at 21.2 nm.

3 Polarization Dynamics and Amplification

The amplification of a short (tens of femtoseconds) HOH pulse inside a plasma has been studied recently in several papers [1, 5, 6, 12]. The HOH immediately polarizes the medium and creates a trailing pulse. The harmonic itself is barely amplified and is the trailing pulse (the wake) who extracts the energy stored in the amplifier, but during several picoseconds. The pulse shape is given by the plasma response to the HOH electric field, i.e. by polarization dynamics.

An exact solution of the polarization induced by a Gaussian HOH pulse, assuming that the HOH pulse does not modify the population inversion (i.e. far from the saturation regime) can be written in as a product of three terms $P(t) = P_0 \cdot P_1 \cdot P_2$ given by:

$$P_0(t) = -\frac{iz_{21}^2}{\hbar} E_0 (N_2 - N_1) e^{\frac{\gamma^2 \sigma^2}{2}} \sigma \sqrt{2\pi} \quad (5)$$

$$P_1(t) = \frac{1}{\sigma \sqrt{2\pi}} \int_{-\infty}^t e^{-\frac{(\tau-t_{cent}-\gamma\sigma^2)^2}{2\sigma^2}} d\tau \quad (6)$$

$$P_2(t) = \begin{cases} e^{-\gamma(t-t_{cent})} & t \geq t_{cent} \\ 1 & \text{otherwise} \end{cases} \quad (7)$$

where E_0 is the maximum seeded electric field, σ is the standard deviation of the Gaussian profile of the field and t_{cent} is the time of the maximum seed intensity. P_1 and P_2 define the temporal shape of the polarization. P_1 controls the rising time

(which depends on σ) and P_2 is the decay time, given by γ , the electron-ion collision frequency. Since both terms are normalized to unity, the numerical value of the polarization is given by P_0 . Thus, the temporal shape of the amplified beam is given by the last two factors and controlled by σ and γ . In the case of 20 fs HOH seeded in a plasma with $n_e = 2.2 \times 10^{20} \text{ cm}^{-3}$ and $T_e = 531 \text{ eV}$, the two characteristic times are $\sigma = 9 \text{ fs}$ and $\gamma^{-1} = 176 \text{ fs}$. The small value of σ induces a sudden rise of the polarization, which decays slowly, due to the higher value of γ . This slow decay is the origin of the picosecond wake. Then, if the decay time is shorter, the duration of the output beam would be also shortened. This is achieved increasing the electron density of the plasma. In addition to this, increasing the duration of the pulse will slow the rising of the polarization. This will improve the matching between HOH and polarization, enhancing the HOH amplification and reducing the wake. Electron density is greater in wider plasmas. Then, using wide plasmas will not only benefit from greater gain zone but also from higher electron density and thus, shorter pulse duration. A 200 fs, 1.5 nJ HOH seeded in a 100 μm wide, 2.5 mm long plasma will make an output beam of 1.5 μJ 140 fs, keeping ASE negligible. The 10 MW power attained by this source is 100 times greater than the experimental values using solid target [14] and its spatial and temporal coherences makes it suitable for many applications.

4 Multi-stage Amplifiers

As explained, wider plasmas have a greater amplification zone and thus, more energy (tens of microJoules) can be extracted from them. Nevertheless, in order to keep ASE and wake negligibles and maintain the duration of the amplified pulse below 100 fs, it is necessary to seed at high energies (greater than 1 μJ) while having a duration between 100 fs and 200 fs depending on plasma electron-ion collision [12]. State-of-the-art HOH deliver this energy but, since the bandwidth is between 30 and 100 greater than the bandwidth of the plasma amplifier, only a small part of the energy is coupled, being nowadays not possible to reach the in-band energy requirements. On the other hand, a plasma amplifier seeded with HOH as explained in Sect. 3 can be used as a pre-amplifier. Since both plasmas have similar electron density and temperature, the bandwidth of the pre-amplifier will match that of the main amplifier.

In Fig. 1 the modeled amplification chain is depicted. The pre-amplifier is a 100 $\mu\text{m} \times 2.5 \text{ mm}$ plasma seeded with 50 nJ, 160 fs HOH, similar to the scheme described in Sect. 3. The output is a 1.6 μJ 130 fs beam which is seeded in the 1 $\text{mm} \times 2 \text{ mm}$ main amplifier, taking into account some losses on the focusing optics. This beam is strongly amplified while conserving the short duration till 21.6 μJ and 80 fs. As shown in Fig. 1 the HOH completely dominates the output beam. The high power attained by this source makes it perfect for many challenging experiences.

In conclusion, we have shown that a careful matching of the HOH characteristic with plasma properties and the use of pre-amplifiers to seed wide (1 mm) plasmas

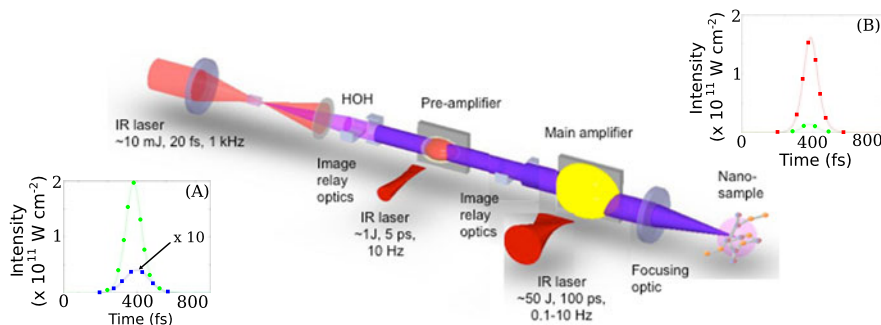


Fig. 1 Artistic view of an amplification chain. Output beam of a 1 mm × 2 mm main amplifier seeded with 1.6 µJ, 130 fs beam (sub-figure A blue, sub-figure B green) coming from a 2.5 mm × 100 µm pre-amplifier plasma. The output beam has an energy of 21.6 µJ and a duration of 80 fs (sub-figure B red)

is the key to obtain tens of microJoules in less than 100 fs. We have simulated a full pre-amplifier main-amplifier chain capable of delivering beams of 21.6 µJ and 80 fs.

Acknowledgements The authors would like to acknowledge the financial support provided by the LASERLAB II 228334 (SFINX) European Project and RTRA “Triangle de la Physique” project (SHYLAX).

References

- Al'miev, I.R., et al.: Dynamical description of transient x-ray lasers seeded with high-order harmonic radiation through Maxwell-Bloch numerical simulations. *Phys. Rev. Lett.* **99**(12), 123902 (2007)
- Chandrasekhar, S.: Stochastic problems in physics and astronomy. *Rev. Mod. Phys.* **15**(1), 1–89 (1943)
- Chapman, H.N.: X-ray imaging beyond the limits. *Nat. Mater.* **8**, 299–301 (2009)
- Goddet, J.P., et al.: Aberration-free laser beam in the soft x-ray range. *Opt. Lett.* **34**(16), 2438–2440 (2009)
- Kim, C.M., Janulewicz, K.A., Kim, H.T., Lee, J.: Amplification of a high-order harmonic pulse in an active medium of a plasma-based x-ray laser. *Phys. Rev. A* **80**, 053811 (2009)
- Kim, C.M., Lee, J., Janulewicz, K.A.: Coherent amplification of an ultrashort pulse in a high- and swept-gain medium with level degeneracy. *Phys. Rev. Lett.* **104**, 053901 (2010)
- Larroche, O., et al.: Maxwell-Bloch modeling of x-ray-laser-signal buildup in single- and double-pass configurations. *Phys. Rev. A* **62**(4), 043815 (2000)
- Mancuso, A., Yefanov, O., Vartanyants, I.: Coherent diffractive imaging of biological samples at synchrotron and free electron laser facilities. *J. Biotechnol.* **149**(4), 229–237 (2010)
- McNeil, B.W.J., Thomson, N.R.: X-ray free-electron lasers. *Nat. Photonics* **2**, 814–821 (2010)
- Oliva, E., et al.: Optimization of soft x-ray amplifier by tailoring plasma hydrodynamics. *Opt. Lett.* **34**(17), 2640–2642 (2009)
- Oliva, E., et al.: Hydrodynamic study of plasma amplifiers for soft-x-ray lasers: a transition in hydrodynamic behavior for plasma columns with widths ranging from 20 µm to 2 mm. *Phys. Rev. E* **82**(5), 056408 (2010)

12. Oliva, E., et al.: Comparison of natural and forced amplification regimes in plasma-based soft-x-ray lasers seeded by high-order harmonics. *Phys. Rev. A* **84**(1), 013811 (2011)
13. Sureau, A., Holden, P.B.: From amplification of spontaneous emission to saturation in x-ray lasers: a Maxwell-Bloch treatment. *Phys. Rev. A* **52**(4), 3110–3125 (1995)
14. Wang, Y., et al.: Phase-coherent, injection-seeded, table-top soft-x-ray lasers at 18.9 nm and 13.9 nm. *Nat. Photonics* **2**, 94 (2008)
15. Zeitoun, P., et al.: A high-intensity highly coherent soft x-ray femtosecond laser seeded by a high harmonic beam. *Nature* **431**, 426 (2004)

Chapter 34

Harmonic Generation in Argon by Femtosecond Ti:Sapphire Laser

Rabia Qindeel, Ricardo Elgul Samad, Anderson Zanardi de Freitas,
Paulo Sergio Fabris de Matos, Edilson Lucena Falcão,
and Nilson Dias Vieira Junior

Abstract Generation of harmonics using a gas nozzle has remarkable feature in various applications. Pulses from a Ti:Sapphire laser, centered at 785 nm, in a 4 kHz train, with 25 femtoseconds and 800 μJ of maximum energy were employed to generate harmonics in an argon gas nozzle. We present the current results on the focusability of the nozzle, harmonic radiation, measurement of the influence of laser power and laser focus position on the divergence of gas nozzle. We have successfully generated 3rd, 5th and 7th harmonics in Argon at different laser powers. The results show that the harmonic signals are almost same for laser average powers over 1.0 W and variation always appears below 1.0 W. It means that there is saturation in the physical phenomenon happening inside the gas nozzle at high laser powers and the variation is non-linear below 1.0 W. These results are embedded in an effort towards x-ray generation in the water window.

1 Introduction

Generation of coherent extreme ultraviolet (EUV) by focusing femtosecond laser into gasses is a well-known method [1–4]. High pulse intensities, greater than $10^{13} \text{ W cm}^{-2}$ and above, are required for the High Harmonic Generation (HHG) nonlinear conversion process. These high pulse intensities are not directly attainable using only the output power of a femtosecond oscillator. Chirped Pulse Amplification (CPA) enables the pulse intensity to exceed this threshold by incorporating several regenerative and/or multi-pass amplifier cavities in tandem [5]. When a very intense laser pulse is focused into a gas at reduced pressures, a strong nonlinear interaction can lead to the generation of odd harmonics of the pulse optical frequency, as an extreme form of nonlinear frequency conversion. Although only a small fraction of the laser power is converted into harmonics, this output can still be useful for

R. Qindeel (✉) · R.E. Samad · A.Z. de Freitas · P.S.F. de Matos · N.D. Vieira Junior
Centro de Lasers e Aplicações, IPEN, CNEN/SP, São Paulo, Brazil
e-mail: plasma_qindeel@yahoo.com

E.L. Falcão
Physics Department, UFPE, Recife, Brazil

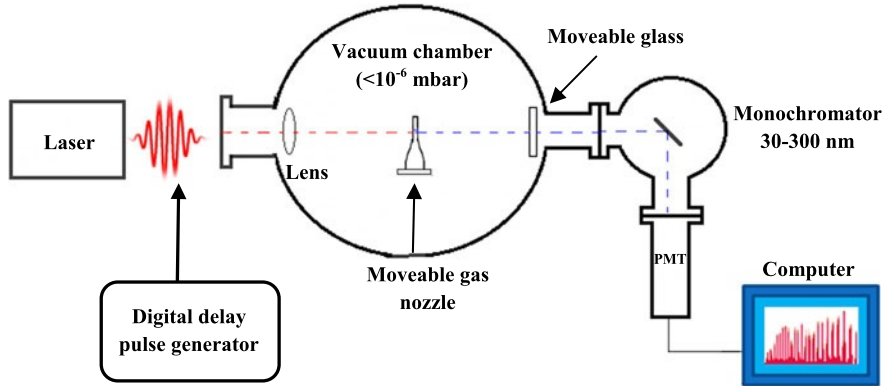


Fig. 1 Experimental setup for High Harmonic Generation in a gas nozzle

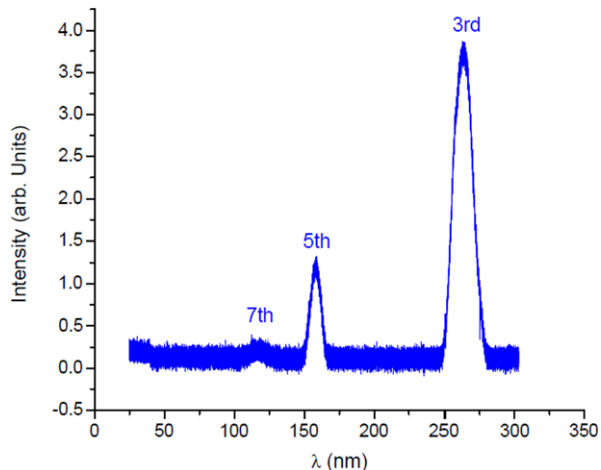
measurements down to wavelengths in the ultraviolet or even the soft X-ray spectral region.

When femtosecond laser pulses propagate in a transparent medium, the light field is localized in a narrow filament, whose formation is the result of the nonlinear optical interaction of the short-duration radiation with a medium [6–9]. Depending on the laser intensity, the creation of free electrons can be described by multiphoton or tunneling ionization. The applied laser intensity exhibits a highly nonlinear behavior, resulting in a saturation of the nonlinear refractive index. The mechanism of harmonic generation and saturation with respect to laser power is still not understood in detail. Therefore we have carried out this research to understand and generate harmonics. In this work we have studied the laser peak power effect on harmonic generation in argon gas flowing through a nozzle. We have discussed the saturation in harmonic signals with respect to increase in laser power.

2 Experimental Set up

The laser facility used in the experiment of high-harmonics generation is a Ti:Sapphire (CPA) system at the Centro de Lasers e Aplicações (CLA), IPEN, CNEN/SP, generating pulses centered at 785 nm, in a 4 kHz train, with 29 femtosecond and 800 μ J of maximum energy. These pulses were focused by a 50 cm focal length lens to generate harmonics in an argon nozzle with back pressure of 140 mbar, placed just after the lens focal point for the short trajectory. The nozzle used was 0.5 mm thick, to minimize the possibility of phase mismatch and re-absorption, and placed inside a vacuum chamber. A turbomolecular vacuum pump was used to evacuate the chamber and an attached monochromator (McPherson 234/302, 30–300 nm range) to a background pressure of 10^6 mbar. Harmonic radiation produced in the nozzle passed into the monochromator where the beam was

Fig. 2 Harmonic generation at after focus at 140 mbar pressure and 2.0 W of laser power, 4 kHz



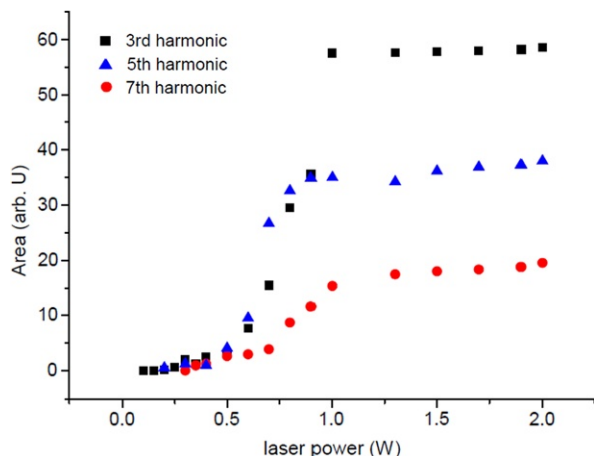
spectrally dispersed by grating and then imaged onto a PMT with a Sodium Silicate scintillator. Only odd harmonics were generated in atomic gases due to the interaction selection rules. When gas was injected into the target chamber, the pressure increases to about 10^{-3} mbar. Pulses with focused intensities in the range from 10^{14} W/cm 2 to 10^{15} W/cm 2 were needed to generate the harmonics. The resulting spectra were recorded in a digital oscilloscope and then processed in a computer. The experiment was carried out with different laser powers. A moveable glass plate was placed to confirm the generation of harmonics. The experimental setup is depicted in Fig. 1.

3 Results and Discussion

The 3rd, 5th and 7th harmonics were successfully generated in the argon filled gas nozzle at various laser powers, under the same gas pressure. Figure 2 shows the harmonics at 2.0 W, 4 kHz repetition rate and 140 mbar of pressure. The phase mismatch due to ionization of the argon is negligible due to the short 0.5 mm gas nozzle.

The observed quadratic increase in harmonic yield with different laser power, shown in Fig. 3, proves that we are operating in a regime that is free of significant phase mismatch or re-absorption. Figure 3 also represents the focusability of nozzle harmonic radiation, measurement of the influence of laser power and laser focus position on the divergence of gas nozzle harmonics. When highly intense laser pulses are focused into the gas target, the pulses propagate over few millimeters, where it can ionize, distort, refract and accelerate particles. The rapid ionization occurs by the fact that the laser field perturbs the Coulomb barrier of the atom, allowing electrons to tunnel free. The kinetic energy of the electrons pulled out from the atom by the laser field is typically smaller than both the ionization potential and quiver

Fig. 3 Area versus laser power of graph for 3rd, 5th and 7th harmonics



energy. This low residual energy arises because within an optical cycle, ionization occurs at the peak of the electric field. The released electron energy is increased by the electric field forced oscillation, and ultimately rises the final temperature of the plasma created and only a tiny fraction of the laser power can be converted into harmonics [10].

The results show that the harmonics signals quickly increase with the laser power, until 1.0 W, over which they become almost constant. It means that there is saturation in the physical phenomenon happening inside the gas nozzle at high laser power and the variation is non-linear below 1.0 Watt. The observed saturation of the harmonic in the gas jet is the result of a combination of neutral atom depletion and free-electron contribution to phase mismatch. The depletion of the ground state occurs when the laser intensity is so high that all the neutral atoms near the focus are ionized. The depletion of the neutral atoms in the gas jet is responsible for the existence of an optimum laser intensity at which the harmonics are generated with maximum efficiency. This is closely related to the saturation intensity of the gas, since it does not seem to depend on the harmonic order, ruling out other possible explanations based on the phase matching with the excitation beam.

The other possibility of saturation is the intensity clamping effect [11], which sets an upper limit to the laser intensity due to the dynamic balance between Kerr self-focusing and plasma defocusing resulting in a stabilized harmonic intensity. We can also say that the intensity clamping effect should be responsible for the saturation in harmonic generation, occurring at high excitation intensities and saturating the conversion efficiencies of the 3rd, 5th, and 7th harmonic processes.

4 Conclusions

In summary, we have performed systematic studies of the harmonic generation in argon using a gas nozzle. We have successfully generated 3rd, 5th and 7th harmonics

using ultrashort laser pulses with intensities in the range from 10^{14} W/cm² to higher than 10^{15} W/cm². We have carefully examined the behavior of the obtained signals in argon with different laser power observed that the saturation in signals are due to depletion of the neutral atoms.

Acknowledgements The authors thank FAPESP, CNPq and FINEP for supporting this work.

References

1. Seungchul, K., Jonghan, J., Young, J.K., In-Yong, P., Yunseok, K., Seung, W.K.: High-harmonic generation by resonant Plasmon field enhancement. *Nature Lett.* **453**(5), 757–760 (2008)
2. Corkum, P.B.: Plasma perspective on strong-field multiphoton ionization. *Phys. Rev. Lett.* **71**, 1994–1997 (1993)
3. Lewenstein, M., Balcou, P., Ivanov, M., L’Huillier, A., Corkum, P.B.: Theory of high-harmonic generation by low-frequency laser fields. *Phys. Rev. A* **49**, 2117–2132 (1994)
4. Chang, Z., Rundquist, A., Wang, H., Murnane, M.M., Kapteyn, H.C.: Generation of coherent soft X rays at 2.7 nm using high harmonics. *Phys. Rev. Lett.* **79**, 2967–2970 (1997)
5. Seres, J., Seres, E., Verhoeft, A.J., Tempea, G., Strelci, C., Wobrauschek, P., Yakovlev, V., Scrinzi, A., Spielmann, C., Krausz, F.: Laser technology: source of coherent kiloelectrovolt X-rays. *Nature* **433**, 596 (2005)
6. Chin, S.L., Hosseini, S.A., Liu, W., Luo, Q., Theberge, F., Akozbek, N., Becker, A., Kandidov, V., Kosareva, O., Schroeder, H.: *Can. J. Phys.* **83**, 863 (2005)
7. Kandidov, V.P., Shlenov, S.V., Kosareva, O.G.: *Quantum Electron.* **39**, 205 (2009)
8. Couairon, A., Mysyrowicz, A.: *Phys. Rep.* **441**, 47 (2007)
9. Berge, L., Skupin, S., Nuter, R., Kasparian, J., Wolf, J.P.: *Rep. Prog. Phys.* **70**, 1633 (2007)
10. Gibbon, P., Forster, E.: Short-pulse laser-plasma interactions. *Plasma Phys. Control. Fusion* **38**, 769–793 (1996)
11. Ni, J., Yao, J., Zeng, B., Chu, W., Li, G., Zhang, H., Jing, C., Chin, S.L., Cheng, Y., Xu, Z.: Comparative investigation of third- and fifth-harmonic generation in atomic and molecular gases driven by midinfrared ultrafast laser pulses. *Phys. Rev. A* **84**, 063846 (2011)

Chapter 35

Demonstration of a 100 Hz Repetition Rate Soft X-Ray Laser and Gain-Saturated Sub-10 nm Table-Top Lasers

J.J. Rocca, B.A. Reagan, Y. Wang, D. Alessi, K. Wernsing, B.M. Luther, M.A. Curtis, M. Berrill, D. Martz, S. Wang, L. Yin, F. Furch, M. Woolston, D. Patel, V.N. Shlyaptsev, and C.S. Menoni

Abstract We report the first operation of a table-top soft x-ray laser at 100 Hz repetition rate. This gain saturated laser produces 0.15 mW average power in the 18.9 nm line of nickel-like molybdenum in the form of 1.5 μ J pulses. This is the highest average power reported to date from a compact coherent soft x-ray laser source operating at wavelengths shorter than 20 nm. The soft x-ray laser is excited by a diode-pumped chirped pulse amplification Yb:YAG laser that produces 1 J pulses of 5 ps duration. We have also demonstrated the efficient generation of sub-9 nm wavelength laser pulses of microjoule energy at 1 Hz repetition rate with a table-top laser. Gain-saturated lasing was obtained at 8.85 nm in nickel-like lanthanum ions. Isoelectronic scaling along the lanthanide series resulted in lasing at wavelengths as short as 7.36 nm. Simulations show that the collisionally broadened atomic transitions in these dense plasmas can support the amplification of sub-picosecond soft x-ray laser pulses.

1 Introduction

The generation of high average power coherent soft x-ray radiation on a table-top is of high interest for numerous applications. However, this is a challenging task, with both high harmonics and plasma-based soft x-ray lasers presently producing average powers in the microwatt range. In the case of plasma-based soft x-ray lasers the

J.J. Rocca · B.A. Reagan · Y. Wang · D. Alessi · K. Wernsing · B.M. Luther · M.A. Curtis · M. Berrill · D. Martz · S. Wang · L. Yin · F. Furch · M. Woolston · D. Patel · V.N. Shlyaptsev · C.S. Menoni

National Science Foundation ERC for Extreme Ultraviolet Science and Technology, Fort Collins, USA

J.J. Rocca (✉) · B.A. Reagan · Y. Wang · D. Alessi · K. Wernsing · B.M. Luther · M.A. Curtis · M. Berrill · D. Martz · S. Wang · L. Yin · M. Woolston · D. Patel · V.N. Shlyaptsev · C.S. Menoni
Department of Electrical and Computer Engineering, Colorado State University, Fort Collins, CO 80523, USA
e-mail: jorge.rocca@colostate.edu

J.J. Rocca · F. Furch
Department of Physics, Colorado State University, Fort Collins, CO 80523, USA

limitation has been their low repetition rate, with the first soft x-ray lasers operating at repetition rates ranging from a few shots per day to one shot per minute [1, 2]. In spite of significant progress that has greatly reduced the size of plasma-based soft x-ray lasers their average power has remained insufficient for applications requiring a high photon flux.

We discuss the operation of a *table-top* soft x-ray laser at 100 Hz repetition rate with a record-breaking average power of 0.15 mW at $\lambda = 18.9$ nm [3]. Gain-saturated, picosecond soft x-ray laser pulses are produced by amplification in a molybdenum plasma rapidly heated by ultra-short laser pulses with a tailored time profile from a diode-pumped chirped pulse amplification Yb:YAG laser that generates picosecond optical pulses of 1 J energy at a record 100 Hz repetition rate. Soft x-ray lasing was also obtained in the $\lambda = 13.9$ nm line of nickel-like silver. In a related effort we have worked in increasing the repetition rate of compact sub-10 nm lasers. We have generated gain-saturated picosecond SXRL pulses at 8.85 nm wavelength at 1 Hz repetition rate. Also, isoelectronic scaling along the lanthanide series has resulted in lasing at wavelengths as short as 7.36 nm [4].

The results increase by an order of magnitude the repetition rate of plasma-based soft x-ray lasers, demonstrating the feasibility of multi-milliwatt average power soft x-ray beams on a table-top. This increase in soft x-ray laser power will open up new scientific research and make possible advanced technology applications requiring high photon flux.

2 Demonstration of a 100 Hz Repetition Rate, Diode-Pumped, Gain-Saturated Soft X-Ray Laser

The average power of plasma-based, sub-20 nm soft x-ray lasers is currently limited by the repetition rate of the solid state optical lasers that drive them. State of the art chirped pulse amplification (CPA) laser systems producing picosecond duration pulses of the energy required to pump table-top soft x-ray lasers based on either neodymium-doped glass or titanium sapphire are limited to about 10 Hz repetition rate by thermal effects originating in the flashlamp-pumped gain medium of these driver lasers. The need for higher average power has motivated the development of high repetition rate directly diode-pumped CPA laser systems [5, 6]. We have developed a compact, directly diode-pumped CPA laser based on cryogenically-cooled Yb:YAG that produces 1 Joule, 5 ps FWHM duration, $\lambda = 1.03$ μm laser pulses at a record high repetition rate of 100 Hz. This laser was employed to drive a gain-saturated 18.9 nm soft x-ray laser in a nickel-like molybdenum plasma producing an average power of ~ 0.15 mW. Strong lasing at 13.9 nm was also achieved at 100 Hz repetition rate from a silver plasma. These results increase the repetition rate and average power of compact, sub-20 nm lasers by about an order of magnitude [5, 7] and are expected to extend the use of these lasers to new applications such as nanoscale surface imaging and nano-scale materials processing [8, 9].

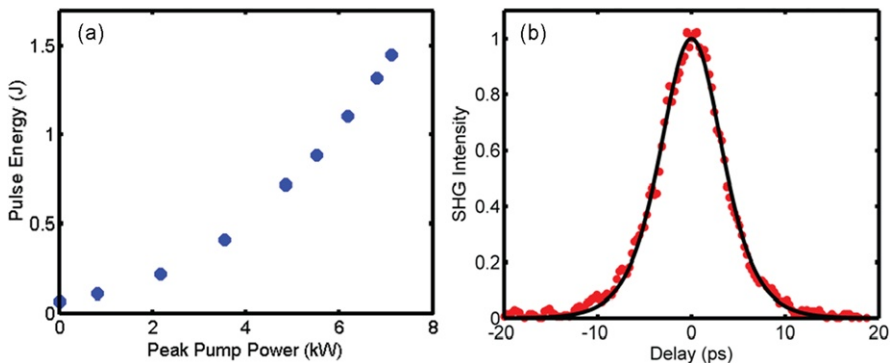


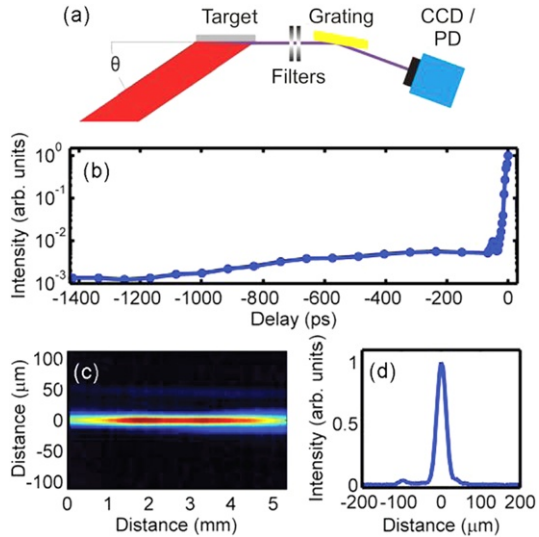
Fig. 1 (a) Output pulse energy prior to compression as a function of total peak pump power at 100 Hz repetition rate. The pump pulse duration was 1.5 ms. (b) Second-order autocorrelation of 1 J pulses after compression at 100 Hz. The *solid curve* is a sech^2 fit of the data, assuming this pulse shape the pulses have durations as short as 4.9 ps FWHM

The all diode-pumped CPA laser that drives the soft x-ray laser consists of a Yb:KYW mode-locked oscillator, a grating stretcher, three stages of amplification, and a grating compressor. This pump laser occupies a single standard optical table, with vacuum chambers for pulse compression, focusing optics, and the soft x-ray laser target on an adjacent table. Stretched pulses from the oscillator are first amplified to the millijoule-level at 100 Hz repetition rate by a diode-pumped regenerative amplifier based on Yb:YAG at room temperature. The pulses are then amplified to about 100 mJ by a four-pass liquid nitrogen-cooled Yb:YAG amplifier pumped by a 500 W peak power fiber-coupled laser diode. The combination of a room temperature preamplifier with cryogenic power amplifiers allows us to exploit the excellent thermal properties and high gain of Yb:YAG at cryogenic temperature while avoiding excessive loss of bandwidth in the preamplifier [10, 11].

The third stage of amplification consists of two Yb:YAG crystals used in the active mirror configuration mounted on a single cryo-cooling head. Each crystal is pumped with ~ 4 kW peak power, 1.5 ms duration laser pulses at 100 Hz repetition rate from laser diode arrays. The 100 mJ level pulses are directed to make three passes through one crystal and two through the other and are amplified to 1.5 J at the maximum pump power. We define a pass as traveling through the crystal, reflecting off the high reflecting face and traveling back through the crystal. Figure 1(a) shows the pulse energy obtained prior to compression as a function of pump power in the 3rd stage. At 100 Hz repetition rate the beam quality remains high, with no observable thermal depolarization and only slight thermal lensing. Following amplification, the laser pulses are compressed with approximately 70 % efficiency by a dielectric grating pair to durations as short as 5 ps FWHM as can be seen from the second-order autocorrelation of Fig. 1(b). The system therefore produces 1 Joule, 5 ps laser pulses at 100 Hz repetition rate.

In order to achieve lasing on the $4d\text{l}_0\text{--}4p\text{l}_1$ transition of Ni-like Mo the output pulses of the pump laser were focused at a grazing incidence angle of 29° onto

Fig. 2 (a) Schematic diagram of the soft x-ray laser pumping configuration and detection spectrometer with either a CCD or Si photodiode. For the 18.9 nm Mo laser a grazing incidence angle of 29° is used. (b) Second-order autocorrelation showing the temporally-tailored single laser pulse that drives the soft x-ray laser. An adjustable nanosecond ASE pedestal is followed by a 6 ps FWHM laser pulse. (c) and (d) Image and lineout of the high quality line focus used to generate the plasma amplifier



a 10 mm wide, polished Mo target as illustrated in Fig. 2(a). This inherently quasi-traveling wave geometry takes advantage of the refraction of the pump beam in the electron density gradient of the plasma to efficiently deposit the energy in the plasma region with optimum density for amplification [12, 13]. A single laser pulse with the tailored temporal profile shown in the autocorrelation of Fig. 2(b) was employed to create and heat the Mo plasma gain medium. Single laser pulses at grazing incidence have been previously demonstrated [14], but with different characteristics. The main laser pulse is preceded by an intentionally-created amplified spontaneous emission (ASE) pedestal with intensity that ramps from $\sim 10^{-3}$ to $\sim 2.5 \times 10^{-3}$ of the peak value in the 1.5 ns prior to the time of the peak intensity. This ASE originates in the regenerative amplifier, and we tuned both its intensity and duration to optimize the 18.9 nm laser output energy. The relative intensity of the ASE was adjusted by controlling the strength of the seed to the first stage amplifier, and its duration was controlled by adjusting the timing of a Pockels cell between the first and second amplifiers. Following this pedestal, a 6 ps duration pulse rapidly heats the plasma generating a transient population inversion and gain. We found that under the optimal conditions the ASE pedestal contained about 25 % of the total pulse energy. These temporally-tailored laser pulses were focused into 5.5 mm FWHM long by $\sim 30 \mu\text{m}$ wide line on the Mo target. Figure 2(c) and (d) show the high quality line focus which is required for strong lasing. On-axis soft x-ray spectra of the plasma emission were measured using a flat-field, grazing incidence diffraction grating and an x-ray CCD with aluminum and zirconium foils used to reject visible plasma emission and scattered driver laser light. For high repetition rate operation of this laser, an x-ray sensitive photodiode was placed in the image plane of the spectrometer to monitor the emission at 18.9 nm.

Figure 3 shows the measured soft x-ray laser pulse energy as a function of plasma length. The laser pulse energy is seen to increase exponentially with a gain coeffi-

Fig. 3 Energy of the 18.9 nm laser pulses as a function of plasma length. Each point represents the mean of 10 shots. The line is a fit of the data with the Linford formula corrected for gain saturation [15] that yields a small signal gain coefficient of 43 cm^{-1}

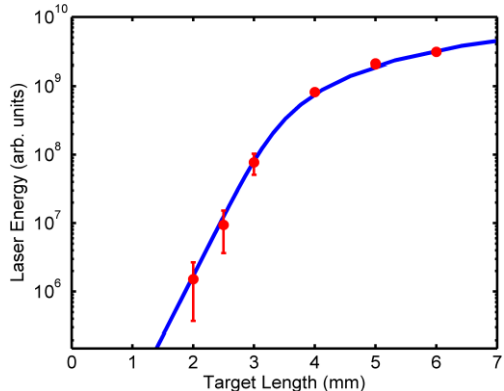
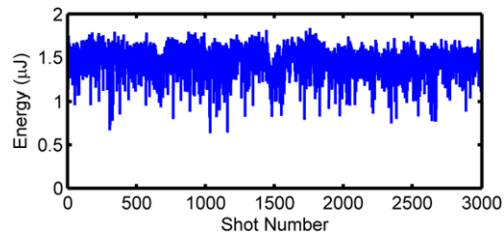


Fig. 4 Sequence of 3000 consecutive $\lambda = 18.9 \text{ nm}$ soft x-ray laser pulses at 100 Hz repetition rate



cient of 43 cm^{-1} until it saturates at a plasma column length of about 3.5 mm. A fit of the data with the Linford formula corrected for gain saturation [15] results in a gain-length product of 16.8, suggesting the rollover is due to gain saturation. Gain-saturated operation was verified by the measurement of a soft x-ray laser output pulse energy of $\sim 1.5 \mu\text{J}$ that, for a pulse duration of $\sim 5 \text{ ps}$ and near field beam spot size of a few tens of μm typical of these plasma amplifiers [16], corresponds to an intensity that comfortably exceeds the computed gain-saturation intensity [13]. Figure 4 shows 3000 consecutive $\lambda = 18.9 \text{ nm}$ laser pulses obtained operating the laser at 100 Hz repetition rate. For this series a 1 cm wide Mo slab target was translated at a constant velocity of $200 \mu\text{m/s}$ ($2 \mu\text{m}$ per shot). Prolonged laser operation at this high repetition rate will require the use of a renewable target with a larger useful surface area, such as that demonstrated in [17]. The mean laser pulse energy in this series was $1.5 \mu\text{J}$ with a shot-to-shot stability defined by a standard deviation of 11.5 %. The corresponding laser average power amounts to 0.15 mW , the highest value reported to date for a sub-20 nm coherent table-top source. Strong lasing was also obtained on the 13.9 nm line of Ni-like Ag by irradiating a 10 mm wide Ag target with a similar laser pump pulse, but impinging on target at a grazing incidence angle of 33° .

3 Demonstration of Sub-9 nm Wavelength Table-Top Laser Operating at 1 Hz Repetition Rate

We have also conducted work to increase the repetition rate of soft x-ray lasers operating at shorter wavelengths, below 10 nm. At the last International Conference on X-Ray lasers we have reported 1 Hz operation of a gain-saturated table-top SXRL at 10.9 nm [18, 19]. At shorter wavelengths the large pump energy required has limited the repetition rate to typically a shot per hour [20–24]. Soft x-ray lasing at sub-10 nm wavelengths in lanthanide ions was first demonstrated using several hundred joules of optical laser pump energy [21, 22]. Latter lasing in nickel-like lanthanum at 8.85 nm was obtained using 18 J pump pulses from a chirped pulse amplification (CPA) laser, but the gain-length product ($g \times 1 = 7.7$) obtained remained insufficient to reach gain-saturation [24]. Progress towards saturated lasing in this transition was reported at the last conference of this series [18, 25]. In turn, lasing at 7.36 nm in nickel-like Sm was initially demonstrated using 130 J pump pulses [21] and latter gain-saturation was reached using a \sim 40 J picosecond pump pulse added to a pre-pulse of similar energy [23]. More recently the lasing threshold in this line was reached using 36 J of total optical pump pulse energy [26]. Below we discuss the generation of gain-saturated picosecond SXRL pulses at 8.85 nm wavelength at 1 Hz repetition rate and isoelectronic scaling along the lanthanide series that resulted in lasing at wavelengths as short as 7.36 nm [4]. Simulations show that the collisionally broadened atomic transitions in these dense plasmas can support the amplification of sub-picosecond soft x-ray laser pulses.

The experiments were conducted irradiating solid slab targets with a sequence of two laser pulses from a $\lambda = 800$ nm Ti:sapphire CPA laser consisting of a normal incidence pre-pulse followed by a main picosecond pulse impinging at a grazing incidence angle of 35° with a traveling wave velocity of $\sim(1.04 \pm 0.03)$ c. The pump laser has four stages of amplification, of which the last two are pumped with the frequency doubled output of Nd-glass slab amplifiers designed to operate at repetition rates of up to 4 Hz [7]. The plasmas were created by normal incidence irradiation at $I = 6 \times 10^{12} \text{ W cm}^{-2}$ with a pre-pulse of 210 ps duration that is focused onto the target to form a \sim 30 $\mu\text{m} \times$ 6.4 mm FWHM line focus using the combination of a spherical and a cylindrical lens. The plasma created by this pre-pulse is allowed to expand to reduce the density gradient and is subsequently rapidly heated by irradiation at $I = 6 \times 10^{14} \text{ W cm}^{-2}$ with a 4 J pulse of 1–3 ps duration shaped into a line-focus of the same dimension. The target surface was tilted with respect to the axis of the short pulse to define a grazing incidence angle of $\theta = 35^\circ$ for efficient heating [12, 13]. At this angle of incidence refraction couples the pump beam energy into the plasma region where $n_e = 5.7 \times 10^{20} \text{ cm}^{-3}$. To assist in achieving efficient pumping we developed a new focusing geometry designed to create a plasma column of constant width along the target (Fig. 5a). In the conventional implementations of grazing incidence pumping in which a parabolic or spherical mirror is used to focus the beam [12, 13, 27–29], the tilted target intercepts the short pulse pump beam at different distances from the beam waist. This creates a “butterfly” shape line-focus on target that for small f-number systems can deposit

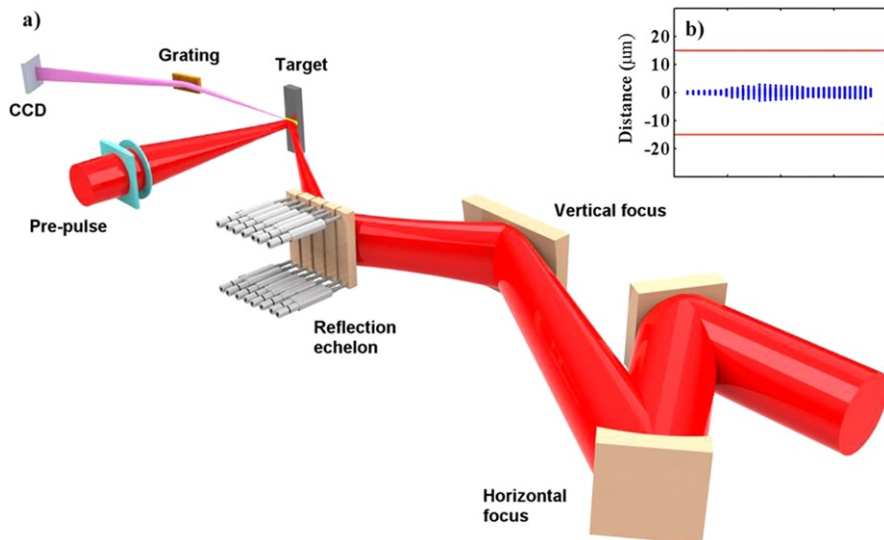


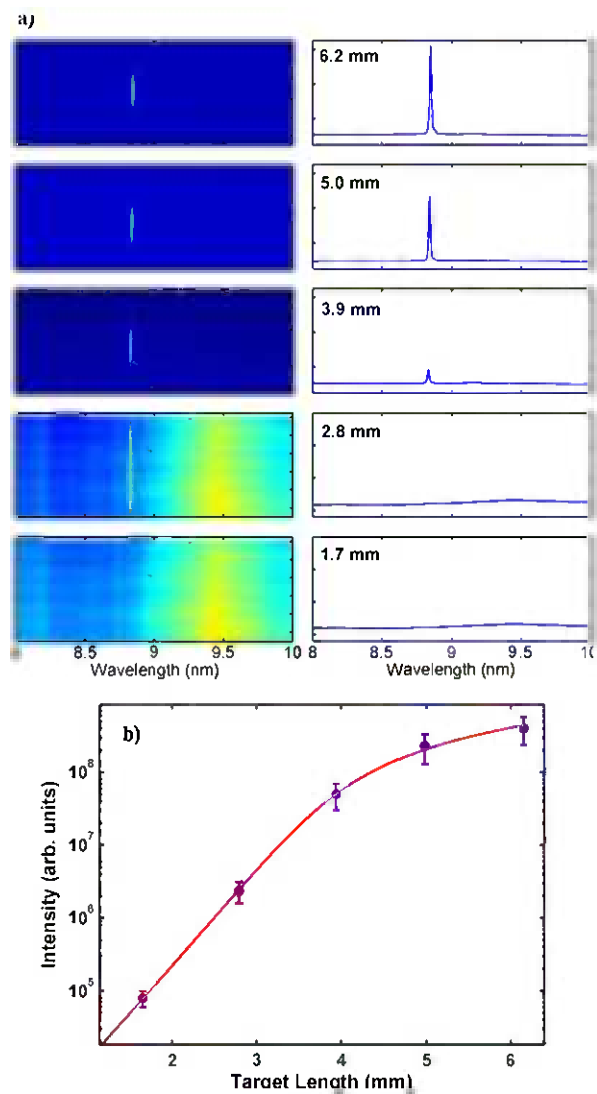
Fig. 5 Schematic representation of the set up used in the sub-9 nm SXRL experiments. (a) A pair of cylindrical mirrors focuses the short pulse beam at 35° grazing incidence on target creating a line-focus of uniform width. A reflection echelon is used to obtain quasi-traveling wave excitation. (b) Raytrace simulation of the line-focus on target. All rays fall within the line width defined by diffraction (red lines)

part of the pump energy outside the useful gain column, decreasing the gain. To overcome this limitation we focused the short pulse beam with a pair of cylindrical mirrors designed to create a line-focus of constant width along a target irradiated at grazing incidence [4]. A reflection echelon composed of five mirror segments was used to obtain a quasi-traveling wave excitation velocity of $\sim(1.04 \pm 0.03)$ c. Measurements at 1-Hz repetition rate were obtained continuously moving the target at a speed of $200 \mu\text{m}/\text{s}$ to renew the surface after each shot. Zirconium filters with thickness up to $2.1 \mu\text{m}$ were used to avoid saturating the detector and to eliminate visible plasma light.

Figure 6a shows a series of on-axis spectra as a function of plasma column length for a lanthanum plasma column created depositing 4 J of short pulse energy and a total of 7.5 J of optical pump energy on target at the irradiation conditions described above. Strong amplification is observed in the 8.85-nm $4d^1S_0 \rightarrow 4p^1P_1$ transition of Ni-like La. Figure 6b shows that the intensity grows by nearly four orders of magnitude as the plasma length increases from 1.7 mm to 6.2 mm. Saturation of the intensity is observed to have an onset at a plasma column length of ~ 4 mm. A fit of the data with an expression that takes into account gain saturation [15] yields a gain coefficient of 33 cm^{-1} and a gain-length product of 14.6. The energy of the most intense laser pulses was estimated to be $2.7 \mu\text{J}$ from the CCD counts. Gain-saturated operation was confirmed by measuring the SXRL flux at the exit of the amplifier. Near field imaging of the 8.85 nm laser amplifier output determined a laser fluence of $\sim 0.6 \text{ J cm}^{-2}$ for the most intense laser shots. Assuming the laser pulse duration of

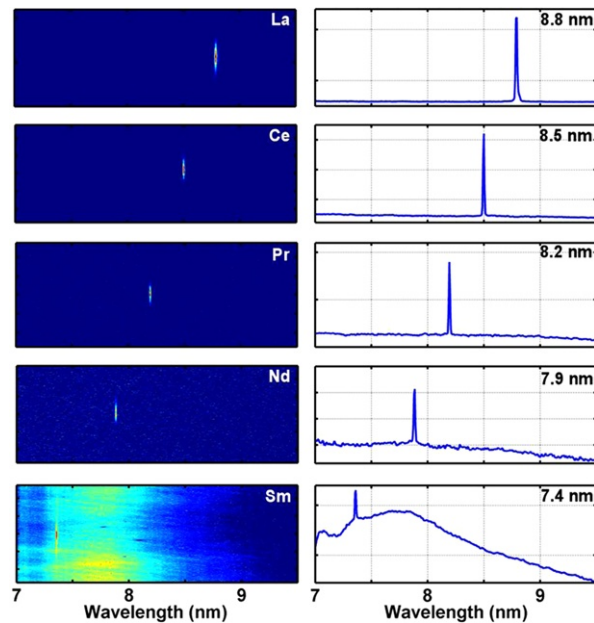
Fig. 6 End-on spectra of a line focus lanthanum plasma column showing saturated amplification in the 8.85-nm line of Ni-like La (**a**).

(**b**) Intensity of the 8.85-nm laser line as a function of plasma column length. The *line* is a fit of the data that yields a gain coefficient of 33-cm^{-1} and a gain-length product of 14.6. The *points* are the average of 10 laser shots and the *error bar* represents one standard deviation



2.5 ps from the simulations, the laser intensity at the amplifier exit is estimated to be $2.4 \times 10^{11} \text{ W cm}^{-2}$, which significantly exceeds the computed saturation intensity of $1.5\text{--}3 \times 10^{10} \text{ W cm}^{-2}$ [4]. The use of similar irradiation conditions resulted in lasing at 8.5 nm in Ni-like Ce, 8.2 nm in Ni-like Pr, and 7.9 nm in Ni-like Nd (Fig. 7). Lasing was also observed at 7.36 nm in Ni-like Sm by reducing the main pump pulse duration to 1.1 ps. The laser emission at 8.5 nm in Ni-like Ce is very strong, with an output energy $>1 \mu\text{J}$. Future advances in diode-pumped CPA pump lasers promise to lead to the realization of high average power table-top lasers at sub 10-nm wavelengths.

Fig. 7 End-on spectra showing lasing at progressively shorter wavelengths in the $4d^1S_0 \rightarrow 4p^1P_1$ line of nickel-like lanthanide ions, down to 7.36-nm in nickel-like samarium



Another aspect of interest in these amplifiers is the fact that they can support the amplification of sub-picosecond seed XRL pulses. Model simulations indicate amplification at 8.85 nm occurs in a plasma region where the plasma density is $5\text{--}9 \times 10^{20} \text{ cm}^{-3}$ and the ion temperature $\sim 150 \text{ eV}$. At the plasma conditions for peak gain the laser line profile is defined by collisional broadening ($\Delta\nu_L = 1.7 \times 10^{12} \text{ Hz}$) and Doppler contributions ($\Delta\nu_D = 2.8 \times 10^{12} \text{ Hz}$) that define a Voigt linewidth of $\Delta\nu = 3.8 \times 10^{12} \text{ Hz}$ that can support the amplification of sub-picosecond pulses. The variation of the bandwidth and pulse duration of an injected high harmonic seed pulse as it propagates through the lanthanum plasma amplifier was computed with a 3D ray-trace post processor that couples the amplification and ray propagation equations with a time and space depended atomic physics model that includes all relevant levels and stimulated emission. The ray trace code is capable of fully resolving the temporal duration and bandwidth of both the amplified stimulated emission and the amplified seed beam. Pulse broadening of a seed due to line-narrowing is included using the Fourier transform of the amplified bandwidth accounting for the group velocity delay caused by the gain profile. Figure 8 shows the computed pulsewidth variation of an injected 8.85 nm, 30 fs duration high harmonic seed pulse as it propagates through the lanthanum plasma amplifier for plasma conditions that result in an ASE laser output energy similar to that obtained in the experiment. Simulations conducted for a range of different pumping parameters predict output pulse durations in the range of 500–700 fs. The computed variation of the pulse duration of the ASE laser pulse as a function of plasma column length is also shown.

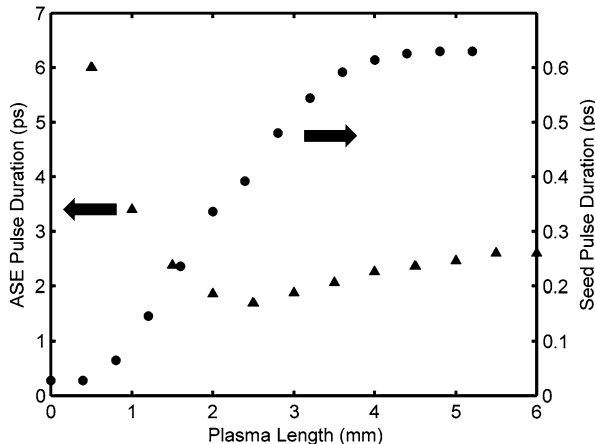


Fig. 8 Computed variation of the FWHM pulse duration of the 8.85 nm ASE laser (*circles*), and amplified high harmonic seed pulse (*triangles*) as a function lanthanum plasma column length. The seed pulse duration initially increases due to linewidth narrowing and later by saturation broadening. The high harmonic seed pulse is assumed to have an energy of 0.1-nJ and the gain and plasma conditions are those resulting from the simulations described in the text

4 Summary

In summary, we have demonstrated 100 Hz generation of soft x-ray laser pulses of microjoule energy at $\lambda = 18.9$ nm, generating a record high average power 0.15 mW soft X-ray laser beam on a table-top. This was accomplished by developing an all diode-pumped CPA laser system based on cryogenic Yb:YAG amplifiers that produce 1 J, 5 picosecond duration pulses at 100 Hz repetition rate. We have also demonstrated bright gain-saturated sub-9 nm wavelengths soft x-ray laser pulses at 1 Hz repetition rate for the first time and obtained laser amplification at wavelengths as short as 7.36 nm. This increase in soft x-ray laser power will open up new scientific research and make possible advanced technology applications requiring high photon flux.

Acknowledgements This work was supported by the NSF ERC for Extreme Ultraviolet Science and Technology under NSF Award EEC 0310717 and by the Chemical Sciences, Geosciences and Biosciences Division, Office of Basic Energy Sciences, U.S. Department of Energy using equipment developed under NSF Award MRI-ARRA 09-561, MB acknowledges the support of an Eugene P. Wigner Fellow for staff members Oak Ridge National Laboratory managed by UT-Battelle, LLC, for the U.S. Department of Energy under Contract DE-AC05-00OR22725.

References

1. Suckewer, S., et al.: Phys. Rev. Lett. **55**, 1753 (1985)
2. Mathews, D.L., et al.: Phys. Rev. Lett. **54**, 110 (1985)

3. Reagan, B.A., et al.: Opt. Lett. (in press)
4. Alessi, D., et al.: Phys. Rev. X **1**, 021023 (2011)
5. Furch, F.J., et al.: Opt. Lett. **34**, 3352 (2009)
6. Tümmler, J., et al.: Opt. Lett. **34**, 1378 (2009)
7. Martz, D., et al.: Opt. Lett. **35**, 1632–1634 (2010)
8. Urbanski, L., et al.: Opt. Lett. (in press)
9. Bravo, H., et al.: IEEE J. Sel. Top. Quantum Electron. **18**, 443 (2012)
10. Curtis, A.H., et al.: Opt. Lett. **36**, 2164 (2011)
11. Reagan, B.A., et al.: IEEE J. Quantum Electron. **48**, 827 (2012)
12. Keenan, R., et al.: Phys. Rev. Lett. **94**, 103901 (2005)
13. Luther, B.M., et al.: Opt. Lett. **30**, 165 (2005)
14. Kim, H.T., et al.: Phys. Rev. A **77**, 023807 (2008)
15. Lin, J.Y., et al.: Opt. Commun. **158**, 55 (1998)
16. Berrill, M., et al.: Opt. Lett. **35**, 2317 (2010)
17. Weith, A., et al.: Opt. Lett. **31**, 1994 (2006)
18. Rocca, J.J., et al.: In: 12th International Conference on X-Ray Lasers, Guanju, Korea (2010)
19. Alessi, D., et al.: Opt. Lett. **35**, 414–416 (2010)
20. MacGowan, B.J., et al.: Phys. Fluids B **4**, 2326 (1992)
21. Daido, H., et al.: Phys. Rev. Lett. **75**, 1074 (1995)
22. Daido, H., et al.: Opt. Lett. **21**, 958–960 (1996)
23. Zhang, J., et al.: Science **276**, 1097 (1997)
24. Kawachi, T., et al.: Phys. Rev. A **69**, 033805 (2004)
25. Balmer, J.E., et al.: In: 12th International Conference on X-Ray Lasers, Guanju, Korea (2010)
26. Zimmer, D., et al.: Phys. Rev. A **82**, 013803 (2010)
27. Wang, Y., et al.: Phys. Rev. A **72**, 053807 (2005)
28. Grunig, M., et al.: Opt. Commun. **282**, 267–271 (2009)
29. Alessi, D., et al.: Opt. Lett. **35**, 414 (2010)

Chapter 36

Optical Correction of X-Ray Laser Illumination for Short-Wavelength Microscopy

Mabel Ruiz-Lopez, Felix Staub, and Davide Bleiner

Abstract A critical aspect in the design of a short-wavelength microscope is the illumination profile and stability. Experimental measurements of the pointing stability and divergence and optical corrections of X-ray laser source are shown. The optical corrections provided one order of magnitude improvement in the illumination performance.

1 Introduction

The continuing progress of the nano-technology has increased the interest on nano-imaging tools. Short-wavelength microscopy allows resolving tens of nanometers by pushing down the diffraction limit. Numerous groups have developed imaging-systems for lithography and nano-inspection applications [1], but the most of them are not for laboratory scale operation. Compact sources from plasma light are interesting to become lab-scale enabling tools. The work in the design of a microscope begins with the understanding of the light's source properties: beam size, divergence, pointing stability, etc. [2]. Aim of this work was to characterize the X-ray laser illumination for the construction of a short-wavelength microscope.

2 Set-ups for Source Characterization

The transmission microscope that is being developed is composed of three optical elements: (i) condenser, (ii) sample and (iii) objective. The illumination should match the geometry of the condenser and provide stable and homogeneous filling. For diagnosing the beam stability and divergence of the pulse at the position of

M. Ruiz-Lopez (✉) · F. Staub · D. Bleiner

Institute of Applied Physics, University of Bern, Sidlerstrasse 5, 3012, Bern, Switzerland
e-mail: maria.ruiz-lopez@iap.unibe.ch

D. Bleiner
e-mail: bleiner@iap.unibe.ch

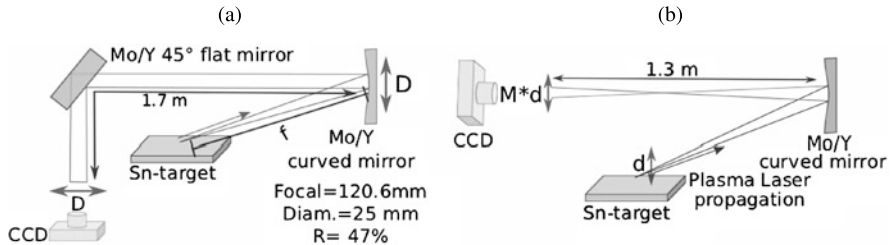
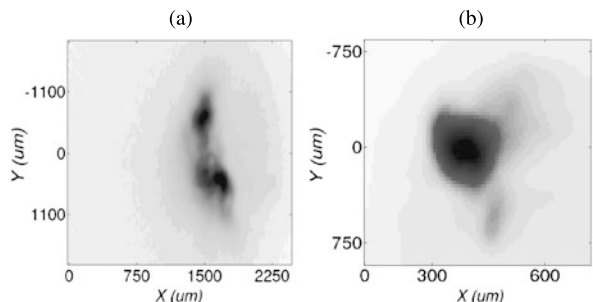


Fig. 1 (a) Experimental set up using a micro-collector for correction of pointing stability and divergence. The curved mirror is at a distance equal to the focal length to collimate the beam. (b) Experimental set up for a relay-imaging. The CCD captures an image of the source magnified 10-fold. Drawings not to scale

Fig. 2 Illumination profile in the image plane obtained with different TCE pre-pulse schemes: (a) single orthogonal long pre-pulse [3], (b) dual collinear short pre-pulses [4]



the condenser, two different set-ups were used. In Fig. 1a the set-up employed to compare the stability of a non-collimated and collimated pulse is shown. The setup in Fig. 1b was used for investigations on relay-imaging (near field). The curved mirror images the plasma source on a phosphor screen which converts the short-wavelength to the visible range. Before the CCD detector, a 150 nm-thick layer of zirconium is used to block optical background light. The CCD camera has 9 μm pixel size.

3 Characterization of Illumination and Optical Correction

Two transient collisional-excitation (TCE) schemes of pre-pulse delivery were compared, i.e. a single orthogonal long pre-pulse (Fig. 2a) versus a GRIP dual collinear short pre-pulse (Fig. 2b). One observes that the illumination profile improves with the latter scheme. Pointing stability and divergence were determined and optical correction setups were implemented. The first setup utilized was a telecentric-collector consisting in a concave normal-incidence Mo/Y mirror positioned at the focal plane distance from the source. Figure 3 shows that the improved pointing stability is a factor 4 (Fig. 3a) and the divergence decreases a factor of 10 (Fig. 3b).

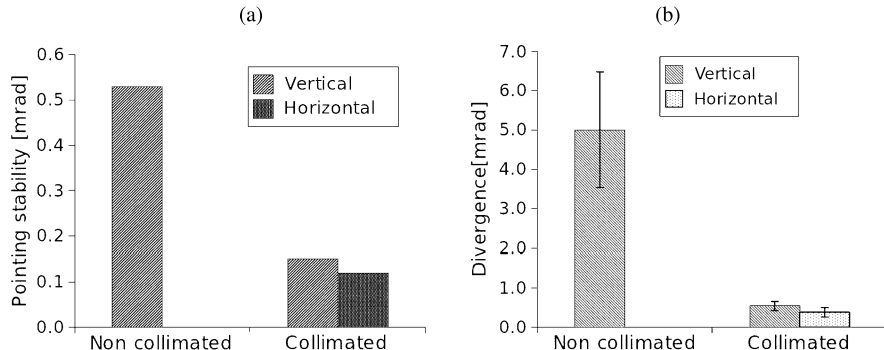


Fig. 3 (a) Pointing stability before and after collimation. (b) Divergence before and after collimation

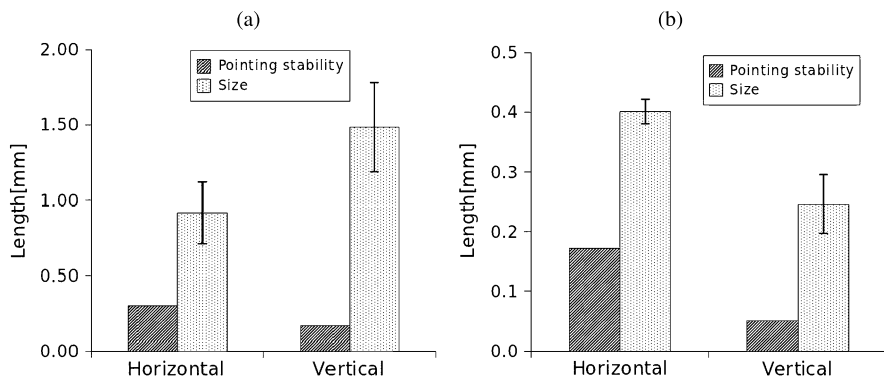


Fig. 4 (a) Size and pointing stability for a single orthogonal long pre-pulse. (b) Size and pointing stability in the current dual collinear pre-pulse. A factor of 1.5 (horizontal)—4 (vertical) improved stability is obtained as well as a decrease of factor of 2 (horizontal)—6 (vertical) in the divergence, when using the scheme with dual collinear pre-pulse

The second optical correction setup deployed relay-imaging. On the detector the near-field image of the X-ray source, magnified 10-fold, was acquired. Comparison of the two pre-pulse schemes showed that the present dual collinear pre-pulse set-up gives factor of 1.5 (horizontal)—4 (vertical) more stable illumination. The divergence was corrected a factor of 2 (horizontal)—6 (vertical). The smaller divergence (overall in the vertical dimension) implies an increment in the illumination brightness (Fig. 4). Pointing stability defines the reproducibility of the pulse position and must be the most precise possible. Both stability and divergence, contribute to the source etendue, which is important for the brightness of the source. All the results are in agreement with our computational study [5].

4 Conclusions

Lab-scale sources for short-wavelength microscopy are possible since an improvement in the pointing stability and the divergence have been demonstrated. We showed an improvement in the pointing stability of a factor 4 by using collimation of the light. The near-field indicates a homogeneous and quite symmetrical source profile and allows correcting the stability to 0.2 mm (horizontal)–0.05 mm (vertical), and the divergence to 0.4 mm (horizontal)–0.2 mm (vertical).

Acknowledgements The present work was supported by the Swiss National Science Foundation under the grant number PP00P2-133564/1.

References

1. Goldberg, K.A., Mochi, I.: *J. Vac. Sci. Technol. B* **28**(6), C6E1(2010)
2. Präg, A.R., Kozlovà, M., Rus, B., Rohlrena, K.: *Eur. Phys. J. B* **26**, 59–65 (2003)
3. Staub, F., Braud, M., Balmer, J.E., Nielsen, J., Bajt, S.: *Appl. Phys. B* **78**, 7–8 (2004)
4. Grünig, M., Imesch, C., Staub, F., Balmer, J.E.: *Opt. Commun.* **282**, 267–271 (2009)
5. Masoudnia, L., Bleiner, D.: In: Sebban, S., et al. (eds.) X-Ray Lasers 2012. Springer Proceedings in Physics, vol. 147. Springer, Cham (2013). Chapter [27](#) in this book

Chapter 37

Repetitive XUV Discharge-Pumped Laser at 46.9 nm

Jiri Schmidt, Karel Kolacek, Oleksandr Frolov, Vaclav Prukner,
and Jaroslav Straus

Abstract For testing and application purposes we built a new small Marx generator capable to run in a repetitive regime. Its repeating frequency is currently up to 1 Hz. The generator is covered by metal sheets and feeds the capillary discharge device. The first experimental measurements were performed for a 400 mm long capillary and these results are presented.

1 Introduction

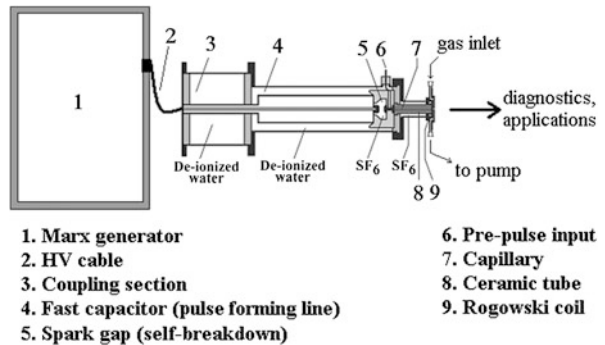
Capillary-discharge-based XUV lasers are sources that appeared about twenty years ago. These lasers, due to their current compactness, good beam quality, and stable operation have become useful tool for applications (e.g. for XUV lithography, for high-resolution microscopy, and for high-plasma-density measurements).

The first demonstration of XUV Ne-like argon laser working on 46.9 nm was published in [1]. Rocca's experiment opened a new way to the development of simpler and compact XUV lasers based on excitation pumping by capillary discharge.

Our research group was inspired by many applications of coherent XUV radiation and began to build the fast capillary discharge device (CAPEX) just about fifteen years ago. The experimental device is currently capable to reach current pulse amplitude of ~ 70 kA (~ 240 ns period) in ~ 230 mm long gas-filled capillary. The short (less than 2 ns) intense spike of the soft X-ray signal has been detected by a vacuum photodiode. This short pulse evidently corresponds to amplified spontaneous emission of neon-like argon line. The time-resolved (~ 30 – 50 ns exposition) XUV spectra recorded the strong spectral line, which dominates the whole observed spectrum in the range of 10–110 nm [2]. The wavelength of this dominating spectral line is just 46.9 nm. According to our experiences with CAPEX the new apparatus CAPEX-U (-Upgrade) was assembled approximately seven years ago [3] with intention to find lasing at shorter wavelength on discharge-pumped installations. Both apparatuses the CAPEX and the CAPEX-U [4] are fully operational.

J. Schmidt (✉) · K. Kolacek · O. Frolov · V. Prukner · J. Straus
Pulse Plasma Systems Department, Institute of Plasma Physics AS CR, v.v.i., Za Slovankou
1782/3, 182 00 Prague, Czech Republic
e-mail: schmidt@ipp.cas.cz

Fig. 1 Schematic drawing of the CAPEX device



2 Experimental Set-up

The CAPEX apparatus consists of a Marx generator, a coupling section, a pulse forming line (fast cylindrical capacitor), a main spark gap and a capillary. Experimental setup of the device is shown in Fig. 1.

As a power supply for the capillary discharge experiment the fully screened Marx generator is used. It consists of two parts—two bodies of commercial Marx generators GIN 400-0.06/5 of the soviet origin, which were equipped with a new system of spark-gaps. Spark-gaps are filled with nitrogen (SF_6 alternatively). The whole generator was successfully tested up to the charging voltage 50 kV (erected voltage 0.5 MV), i.e. up to the stored energy 0.75 kJ.

Significant part of the CAPEX device is the capillary. At present we use ceramic capillaries made from alumina (Al_2O_3). The 400 mm (232 mm alternatively) long capillary is directly attached to the main spark gap (having one common electrode). The gas filling and pumping part is attached to the outer end of the capillary (through the orifice in the outer electrode). The soft X-ray measurements were performed in the argon-filled-capillary with inner diameter of 3.2 mm. The capillary is placed in a shielding and circuit closing metallic cylinder of the diameter of 80 mm. The generated radiation was brought out through ~ 0.5 mm orifice in the outer electrode. Typical values of gas (argon) pressure inside the capillary prior to breakdown are in the range from 10 Pa to 100 Pa. More details of the experimental setup can be found in [2, 5].

3 XUV Radiation

The first experimental measurements were performed for a 400 mm long capillary. The XUV radiation emitted during the radial compression of the plasma column was measured using a vacuum diode.

The vacuum photodiode with Au photocathode was powered by 500 V. HP 54542C oscilloscope (0–500 MHz analog bandwidth, 700 ps rise-time, 2 GSa/s maximum sampling rate in each of four channels) was used for recording signals. The diode was placed at a distance of ~ 2 m from capillary output.

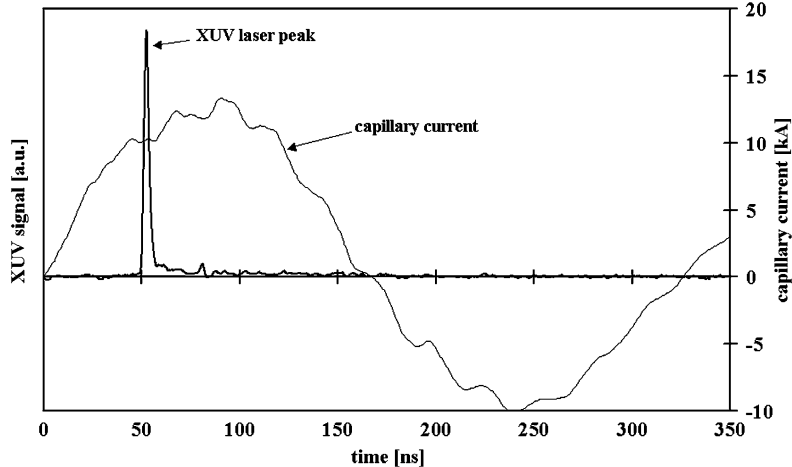


Fig. 2 Temporal evolution of XUV emission in the correlation with the main capillary current

The dependence of XUV pulse shape in the correlation with the capillary current is shown in Fig. 2. The full width at half maximum (FWHM) of the large short intense spike of the soft X-ray signal is approximately ~ 1.5 ns and it appears ~ 30 ns prior to the capillary current maximum (the current quarter-period is ~ 80 ns). This short pulse detected by vacuum diode corresponds to amplified spontaneous emission of neon-like argon line ($\lambda = 46.9$ nm). The amplitude and period of the capillary current pulse are approximately 15 kA and 320 ns. The main capillary current pulse was preceded by a pre-ionization current pulse of the amplitude ~ 160 A and of the duration 20 μ s to produce a uniform pre-plasma. The capillary pre-pulse was generated by an external driver [5].

4 Conclusion

The paper reports on some technological modification (the new repetitive high voltage Marx generator) and the recent experimental measurement (400 mm long capillary). The new small Marx generator is capable to run in the repetitive regime with frequency up to a few Hz.

The optimal conditions (initial pressure of argon, capillary pre-pulse amplitude and duration, etc.) for lasing were found for 400 mm long capillary. The short intense spike was detected by vacuum diode in XUV region. This pulse corresponds to amplified spontaneous emission of neon-like argon line ($\lambda = 46.9$ nm).

Acknowledgements This work was performed under auspices and with the support of the Ministry of Education, Youth, and Sports of the Czech Republic (contract LA08024).

References

1. Rocca, J.J., et al.: Demonstration of a discharge pumped table-top soft X-ray laser. *Phys. Rev. Lett.* **73**(16), 1236 (1994)
2. Schmidt, J., et al.: Strong amplification of Ne-like Ar line in the source based on capillary discharge. In: IEEE 15th International Pulsed Power Conference, Monterey, CA, USA, pp. 370–373 (2005)
3. Schmidt, J., et al.: Comparing of calculated and experimental results of CAPEX-U device. *Czechoslov. J. Phys., Suppl. B* **56**, 371–376 (2006)
4. Kolacek, K., et al.: Recent progress in discharge-based soft X-ray lasers at IPP ASci CR. In: Atomic and Molecular Pulsed Laser VII. Proc. SPIE, vol. 6938 (2008), Art. No. 693805
5. Schmidt, J., et al.: Soft X-ray emission of a fast-capillary-discharge device. *Plasma Devices Oper.* **13**(2), 105–109 (2005)

Chapter 38

Line-Focus Generation for X-Ray Laser Pumping

F. Staub, D. Bleiner, F. Jia, and J.E. Balmer

Abstract Down-scaling of X-ray lasers towards shorter wavelengths imposes the need for higher irradiance of the pump laser systems. Typically, for a factor of 2 reduction in wavelength, a factor of ~ 10 increase in irradiance was so far required. This discourages the use of refractive optics after the compressor stage of the high-power CPA laser systems commonly used for pumping X-ray lasers due to increasing nonlinear phase distortion (B-Integral). We present ray-tracing calculations of alternative focusing schemes applying reflective optics for grazing-incidence line-focus generation. The proposed mirrors deliver a narrow and shortened line focus from a high-aperture input beam, yielding an increase of irradiance on target.

1 Introduction

Grazing-incidence pumping (GRIP) combined with pico-second pulses puts high demands on the optics forming a line focus from the beam exiting the pulse compressor stage of a chirped-pulse amplifier (CPA) laser system. The beam diameter is usually determined by the damage threshold of the last compressor grating. This results in a large-aperture, high-irradiance beam, which has to be converted to a high-aspect-ratio line focus. The development of collisionally excited X-ray lasers towards shorter wavelengths asks for increasing irradiance on target. For a given laser energy (and power) this can be addressed by optimizing the length and the quality of the pump line focus intensity distribution.

2 Focusing Schemes

The simplest focusing optics consists of a tilted spherical mirror, which geometrically forms a perfect line parallel to the collimated incident beam. However, the length of the focal line can not be adjusted independently of the GRIP angle and has

F. Staub (✉) · D. Bleiner · F. Jia · J.E. Balmer
Institute of Applied Physics, University of Bern, Sidlerstrasse 5, 3012 Bern, Switzerland
e-mail: felix.staub@iap.unibe.ch

Fig. 1 Line focus generation by imaging an intermediate point focus F [1, 2]

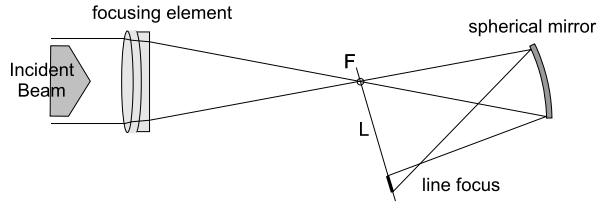


Table 1 B-integrals of 10 TW in a 132-mm beam

Nonlinear medium	B
1:1.7 reduction telescope	17.5
focusing objective	4.6
1-inch vacuum window	3.8
5 m air	1

to be adapted by the numerical aperture (NA) of the sphere. The NA can be reduced by means of a reduction telescope. More versatile is the method of imaging a point source in finite distance from the spherical mirror to adjust the length of the line focus and the GRIP angle via the location of the point source with respect to the line focus [1, 2], as shown in Fig. 1. Both methods need additional optics.

The high irradiance of the beam exiting the compressor of a CPA system can lead to severe nonlinear phase distortion in subsequent transmission optics (B-integral), given by

$$B = 2\frac{\pi}{\lambda} \int \gamma I(z) dz$$

where λ is the wavelength, γ the nonlinear index of refraction in SI units and I the irradiance. Examples of the B-integral for typical transmission optics used in our setup are given in Table 1 for a 10-TW beam having a diameter of 132 mm.

As can be seen, the B-Integral in glass dominates over propagation in air. The propagation in glass after pulse compression limits the quality of the (line) focus, as the focus breaks up for B between 4 and 10 [3]. In order to keep the B-integral as low as possible, transmission optics should be avoided.

As an alternative to refractive optics, the intermediate focus can be formed by an off-axis parabola, which is expensive. A further possibility is to use a tilted on-axis parabola, forming a distorted intermediate focus. A spherical mirror is used to image the distorted spot, resulting in a widened propeller-shaped line-focus. Ray-tracing calculations showed that the focal line is rotated with respect to the setup shown in Fig. 1, as indicated in Fig. 2. As a consequence, the line L , indicating the direction of the narrowest line focus, does not intersect the point F , but is tilted in the direction of the tilt φ of the parabolic mirror. In Fig. 2a the spherical mirror is tilted to form a down-folded line focus, while it is up-folded in Fig. 2b. The distance between the two mirrors is roughly the sum of their focal lengths. The narrowest focus is obtained by optimizing the distance between the parabolic and spherical mirror for each GRIP angle.

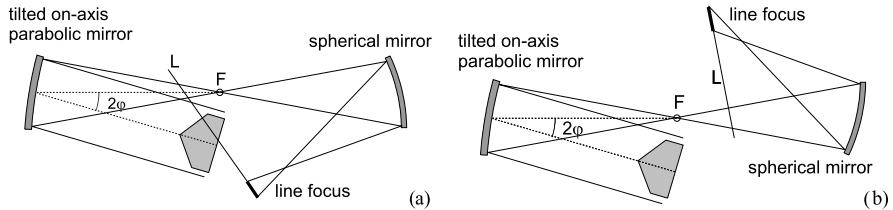


Fig. 2 Line focus generation by imaging a distorted intermediate focus F formed by an on-axis parabola tilted by the angle φ . On the left (a), the spherical mirror is tilted to form a down-folded line focus, while the setup on the right (b) forms an up-folded line focus

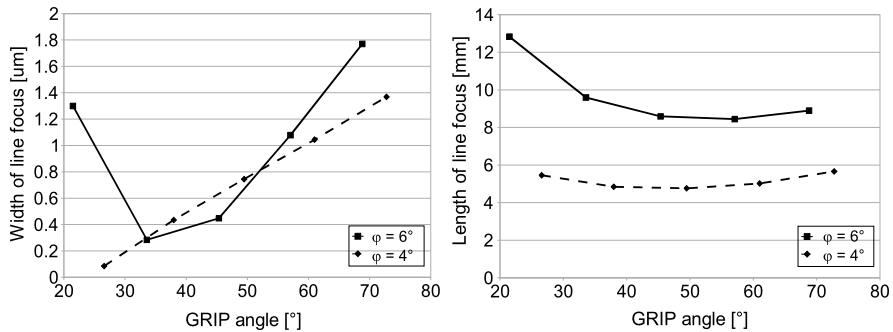


Fig. 3 Calculated geometrical size of the line focus of the setup shown in Fig. 2a. The tilt angle φ of the parabolic mirror is 6° (solid line) and 4° (dashed line)

Calculations were performed for the focusing schemes of Fig. 2 using a diameter of the incident beam of 132 mm in a top hat profile. The focal length of the parabolic mirror is $f_1 = 609.6$ mm, the focal length of the spherical mirror $f_2 = 304.8$ mm, respectively. The ratio $f_1/f_2 = 2$ was chosen in order to achieve identical beam diameters on both mirrors. The pump laser wavelength is 1054 nm, yielding a diffraction limit of the line-focus width of 6 μm .

Figures 3 and 4 show the calculated length and width of the line focus as a function of GRIP angle for the setups of Figs. 2a and 2b, respectively. Each data point is optimized for minimum width of the focal line. The geometrical line width is seen to stay well below the diffraction limit over a wide range of GRIP angles. The line foci of Figs. 3 and 4 are not identical, as the intensity distribution at F is not symmetric. Consequently, the spherical mirror forms different line foci for the up or down-folded configuration of Fig. 2. The length of the line focus shows less variation for Fig. 2a, while Fig. 2b offers shorter lines for GRIP angles below 60° .

In conclusion, a scheme for line-focus generation is presented using a standard parabolic mirror and a spherical mirror. Ray-tracing calculations imply that it is possible to keep the distortions well below the diffraction limit without the need for an expensive off-axis parabolic mirror. Due to the absence of transmission optics, there is no contribution to the B-Integral of the focusing optics.

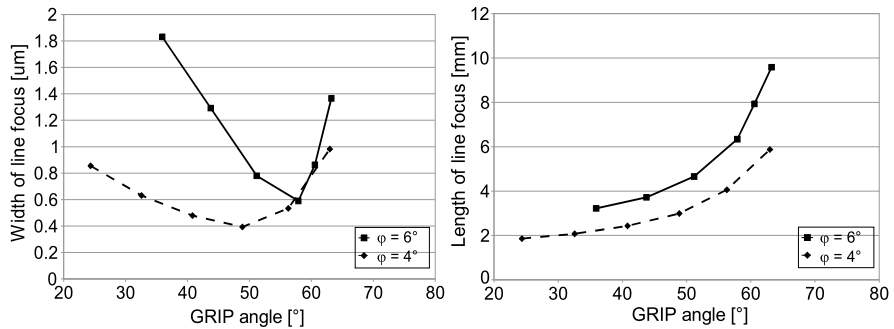


Fig. 4 Calculated geometrical size of the line focus of the setup shown in Fig. 2b. The tilt angle φ of the parabolic mirror is 6° (solid line) and 4° (dashed line)

Acknowledgements This work was supported by the Swiss National Science Foundation (SNSF). F. Staub was supported by the Swiss National Science Foundation under D. Bleiner's Förderungsprofessur (grant PP00P2-133564/1).

References

1. Ross, I.N., et al.: Some optical designs for the generation of high quality line foci. *J. Phys. E, Sci. Instrum.* **18**, 169 (1985)
2. Ross, I.N., et al.: Design and performance of a new line focus geometry for x-ray laser experiments. *Appl. Opt.* **26**(9), 1584 (1987)
3. Seznec, S., et al.: *Opt. Commun.* **87**, 331–339 (1992)

Chapter 39

Critical Components for XUV Probing of Laser Driven Shocks

C. Stehlé, R. Lefèvre, U. Chaulagain, N. Champion, P. Barroso, F. Reix, P. Jagourel, J. Larour, E. Meltchakov, R. Mercier, F. Delmotte, M. Kozlova, J. Nejdl, M. Krus, J. Dostal, J. Prokupek, C. Constancias, F. Suzuki-Vidal, and O. Acef

Abstract Radiative shocks can be produced in gases using high-energy lasers. As the electron density may be higher than the critical density for visible light, radiography with soft x-ray radiation becomes very promising technique to probe these shocks. Feasibility of this method has been proven employing zinc soft x-ray laser at 21.2 nm as backlighter. The experiment has shown high requirements on quality of the imaging optics and windows of the gas filled cell.

1 Introduction

Radiative shocks (RS) are strongly hypersonic shocks, where the high temperature generates a strong radiation structuring the shock. For instance, these shocks

C. Stehlé (✉) · R. Lefèvre · U. Chaulagain · N. Champion
Lerma, Observatoire de Paris, UPMC, CNRS, Meudon, France
e-mail: chantal.stehle@obspm.fr

P. Barroso · F. Reix · P. Jagourel
GEPI, Observatoire de Paris, CNRS, Paris, France

J. Larour
LPP, Ecole Polytechnique, UPMC, Palaiseau, France

E. Meltchakov · R. Mercier · F. Delmotte
LCF, Institut d'Optique, CNRS, PXI, Palaiseau, France

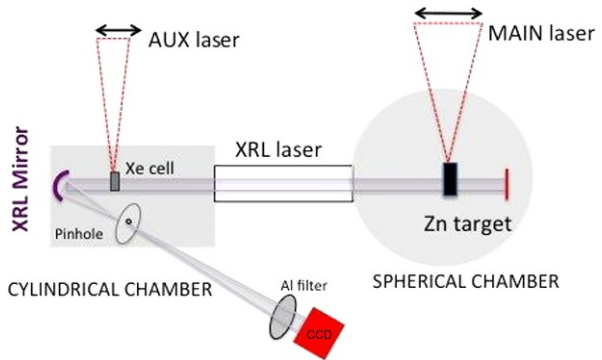
M. Kozlova · J. Nejdl · M. Krus · J. Dostal · J. Prokupek
Institute of Physics, Prague, Czech Republic

C. Constancias
CEA-LETI, Grenoble, France

F. Suzuki-Vidal
Imperial College, London, UK

O. Acef
SYRTE, Observatoire de Paris, UPMC, CNRS, Paris, France

Fig. 1 Experimental setup with the 3 laser beams and the imaging diagnostic



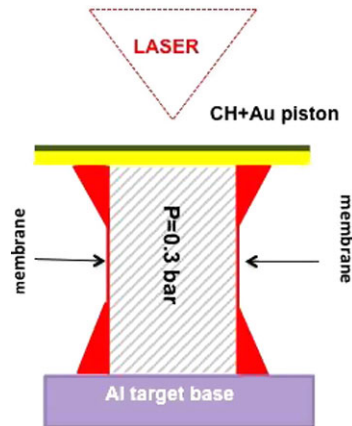
may present a radiative precursor. Radiative shocks can be found in astrophysical media and in laboratory. Producing such shocks on large scale lasers requires an intensity in the range of 10^{14} W/cm 2 at least. Several experiments have been performed at PALS installation on Xenon at 0.2–0.3 bar, either using visible (0.4 μ m) or the infrared (1.3 μ m) laser beam (0.3 ns) and producing shocks at \sim 50 km/s [1]. Visible interferometry demonstrated the presence of a radiative precursor and an electron density up to 10^{19} cm $^{-3}$ was measured. As the plasma is opaque for electron density exceeding the critical density: n_c (cm $^{-3}$) \sim $10^{21}/\lambda$ (μ m) 2 (where λ is the laser wavelength), and strongly absorbing one decade below, it is difficult to probe the shocked part of the plasma, where 1D simulations predicts a density of 10^{20} – 10^{21} cm $^{-3}$. We recently showed that XRL laser beam at 21 nm may be used to probe these shocks [2]. New results are presented below.

2 Experimental Setup and Critical Components

The PALS laser beam (operating at 1.3 μ m) is split into two beams: one (AUX, 60 J) is focalized on a target located in the “cylindrical” vacuum chamber. It is used to generate the shock wave. The second beam (MAIN, 500 J) is focused on a Zn target, located in the “spherical” chamber, to generate a laser beam at 21.2 nm (3 mJ, 0.2 ns) [3], which is sent towards the cylindrical chamber, shining the cell perpendicularly to the direction of AUX, with a precise delay of 20 ns. The XRL beam then reaches a spherical mirror and a CCD camera. A pinhole, placed at the focus of XRL beam, and an Aluminum foil placed in front of the CCD, perform a filtering of the plasma stray light. The XRL mirror also images the target on the CCD, with a magnification G of 8 or 4 (see Fig. 1 for the experimental setup).

The targets are miniaturized shocks tubes, with an internal canal of $6 \times 0.4 \times 0.4$ mm 3 , filled *in situ* with Xe. They are closed on one end by a gilt foil of polystyrene (10 μ m), on which the AUX laser is focalized and which acts as a piston. They are closed laterally by two membranes (see below) through which the XRL beam propagates (Fig. 2). These membranes have not only to be transparent at 21.2 nm (i.e. they have to be thin) but also to withdraw a difference of pressure

Fig. 2 Principle of the target with the gilt piston and the 2 membranes



of ~ 0.3 bar between the two faces (pressure inside the target, vacuum outside). A crude approximation of the minimum thickness h required to withdraw a difference of pressure ΔP is, for a long window of section a , given by:

$$\Delta P = \frac{h}{a} \sqrt{\frac{\sigma^3}{0.167E}},$$

where σ and E are the breaking point stress and the Young modulus respectively. Two types of membranes were used: (i) Si_3N_4 ($h = 100$ nm, $0.4 \times 3 \text{ mm}^2$) and (ii) Si ($h = 100$ nm, $0.6 \times 5 \text{ mm}^2$), respectively manufactured by SILSON and CEA-LETI.

The Si_3N_4 membranes are manufactured using hydroxide-based anisotropic etching of silicon wafers coated with LPCVD silicon nitride [4]. Using the values $\sigma = 2 \times 10^9 \text{ N/m}^2$ and $E = 2.6 \times 10^{11} \text{ N/m}^2$, one obtains ΔP (bar) = $4.3 \times 10^3 h/a$ (here $a = 0.4 \text{ mm}$), in qualitative agreement with the measured value of ± 0.5 bar at least. The transmission of each membrane is ~ 0.13 and their optical properties are excellent. The only difficulty was the roughness of the external section of the Si frame which was presenting small defaults of $\sim 0.1 \text{ mm}$, causing difficulties in the gluing of the polystyrene foil on the membranes.

Few Si membranes were also tested. They were manufactured starting from SOI substrate. The deep etching is: RIE on $500 \mu\text{m}$ then completed by a wet etching with TMAH to be stopped on SiO_2 , finally removed by HF acid [5]. The transmission (0.75) at 21 nm is excellent. The membranes withdraw the required difference of pressure. Our prototypes presented wrinkles. However, flat high stress membranes can be provided and these membranes are very promising.

Spherical XUV mirrors ($f = 300 \text{ mm}$, used of axis, with a total deviation of 11 degrees) required special attention. Two mirrors were used:

- Mirror 1: fused silica substrate (roughness 0.2 nm rms, pitch polished at Institut d’Optique). The layer deposition consisted of 20 periods of Al/Mo/B4C with B4C capping layer, made at CEMOX platform of Institut d’Optique [6]. The expected reflectivity at 21.2 nm is 45 %.

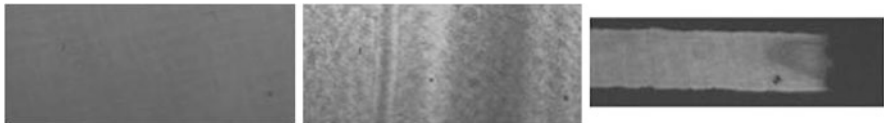


Fig. 3 Image of the laser with mirror 1 (*left*; G = 8; $\sim 5.5 \times 13 \text{ mm}^2$), mirror 2 (*center*; G = 8; $\sim 5.5 \times 13 \text{ mm}^2$), image of a shock wave (*right*; G = 4; $\sim 9 \times 3 \text{ mm}^2$)

- Mirror 2: fused silica substrate (roughness 0.2 nm rms, shape $\lambda/50$, from Winlight Optics) with 30 periods of Mo/Si deposited at CEMOX (expected reflectivity = 35 %).

The images of the XRL laser beam at the position of the target, taken with these mirrors are given in the Fig. 3 together with a sharp image of a RS shock using mirror 1. Due to several defaults, the mirror 2 is less adequate for XUV radiography. Indeed, a similar mirror (EAGLE substrate, MoSi deposition performed at Brno) was used in previous experiment. Although the image of the shock wave was visible, it was difficult to analyze.

3 Conclusions

To conclude, XRL radiography is a powerful diagnostic for probing laser generated shock waves. This requires an energetic XRL laser, good quality windows for the shock tube and a XUV mirror, with a well polished substrate and an adequate multi-layer deposition. Additive tests have to be made to understand the underachievement of our MoSi mirrors.

Acknowledgements The authors thank the CEA-LETI and the Basic Technological Research French program for providing the silicon membranes. The work was supported by LASERLAB access program, French ANR (grant 08-BLAN-0263-07), Observatoire de Paris, PICS4343 of CNRS, Academy of Sciences of the Czech Republic (Project No M100100911), Czech Ministry of Education Youth and Sports (Project Nos. 7E08099 and 7E09092), and by the Czech Science Foundation (Grant No. 202/08/1734).

References

1. Stehlé, C., et al.: *Laser Part. Beams* **28**, 253 (2010)
2. Stehlé, C., et al.: *Opt. Commun.* **285**, 64 (2012)
3. Kozlova, M., et al.: In: Sebban, S., et al. (eds.) *X-Ray Lasers 2012*. Springer Proceedings in Physics, vol. 147. Springer, Cham (2013). Chapter 24 in this book
4. Anastasi, P., et al.: In: Michette, A., et al. (eds.) *X Ray Microscopy III*. Springer Series in Optical Sciences, vol. 67, p. 441 (1992)
5. Constancias, C., et al.: *J. Vac. Sci. Technol. B* **28**, 194 (2010)
6. Melchakov, E., et al.: *Proc. SPIE* **8168**, 816819 (2011)

Chapter 40

High Density Optical-Field-Ionization Soft X-Ray Lasers

F. Tissandier, S. Sebban, M. Kozlova, J. Gautier, P. Zeitoun, A. Klisnick, and G. Maynard

Abstract Generating an optical-field-ionization (OFI) collisional soft X-ray laser amplifier in a high density plasma would allow a significant increase of the saturation intensity, laser gain, and reduction of the emitted pulse duration. Due to strong refraction of the pump infrared beam in the plasma, guiding techniques have to be implemented. Using an optically preformed plasma waveguide, we successfully achieved guiding of J-energy pulses in a near-critical density krypton plasma with 50 % total transmission over 5 to 10 mm. X-ray lasing at 32.8 nm has also been demonstrated. This technique is a step towards OFI recombination soft X-ray lasers. This pumping scheme requires the production of a cold and dense plasma. We propose to pump a high density neon VIII plasma by a frequency doubled intense Ti:Sa laser. Guiding of the 405 nm pump pulse has already been achieved at LOA.

1 Introduction

In the past few years, there has been noticeable progress in the development of high-brightness coherent radiation beams in the X-ray and soft X-ray range. The X-ray free electron lasers have demonstrated unprecedented peak powers in the nanometer and angström regions with femtosecond time resolution and have been used for numerous applications since available. However, due to the relative lack of these

F. Tissandier (✉) · S. Sebban · J. Gautier · P. Zeitoun

Laboratoire d'Optique Appliquée, ENSTA, 104 Bd des Maréchaux, 91120 Palaiseau, France
e-mail: fabien.tissandier@ensta-paristech.fr

M. Kozlova

Institute of Physics, AVČR, Na Slovance 2, 18221 Prague 8, Czech Republic

A. Klisnick

Institut des Sciences Moléculaires d'Orsay, Université Paris Sud (Bât. 210-350-351), 91405 Orsay, France

G. Maynard

Laboratoire de Physique des Gaz et des Plasmas, Université Paris Sud (Bât. 210), 91405 Orsay, France

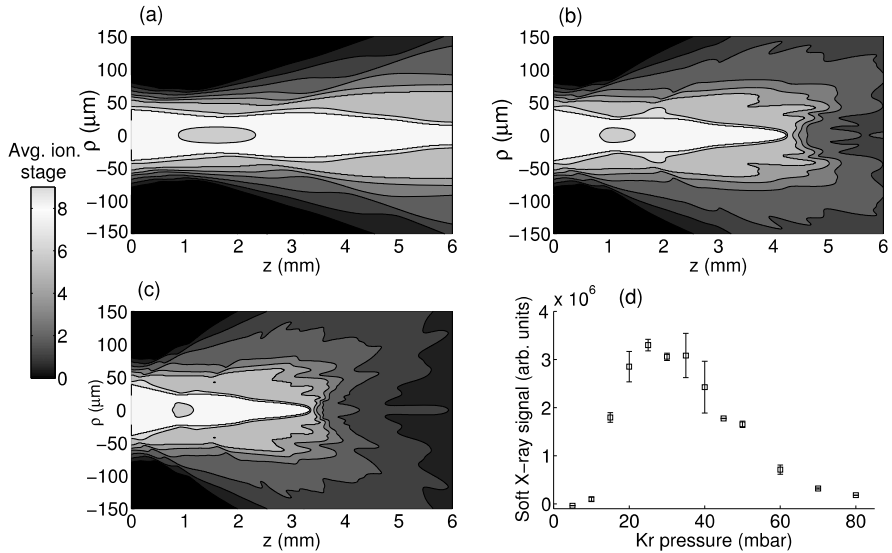


Fig. 1 Calculated ionization map of the OFI plasma for a pump intensity in vacuum of 10^{18} W/cm^2 and a krypton pressure of (a) 10 mbar, (b) 30 mbar and (c) 50 mbar. The laser propagates from left to right. The lasing Kr^{8+} is represented in white. (d) Measured and calculated output intensity of the soft X-ray laser as a function of krypton pressure

large and costly facilities, there is a need to develop more compact and less expensive sources. Soft X-ray lasers (SXRLs) generated through laser amplification in a collisional plasma are a promising alternative. Since their first experimental demonstration in 1985, dramatic progress has been made worldwide in the understanding and performances of these sources. However, they remain strongly limited in terms of focusable intensity or temporal resolution (ps pulse duration at best).

The work we report here mostly deals with an optical-field-ionization (OFI) collisional SXRL at 32.8 nm generated in a Ni-like krypton plasma [1]. We will first summarize the performances of that SXRL in the amplification of spontaneous emission (ASE) regime and when seeded by a high-order harmonic (HOH) of an intense infrared laser, in both cases with a maximum gas pressure of a few tenths of mbar (atom density around 10^{18} cm^{-3}). We will then discuss the advantages and drawbacks of drastically (2 orders of magnitude) increasing the gas density and report experimental measurements—including soft X-ray lasing—in a near-critical density plasma. Before concluding, we will discuss the possibility of generating a plasma suitable to the SXRL recombination pumping scheme.

2 Low-Density Performances

In the OFI scheme, both the creation of the lasing Kr^{8+} ion and the pumping of the population inversion are driven by the pump laser pulse. In its simplest form,

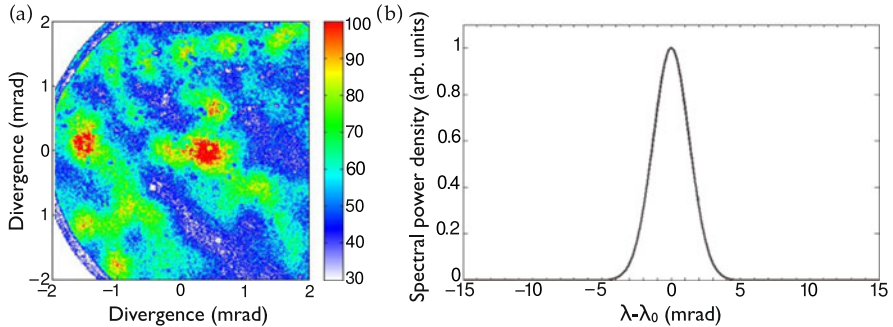


Fig. 2 (a) Far-field profile of the ASE SXRL beam. The beam was clipped by the Al filter mounting. (b) Spectrum of the ASE radiation, deducted from longitudinal coherence measurements

it consists in focusing an ultrashort and intense laser pulse into a cell filled with krypton at a pressure of a few tenths of mbar. The SXRL is then generated along the propagation of the pump beam in the plasma. We remind here the low-density soft X-ray amplifier performances obtained using the 10 Hz multi-terawatt “Salle Jaune” Ti:Sapphire laser installation at LOA. The 1 J, 35 fs pulses at a central wavelength of 815 nm were focused into a variable-length krypton cell. A quarter-wave plate was used to ensure the pump field has a circular polarization, and an aluminum filter was used to separate the SXRL beam from the remaining infrared pump beam. The best performances of the 32.8 nm SXRL were usually obtained for a gas pressure of 30 mbar [2] as can be seen on Fig. 1(d). The reason they were not obtained for the highest pressure is the main issue of the OFI scheme: this is a longitudinal pumping scheme, so the pump laser propagates in the plasma it created. This plasma exhibits an refraction index radial profile such that the pump beam suffers strong defocusing along its propagation. This defocusing gets stronger for higher plasma densities, as can be seen on Fig. 1(a-c) giving a 2D (ρ, z) map of the ionization stage in the plasma. It was calculated in a cylindrical geometry using the code OFI_PROP. While the amplifier is more than 6 mm long for a gas pressure of 10 mbar, its length drops to 3 mm at 50 mbar. This effect indirectly seriously limits the output pulse energy, which may vary from 1 to 100 nJ.

In the ASE regime, the divergence of the emitted SXRL beam is determined by the geometry of the amplifier. It is usually set between 10 and 15 mrad. The spatial profile also exhibits speckle (Fig. 2(a)) patterns. They are a consequence of the fact that the source behaves as a collection of micro sources mutually temporally coherent but spatially incoherent [3]. These modulations are characteristic of “short” pulse duration SXRLs (OFI and transient pumping); in the case of a long pulse duration SXRL (quasi-steady state), time averaging contributes to a drastic dampening of these speckle patterns. The spatial coherence of this source was also measured using variable-spacing Young slits and was found to be almost nil at the source, yielding a beam with a coherent zone diameter accounting for only of few percent of the beam diameter at 4 m from the source.

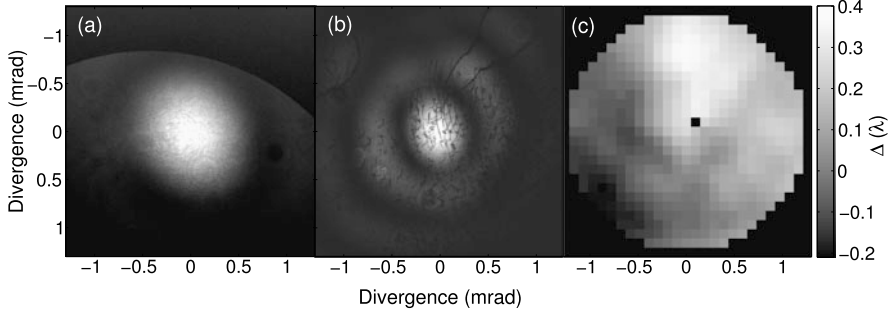


Fig. 3 (a) Usual Gaussian far-field profile of the seeded SXRL beam. (b) Bessel far-field profile of the seeded SXRL beam, due to a hole in the amplifier caused by over ionization of krypton. (c) Wavefront of the seeded SXRL beam. The RMS distortions are of the order of $\lambda/11$

At last, the temporal coherence of the ASE source was measured by longitudinal variable-path difference interferometry using a Fresnel bi-dihedron interferometer. Using Wiener-Khinchin theorem, we could calculate the power density spectrum of the pulse (equal to the Fourier transform of the fringe visibility as a function of optical path difference curve), given in Fig. 2(b). The bandwidth is extremely narrow, around $3 \text{ m}\text{\AA}$, corresponding to $\Delta\lambda/\lambda = 10^{-5}$. The $1/e$ coherence time was found to be 6 ps for a krypton pressure of 30 mbar, and since this duration is the same as the gain duration at the same gas pressure, we concluded that the soft X-ray pulse is Fourier limited, with a duration around 6 ps [4].

The OFI ASE SXRL source offers then poor spatial characteristics, a low pulse energy and a long pulse duration. Seeding the amplifier by a high-order harmonic allowed a drastic improvement of the soft X-ray beam [5]. In this configuration, a second Ti:Sa beam (a few tenths of mJ, 35 fs) is used to generate in particular the 25th harmonic of the infrared frequency. This harmonic can be accurately tuned to wavelength of 32.8 nm by adjusting the chirp of the driving laser. The HOH are generated in a argon gas cell at a pressure of 20 mbar, and the source is imaged onto the amplifier entrance plane using a grazing incidence toroidal mirror. Figure 3(a–b) shows two typical far-field profile of the seeded SXRL beam. Due to spatial filtering of the harmonic by the plasma [6], the output amplified beam profile exhibits a symmetric Gaussian (a) or Bessel (b) profile [7], depending on the shape of the amplifier. The beam is also well collimated, with a divergence of the order of 1 mrad. Another interesting new feature of this source is that it offers a high spatial coherence, and an almost diffraction-limited wavefront (Fig. 3(c)) with RMS distortions of $\lambda/11$ [8].

On the other side, the output pulses still have a duration in the ps range. Since the HOH duration (fs) is much shorter than the amplifier characteristic time scale (ps), the amplified field grows as a coherent wake behind the harmonic peak, with a duration of the order of the phase relaxation time of the dipoles constituting the amplifier medium. The amplification is well saturated, but Rabi oscillations of the fields were neither observed, nor expected [9]. Since that saturation is quickly reached (after

1 or 2 mm of propagation in the amplifier), the output pulse energy is not very high. Pulses with energy up to 1 μJ were produced.

On the whole, the seeded SXRL source is promising but suffers from a lack of focusable intensity of temporal resolution. This could be taken care of by increasing the amplifier density. When increasing the density, collisional processes are faster. In particular, collisional excitation (thus pumping) is faster, but also collisional ionization—that destroys the lasing ion—is also faster. The gain lifetime mechanically decreases. On Fig. 4 are given the SXRL intensity as a function of the harmonic injection delay into the amplifier, for different krypton pressures. These are basically gain temporal evolution measurements. Time-dependent only collisional-radiative calculations of the gain dynamics are also reported on the same graphics.

As expected, the gain duration decreases when we increase the plasma density. That decrease is however not of great importance: the gain duration (FWHM) is around 10 ps at 15 mbar, and 5 ps at 40 mbar. The gain peak value is also slightly higher at 40 mbar (180 cm^{-1}) than at 15 mbar (150 cm^{-1}). It could nonetheless be interesting to see the effects of an increase of density by 2 orders of magnitude, up to 10^{20} at/cm^3 . Using the same-as-before time-dependent OFI_0D collisional-radiative code, we have been able to calculate the resulting gain maximum value, and saturation intensity. They are reported on Fig. 5 for a krypton density ranging from 10^{18} cm^{-3} (40 mbar) to $2 \times 10^{20} \text{ cm}^{-3}$.

It can be seen that at a density of 10^{20} cm^{-3} , the peak gain value is only twice that obtained for a density of 10^{18} cm^{-3} . The most important improvement we can expect is the saturation intensity. Over the same range of density, it gains 4 orders of magnitude. If we are able to let the pump pulse propagate over a significant distance in the plasma (a few mm), we can expect a very strong increase of the emitted pulse energy. The gain duration is also expected to decrease drastically.

3 High-Density Waveguiding and Soft X-Ray Lasing

As we have already seen, the main issue of this OFI scheme is the pump pulse propagation. Using a neutral density of 10^{20} cm^{-3} , some waveguiding technique must be implemented to allow the pump laser to propagate over more than a few hundreds of microns. Guiding of the pump pulse of an OFI SXRL has already been achieved using a capillary discharge [10, 11], hollow capillary tubes [12, 13], or an laser-preformed plasma waveguide [14, 15]. Although the results obtained with capillary discharge or tubes were convincing, both these methods are not suited for a high density plasma. Using a laser-produced plasma waveguide however gave very interesting and promising results at neutral densities around 10^{20} cm^{-3} .

The principle of plasma guiding is to generate a plasma channel with an electron density profile that will compensate the effects of diffraction, i.e. lower along the propagation axis than further away from that axis. An effective method to generate such a plasma channel is the so-called “ignitor-heater” method [16–18]. It basically follows three steps. The first step is the creation of primary electrons. A first

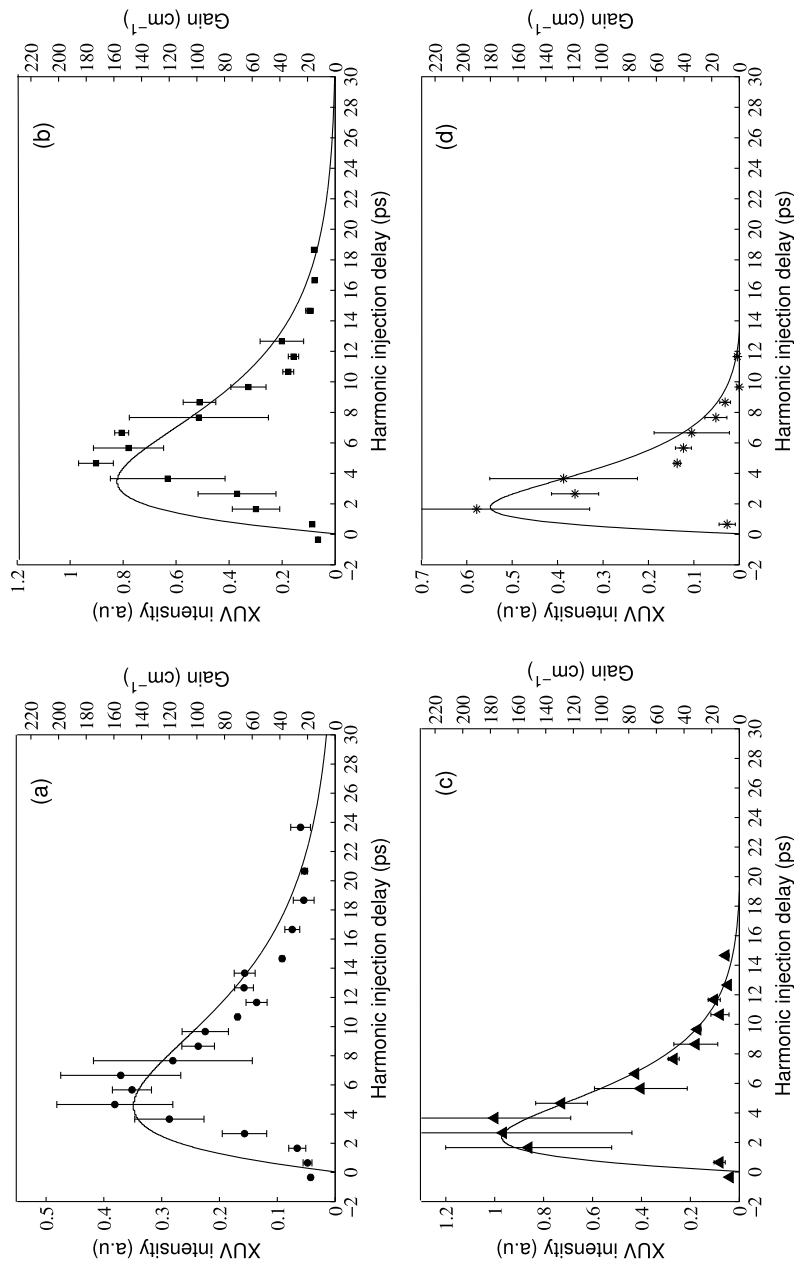
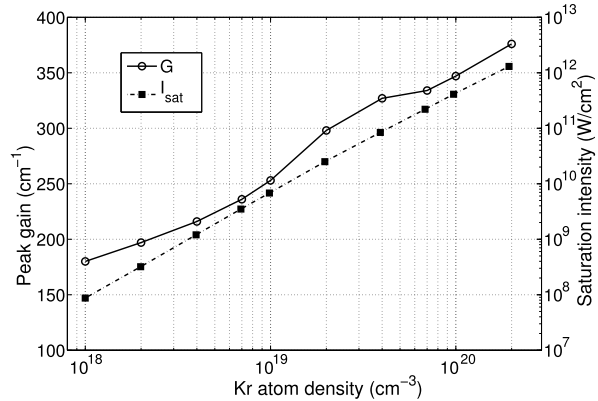


Fig. 4 Soft X-ray output intensity as a function of harmonic injection time into the amplifier for a pressure of (a) 15 mbar, (b) 20 mbar, (c) 30 mbar and (d) 40 mbar. Gain calculations are also reported on each graph

Fig. 5 Calculated peak gain and saturation intensity for a krypton density up to $2 \times 10^{20} \text{ cm}^{-3}$



short (fs) and intense pulse, called the ignitor, is then focused into the gas. Via tunnel ionization, a weakly-ionize plasma is generated. A second long duration (100's ps) and energetic (100's mJ) pulse, called the heater, will then heat the free electrons and trigger collisional avalanche ionization that will lead to a plasma of ionization stage around 3–4 and thus greatly increase the electron density. The last step is the hydrodynamic expansion of that plasma at the local sound speed. This expansion will result in a decrease of the electron density along the axis.

We implemented that technique for our Kr^{8+} amplifier using an axicon [18], that focuses the ignitor and heater pulses along a longitudinal line. The experimental setup is detailed on Fig. 6. The plasma channel is created using a 100 mJ, 35 fs ignitor pulse and a cross-polarized 250 mJ, 400 ps heater pulse delayed by 350 ps. These pulses are focused by the axicon along a line 2–3 cm-long into the gas jet. The gas jet is a prototype that is able to deliver a neutral density up to $2 \times 10^{20} \text{ cm}^{-3}$ with a

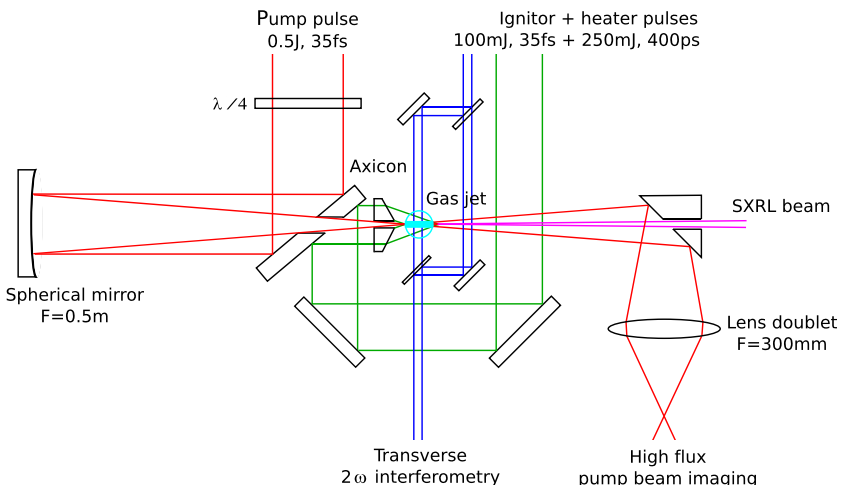


Fig. 6 High density plasma waveguiding and soft X-ray laser: experimental setup

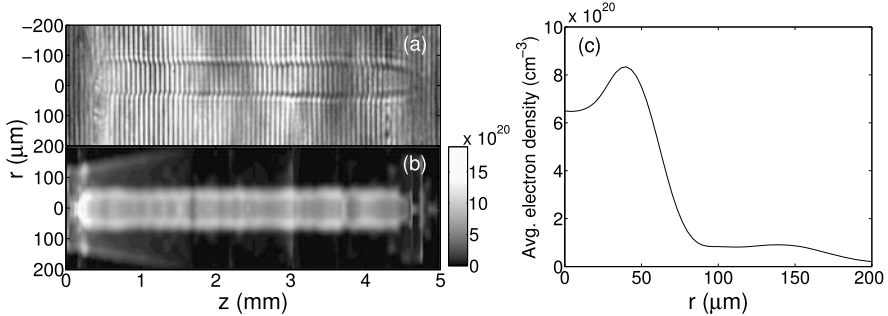


Fig. 7 (a) Typical plasma channel interferogram and (b) electron density map calculated from that interferogram. The pump laser propagates from left to right. (c) Averaged electron density profile along the channel

slit nozzle 0.2×5 mm or 0.2×10 mm. After a delay of 3.5 ps, the main pulse (0.5 J, 35 fs) is focused into the plasma channel by a 0.5 m focal length spherical mirror. Our main diagnostics are plasma transverse Mach-Zehnder interferometry using a frequency-doubled Ti:Sa pulse, high flux pump beam imaging in the entrance and exit planes of the channel, and a flat-field soft X-ray spectrometer (not showed here) using a grazing incidence toroidal mirror coupled to a 1000 mm^{-1} reflexion grating.

In Fig. 7(a) is given a typical plasma channel interferogram obtained with the 5 mm-long nozzle. The channel clearly runs over most of the 5 mm of gas and has a diameter around 100 μm . This interferogram can be used to calculate the electron density map in the channel. It is given on Fig. 7(b) and the longitudinally-averaged profile is given on Fig. 7(c). The density is very high at the entrance of the channel, more than 10^{21} cm^{-3} , and quickly decreases to a value slightly below 10^{21} cm^{-3} . On average, the density inside the channel is around $7 \times 10^{20}\text{ cm}^{-3}$. We can also notice that the channel exhibits an electron density difference $\Delta n_e > 10^{20}\text{ cm}^{-3}$ over a radius of 40 μm , more than sufficient to allow waveguiding.

On Fig. 8(a) and (b) are given respectively the focal spot of the pump beam in the entrance plane of the gas jet and in the output plane without waveguide (and without gas). It is focused down to a spot size of 15 μm FWHM, close to the diffraction limit. On Fig. 8(c) is given the pump beam profile in the output plane of the gas jet when the plasma waveguide is present (using the 5 mm nozzle). The beam is clearly guided, and exhibits after 5 mm of guided propagation dimensions comparable the focal spot. On this image, the guided beam is mainly monomode while in others cases, it is composed by 2, 3 or more spots. This is due to the pointing fluctuations of the pump beam that have multimode guiding as a consequence. However, it does not affect the overall energy transmission of the waveguide, which usually ranges between 35 % et 50 % with a good shot-to-shot stability.

We were able to generate a SXRL using that waveguide technique both the 5 mm and 10 mm-long nozzles. On Fig. 9(a) is given the spectrum of the emitted radiation. It is only composed by the 32.8 nm SXRL line. We have not been able to calibrate our sensor, but we estimate the energy contained in the SXRL pulses to

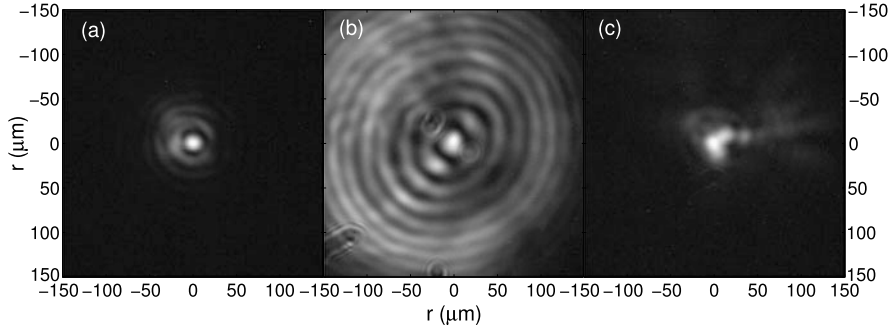


Fig. 8 High flux images of the pump beam (a) in the entrance plane of the jet, (b) in the output plane, without waveguide, and (c) in the output plane, guided in the 5 mm-long plasma channel

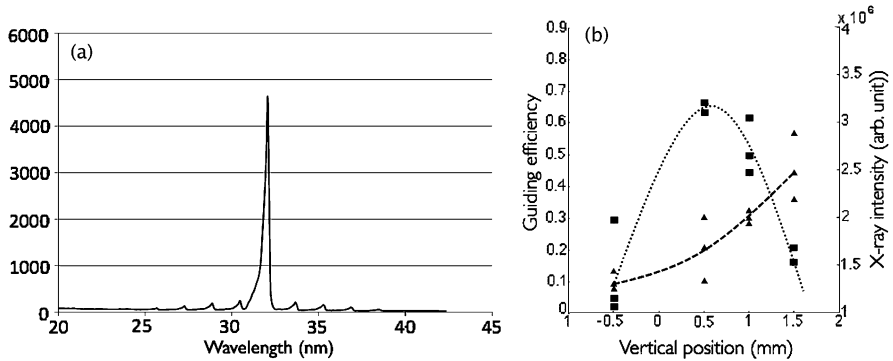


Fig. 9 (a) Spectrum of the emitted soft X-ray radiation. (b) Guiding efficiency (*dotted line*) and SXRL intensity (*dashed line*) as a function of the relative spacing between the jet nozzle and the plasma channel. The density rises when the vertical position decreases

several μJ . On Fig. 9(b) is given the dependence of the guiding efficiency of the waveguide and the output soft X-ray signal on the gas density. It can be seen that the guiding efficiency increases while the density decreases, because propagation of the preforming beams is easier at lower densities. The resulting channel is also slightly smaller when the density is increased, so that the pump beam is harder to couple to the waveguide. On the other hand, there is a density optimum in terms of soft X-ray generation. This is due to some competition between the high gain and saturation intensity, and the less efficient guiding that are all consequences of a higher density.

At last, the far-field pattern of that SRL beam has been recorded using a spherical mirror to ensure all the light is collected on our soft X-ray CCD camera. A typical footprint of the beam, generated using the 1 cm-long nozzle, is presented on Fig. 10. It exhibits the speckle patterns common to short-duration ASE SXRLs, and a doughnut shape due to steep density gradients inside the waveguide that deflect the soft X-ray beams away from the axis. Its divergence, between 10 and 15 mrad, is deter-

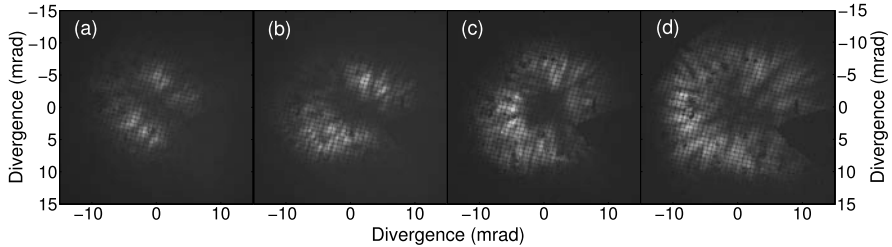


Fig. 10 Far-field profile of the SXRL beam using the 10 mm-long nozzle and a distance between the jet and the plasma channel of **(a)** $\simeq 0$, **(b)** 0.5 mm, **(c)** 1 mm, and **(d)** 1.5 mm. The density decreases from left to right

mined by the geometry of the amplifier column. For the same reason, we notice that when the gas density decreases (Fig. 10(a–d)), the beam divergence increases (larger and potentially longer amplifier). When using a 5 mm-long nozzle, the SXRL beam is usually a little more divergent (20 mrad) since the amplifier is shorter.

4 Recombination Scheme

These results are very promising, but still limited in terms of short wavelength SXRL generation. The ability to guide an intense pulse in a near-critical density plasma could be the first step to reinvestigate the recombination pumping scheme [19]. This scheme is very interesting because it would allow for the possibility of lasing from an excited state of an ion down to the ground state. The advantage of lasing down to the ground state is the higher energy (thus shorter wavelength) of the lasing transition as compared with lasing between excited states. The plasma conditions that are required are a very complete emptying of the ground state and an electron temperature which is small compared to the ionization energy in order to favor collisional recombination (over radiative recombination). Since the collisional recombination rate varies as n_e^3/T_e , the plasma needs also to be as dense as possible. If these requirements are met, the upper energy levels of the ion of charge n will be populated from recombination of the ion of charge $n + 1$. Collisional-radiative cascades will occur and will populate the lower energy levels before the ground state, allowing a population inversion between the ground state and the first energy level (among others). This population inversion is expected to be very short, below 1 ps [20]. Good candidates for this scheme are H-like or Li-like ions. In particular, an intensity of only $2 \times 10^{17} \text{ W/cm}^2$ is needed to ionize neon to He-like Ne which may recombine to Li-like Ne [21]. In Li-like Ne, the transition between the first excited level (3d) and the ground state (2p) corresponds to a wavelength of 9.8 nm.

We propose to use the preformed plasma waveguide technique in a near-critical density Ne plasma to investigate the OFI recombination scheme. To limit electron heating by the pump pulse, the pump field has to be linearly polarized. The smaller pump field wavelength, the less heating it provides, so we decided to use a

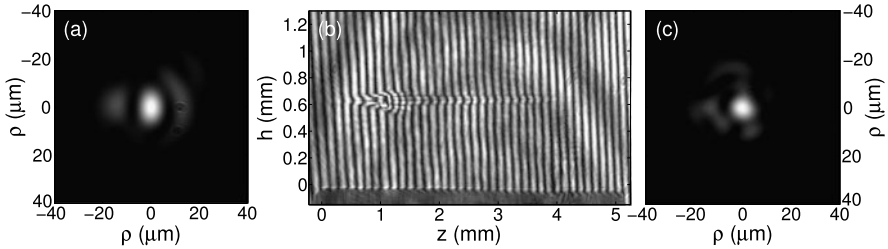


Fig. 11 (a) Focal spot of the 2ω beam, in the entrance plane of the plasma channel. (b) Interferogram of the plasma channel guiding the 2ω pulse over 5 mm of neon plasma. (c) Guided 2ω beam output profile in the exit plane of the channel

frequency-doubled pump pulse. We used a 120 mm-diameter, 0.8 mm-thick type I KDP crystal to generate the second harmonic of the main pulse of our Ti:Sa laser system. Up to 40 % of the infrared was converted to 405 nm. Figure 11(a) shows the 2ω focal spot focused by a 0.5 m-focal length spherical mirror. The ω beam is focused down to a spot size of 16 μm FWHM encircling 50 % of the energy while the 2ω focal spot is twice smaller (8 μm) and contains 57 % of the energy. We have not been able to measure the spectrum of the 2ω pulse, but manufacturer data shows no significant temporal broadening of that pulse.

Figure 11(b) is a typical interferogram of the Ne plasma using a 5 mm-long nozzle. We can notice a plasma channel running over most of the 5 mm of neon, and the guided 2ω pulse in the channel. On Fig. 11(c) is given the beam profile of the guided 2ω beam in the exit plane of the channel. It is comparable to the input beam, with the same spot diameter of 8 μm. We measured an energy transmission of the waveguide of 60 %. This is even better than when guiding the ω beam, and probably due to the smaller size of the 2ω beam at the entrance of the channel. We have not observed any soft X-ray signal, but this was only a preliminary experiment.

5 Conclusion

We have seen that—although they offer interesting features—low density OFI collisional SXRL amplifiers are limited in terms of pulse energy, duration, and wavelength of emission. We successfully increased the density of the amplifier by 2 orders of magnitude, with prospects of multi-10th μJ soft X-ray pulses also expected to have a shorter duration. To achieve that, an ignitor+heater optically preformed plasma waveguide with a transmission of 50 % has been implemented. The ability to guide ultra-intense pulses in near-critical plasmas is a good start to a reinvestigation of the OFI recombination pumping scheme. As a preliminary experiment, we have been able to frequency-double the main IR pump pulse and guide this pulse in a neon plasma at a density around 10^{21} cm^{-3} . If successful, this experiment would allow the production of sub-ps pulses below 10 nm.

References

- Sebban, S., Mocek, T., Ros, D., Upcraft, L., Balcou, Ph., Haroutunian, R., Grillon, G., Rus, B., Klisnick, A., Carillon, A., Jamelot, G., Valentin, C., Rousse, A., Rousseau, J.P., Notebaert, L., Pittman, M., Hulin, D.: Demonstration of a Ni-like Kr optical-field-ionization collisional soft x-ray laser at 32.8 nm. *Phys. Rev. Lett.* **89**, 253901 (2002)
- Sebban, S., Upcraft, L.M., Balcou, Ph., Pittman, M., Haroutunian, R., Grillon, G., Valentin, C., Rousse, A., Rousseau, J.-Ph., Notebaert, L., Hulin, D., Mocek, T., Rus, B., Ros, D., Klisnick, A., Carillon, A., Jamelot, G.: Investigations of collisionally pumped optical field ionization soft-x-ray lasers. *J. Opt. Soc. Am. B* **20**(1), 195–202 (2003)
- Guilbaud, O., Klisnick, A., Cassou, K., Kazamias, S., Ros, D., Jamelot, G., Joyeux, D., Phalippou, D.: Origin of microstructures in picosecond x-ray laser beams. *EPL* **74**(5), 823 (2006)
- Guilbaud, O., Tissandier, F., Goddet, J.-P., Ribière, M., Sebban, S., Gautier, J., Joyeux, D., Ros, D., Cassou, K., Kazamias, S., Klisnick, A., Habib, J., Zeitoun, P., Benredjem, D., Mocek, T., Nedjl, J., de Rossi, S., Maynard, G., Cros, B., Boudaa, A., Calisti, A.: Fourier-limited seeded soft x-ray laser pulse. *Opt. Lett.* **35**(9), 1326–1328 (2010)
- Zeitoun, Ph., Faivre, G., Sebban, S., Mocek, T., Hallou, A., Fajardo, M., Aubert, D., Balcou, Ph., Burgy, F., Douillet, D., Kazamias, S., de Lacheze-Murel, G., Lefrou, T., le Pape, S., Mercere, P., Merdji, H., Morlens, A.S., Rousseau, J.P., Valentin, C.: A high-intensity highly coherent soft x-ray femtosecond laser seeded by a high harmonic beam. *Nature* **431**(7007), 426–429 (2004)
- Goddet, J.Ph., Sebban, S., Morlens, A.S., Gautier, J., Rousseau, J.Ph., Burgy, F., Zeitoun, Ph., Valentin, C., Hauri, C., Maynard, G., Boudaa, A., Caumes, J.P., Merdji, H., Mocek, T., Kozlova, M., Jakubczak, K.: Demonstration of a spatial filtering amplifier for high-order harmonics. *Opt. Lett.* **32**(11), 1498–1500 (2007)
- Tissandier, F., Sebban, S., Ribière, M., Gautier, J., Zeitoun, Ph., Lambert, G., Goddet, J.-Ph., Burgy, F., Valentin, C., Rousse, A., Nejdl, J., Mocek, T., Maynard, G.: Bessel spatial profile of a soft x-ray laser beam. *Appl. Phys. Lett.* **97**(23), 231106 (2010)
- Goddet, J.Ph., Sebban, S., Gautier, J., Zeitoun, Ph., Valentin, C., Tissandier, F., Marchenko, T., Lambert, G., Ribière, M., Douillet, D., Lefrou, T., Iaquaniello, G., Burgy, F., Maynard, G., Cros, B., Robillard, B., Mocek, T., Nejdl, J., Kozlova, M., Jakubczak, K.: Aberration-free laser beam in the soft x-ray range. *Opt. Lett.* **34**(16), 2438–2440 (2009)
- Tissandier, F., Sebban, S., Gautier, J., Zeitoun, Ph., Oliva, E., Rousse, A., Maynard, G.: 3d Maxwell-Bloch calculation of the temporal profile of a seeded soft x-ray laser pulse. *Appl. Phys. Lett.* **101**, 251112 (2012). doi:[10.1063/1.4773208](https://doi.org/10.1063/1.4773208)
- Butler, A., Gonsalves, A.J., McKenna, C.M., Spence, D.J., Hooker, S.M., Sebban, S., Mocek, T., Bettaibi, I., Cros, B.: Demonstration of a collisionally excited optical-field-ionization XUV laser driven in a plasma waveguide. *Phys. Rev. Lett.* **91**, 205001 (2003)
- Butler, A., Gonsalves, A.J., McKenna, C.M., Spence, D.J., Hooker, S.M., Sebban, S., Mocek, T., Bettaibi, I., Cros, B.: 41.8nm Xe^{8+} laser driven in a plasma waveguide. *Phys. Rev. A* **70**, 023821 (2004)
- Mocek, T., McKenna, C.M., Cros, B., Sebban, S., Spence, D.J., Maynard, G., Bettaibi, I., Vorontsov, V., Gonsalves, A.J., Hooker, S.M.: Dramatic enhancement of XUV laser output using a multimode gas-filled capillary waveguide. *Phys. Rev. A* **71**, 013804 (2005)
- Cros, B., Mocek, T., Bettaibi, I., Vieux, G., Farinet, M., Dubau, J., Sebban, S., Maynard, G.: Characterization of the collisionally pumped optical-field-ionized soft-x-ray laser at 41.8 nm driven in capillary tubes. *Phys. Rev. A* **73**, 033801 (2006)
- Chou, M.-C., Lin, P.-H., Lin, C.-A., Lin, J.-Y., Wang, J., Chen, S.-Y.: Dramatic enhancement of optical-field-ionization collisional-excitation x-ray lasing by an optically preformed plasma waveguide. *Phys. Rev. Lett.* **99**, 063904 (2007)
- Lin, P.-H., Chou, M.-C., Lin, C.-A., Chu, H.-H., Lin, J.-Y., Wang, J., Chen, S.-Y.: Optical-field-ionization collisional-excitation x-ray lasers with an optically preformed plasma waveguide. *Phys. Rev. A* **76**, 053817 (2007)

16. Durfee, C.G., Milchberg, H.M.: Light pipe for high intensity laser pulses. *Phys. Rev. Lett.* **71**, 2409–2412 (1993)
17. Durfee, C.G., Lynch, J., Milchberg, H.M.: Mode properties of a plasma waveguide for intense laser pulses. *Opt. Lett.* **19**(23), 1937–1939 (1994)
18. Durfee, C.G., Lynch, J., Milchberg, H.M.: Development of a plasma waveguide for high-intensity laser pulses. *Phys. Rev. E* **51**, 2368–2389 (1995)
19. Nagata, Y., Midorikawa, K., Kubodera, S., Obara, M., Tashiro, H., Toyoda, K.: Soft-x-ray amplification of the Lyman- α transition by optical-field-induced ionization. *Phys. Rev. Lett.* **71**, 3774–3777 (1993)
20. Eder, D.C., Amendt, P., Wilks, S.C.: Optical-field-ionized plasma x-ray lasers. *Phys. Rev. A* **45**, 6761–6772 (1992)
21. Amendt, P., Eder, D.C., Wilks, S.C.: X-ray lasing by optical-field-induced ionization. *Phys. Rev. Lett.* **66**, 2589–2592 (1991)

Chapter 41

Spectral Linewidth Measurement of a Ne-Like Ar Capillary Discharge Soft X-Ray Laser

L. Urbanski, M.C. Marconi, L.M. Meng, M. Berrill, O. Guilbaud, A. Klisnick, and J.J. Rocca

Abstract We report on the measurement of spectral linewidth of a Ne-like Ar table-top capillary discharge laser. The linewidth was measured as a function of the gain medium length. Due to inhomogeneous character of the linewidth, saturation re-broadening is expected. However no such behavior was observed while the amplifier length was extended beyond saturation. This situation is compared with a numerical model, identifying that even a small amount of collisional broadening effectively homogenizes the line profile.

1 Introduction

The table top capillary discharge Ne-like Ar laser has been widely used in many applications requiring combination of light coherence and high photon flux [1]. In past experiments the spatial coherence of the Ne-like Ar laser was measured using a Young's interferometer. The measurement was performed for different amplifier lengths yielding to the conclusion that a fully spatially coherent beam is obtained for 36 cm long plasma column [2]. However there was no direct measurement of the temporal coherence and thus the linewidth of the capillary discharge laser. The measurement of the linewidth can give insight on the plasma conditions in the amplifier and provide a better understanding of the laser dynamics. In a capillary discharge laser, the electron density is of the order of 10^{18} cm^{-3} and the ion temperature ex-

L. Urbanski · M.C. Marconi (✉) · J.J. Rocca

NSF ERC for Extreme Ultraviolet Science and Technology, Colorado State University, Fort Collins, CO 80523, USA

e-mail: marconi@engr.colostate.edu

L.M. Meng · A. Klisnick

ISMO, Bât. 350, CNRS, Université Paris-Sud 11, Orsay, France

M. Berrill

Oak Ridge National Laboratory, Oak Ridge, TN 37831, USA

O. Guilbaud

LPGP, Bât. 210, CNRS, Université Paris-Sud 11, Orsay, France

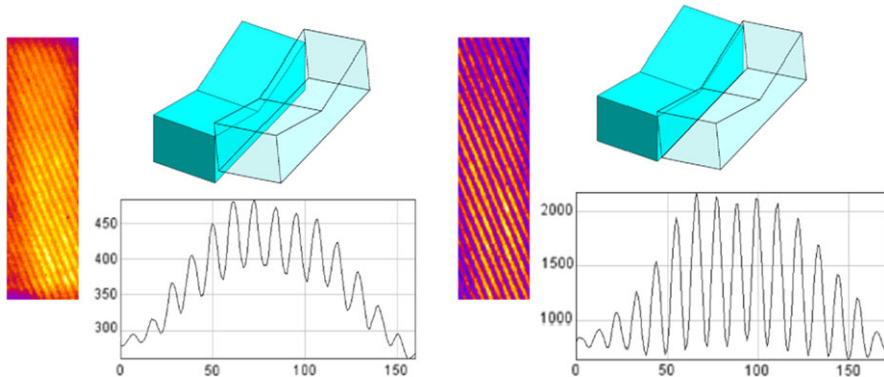


Fig. 1 Different position of the scanning mirror resulting in different interference contrast. Insets showing relative mirror placement, interferogram and a corresponding line-out

ceeds the electron temperature. In such conditions, Doppler broadening dominates the line profile and the collisional component that homogenizes it should be less significant.

This situation gives a justified premise to expect linewidth re-broadening after saturation. Several attempts to measure the linewidth of different types of optically pumped soft-x-ray lasers have been reported in the past [3, 4]. Due to extremely narrow line, they had to be conducted using very high resolution spectrometers [3]. In the experiment described herein, we measured the laser linewidth using a Fresnel bi-mirror interferometer [4]. The line profile was inferred from the visibility profile obtained by measuring the fringe visibility of the interferograms as a function of the path difference in the interferometer. We measured the laser linewidth for different amplifier lengths between 18 and 36 cm and compare the results to the numerical simulations.

2 Measurement Principle

The capillary discharge laser illuminates the Fresnel bi-mirror interferometer after reflecting in a pair of multilayer mirrors (Sc/SiO), with peak reflectivity at 46.9 nm. This arrangement serves in the experiment twofold. First, it allows aligning the laser beam with the optical axis of the interferometer. Second, due to the narrow reflectivity bandwidth of the multilayers, the double reflection provides extra spectral filtering at the laser wavelength. The wavefront is then split at the interferometer and brought to interference at the detector plane (CCD). The optical path difference between the arms of the interferometer can be varied displacing one of the bi-mirrors in the vertical direction as schematically shown in Fig. 1.

This produces a change in the visibility of the interference fringes with the different path differences that allows the construction of the visibility curve. A typical

Fig. 2 Visibility curve obtained for a single capillary length. Experimental data with a calculated fit

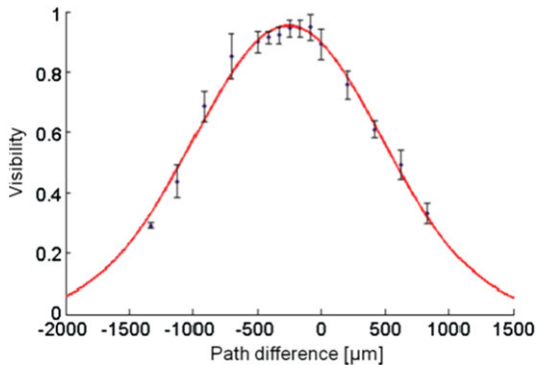
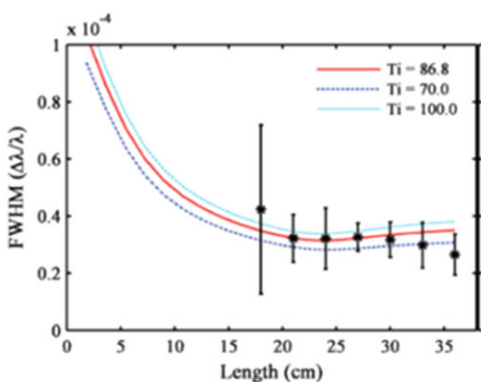


Fig. 3 Experimental results. Linewidth as a function of the amplifier length. Data set is fitted with numerical calculation



visibility curve is shown in Fig. 2. The coherence length is obtained from the optical path difference at which the fit drops to 1/e of its maximum in the Gaussian fit of the curve. From this measurement the linewidth is calculated. The results of the linewidth measurement are illustrated in Fig. 3.

The bandwidth decreases slowly as the plasma length increases maintaining an almost constant value for long capillaries, without any significant rebroadening for the longest lengths even though the laser was operated above saturation. Each data point in Fig. 3 corresponds to an average of 5 measurements and the error bars were selected to include all measurements. The lines show the computed linewidth assuming ion temperatures of 100, 87 and 70 eV from top to bottom, respectively. The model simulates the amplification of the laser line by solving the frequency-dependent intensity and population equations accounting for Doppler and collisional broadening, gain saturation, beam refraction, and collisional redistribution. The calculations predict a weak rebroadening of the line beyond $L = 24$ cm. However this effect is small compared to our experimental error bars, and no conclusive rebroadening can be derived from the experimental data.

3 Summary

In conclusion, we have measured the linewidth and temporal coherence of a capillary discharge soft-x-ray laser, and have studied its variation as a function of amplifier length. While the line profile in this discharge amplifier is clearly dominated by Doppler broadening, the relatively small collisional broadening component is still sufficiently large to homogenize the line to the point at which no rebroadening was measured to take place as the line intensity continued to increase beyond gain saturation. The narrow relative linewidth of this laser $\Delta\lambda/\lambda = 3.5 \times 10^{-5}$ corresponds to a coherence time of 2 ps that is much shorter than the pulse duration of 1.2–1.8 ns [1, 5, 6]. The temporal coherence length $L_c = 700 \mu\text{m}$ measured for this capillary discharge SXRL is either similar or in some cases even larger than that of other collisional soft-x-ray lasers [7–9], which facilitates applications requiring high temporal coherence, such as interferometry [1] and large-area Talbot nanopatterning [10].

Acknowledgements We acknowledge fruitful discussion with A. Calisti (PIIM, Universite de Marseille, France) on ionic correlations. The support and expertise from D. Joyeux and S. de Rossi (LCF, Institut d’Optique, Palaiseau, France) are greatly appreciated. This work was supported by NSF Grant No. PHY-1004295, the NSF Center for Extreme Ultraviolet Science and Technology under NSF Grant No. EEC-0310717, DTRA under Contract No. HDTRA 1-10-1-0070, and by the AMOS program of the Office of Basic Energy Sciences, US Department of Energy. M.B. acknowledges support for staff members at Oak Ridge National Laboratory managed by UT-Battelle, LLC, for the US Department of Energy under Contract No. DE-AC05-00OR22725.

References

- Urbanski, L., Marconi, M.C., Meng, L.M., Berrill, M., Guilbaud, O., Klisnick, A., Rocca, J.J.: Spectral linewidth of a Ne-like Ar capillary discharge soft-x-ray laser and its dependence on amplification beyond gain saturation. *Phys. Rev. A, Am. Phys. Soc.* **85**, 033837 (2012)
- Liu, Y., Seminario, M., Tomasel, F., Chang, C., Rocca, J., Attwood, D.: Achievement of essentially full spatial coherence in a high-average-power soft-x-ray laser. *Phys. Rev. A* **63**(3), 1–5 (2001)
- Koch, J.A., MacGowan, B.J., Da Silva, L.B., Matthews, D.L., Underwood, J.H., Batson, P.J., et al.: Experimental and theoretical investigation of neonlike selenium x-ray laser spectral linewidths and their variation with amplification. *Phys. Rev. A* **50**, 1877–1898 (1994)
- Klisnick, A., Guilbaud, O., Ros, D., Cassou, K., Kazamias, S., Jamelot, G., et al.: Experimental study of the temporal coherence and spectral profile of the 13.9 nm transient X-ray laser. *J. Quant. Spectrosc. Radiat. Transf.* **99**(13), 370–380 (2006). Radiative Properties of Hot Dense Matter
- Benware, B.R., Macchietto, C.D., Moreno, C.H., Rocca, J.J.: Demonstration of a high average power tabletop soft X-ray laser. *Phys. Rev. Lett.* **81**, 5804–5807 (1998)
- Macchietto, C.D., Benware, B.R., Rocca, J.J.: Generation of millijoule-level soft x-ray laser pulses at a 4-Hz repetition rate in a highly saturated tabletop capillary discharge amplifier. *Opt. Lett.* **24**(16), 1115–1117 (1999)
- Smith, R.F., Dunn, J., Hunter, J.R., Nilsen, J., Hubert, S., Jacquemot, S., et al.: Longitudinal coherence measurements of a transient collisional x-ray laser. *Opt. Lett.* **28**(22), 2261–2263 (2003)
- Meng, L.M., Alessi, D., Guilbaud, O., Wang, Y., Berrill, M., Luther, B.M., et al.: Temporal coherence and spectral linewidth of an injection-seeded transient collisional soft x-ray laser. *Opt. Express* **19**(13), 12087–12092 (2011)

9. Meng, L., Klisnick, A., Kozlova, M., Bohacek, K., Krus, M., Prokupek, J., Urbanski, L., Marconi, M.C., Berrill, M., Rocca, J.J., Guilbaud, O., Tissandier, F., Sebban, S., Zeitoun, P., Calisti, A., Ferri, S., Mossé, C., Talin, B.: Temporal coherence and spectral linewidth of neon-like XUV lasers pumped in the quasi-steady state regime. In: Sebban, S., et al. (eds.) *X-Ray Lasers 2012*. Springer Proceedings in Physics, vol. 147. Springer, Cham (2013). Chapter 28 in this book
10. Isoyan, A., Jiang, F., Cheng, Y.C., Cerrina, F., Wachulak, P., Urbanski, L., et al.: Talbot lithography: self-imaging of complex structures. *J. Vac. Sci. Technol.* **27**, 2931–2937 (2009)

Chapter 42

Defect Tolerant Talbot Nanopatterning

L. Urbanski, M.C. Marconi, A. Isoyan, A. Stein, C.S. Menoni, and J.J. Rocca

Abstract We report on a defect tolerant extreme ultraviolet (EUV) nanopatterning method. This technique is capable of printing arbitrarily shaped features arranged into periodic arrays with sub-micron resolution. The method is based on the Talbot effect. Masks with different defect layouts were fabricated and tested producing defect free prints regardless of presence of large amount of defects covering up to 1 % of the area of the mask. Numerical simulation was conducted in very good agreement with the experimental data.

1 Introduction

The demand for effective methods for nanostructures fabrication is driven by an increased interest in the field of nanosciences and advocates the emergence of alternative lithographic techniques. Nano structures have been widely investigated in multiple applications such as photonics, plasmonics, microfluidics, biosensors etc. [1–11]. A versatile and robust method to fabricate such structures will contribute to the continuing advancement of this field in the future.

In this paper, we present a nanofabrication technique which has the potential to print features in a photoresist with high spatial resolution and to produce faithful replicas of the original mask even though a significant amount of defects are present in the mask. The method is based on the classical Talbot effect, where a diffraction grating produces replicas of itself under coherent illumination [12, 13]. The image

L. Urbanski · M.C. Marconi (✉) · C.S. Menoni · J.J. Rocca
NSF Engineering Research Center for Extreme Ultraviolet Science & Technology and
Department of Electrical and Computer Engineering, Colorado State University, Fort Collins, CO,
USA
e-mail: marconi@engr.colostate.edu

A. Isoyan
Synopsys Inc., Hillsboro, OR, USA

A. Stein
Center for Functional Nanomaterials, Brookhaven National Laboratory, Upton, NY, USA

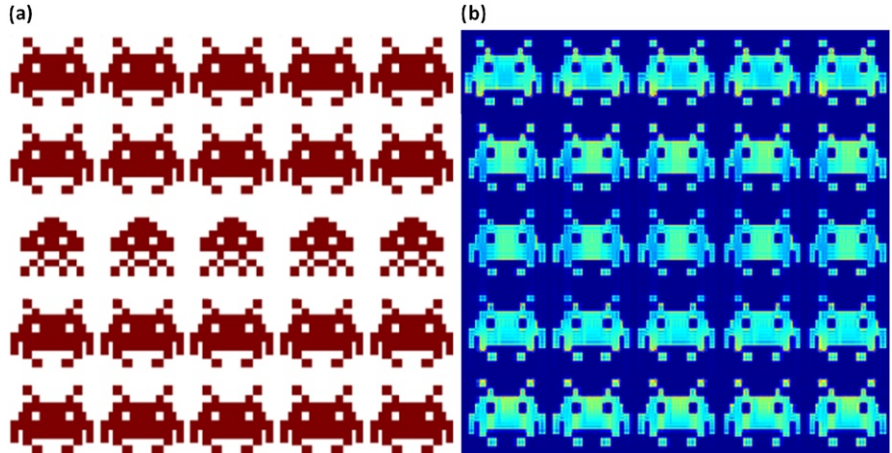


Fig. 1 Mask with 1 % defect (a) and corresponding reconstruction at the Talbot plane calculated numerically (b)

that replicates the diffraction grating emerges at a specific distance and its integer multiples from the master grating. These distances are called Talbot distances.

In an extension of this concept, the generalized Talbot effect (GTI), the grating is replaced by a periodic two dimensional array of arbitrarily designed motifs also referred to as the diffractive mask, or mask for brevity. Also the GTI renders replicas of the original mask at the Talbot distances, in a similar way as the classical Talbot effect. A more detailed description of the GTI can be found in [14].

The diffractive mask is composed of an array of periodically tiled cells of arbitrary design (native cells). For the purpose of this experiment, the native cell motif has been chosen to be a character from a 1970s video game, “Space Invaders”. The defect was represented as a cell with a different motif, also corresponding to a different species of space invader. We will refer the defect as the impostor cell.

In order to characterize the extent of defect tolerance, we have designed masks with purposefully embedded defects. The masks were composed of 10,000 unit cells arranged in a square matrix where a certain number of impostor cells were included with different layouts. In one case a single impostor cell was introduced in the central cell of the mask. In the second case, the entire middle row of native cells was replaced with impostor cells. These two layouts correspond to a defect density of 0.01 % and 1 % respectively.

Figure 1(b) shows the numerical reconstruction of the mask with a row of impostor cells calculated at the first Talbot plane. The figure shows only the 5×5 central section of the 10,000 cells array. The reconstruction was performed using the Fresnel-Kirchhoff diffraction integral formalism to calculate the diffracted light intensity. No sign of defect is present in the reconstruction plane and the impostor cells are completely eliminated in the Talbot plane.

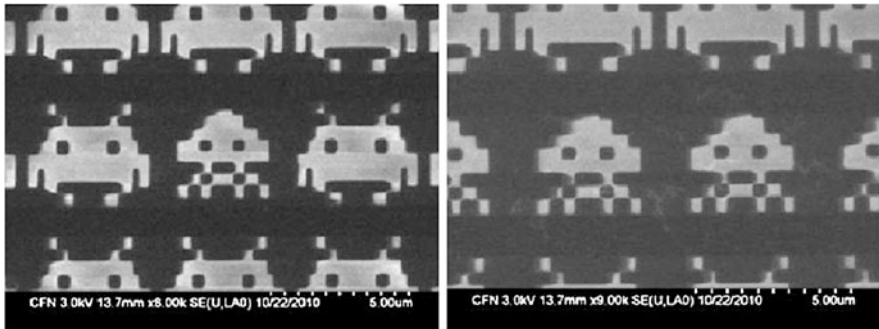


Fig. 2 The diffractive mask layout for two different defect concentrations. *Left:* 0.01 %, *right:* 1 %

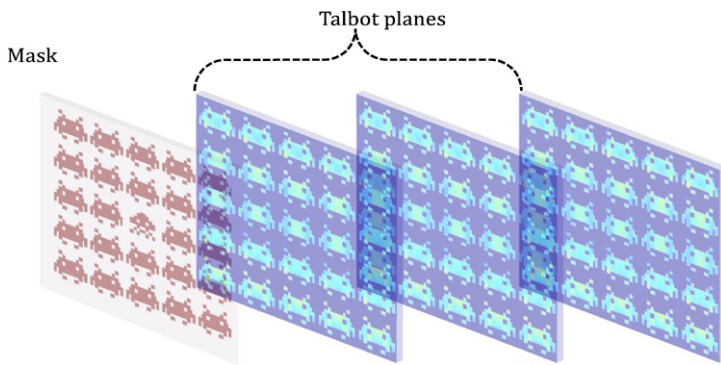


Fig. 3 Scheme of the experimental setup. In-line reconstruction of the mask

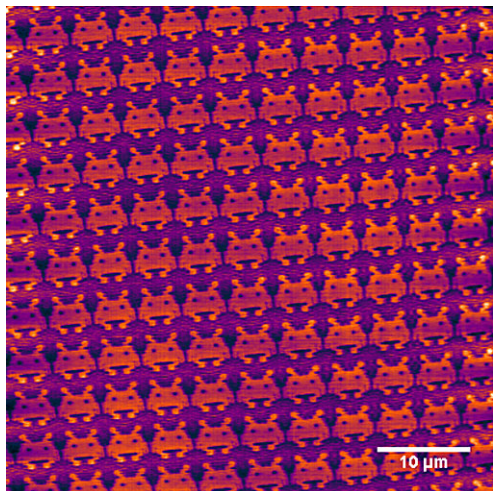
2 Experiment

In order to verify the numerical result experimentally, two masks were fabricated. To fabricate the masks with reasonable diffraction efficiency we used a thin (25 nm) silicon nitride membrane that provided an adequate transparent substrate on which the cells were defined in HSQ photoresist by electron beam lithography.

Figure 2 shows the SEM micrographs of the two masks. In the left hand side is pictured the central region of the mask with a single impostor cell. The right hand side of Fig. 2 is the micrograph of the second mask where the central row was replaced by the impostor motif. More details on the mask fabrication can be found in [14].

The schematic of the experimental setup is represented in Fig. 3. The mask with a defect was illuminated with coherent beam from a table top capillary discharge soft X-ray laser. At the first Talbot plane a resist-coated silicon wafer was placed in order to record the self-image. The exposed resist was then developed and scanned using an atomic force microscope (AFM). Figure 4 shows the AFM micrograph of the print obtained for the mask with a row of defects. The print recreates the original

Fig. 4 Atomic force microscope scan of the resist patterned with a defective mask with 1 % defect



mask without any defect, producing a defect free print event though the diffractive mask had a severe defect equivalent to 1 % of the total area. Similar results were obtained with the mask with a single impostor cell.

This result is in very good correspondence with numerical simulations shown in Fig. 1. It is important to notice that the amount of defect included in the masks we tested is significantly larger than the tolerable defect count in a lithography mask. Our results demonstrate a versatile and robust methodology to print photoresist with defect tolerant characteristics. This approach can have impact in the fabrication of periodic structures like plasmonic surfaces, photonic crystal structures, calibration gratings, etc. and can contribute to the widespread of small scale nanofabrication.

Acknowledgements This work was supported by the National Science Foundation, award ECCS 0901806, the NSF ERC for Extreme Ultraviolet Science and Technology, award EEC 0310717. This research was carried out in part at the Center for Functional Nanomaterials, Brookhaven National Laboratory, which is supported by the U.S. Department of Energy, Office of Basic Energy Sciences, under Contract No. DE-AC02-98CH10886.

References

1. Kneipp, K., et al.: Single molecule detection using surface-enhanced Raman scattering (SERS). *Phys. Rev. Lett.* **78**(9), 1667–1670 (1997)
2. Liu, Z.W., et al.: Focusing surface plasmons with a plasmonic lens. *Nano Lett.* **5**(9), 1726–1729 (2005)
3. Liu, Z.W., Wei, Q.H., Zhang, X.: Surface plasmon interference nanolithography. *Nano Lett.* **5**(5), 957–961 (2005)
4. Luo, X.G., Ishihara, T.: Surface plasmon resonant interference nanolithography technique. *Appl. Phys. Lett.* **84**(23), 4780–4782 (2004)
5. Soukoulis, C.M., Wegener, M.: Optical metamaterials—more bulky and less lossy. *Science* **330**(6011), 1633–1634 (2010)

6. Vedantam, S., et al.: A plasmonic dimple lens for nanoscale focusing of light. *Nano Lett.* **9**(10), 3447–3452 (2009)
7. Brueck, S.R.J.: Optical and interferometric lithography—nanotechnology enablers. *Proc. IEEE* **93**(10), 1704–1721 (2005)
8. Chen, Y., et al.: Nanoimprint fabrication of micro-rings for magnetization reversal studies. *Microelectron. Eng.* **57–58**, 405–410 (2001)
9. Chou, S.Y., Krauss, P.R.: Imprint lithography with sub-10 nm feature size and high throughput. *Microelectron. Eng.* **35**(1–4), 237–240 (1997)
10. Himmelhaus, M., Takei, H.: Self-assembly of polystyrene nano particles into patterns of random-close-packed monolayers via chemically induced adsorption. *Phys. Chem. Chem. Phys.* **4**(3), 496–506 (2002)
11. Juillerat, F., et al.: Fabrication of large-area ordered arrays of nanoparticles on patterned substrates. *Nanotechnology* **16**(8), 1311–1316 (2005)
12. Talbot, W.H.F.: Facts relating to optical science. *Philos. Mag.* **9**, 403 (1836)
13. Rayleigh, Lord, F.: On copying of diffraction gratings, and on some phenomena connected therewith. *Philos. Mag.* (1881)
14. Isoyan, A., et al.: Talbot lithography: self-imaging of complex structures. *J. Vac. Sci. Technol.* **27**(6), 2931–2937 (2009)

Chapter 43

Imaging in Nanoscale Using Laser-Plasma Sources of Extreme Ultraviolet (EUV)

P.W. Wachulak, A. Bartnik, A. Baranowska-Korczyc, D. Pánek, P. Brůža, J. Kostecki, Ł. Węgrzyński, R. Jarocki, M. Szczurek, K. Fronc, D. Elbaum, and H. Fiedorowicz

Abstract New developments in nanoscience and nanotechnology require nanometer scale resolution imaging tools and techniques such as an extreme ultraviolet (EUV) and soft X-ray (SXR) microscopy, based on Fresnel zone plates. In this paper, we report on applications of a desk-top microscopy using a laser-plasma EUV source based on a gas-puff target for studies of morphology of thin silicon membranes coated with NaCl crystals and samples composed of ZnO nanofibers.

1 Introduction

Recent rapid developments of nanoscience and nanotechnology require nanometer scale resolution imaging tools and methods. One of the methods, extensively studied for the last few decades, is an extreme ultraviolet (EUV) and soft X-ray (SXR) microscopy, based on Fresnel zone plates (FZP) [1]. The introduction of compact sources of bright EUV and SXR radiation paved the way for the development of table-top microscopes that can render images of nanoscale objects with short exposures and spatial resolution approaching that of synchrotron-based microscopes [2–4].

In this paper, we report on applications of a desk-top microscopy using a laser-plasma EUV source, based on a gas-puff target, for thin-film studies of silicon membrane coated with NaCl crystals and imaging of ZnO nanofibers. The fact of recently increased interest in ZnO nanostructures in electronics is due to their morphology, availability, possibility of doping with other materials, low cost of fabrication and processing [5] and possibility to use in sensor applications [6]. Additionally, our

P.W. Wachulak (✉) · A. Bartnik · J. Kostecki · Ł. Węgrzyński · R. Jarocki · M. Szczurek · H. Fiedorowicz

Institute of Optoelectronics, Military University of Technology, Warsaw, Poland
e-mail: wachulak@gmail.com

A. Baranowska-Korczyc · K. Fronc · D. Elbaum
Institute of Physics, Polish Academy of Sciences, Warsaw, Poland

D. Pánek · P. Brůža
Czech Technical University, Prague, Czech Republic

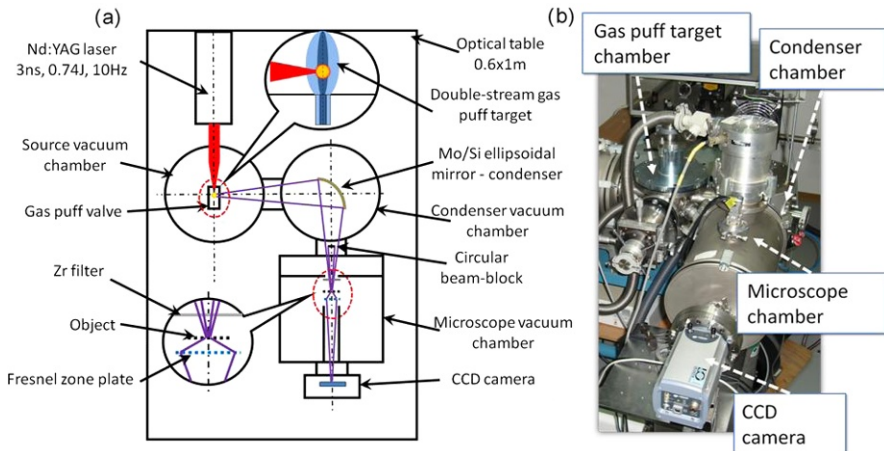


Fig. 1 An experimental arrangement of the EUV microscope (not to scale) using a laser-plasma EUV source (a) and its photograph in (b)

motivation is to test recently developed EUV microscopy setup on non-trivial objects. Utilization of the short wavelength EUV radiation allows to demonstrate the intrinsic advantage of this radiation for extraction of additional information about the investigated object, which cannot be obtained directly from optical micrographs and SEM images. Moreover, this microscope does not require additional sample preparation necessary for SEM microscopy.

2 Experimental Arrangement

The scheme of the experimental arrangement of the EUV microscope is shown in Fig. 1(a) and the photograph in (b). The source, emitting short wavelength radiation that is used for imaging, is a laser-plasma EUV source, presented in [7] and later modified for quasi-monochromatic emission in the 13–14 nm wavelength range, as described in [8]. The gaseous target does not produce any debris associated with solid targets and allow to change the emission bandwidth and the wavelength of emitted radiation simply by changing a gas. EUV radiation from the argon plasma was focused onto a sample and spectrally filtered by a Mo/Si multilayer ellipsoidal mirror.

We have imaged three different samples, to show advantages of EUV microscopy comparing to SEM and optical microscopy. Firstly we used NaCl crystallized on a 15 nm thick non-porous silicon membrane (SPI Supplies) with dimensions $0.07 \times 1.5 \text{ mm}^2$. The substrate, a silicon wafer $3 \times 3 \text{ mm}^2$ in size and $100 \mu\text{m}$ thick, contains two rectangular shape membrane windows. The NaCl crystals were prepared from phosphate buffered saline (PBS) solution (Lonza, Cat. No. BE17-516Q, contents: KH_2PO_4 —144 mg/L, NaCl—9000 mg/L, Na_2HPO_4 —795 mg/L). Five

microliters of the solution were deposited onto the membrane. The water from the solution was evaporated at the temperature of 21 °C and atmospheric pressure, resulting in re-crystallization of NaCl. During the process a stress was introduced to the membrane causing random cracks of various sizes to appear in the NaCl crystal film and the silicon membrane. Second type of sample was composed of ZnO nanofibers. A 10 wt.% poly(vinyl alcohol) (PVA, MW = 72,000) solution was prepared from PVA powder and deionized water. Then 0.25 g of zinc acetate dihydrate ($\text{Zn}(\text{CH}_3\text{COO})_2 \cdot 2\text{H}_2\text{O}$) was dissolved in 1.25 g solution of PVA as a precursor to obtain ZnO nanofibers. Solution, prepared in this way, a precursor, was placed in a syringe and then a constant flow rate of 0.1 ml/h through a syringe pump was established. For electrospinning a high electric potential of 10 kV was applied between the metal tip of a needle of the syringe and grounded collector. The fibers were formed in ambient temperature at 22 °C and humidity in the range from 30 % to 40 %. Finally, the process of calcination at 500 °C for 4 h in air was performed, producing high length/diameter aspect ratio ZnO fibers attached to gold mesh by van der Waals forces. The fibers, deposited in this way, can be seen in transmission mode in rectangular openings of the mesh. The third sample was similar to the second one: ZnO nanofibers were electrospun on top of a 50 nm thick silicon nitride membrane but without the calcination process.

The objects are imaged using a FZP objective (Zone Plates Ltd.) onto a EUV sensitive CCD camera iKon-M, DO934N-BN (Andor). Previously, different test objects (samples) were imaged using this microscope: Cu mesh with 5 μm bars and thickness of ~4 μm [3] and carbon foil, 70 nm thick, with 1.5 μm diameter holes [4], where the EUV images have been obtained with a half-pitch spatial resolution approaching ~50 nm (3.7λ) in a very compact setup (more technical information about the microscope can be found there). The required exposure for imaging of NaCl crystals, deposited on the silicon membrane, was 200 EUV pulses, while for the nanofiber samples –100 EUV pulses at 2 Hz repetition rate. The CCD camera was cooled down to –20 °C to decrease intrinsic noise during the image acquisition.

3 EUV Imaging Results

The objects were imaged using optical, SEM and EUV microscopes. Optical image of the NaCl crystals, deposited on top of a membrane, obtained with 100× (NA ~ 1) objective is shown in Fig. 2(a). Dashed box indicates the region imaged later with the EUV microscope. For the purpose of comparison, the same area of the sample was imaged with an SEM microscope (Tescan VEGA II SBU) and with the EUV microscope. SEM image was obtained after deposition of ~10 nm of Au to avoid charging during image acquisition at 30 kV at magnification of 4000× (sample to screen magnification). SEM image of the sample, ~54 × 54 μm² in size, is shown in Fig. 2(b) and corresponding EUV image—in Fig. 2(c). To show the same area, EUV image was obtained by stitching and partially overlapping 4 × 4 smaller EUV sub-images. Typically, the magnification was 520× (FZP magnification). This results in 25.9 × 25.9 nm² pixel size and the field of view 26.4 × 26.4 μm².

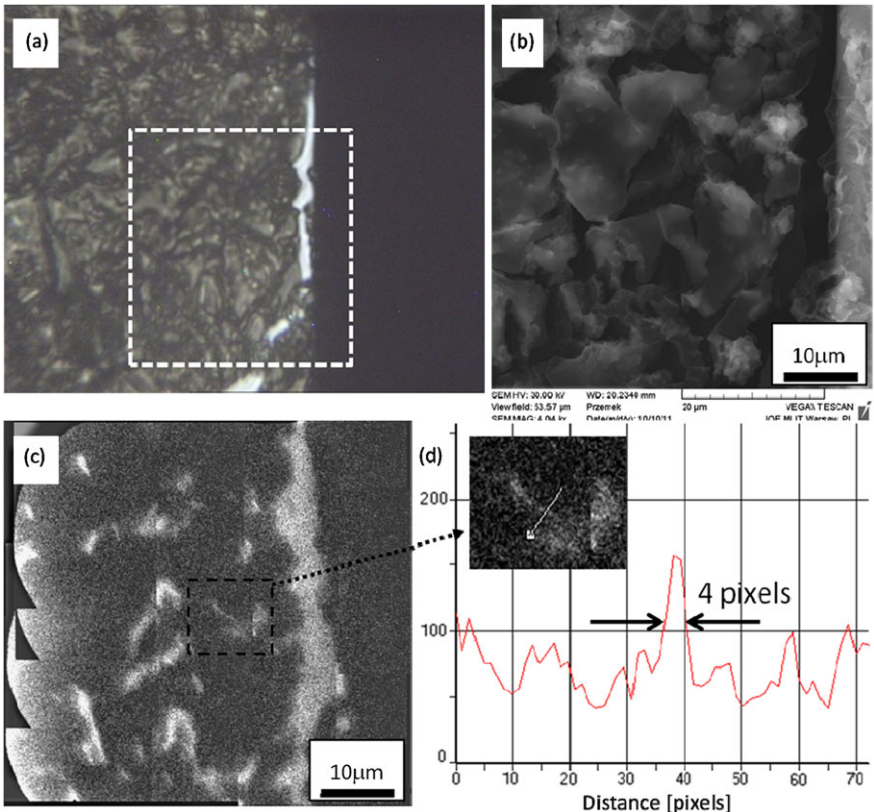


Fig. 2 Optical image of thin Si membrane with re-crystallized NaCl layer deposited on top, obtained with $100\times$ (NA ~ 1) objective (**a**). Dashed box indicates the region imaged with the EUV and SEM microscopes. SEM image of the sample, $\sim 54 \times 54 \mu\text{m}^2$ with re-crystallized NaCl (**b**) and corresponding EUV image (**c**) showing the same region of the sample. Intensity profiles of one of the smallest features in the EUV image showing visible features as small as 4 pixels (**d**)

The cracks in thin silicon membrane are usually quite large, observed with the optical microscope, in the range of one to tens of microns. Crystal film exhibits also a variable transmission to the visible light, but to extract any additional information another techniques need to be used. The SEM image shows NaCl crystal surface in detail. Its complex structure obscures, however, the information about the underlying membrane. In the SEM image, it is possible to see the surface features, such as cracks, but in some cases, it is not possible to determine their depth.

The EUV mosaic, on the other hand, does not show any surface features because the thick layer of crystallized salt has very low transmission at EUV wavelengths. However, the EUV image shows regions with low thickness, smaller than approx. ~ 100 nm, which are represented by the bright regions. These are very deep gaps in the NaCl layer and small cracks and holes in the supporting Si membrane. Intensity of these regions is in this case related to their transmission. Moreover, as can be seen

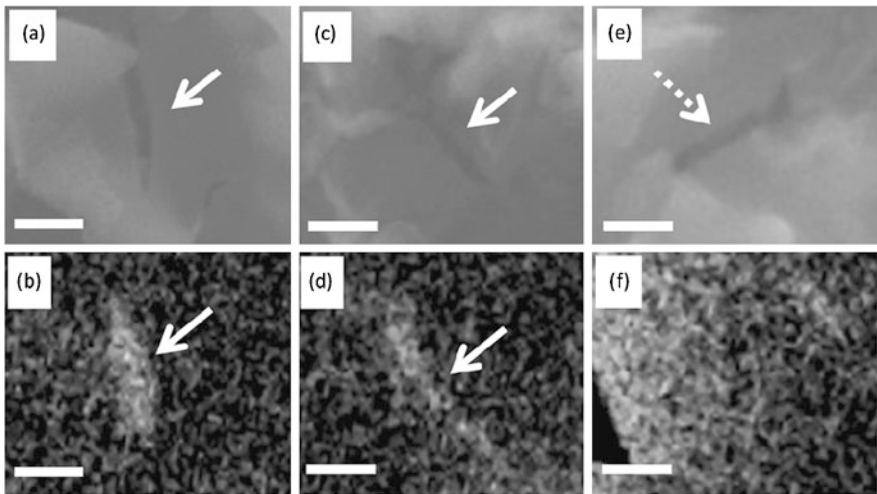


Fig. 3 Comparison between small sections of SEM images (a, c, e) and EUV images (b, d, f) showing different regions of the sample. Some cracks in the sample are deep all the way to the membrane and can be seen in both SEM and EUV images (marked with *white arrows*)—(a–d) and some of the features (marked with *dotted arrow*), are visible in the SEM image (e) but are not present in the corresponding EUV image (f). Scale bar is 2 μm

in Fig. 2(d), features with characteristic size as small as 4 pixels can be resolved. For the given magnification and pixel size of 25.9 nm square, the FWHM width of this small feature approaches 100 nm.

One can notice that there are some features, marked with white arrows in Fig. 3(a–d), that are visible in both SEM and EUV images, showing exactly the same region of the sample. There are also, however, some cracks in the crystal film, visible in the SEM image, such as one marked with dotted arrow in Fig. 3(e), but not present in the EUV image, as can be seen in Fig. 3(f).

Interestingly, some features, such as the cracks in Fig. 3(a, c, e), quite similar in the SEM images, show completely different depth in corresponding EUV images. Because of EUV images we can tell, that the ones, shown in Fig. 3(a, c), are undoubtedly deep all the way to the supporting membrane, while another one in Fig. 3(e) is only a near-surface feature. Thus, the EUV radiation enables additional, complementary information about the object to be obtained, which is based on an intrinsic property of EUV light, and that cannot be obtained directly using SEM microscopy or visible light microscopy.

Similarly, the second sample, composed of ZnO nanofibers, was imaged employing three, previously mentioned, microscopes. Optical micrograph of small region, $\sim 20 \times 20 \mu\text{m}^2$ in size, of the mesh, containing the nanofibers, near one of the bars of the mesh, is shown in Fig. 4(a). The micrograph was obtained with the same objective. Again, for comparison, the same region was imaged using EUV microscope and SEM microscope (Quanta 3D FEG, from FEI). SEM image was obtained at 30 kV with magnification of $\sim 5000\times$ (sample to screen magnification). SEM im-

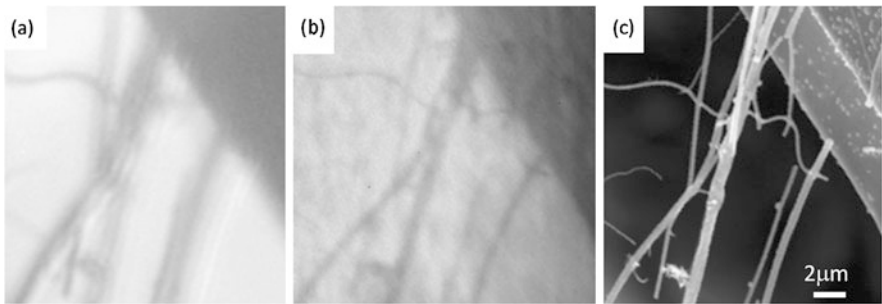
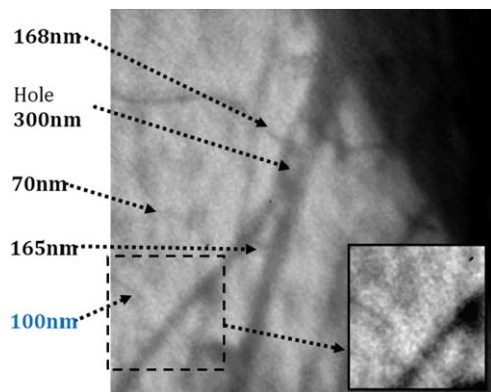


Fig. 4 Comparison between images of ZnO nanofibers, image size $\sim 20 \times 20 \mu\text{m}^2$, obtained with different methods. Optical micrograph (a) with $100\times$, $\text{NA} \sim 1$ objective, EUV microscope image (b), 100 EUV pulses exposure, $690\times$ magnification, $\text{NA} \sim 0.138$, (c) SEM micrograph at acceleration voltage of 30 kV, magnification $\sim 5000\times$ (sample to screen magnification)

Fig. 5 EUV microscope image showing ZnO nanofibers. Nanofibers as small as 100 nm are visible, especially in the contrast enhanced section



age of the sample, $\sim 20 \times 20 \mu\text{m}^2$ in size, is shown in Fig. 4(c) and corresponding EUV image—in Fig. 4(b). For the EUV image the magnification was $690\times$ (FZP magnification).

It is easy to notice, that EUV image of the nanofibers has much better spatial resolution than the diffraction limit of the optical microscope, theoretically equal to $0.61\lambda/\text{NA} \sim 300 \text{ nm}$ ($\lambda = 500 \text{ nm}$, $\text{NA} \sim 1$).

Figure 5 shows some characteristic dimensions of the sample, where single, separated nanofibers, as small as 100 nm, are visible. Smaller nanofibers, $\sim 70 \text{ nm}$ in diameter, scatter much less light, their transmission is higher and they appear much wider due to the diffraction limit, $0.61\lambda/\text{NA} = 61 \text{ nm}$ ($\lambda = 13.8 \text{ nm}$, $\text{NA} \sim 0.138$).

The last sample, composed of ZnO nanofibers on top of a silicon nitride membrane, imaged using EUV microscope can be seen in Fig. 6(a, b). Size of the EUV images is $\sim 20 \times 20 \mu\text{m}^2$, 100 EUV pulses exposure, $690\times$ magnification. White, solid arrows indicate cracks in 50 nm thick silicon nitride membrane, while dotted arrows show ZnO nanofibers. The fibers are larger here, usually between 380 and 570 nm in diameter, as measured from the EUV image.

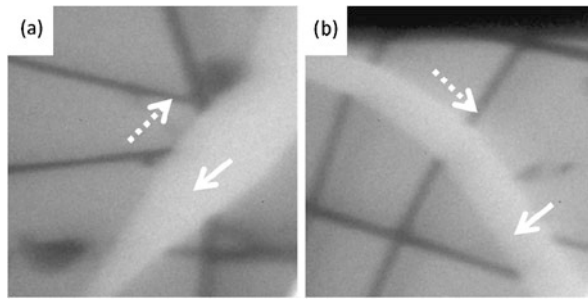


Fig. 6 Two examples of EUV images of ZnO nanofibers (no annealing) deposited on silicon nitride membrane **(a, b)**, image size $\sim 20 \times 20 \mu\text{m}^2$, 100 EUV pulses exposure, $690\times$ magnification, NA ~ 0.138 . Solid arrows indicate cracks in 50 nm thick silicon nitride membrane, dotted arrows show ZnO nanofibers 380–570 nm in diameter

4 Conclusions

We have demonstrated imaging of nanostructures using a desk-top EUV transmission microscope based on laser-produced plasma from argon-based gas-puff target and Fresnel optics. Features with characteristic dimensions as small as 100 nm were resolved; moreover, we showed that EUV light allows straightforward extraction of meaningful information about sub-100 nm thin, dielectric films by a direct observation. No specific sample preparation is required, such as conductive coating for the SEM and it is still photon-based imaging, important in some applications, such as thin film studies of electron beam photoresists. The short attenuation length of EUV photons in almost any material can be utilized to perform imaging with enhanced optical contrast. Thus, EUV microscopy can be employed in thin layer studies providing information complementary to optical and SEM microscopy. We also presented results of imaging of ZnO nanofibers, showing improved spatial resolution and good optical contrast of this material at EUV wavelengths.

The work, presented in this paper, is a part of an effort to develop a novel compact high-resolution imaging system that may find applications in different areas of science and technology, such as material science, biomedicine, nanotechnology, and other fields. Our future plans also include development of a SXR microscope based on Ar gas puff target source [9], capable of imaging in the XUV “water window” spectral region.

Acknowledgements The research was supported by the Foundation for Polish Science, HOMING 2009 Programme, Grant number HOM/2009/14B, the Ministry of Science and Higher Education of Poland, LASERLAB-EUROPE III and GA AV CR KAN300100702 project. We thank L. Pina and T. Feigl for their help in the preparation of EUV optics.

References

1. Attwood, D.: Soft X-Rays and Extreme Ultraviolet Radiation. Cambridge University, Cambridge (1999)

2. Vaschenko, G., Brewer, C., Brizuela, F., Wang, Y., Larotonda, M.A., Luther, B.M., Marconi, M.C., Rocca, J.J., Menoni, C.S.: Sub-38 nm resolution tabletop microscopy with 13 nm wavelength laser light. *Opt. Lett.* **31**, 1214–1216 (2006)
3. Wachulak, P.W., Bartnik, A., Fiedorowicz, H.: Sub-70 nm resolution tabletop microscopy at 13.8 nm using a compact laser–plasma EUV source. *Opt. Lett.* **35**(14), 2337–2339 (2010)
4. Wachulak, P.W., Bartnik, A., Fiedorowicz, H., Kostecki, J.: A 50 nm spatial resolution EUV imaging–resolution dependence on object thickness and illumination bandwidth. *Opt. Express* **19**(10), 9541–9550 (2011)
5. Djurisic, A.B., Ng, A.M.C., Chen, X.Y.: ZnO nanostructures for optoelectronics: material properties and device applications. *Prog. Quantum Electron.* **34**, 191–259 (2010)
6. Stafiniak, A., Boratynski, B., Baranowska-Korczyk, A., Szyszka, A., Ramiaczek-Krasowska, M., Prazmowska, J., Fronc, K., Elbaum, D., Paszkiewicz, R., Tlaczala, M.: A novel electrospun ZnO nanofibers biosensor fabrication. *Sens. Actuators B* **160**, 413–418 (2011)
7. Fiedorowicz, H., Bartnik, A., Jarocki, R., Kostecki, J., Krzywinski, J., Mikołajczyk, J., Rakowski, R., Szczurek, A., Szczurek, M.: Compact laser plasma EUV source based on a gas puff target for metrology applications. *J. Alloys Compd.* **401**, 99 (2005)
8. Wachulak, P.W., Bartnik, A., Fiedorowicz, H., Feigl, T., Jarocki, R., Kostecki, J., Rakowski, R., Rudawski, P., Sawicka, M., Szczurek, M., Szczurek, A., Zawadzki, Z.: A compact, quasi-monochromatic laser-plasma EUV source based on a double-stream gas-puff target at 13.8 nm wavelength. *Appl. Phys. B* **100**(3), 461–469 (2010)
9. Wachulak, P.W., Bartnik, A., Fiedorowicz, H., Rudawski, P., Jarocki, R., Kostecki, J., Szczurek, M.: “Water window” compact, table-top laser plasma soft X-ray sources based on a gas puff target. *Nucl. Instrum. Methods Phys. Res., Sect. B, Beam Interact. Mater. Atoms* **268**(10), 1692–1700 (2010)

Chapter 44

Experiments to Diagnose Plasma with a Soft X-Ray Laser Double-Frequency Grating Interferometry

C. Wang, H.H. An, Z.H. Fang, J.R. Sun, W. Wang, W.D. Zheng, X.M. Qiao, and S.J. Wang

Abstract We developed a kind of soft x-ray double frequency grating shearing interferometry to diagnose hot dense plasma electron density. The method is very suitable for the measure on high-Z material plasma near critical surface, because of its special advantages of suppression of plasma radiation noise and responding to density dispersion. Experiments on diagnosing a series of plasma, such as plasma of Au foil target, plasma inside a tube, collision plasma between different material, were carried out with this method. The experiments acquired good interference pattern images. The high quality images well proved the method was stable and practical.

1 Introduction

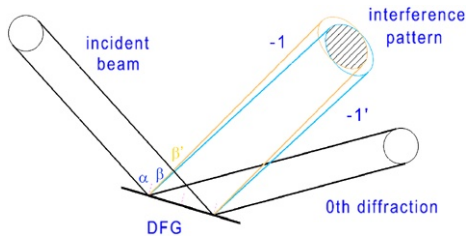
Experimental diagnosis on hot dense plasma near critical surface has important meaning to the research works of inertial control fusion (ICF) and plasma physics fields. There is special advantage of soft x-ray laser probe method, which has become an valid and practical technique. Many methods of measuring plasma have been developed with soft x-ray laser as a probe, such as interferometry [1–6], deflectometry [7, 8], shadow image [9] and Tomeson scatter [10, 11] in the past years. The interferometry is more advantage for understanding plasma developing process and comparing between theoretic simulations and experimental results.

The first demonstration of soft x-ray laser interferometry on measuring plasma was exhibited in 1995 by LLNL [1]. They used multilayered component as beam-splitter and made use of a tilt Mach-Zehnder interferometry. A few years later, the author's group also repeated the same experiments [5]. The well results of both experiments indicated the interferometry were feasible with advantages of clear optical road, big sight field and simple data processing. However there are some considerable points for real practice. The first one was surface figure problem of multilayered

C. Wang (✉) · H.H. An · Z.H. Fang · J.R. Sun · W. Wang · S.J. Wang
Shanghai Institute of Laser Plasma, Shanghai, China
e-mail: wangch@mail.shcnc.ac.cn

W.D. Zheng · X.M. Qiao
Institute of Applied Physics and Computational Mathematics, Beijing, China

Fig. 1 Basic principle of a DFG interference



beam-splitter. The second one was very complicated regulation of optical road and the last one was hard request of soft x-ray laser probe source. A new technique, which used gratings as beam-splitter, was developed and well resolved the surface figure problem of multilayered beam-splitter in about 2000 [4]. But the others difficulties still existed. Besides of M-Z interferometry, some other interferometries, such as Lloyd's mirror [3] and Fresnel bi-mirrors, were tried to measure plasma, but these were less than M-Z method at both stripe quality and applied effect.

In recent years, we have developed a kind of method, so called soft x-ray laser double frequency grating (DFG) interferometry. The DFG interferometry is a common technique in visible light band [12, 13]. There is no report that this method was carried out in soft x-ray wave band. The method is good to avoid the difficulties of M-Z interferometry system, and the stripe quality was also very well.

2 Basic Principle of DFG Interference

The key element is a DFG that owns two kinds of different frequency periods, such as d and d' . When a beam of light injects a DFG, all the 0 order diffraction beams are at the same direction and the DFG is just like a plane mirror. But for other order diffraction, for example –1st order, each beam is divided to two beams with difference directions due to the different grating frequency periods. The diffraction angles β and β' accord to the formula:

$$\begin{cases} \sin \beta - \sin \alpha = -\lambda/d \\ \sin \beta' - \sin \alpha = -\lambda/d' \end{cases} \quad (1)$$

where α is incident angle, λ is the wavelength of light. There may be a large area where the two beams overlap and the interference may happen. The basic principle is shown in Fig. 1.

The two beams which participate an interference are in fact from a same beam of light by deviating a part of distances breadthwise each other, and the optical path difference comes from the subtraction value between different positions of the same beam. The optical path difference causes the deflexion of interference fringes, from which the electron density distribution can be calculated. The given result is not the real electrical density distribution but a subtraction difference one, labeled $\Delta n_e(z)$ if only taking one dimension condition as an example, where z is the vertical direction of interference fringe. Then the real electron density can be obtained by:

$$n_e(z) - n_e(z + z_\Delta) = \Delta n_e(z) \quad (2)$$

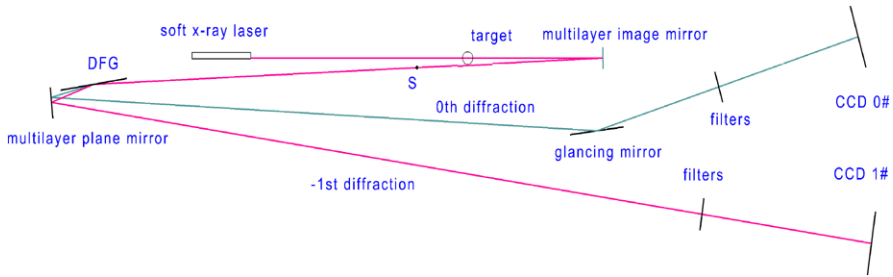


Fig. 2 The experimental setup of DFG interferometry

where z_Δ is the respective offset at z direction, and $n_e(z)$ means the electron density at the position of z .

3 Experimental Setup

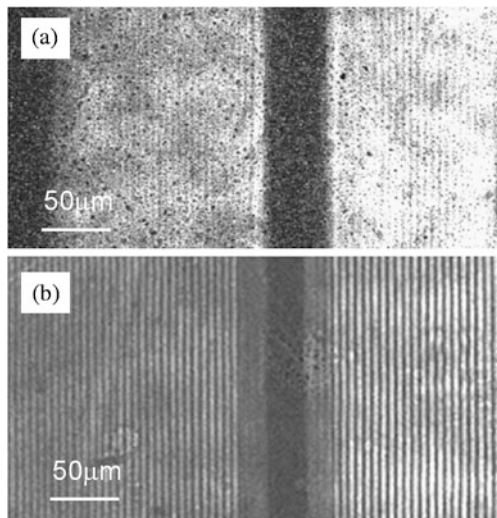
The experiments were carried out with SG-II high power laser system of Chinese National Laboratory on High Power Laser and Physics. The experimental setup is schematically shown in Fig. 2. The system consisted of a soft x-ray laser source, an image multilayer mirror, a DFG and several plane multilayer mirrors.

A collisionally pumped nickel-like silver soft x-ray laser operating at 13.9 nm was used as the probe source. The x-ray laser was produced with double targets coupling technique by irradiating two 16 mm long Ag-coated glass targets with two beam from SG-II ($\lambda = 1.053 \mu\text{m}$, 70 ps, 70 J, 1 % prepulse ahead 3 ns) at an intensity of $6 \times 10^{13} \text{ W cm}^{-2}$. The output energy of the x-ray laser is approach to several hundreds μJ . The divergence is approximately $3 \text{ mrad} \times 5 \text{ mrad}$ and output pulse duration $30 \sim 50 \text{ ps}$. The short pulse and high brightness of the soft x-ray laser allowed us to obtain an interferogram in a single 50 ps exposure. The exposure time was so short that the effects of vibrations could be ignored. The probe source injected directly into plasma to be probed where was 500 mm from x-ray laser without collimation, so the field of view was about $1.5 \text{ mm} \times 2.5 \text{ mm}$ and it is enough to measure all the interesting area of large scale plasma.

The plasma to be probed produced by another beam laser irradiating a target was imaged onto a CCD with a 10 mm radius of curvature multilayer mirror with the focus of about 270 mm. A series of plasma may be studied by changing different targets and drive conditions. We mainly payed attention to the 0 and -1 st order diffraction, so two CCD were used to record the signals respectively. The CCD 0# recorded the 0 diffraction and the image was just like a shadow of plasma. The CCD 1# recorded the -1 st diffraction that might show the interference patterns.

The DFG is the most critical element of this system. For our experiments we chose the frequency periods of 1000 and 1003 lines per mm. The incident angle was designed as about 84° . The diffraction angle difference $\beta - \beta'$ was about 0.012° and the fringe separation could be estimated to about $150 \mu\text{m}$.

Fig. 3 Experimental static images. (a) came from the 0 order diffraction. (b) came from the -1 st order diffraction



4 Experimental Results

Figure 3 shows a typical experimental static images. The static experiments means the object was only a target and no plasma was created. So the images were not disturbed by plasma. Figure 3(a) came from the 0 order diffraction signal, so it can be regarded as the static target shadow image. The shadow of target was clear, however some slight stripes can be seen, which could be caused by the effect of beat frequency of DFG. Figure 3(b) came from the -1 order diffraction signal, so it is a static DFG interference pattern. There were two clear target shadows overlapped each other. The interference stripes are clearly observed in Fig. 3(b), and the fringe visibility is about 0.5 ± 0.1 .

Figure 4 shows a series of DFG interference experimental results with different plasmas. Figure 4(a) and (b) show the simple experimental setup and the result of collision plasma. The plasma was created by a drive laser irradiating a pair of vertical plane target with a lens array uniform focus of about $450 \mu\text{m} \times 450 \mu\text{m}$. The two targets were coated with $5 \mu\text{m}$ -thickness aurum, so the component of plasma was Au ions. The clear inference stripes and obvious stripe movement indicate abundant physical contents.

Figure 4(c) and (d) showed another experimental setup and the result of the plasma in a hohlraum. The hohlraum was indeed a tube cavity with a hole at side. The drive laser injected from the hole and heated the plasma in hohlraum, and a soft x-ray laser probe passed along the axis direction of hohlraum and diagnosed the plasma. (d) is the experimental image and the stripes in hohlraum was fairly clear.

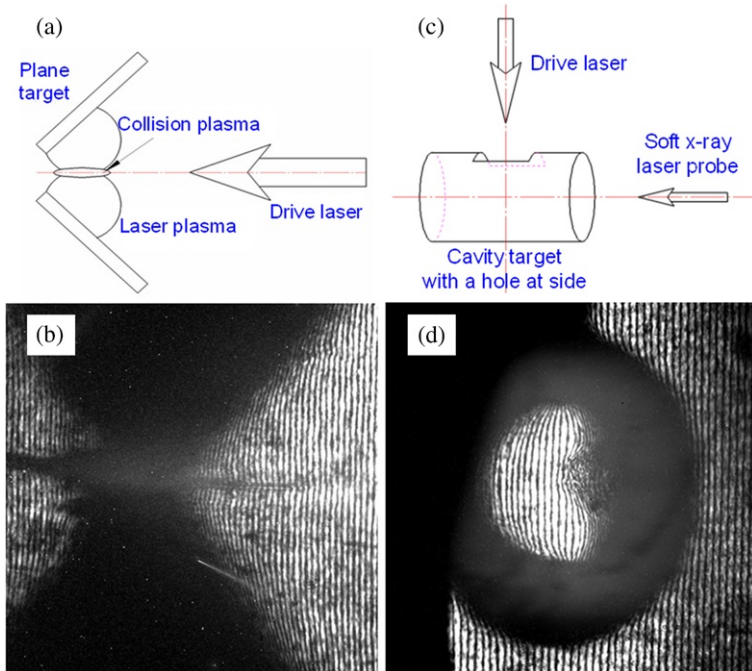


Fig. 4 Some DFG interference experimental results. (a) and (b) showed the setup and result about collision plasma. (c) and (d) showed the setup and result about the plasma in a hohlraum

5 Conclusion

The experiments show the method of soft x-ray laser DFG interferometry is a good tool to diagnose laser plasma near critical density, especially high-Z matter plasma. The experimental images of inference patterns are simply shown and the data processing are going now.

References

1. Da Silva, L.B., et al.: Electron density measurements of high density plasmas using soft X-ray laser interferometry. *Phys. Rev. Lett.* **74**, 3991 (1995)
2. Wan, A.S., et al.: Electron density measurement of a colliding plasma using soft-x-ray laser interferometry. *Phys. Rev. E* **55**, 6293 (1997)
3. Rocca, J.J., et al.: Soft-x-ray laser interferometry of a plasma with a tabletop laser and a Lloyd's mirror. *Opt. Lett.* **24**, 420 (1999)
4. Filevich, J., et al.: Dense plasma diagnostics with an amplitude-division soft-x-ray laser interferometer based on diffraction gratings. *Opt. Lett.* **25**, 356 (2000)
5. Wang, C., et al.: Experimental diagnoses of plasma electron density by interferometry using an x-ray laser as probe. *Acta Phys. Sin.* **54**, 202 (2005)
6. Purvis, M., et al.: Dynamics of converging laser-created plasmas in semicylindrical cavities studied using soft x-ray laser interferometry. *Phys. Rev. E* **76**, 046402 (2007)

7. Ress, D., et al.: Measurement of laser-plasma electron density with a soft X-ray laser deflectometer. *Science* **265**, 514 (1994)
8. Wang, C., et al.: Measurement of electron density distribution in a laser plasma with soft x-ray laser deflectometry. *Acta Phys. Sin.* **51**, 847 (2002)
9. Cauble, R., et al.: Micron-resolution radiography of laser-accelerated and X-ray heated foils with an X-ray laser. *Phys. Rev. Lett.* **74**, 3816 (1995)
10. Baidis, H.A., et al.: Thomson scattering diagnostic of solid density plasmas using X-ray lasers. *Rev. Sci. Instrum.* **73**, 4223 (2002)
11. Rus, B., et al.: X-ray laser Thomson scattering at 21 nm of laser-heated high-density foil plasmas. In: *X-Ray Laser 2006*, pp. 577–583 (2006)
12. Wyant, J.C.: Double frequency grating lateral shear interferometer. *Appl. Opt.* **12**, 2057 (1973)
13. Ming, H., et al.: Phase shifting in shearing interferometry with double frequency grating and semiconductor laser to measure temperature field. In: *Proc. SPIE*, vol. 2321, p. 246 (1994)

Chapter 45

Heavy-Ion Spectroscopy with X-Ray Lasers at GSI

**B. Zielbauer, B. Ecker, P. Neumayer, K. Cassou, S. Daboussi, O. Guilbaud,
S. Kazamias, D. Ros, T. Kuehl, U. Eisenbarth, S. Goette, D. Winters,
V. Bagnoud, and T. Stoehlker**

Abstract Different pumping schemes for soft X-ray lasers have been investigated at the PHELIX laser facility, including a double-target seeding approach at 18.9 nm. A technical feasibility study of using a Mo XRL beam of several μJ as an excitation source for heavy-ion spectroscopy in a storage ring has been carried out. XRL photon numbers and the beam transport under ultra-high vacuum conditions over almost 30 m are the major challenges.

1 Introduction

One of the strong motivations to develop XRL sources at GSI and FAIR was their applicability in the spectroscopy of highly charged heavy-ions in storage rings. For example, in Li-like systems, the measurement of fine structure transitions enables a direct experimental access to nuclear structure which allows the comparison to theoretical predictions [1]. Several such investigations have already been carried out using lasers in the visible wavelength range, but the application of XRLs with their short wavelength will allow a much deeper insight. And although the XRL wavelength cannot be tuned to perform scans, the effective wavelength exciting the stored ions can be changed very precisely by changing the ions' velocity and using the Doppler up-shift in counter-propagation.

B. Zielbauer (✉) · B. Ecker · T. Kuehl · V. Bagnoud · T. Stoehlker
Helmholtz Institute Jena, Helmholtzweg 4, 07743 Jena, Germany
e-mail: b.zielbauer@gsi.de

B. Zielbauer · T. Kuehl · U. Eisenbarth · S. Goette · D. Winters · V. Bagnoud · T. Stoehlker
GSI Helmholtz Center for Heavy-Ion Research, Planckstr. 1, 64291 Darmstadt, Germany

B. Ecker · T. Kuehl
Johannes Gutenberg University Mainz, Saarstr. 21, 55122 Mainz, Germany

P. Neumayer · T. Kuehl
ExtreMe Matter Institute EMMI, Planckstr. 1, 64291 Darmstadt, Germany

K. Cassou · S. Daboussi · O. Guilbaud · S. Kazamias · D. Ros
LASERIX-CLUPS/Laboratoire de Physique des Gaz et des Plasmas, 91400 Orsay, France

2 X-Ray Laser Development

Since the heavy-ions can be stored in the experimental storage ring (ESR) over, depending on the ion species, up to several tens of minutes, a high repetition rate pump laser system would be rather beneficial. Due to the high-energy (Nd:glass based) orientation of the PHELIX laser system at GSI, the high repetition rate developments are carried out off-site at the LASERIX facility [2], while first XRL spectroscopy experiments will be performed with the available PHELIX preamplifier with shots every 2 minutes. However, also here, an upgrade to 3 shots/min is under way.

The amount of XRL photons available for the excitation process proves to be the most critical factor, and calculations show that with reasonable efficiency assumptions on the XRL as well as the spectroscopy part, at least 1 μJ of XRL pulse energy is required in order to reach a fluorescence signal of more than a few counts/shot. Thus, the XRL development here is driven by optimization towards high and stable XRL photon numbers.

Our most recent approach to this, outlined in more detail in [3], is the amplification of a standard DGRIP Mo XRL in a comparably wide plasma column using a butterfly-shaped setup with two independent targets. Recent simulations with the ARWEN code [4] show that with this approach, it should be possible to overcome the transversal lasing in the amplifier plasma and achieve a high XRL output signal with good beam quality. The Mo XRL was chosen as a source because of the comparably low pump laser energy requirements, which gives a lot of margin with a 5 J/IR pulse pump laser, but which also allows for stable 10 Hz operation with a high yield of shots per target position [5]. Also, the Mo XRL wavelength of 18.895 nm has been measured [6] with a precision which is sufficient for the spectroscopy experiment where the uncertainty of the ion velocity is on the same order of magnitude.

3 Installation and Setup

Figure 1 shows a top view of the planned installation. The PHELIX preamplifier beam (60 mm diam., 10 J, 1053 nm) will be transported over more than 50 m from the PHELIX building to the ESR hall where it will be compressed to a few ps pulse duration in a dedicated double-pass compressor inside the ESR radiation shielding environment. Another beamline will transport the IR beam over about 5 m to the XRL target chamber with the butterfly setup. In order to minimize XRL beam losses, this chamber is situated as closely to the injection into the straight section of the ESR as possible and the XRL beam transport and collimation will be achieved with only one 90° off-axis parabola and one flat mirror, both XUV multilayer coated. After the flat (steering) mirror, the XRL beam has to propagate almost 15 m to the center of the straight section of the ESR which is the only convenient spot where the fluorescence light can be detected. The excited ions, propagating clockwise seen from top, emit this light in a cone in their forward direction, and since the decay is so fast, this happens mostly within the interaction region of about 1 m length

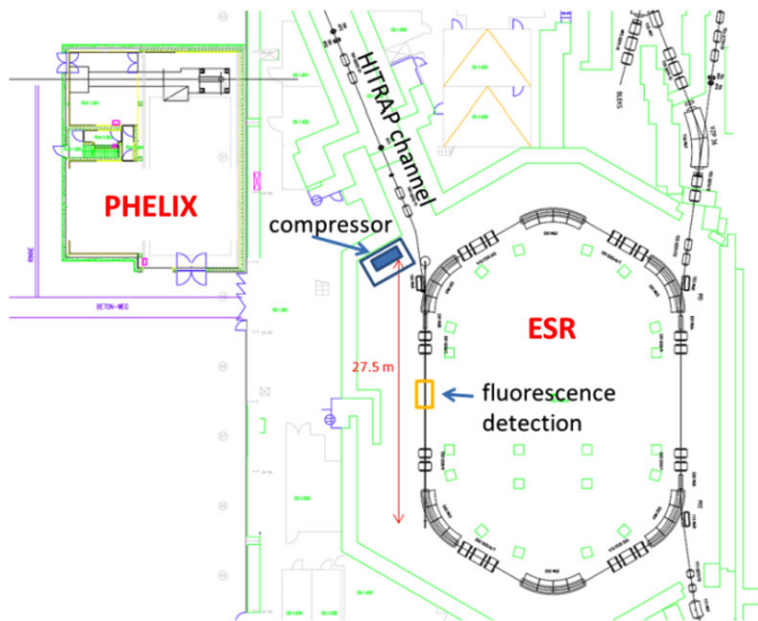


Fig. 1 Top view of the planned installation. The IR pump pulse is generated in the PHELIX building, transported to a compressor and then on into the XRL target chamber. The XRL beam is then propagating through the entire straight section of the ESR on the left side, exciting the ion bunch which is running clockwise

between the few-meter long ion bunch and the XRL beam. For alignment and on-shot diagnostics purposes, the XRL pulse is propagating on to the end of the straight section onto an in-vacuum XUV CCD camera.

A major challenge in this scenario comes from the fact that the ESR is operating at a vacuum level around 10^{-11} mbar which is not compatible with a typical XRL setup. Thus, the XRL beam needs to be coupled in and out of the ESR vacuum through a system of shutter valves, equipped with thin metal filters and differential pumping through small apertures. In addition, a set of rapid shutter valves equipped with glass windows allows for a pre-alignment of the beamline with a visible pilot laser as well as for maintaining the vacuum integrity in case of metal filter damage.

References

1. Otten, E.: *Treatise on Heavy-Ion Sciences*. Plenum, New York (1989)
2. Guilbaud, O., et al.: In: Sebban, S., et al. (eds.) *X-Ray Lasers 2012*. Springer Proceedings in Physics, vol. 147. Springer, Cham (2013). Chapter 18 in this book
3. Ecker, B., et al.: In: Sebban, S., et al. (eds.) *X-Ray Lasers 2012*. Springer Proceedings in Physics, vol. 147. Springer, Cham (2013). Chapter 16 in this book

4. Oliva, E., et al.: In: Sebban, S., et al. (eds.) X-Ray Lasers 2012. Springer Proceedings in Physics, vol. 147. Springer, Cham (2013). Chapter 33 in this book
5. Zielbauer, B., et al.: Appl. Phys. B **100**, 731–736 (2010)
6. Li, Y., et al.: Phys. Rev. A **58**, R2668 (1998)

Index

1–9

100 Hz repetition rate, 216
1D-radiative transfer code, 181, 182
8.85 nm, 215
8.85 nm wavelength, 216

A

Ablation, 148
Al/Mo/B4C multilayer mirror, 159
Amplification, 159
Amplification chain, 206, 207
Amplification of sub-picosecond duration, 154
Amplified line profile, 181–183
Amplified spontaneous emission, 203, 204
An atom in the external field, 7
Applications, 39
Argon laser, 231
Argon-based gas-puff target, 275
ARWEN code, 159
ASE, 203, 204, 206
ASE level, 89
Atomistic model, 122
Attenuation length, 275
Average-atom code, 194, 196, 197

B

B-integral, 33, 235–237
Barrier layer, 161, 163, 164
Baskakov-Popov-Papadakis, 106
Beam pointing, 129
Beam stability, 227
Biomedicine, 275
Brightness, 229
Brilliance, 3

C

Calcination, 271
Capillary discharge, 231, 232

Channel, 251

Chirped-pulse amplification, 35, 209
Classical molecular dynamics (MD) simulations, 50
Coherence volume, 129, 130
Coherent imaging of inclined objects, 19
Collector, 228
Collision plasma, 280
Collisional-radiative, 83
Collisionally pumped, 279
Complementary information, 273
Computational domain, 105
Condenser, 227, 228
Contrast, 132
Critical density, 154, 281
Crystal film, 272
Cut-off frequency (CF), 7, 9, 11, 12

D

Deflectometric technique, 155
Deflectometry, 155
Deflectometry technique, 159
Degeneracy factor, 130
Dense plasmas, 152, 154, 155, 159
Density gradient, 155, 156
DFG, 278
DGRIP, 89, 100, 101, 103, 284
Diffraction, 278
Diffraction imaging, 80
Diffraction limit, 274
Diffusion barrier layer, 161, 163
Discharge-pumped XUV laser, 231
Divergence, 227–230
Doppler broadening, 49
Double frequency grating, 278
Double pass, 152

Double targets coupling technique, 279
Double-stage, 97, 101

E

Eikonal, 171
Electron density, 278
Electrospinning, 271
Etendue, 229
EUV ablation, 144
EUV microscope, 270, 271
EUV microscopy, 270
EUV radiation, 270, 273
EUV transmission microscope, 275
Extreme ultraviolet (EUV), 263, 269
Extreme ultraviolet (XUV), 7, 8

F

Femtosecond laser, 63
Femtosecond laser ablation, 199
Elettra, 1, 2
Few-Hz repetition rate, 137
Flash imaging, 188
Fourier optics, 35
Fourier transform holography, 166
Fourth generation light source, 1
Free electron laser, 1, 39, 55
Fresnel bi-mirror interferometer, 258
Fresnel optics, 275
Fresnel zone plate, 165, 269
Fringe visibility, 258
Full coherence, 130
FZP magnification, 274
FZP objective, 271

G

Gain duration, 247
Gain media, 171
Gain-guiding, 41
Gain-length product at saturation, 41
Gain-narrowing effect, 128
Gas-puff target, 269
Generalized Talbot effect (GTI), 264
Generation of harmonics, 209
Grazing-incidence, 235
Grazing-incidence pump geometry (GRIP), 137
Grazing-incidence pumping (GRIP), 29, 102

H

Half-pitch spatial resolution, 271
High densities, 152
High electron density, 152
High gain harmonic generation (HGHG), 2
High gain single pass FELs, 2

High harmonic generation, 63, 67
High intensity optical lattice, 14
High order harmonics, 203, 204
High power OPA, 78
High-order harmonic generation (HHG), 7, 8
High-resolution imaging system, 275
Higher-order harmonics, 144, 146
HOH, 203–206
Hohlraum, 41
Hollow targets, 172
Homogeneous broadening, 50
Hydro-code, 171

I

Illumination, 227–229
Imaging, 269
Inhomogeneous broadening, 50
Injection-seeding, 97, 101, 103
Interference patterns, 279
Interferometer, 144, 147
Interferometry, 277
Intrinsic, 181
Intrinsic line profiles, 182
Intrinsic property of EUV light, 273
Irradiance, 235

L

Laboratory-scale sources, 41
Laser ablation dynamics, 117
Laser like pulses in the x-ray, 1
Laser wake field accelerator (LWFA), 55
Laser-plasma EUV source, 270
Laser-plasma sources, 269
Laser-produced plasma, 171, 275
Lensless imaging, 39
Light atom interaction theory, 7, 8
Line profile, 181
Line-focus, 236, 237
Line-focus generation, 235
Linewidth, 258
Linewidth measurement, 159
Low ablation threshold, 122

M

Magnification, 273, 274
Material science, 275
Maxwell-Bloch, 203, 204
Measuring plasma, 277
Microscopy, 185, 227, 230
Mo/Si mirror, 159
Multilayer, 161–163
Multilayer mirror, 161

N

- NaCl crystals, 270
Nanofibers, 273
Nanometer scale resolution imaging, 269
Nanoscale resolution time resolved microscopy, 185
Nanostructures, 275
Nanotechnology, 275
Nd:YLF, 137
Ne-like Zn x-ray laser, 152, 156
Near-field, 229, 230
Ni-like, 29
Ni-like Ag laser $4d - 4p$ ($J = 0-1$) line at 13.9 nm, 51
Nonlinear optics, 63
Non-perturbative theory, 8, 12
Normalized pulse integrated intensity, 130

O

- OFI, 247
Optical contrast, 275
Optical-field-ionization, 244
Optical-parametric chirped-pulse amplification (OPCPA), 137
Optical path difference, 278
Optical transformation, 19

P

- PALS centre, 151, 152
PALS facility, 159
PALS laser facility, 157
Parabolic wave equation, 19, 105
Partial coherence, 126
Partially coherent, 130
Particle correlation effects, 49
Plasma amplifier, 206
Plasma based seeded soft x-ray lasers, 204
Plasma channel, 249
Plasma guiding, 247
Plasma in a hohlraum, 280
Plasma physics, 277
Plasma self-emission, 156
Plasma waveguide, 247, 252
Plasma-based soft-x-ray lasers, 203
Pointing stability, 227–230
Polarization, 127, 143–145, 205, 206
Polarization of radiation emitted by the x-ray laser, 127
Pre-amplifier, 206
Pre-amplifier main-amplifier chain, 207
Prepulses, 89
Probability density, 130
Pulse-front tilt, 35

Q

- QSS, 152, 175, 176
Quasi-steady state, 175

R

- Rabi oscillations, 204
Radiation in the water window, 78
Radiation polarization, 126
Radiative shocks, 239, 240
Ray-tracing, 235–237
Recombination pumping, 252
Reflective optics, 235
Reflective x-ray microscopy, 201
Refraction, 171
Refractive optics, 235, 236
Repetitive laser, 231

S

- Saturation rebroadening, 183
Seeded, 244
Seeding, 246, 283
Shadow of plasma, 279
Soft x-ray, 155, 185, 186
Soft x-ray holograms, 165
Soft x-ray laser, 29, 89, 121, 137, 143, 175, 239
Soft x-ray laser probe method, 277
Soft x-ray laser (SXRL) probe, 117, 118
Soft x-ray range, 2
Spatial coherence, 130, 245
Spatial resolution, 274, 275
Speckle, 126, 245
Speckle contrast, 132
Speckle effect, 126
Speckle structure, 126
Spectral broadening, 49
Spectral linewidth, 175–178
Spectral width, 176
Spectroscopy, 98, 100, 283, 284
Spontaneous emission, 205
SPring-8, 69, 71
Surface modifications, 122
SXRL, 175–179
SXRL ablation, 144, 147

T

- Table-top soft x-ray laser, 216
Talbot distances, 264
Talbot effect, 263
Talbot pattern, 155
TCE, 152
Temperature effect on ASE, 46
Temporal coherence, 175–179, 246
TGRIIP, 101

- Thomson scattering, 193–195, 197
 Time-dependent radiation transport, 83
 Time-dependent Schrodinger equation (TDSE), 8
 Transient collisional-excitation, 30, 228
 Transmission mode, 271
 Transparent boundary condition, 106
 Traveling-wave, 31
 Traveling-wave excitation, 35
 Triple-pulse scheme, 30
 Turning point, 172
- U**
 Ultraviolet, 2
 Undulator, 69, 74, 75
- V**
 Van der Waals forces, 271
 Velocity redistribution, 52
 Visibility curve, 258
 Visibility profile, 258
- W**
 Wake, 203–206
 Water window, 161
- Waveguide, 250, 251
 Waveguiding, 171
 Wavelengths as short as 7.36 nm, 216
- X**
 X-ray laser backlighting, 155
 X-ray laser at 100 Hz repetition rate, 215
 X-ray lasers, 155, 235
 X-ray movie, 72–74
 X-ray reflective microscope, 199
 X-ray source, 159
 X-ray techniques for real time observation of melting and solidification processes, 69
 XRL, 153, 154, 156, 157, 159
 XRL's amplifiers, 152
 XUV laser, 231
 XUV lasers pumped by collisional excitation of Ni-like ions, 50
- Y**
 Young's interferometry, 126
- Z**
 Zn x-ray laser, 151, 153, 154, 157, 159
 ZnO nanofibers, 271